ABSTRACT

This study investigates the behavior of High Strength Concrete (HSC) under uniaxial state of stresses. Emphasis is placed on experimental evaluation of important mechanical and fracture properties. Owing to high brittleness of HSC, experimental results especially on tensile behavior have been largely limited and scarce. In this research, direct uniaxial tension tests are employed for determination of the post-peak tensile softening characteristics of HSC. The softening characteristics of high strength concrete is found to be considerably different than that of normal strength concrete (NSC). Fracture energies evaluated form the descending branch of the stress softening reveal significant drop in the post peak compliance of the high strength concretes. Such relationships of stress-crack separation are vital input for developing a model capable of accurately predicting behavior of HSC in tension.

The obtained softening relationship is incorporated into an non-linear finite element model using ABAQUS program. The model is shown to be successful in predicting the test results of the present study as well as the ones of other researchers. The predictions are of equal degree in accuracy for both the load-crack mouth opening displacement (CMOD) and load-Deflection (LPD) responses. Performing of a parametric study as well as development of a methodology that suggests the use of load-CMOD response in beam fracture tests as an alternative method of determining the fracture toughness (G_F) from beam tests are undertaken. Important parameters such as flexural strength, size of process zone of normal and high strength concrete are also determined using the FEM model. It is found that for an increase of about 30% in the fracture

toughness G_F and the tensile strength f'_t of HSC, the reduction in the difference between flexural strength and tensile strength is considerable and the size of process zone is also significantly smaller in HSC as compared to NSC. It is shown that to apply Linear Elastic Fracture Mechanics (LEFM) principles, a minimum size (depth) of beam of HSC is about 9.0" whereas for NSC the minimum depth of the beam is almost twice as much i.e. about 18.0". An important recommendation for determining the fracture energy G_F from load-CMOD curves instead from the conventional Load-Deflection response is shown to produce lesser variation in G_F values since CMOD measurements are less likely to be affected by experimental setups and errors. Errors that are known to generally affect the load-line deflection (LPD) measurements can cause significant inflated values of fracture energy G_F to be reported. Finally based on the test results of beam bending tests, a recommendation is made regarding a suitable size of beam specimen that can be used as a standardized fracture test specimen. The beam specimen of span depth (S/D) ratio of 4 is found to be more suitable than the RILEM recommended beam size S/D = 8.

FRACTURE MECHANICS OF HIGH STRENGTH CONCRETE MEMBERS

by
Rajendra K. Navalurkar

A Dissertation
Submitted to the Faculty of
New Jersey Institute of Technology
in Partial Fulfillment of the Requirements for the Degree of
Doctor of Philosophy

Department of Civil and Environmental Engineering

October 1996

APPROVAL PAGE

FRACTURE MECHANICS OF
HIGH STRENGTH CONCRETE MEMBERS

Rajendra K. Navalurkar

Dr. C. T. Thomas Hsu, Thesis Advisor — Date
Professor of Civil and Environmental Engineering, NJIT

Dr. Methi Wecharatana, Thesis Co-Advisor — Date
Professor of Civil and Environmental Engineering, NJIT

Dr. William Spillers, Committee Member — Date
Distinguished Professor and Chairman of Civil and Environmental Engineering, NJIT

Professor Edward Dauenheimer, Committee Member — Date
Professor and Associate Chairman of Civil and Environmental Engineering, NJIT

Dr. Perumalasamy Balaguru, Committee Member — Date
Professor of Civil and Environmental Engineering, Rutgers University

BIOGRAPHICAL SKETCH

Author: Rajendra K. Navalurkar

Degree: Doctor of Philosophy

Date: October 1996

Undergraduate and Graduate Education:

- Doctor of Philosophy in Civil Engineering,
  New Jersey Institute of Technology, Newark, NJ, 1996

- Master of Science in Civil Engineering,
  New Jersey Institute of Technology, Newark, NJ, 1991

- Bachelor of Science in Civil Engineering,
  R. V. College of Engineering, Bangalore, India, 1988

Major: Civil Engineering

Presentations and Publications:

Farhad Ansari and Rajendra K. Navalurkar
"Kinematics of Crack Formation in Cementitious Composites using Fiber Optics", Journal of Engineering Mechanics, ASCE, Vol. 119, No. 5, May 1993, pp. 1048-1061.

Farhad Ansari and Rajendra K. Navalurkar
A Fiber Optic Sensor for the Determination of Dynamic Fracture Parameters in Fiber Reinforced Concrete," Applications of Fiber Optic Sensors in Engineering Mechanics, Ed. *Farhad Ansari,* ASCE Publication, Feb. 1993, pp. 160-176.

Farhad Ansari and Rajendra K. Navalurkar
"Crack Opening Mechanism in Fiber Reinforced Concrete subjected to Impulsive Loading," Proceedings of RILEM International Workshop, High Performance Fiber Reinforced Cement Composites, Mainz, Germany, Eds. *H. W. Reinhardt & A. E. Naaman,* June 1991, pp. 242-252.

Farhad Ansari and Rajendra K. Navalurkar

"Fracture Properties of Fiber Reinforced Concrete subjected to Impulsive Loading," Materials Research Society, Symposium Proceedings, Vol. 211, 1991, pp. 159-168.

Rajendra K. Navalurkar and Farhad Ansari

"Tensile Properties of High Performance Concrete", Presented at the International Workshop on High Performance Concrete cosponsored by ACI held at Bangkok, Thailand, November 21-22, 1994.

ACKNOWLEDGMENT

The author wishes to express his sincere gratitude to his advisor, Professor C. T. Thomas Hsu and to co-advisor Professor Methi Wecharatana for their guidance, patience and timely moral support during this research.

Special thanks to Professor William Spillers, Professor Edward Dauenheimer and Professor P. N. Balaguru for serving as members of the committee.

The author acknowledges the NSF grant # CEE 8308339 which enabled the purchase of the 100 kip MTS testing system and also NSF grant # CMS 9413725 which was used for developing the Material Testing System (1000 kip MTS 815) for Research and Development of High Performance Cementitious Composites here at New Jersey Institute of Technology. This study would not have been possible without the availability of the machines funded by the above mentioned grants. Also, the financial assistance received over the course of study from the Civil Engineering Department is gratefully appreciated.

The author wishes to thank Mr. Allyn Luke for all his efforts in solving any problems with the equipment encountered during the experiments in the Concrete Laboratory. The help and expertise provided by Mr. John Eimess in developing testing setups is greatly appreciated.

The author also thanks Mr. Mohammad Shams and Dr. Sanjay Mehta for their help and guidance.

And finally, I am greatly indept to the moral support and patience shown by my wife and rest of my family.

TABLE OF CONTENTS

Chapter **Page**

TABLE OF CONTENTS
(Continued)

Chapter **Page**

TABLE OF CONTENTS
(Continued)

Chapter **Page**

LIST OF TABLES

LIST OF TABLES
(Continued)

Table **Page**

LIST OF FIGURES

Figure **Page**

LIST OF FIGURES
(Continued)

Figure **Page**

LIST OF FIGURES
(Continued)

Figure **Page**

LIST OF FIGURES
(Continued)

Figure **Page**

LIST OF FIGURES
(Continued)

Figure **Page**

LIST OF FIGURES
(Continued)

Figure **Page**

LIST OF FIGURES
(Continued)

Figure **Page**

LIST OF FIGURES
(Continued)

Figure **Page**

LIST OF FIGURES
(Continued)

Figure **Page**

LIST OF FIGURES
(Continued)

Figure **Page**

LIST OF FIGURES
(Continued)

Figure **Page**

LIST OF FIGURES
(Continued)

Figure **Page**

CHAPTER 1

INTRODUCTION

1.1 General

The tensile capacity of concrete is only a small portion of the compressive strength capacity (about 1/10 for normal concrete). In order to raise the tensile capacity, reinforcement of various kinds are often used. When the reinforcement is anchored or spliced the tensile and shear strength of the concrete will be very critical for the strength of the structure. In all structures we have to rely on the tensile and shear capacity of the concrete whether it is reinforced or not.

When the tensile strength of a material is reached in a structure, cracking will occur. The study of the conditions around the crack tip is called "Fracture Mechanics". In this dissertation, the application of fracture mechanics to various structural (unreinforced) members is studied. Emphasis is given to the experimental determination of various important fracture parameters and also to study the behavior of High Strength Concrete (HSC) members.

Fracture mechanics is a theory of failure which was originated in 1920 by Griffith (1920, 1924) and was for a long period applied only to metallic structures and ceramics. Concrete structures, on the other hand, have been so far successfully designed and built without any use of fracture mechanics, even though the failure process involves crack propagation. This is not surprising since fracture mechanics takes into account the growth of distributed cracking and its localization which was unknown until about 1980. During the 1980's however the study of fracture mechanics in concrete has emerged and

as a result there is an explosion in research activities. The application of fracture mechanics to concrete is important for various reasons (ACI 446.1 R-91 1991). Important and compelling reasons for using fracture mechanics are:

- Energy is used as a failure criterion, in conjunction with stresses and strains
- It takes into account crack propagation
- It accounts for effect of size of structures on their nominal strength

The science of fracture mechanics can be divided into two general categories: Linear Elastic Fracture Mechanics (LEFM) and Elastic Plastic Fracture Mechanics (EPFM). The theory of LEFM has been well developed for the past thirty years and has been successfully applied to metallic structures. Its application to concrete was first attempted long ago. The idea of using stress intensity factors had already appeared in early 1950's and serious investigation started in the 1960's by Kaplan et. al. (Kaplan 1961). Initially the application of LEFM to concrete did not yield good results (Kesler, Naus and Lott 1971). The reason, it is now understood, is that in concrete there is a large microcracking zone (also known as the process zone) in front of the crack tip. Failure of concrete involves stable crack growth in the large cracking zone and formation of a large process zone even before the maximum load is reached. To take into account the size of the process zone one must consider the softening behavior of concrete. This modification to the LEFM theory has only been developed during the last fifteen years.

1.2 General Background about High Strength Concrete

1.2.1 Introduction

High Strength Concrete (HSC) is a relatively new material and its development has been gradual over the past few decades. The uses of microsilica, fly ash and high range water reducers (superplasticizers) along with carefully selected materials have made the production of HSC easier and more economical. Currently, more and more structures are being constructed using High Strength Concrete. Besides higher strength, HSC material also offers favorable properties with regards to frost, abrasion, durability and permeability. Due to lower porosities and higher densities, HSC usage in the construction of storage tanks and pipes carrying hazardous substances is becoming more appropriate. Life-cycle cost effectiveness of HSC will result in more widespread usage in transportation structures and high-rise buildings all over the world.

As the development of HSC has continued, the definition of HSC has changed from time to time. In the 1950's, concrete with compressive strength over 5000 psi (34 MPa) was considered as high strength concrete. In the 1960's, high strength concrete with 6000 and 7500 psi (41 and 52 MPa) were commercially used. In 1970's, 8000 psi concrete was frequently being produced and used. Presently, concrete with compressive strength exceeding 20,000 psi (138 MPa) has been reported to have been used in high rise buildings. Currently, according to ACI, High Strength Concrete is defined as concrete having a compressive strength f'_c of 6000 psi (41 MPa) and greater (ACI 363). Two examples of usage of high strength concrete in construction are Chicago's Water Tower Place and 311 South Wacker Drive buildings. The long span cable swayed

bridges such as East Huntington, W.V. bridge over the Ohio River would not have been possible without the availability of high performance concrete.

In spite of its valuable properties, high strength concrete has a reputation of being more brittle than normal concrete, which may be a penalizing factor with respect to its use in certain structures. This observation, along with the fact that at present there is no quantitative measure for this presumed brittleness of high strength concrete, accounts for the increasing amount of research being carried out on crack propagation in this new material.

It has been observed that the cracking in high strength concrete is more localized and that it approaches the behavior of an homogeneous material as compared to cracking in normal strength concrete. It is also observed that in normal strength concrete cracks generally develop between the interface of aggregates and the cement paste. This leads to a distinct interlocking of the crack faces resulting in increased resistance to failure. On the other hand, in high strength concrete cracks propagate through the aggregates and consequently there is less resistance across crack surfaces due to reduced interlocking. High strength concrete exhibits a very linear load-deformation response prior to peak load and a very brittle behavior after the peak. This observation, has made many researchers (John and Shah 1989b; Gettu, Bazant and Karr 1990) believe that LEFM may be more applicable to high strength concrete.

1.2.2 Mechanical Properties of High Strength Concrete

The reputation of brittleness in HSC stems from the uniaxial compressive tests which indicate that its post peak behavior is less stable (steeper downward slope) than in

normal concrete. Thus for HSC, it is practically very difficult to obtain the post peak, even with very rigid presses and displacement control. This aspect was discussed by Rukugo et. al. (Rokugo, Ohno and Koyanagi 1986) who used the catastrophe theory to develop a new method for allowing the control of the descending part of the stress-strain curves. By contrast, the results of three point tests on HSC beams (John and Shah 1987, 1989b) seemed to have indicated very stable post peak behavior of HSC. These results are important because they appear to confirm the fact that the post peak behavior obtained during tests are dependent on geometrical and mechanical type boundary conditions of specimens (Desai, Krempl, Kiousis and Kundu 1987).

During the last decade or so, most of the research was concerned with increasing the "strength" of HSC. The need for research directed towards understanding the mechanical and fracture behavior of HSC is lacking. Very few researchers have attempted to quantify HSC fracture properties. The present scope of study includes determination of fracture properties and the application of the fictitious crack model for study of crack propagation in HSC members.

1.3 Research Significance

It is now clear that the presence of the "fracture process" zone ahead of the crack tip has necessitated the consideration of the tensile softening characteristic of concrete. The area (energy) under the tensile softening curve is defined as the fracture energy G_F of concrete. The tensile behavior of concrete can only be captured by performing the direct uniaxial test. In the past it was difficult to obtain tension test results and hence it was proposed by Hillerborg et. al. (Hillerborg, Modeer and Petersson 1976; Hillerborg 1980,

1983, 1985a, 1985b and 1985c) to use the beam bending test for determination of the fracture energy. Fracture energy determined from beam tests and indirect tensile strength (obtained from split cylinder test) were used to assume different shapes (linear, bi-linear) of the post peak softening behavior of concrete. It has been clearly demonstrated in the past by many researchers (Ratanalert and Wecharatana 1988) that the shape of tension softening curve has significant effect on the post peak behavior of specimens as obtained by using standard finite element calculations.

Presently, the RILEM committee (RILEM 1985-TC 50) has adopted Hillerborg's "Work of Fracture Test" (WFT) as the "standard test method" for calculating the fracture energy G_F^R for plain concrete using the three point test on notched beam specimens(Hillerborg 1985b). In addition, two other methods have been proposed in evaluating the fracture parameters of concrete. These two methods are based on Bazant's size effect method (SEM) (Bazant and Kazemi 1988, 1989a, 1989b) and Jenq and Shah's two parameter model (TPFM) (Jenq and Shah 1985a, 1985b). Although the validity of a direct comparison of the fracture energies obtained according to the above methods may be questionable, the evaluation of the effect of the geometrical macroscale (geometry and size), testing method (measurement technique), effect of concrete mix (compressive strength) on the fracture energy is crucial in defining a size-independent fracture energy parameter.

Hillerborg's Work of Fracture method was developed, as mentioned earlier, as an alternative means of determining the fracture energy. The ideal way of determining the fracture energy is by means of a direct uniaxial tension test. Since the direct tensile tests are not easy to perform especially in most laboratories, an alternative of testing

three point bend beam specimens is recommended by RILEM. In this method the fracture energy is computed from the area under the load-deflection response of the specimen. A literature survey of fracture test results conducted at numerous universities around the globe indicates that the load-deflection responses are significantly affected by:

- Specimen size (depth, span, and notch depth)
- Loading configuration (three point, four point, etc.)
- Test control type (load-point displacement, crack mouth opening control. etc.)
- Loading rate

The observed size dependency of G_F^R reported by researchers (Hillerborg, 1985c) can be attributed to many factors. For instance, neglecting the area under the load-deflection tail responses can cause an appreciable error in the values of fracture energy. Major causes of overestimation of fracture energy can also be linked to errors in measurements particularly the load-point displacements. Support crushing contributes to the total displacement of the beam. These extraneous deformations can be of equal magnitudes as compared to the actual displacement of the beam.

This study deals with the application of non-linear fracture mechanics concept to study the fracture behavior of High Strength Concrete. It is proposed that better estimates of fracture energy of concrete can be obtained by relating the fracture energy to load and crack mouth opening displacement responses (P-CMOD), since CMOD measurements automatically exclude all extraneous sources of deformations typically associated with deflection measurements. Among other potential advantages of using

CMOD to characterize the fracture energy is that CMOD deformations can be readily related to crack width levels and, as a result, to levels of serviceability.

1.4 Objectives of Present Study

The objectives of the present study are:

1. To develop an experimental program to evaluate the fracture properties of high strength concrete (10,000 psi < f'_c < 14,000 psi range). To evaluate important fracture parameters for high strength concrete, including the fracture energy, G_F, Tensile strength, f'_t, and the critical crack tip opening displacement, w_c by performing tension tests, beam bending tests and compression tests.
2. To implement the tensile softening characteristics obtained from the direct uniaxial tests into the commercially available finite element program - ABAQUS ver. 5.4. To perform a parametric study on normal strength and high strength concrete members using ABAQUS.
3. To propose a methodology for the calculation of Fracture Energy, G_F, of Concrete from Load-CMOD responses of three point bend beam tests instead of using traditional Load-Deflection responses as outlined by the Work of Fracture Test (RILEM - WFT).

1.5 Limitations

The fracture of materials is studied at a macroscale, at which the composite materials like cement paste, concrete etc. are treated as homogeneous and isotropy is assumed.

The Finite Element analysis considers presence and propagation of only one crack along a path pre-determined. The specimens studied are assumed to be in a state of plane stress. Time dependency of material properties are not taken into account.

CHAPTER 2

LITERATURE REVIEW

2.1 Introduction to Fracture Mechanics

Fracture mechanics deals with the mechanical responses of a flawed or a cracked member subjected to the application of forces or stresses. The mechanical response of a cracked member is described in terms of crack extension which in isotropic materials, occurs along a direction normal to the maximum principal tensile stress. Most structural members have discontinuities of some type, for example, holes, notches, cracks etc. These discontinuities produce stress concentrations near the crack tip. Using theory of elasticity it can be shown that the stress fields are singular at the crack tip, the stress components approach infinity as the radial distance 'r' from the crack tip approaches zero (see Figure 2.1).

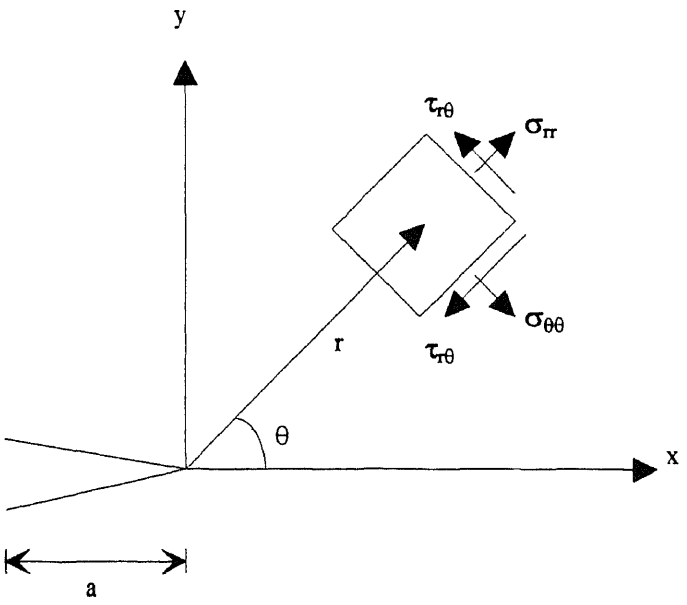

Figure 2.1 Stress State Close to the Crack Tip

The presence of cracks (flaws) and stress concentrations have been proven to be responsible for failures of many structures even under conditions of low stresses. Due to repeated application of loads or a combination of loads and environmental attacks, the flaws within the structures grow with time. The longer the crack extends, the higher the stress concentration exists. This means that the rate of propagation will increase with time. Due to the continuos growth of cracks the strength of the structure is continually reduced. Under normal service loads this growth may reduce the strength of the structure to such an extent that fracture occurs causing a sudden failure.

2.1.1 Modes of Fracture

Fracture behavior can be classified into three categories, depending on the modes of failures (see Figure 2.2). Mode I also known as the opening mode, Mode II which is the sliding mode or the planar shear mode and Mode III which is also known as the tearing mode or antiplane shear mode. In general, fracture is a linear combination of these three modes. As far as fractures of homogeneous materials are concerned, it is in practice difficult, if not impossible, to develop pure mode II or mode III fractures. Therefore, besides pure mode I, modes of failure are often a combination of basic modes which are called mixed mode.

2.1.2 Linear Elastic Crack Propagation

In a linear and isotropic material, the in plane stress state close to the crack tip in polar coordinates can be expressed by means of equation 2.1 (Broek 1982).

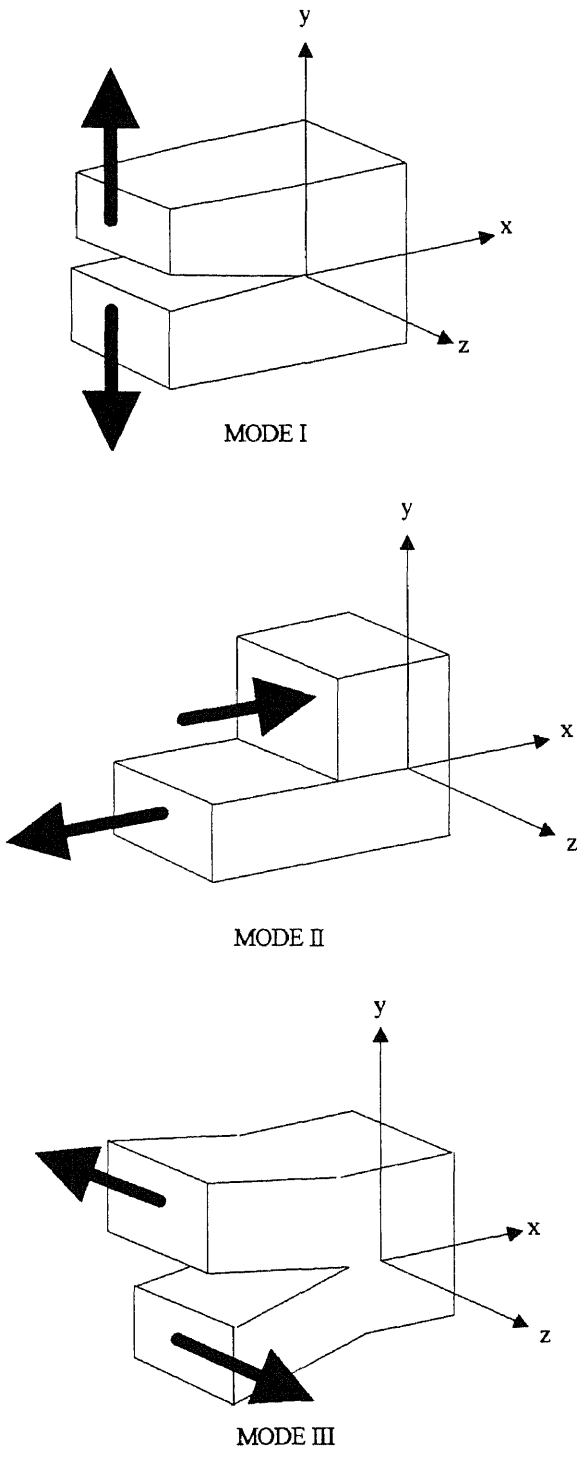

Figure 2.2 Modes of Fracture

$$\begin{bmatrix}\sigma_{rr}\\ \sigma_{\theta\theta}\\ \tau_{r\theta}\end{bmatrix}=\frac{K_I}{\sqrt{2\pi r}}\begin{bmatrix}+\frac{5}{4}\cos\frac{\theta}{2}-\frac{1}{4}\cos\frac{3\theta}{2}\\ +\frac{3}{4}\cos\frac{\theta}{2}+\frac{1}{4}\cos\frac{3\theta}{2}\\ +\frac{1}{4}\sin\frac{\theta}{2}+\frac{1}{4}\sin\frac{3\theta}{2}\end{bmatrix}+\frac{K_{II}}{\sqrt{2\pi r}}\begin{bmatrix}-\frac{5}{4}\sin\frac{\theta}{2}+\frac{3}{4}\sin\frac{3\theta}{2}\\ -\frac{3}{4}\sin\frac{\theta}{2}-\frac{3}{4}\sin\frac{3\theta}{2}\\ +\frac{1}{4}\cos\frac{\theta}{2}+\frac{3}{4}\cos\frac{3\theta}{2}\end{bmatrix}+\cdots \qquad (2.1)$$

In this equation, K is the stress intensity factor and the indices denote the mode of the stress state, the other terms are described in Figure 2.1

In pure mode I, $K_{II}=0$, and pure mode II, $K_I=0$. The condition for crack propagation is fulfilled when the stress intensity factor assumes a critical value, which is denoted K_{IC} in mode I and K_{IIC} in mode II.

For a structure (specimen) with given geometry and loading conditions, the relation between remote stress and stress intensity factor is given by the following equation (Broek 1982):

$$\sigma_\infty=\frac{K}{\sqrt{\pi a f}} \qquad (2.2)$$

where σ_∞ is either remote tensile stress or remote shear stress, calculated according to the linear elastic theory for the case of a non-cracked body, K is either the mode I or mode II stress intensity factor, a is the crack length and f is a factor which is a function of loading conditions and the geometry of the body. Expressions for f, for simple loading conditions and geometries, can be derived analytically, whereas other methods should be utilized for complicated cases.

Besides the stress intensity criterion, the energy release rate is also utilized. When the energy release rate criterion is utilized, the condition for crack propagation is fulfilled when the energy release rate (G) assumes a critical value (G_c). The relationship

between K the stress intensity factor, and G is given by the following equation (Broek 1982).

$$G = \frac{K^2}{E} \tag{2.3}$$

In mixed mode $K^2 = K_I^2 + K_{II}^2 + K_{III}^2$ and E is the Modulus of Elasticity.

In LEFM it is assumed that all of the fracture processes happen at the crack tip and the entire volume of the body remains elastic. Under these circumstances, the method of elasticity is useful in predicting fracture growth and failures.

Fracture researchers have at present no doubt that the introduction of fracture mechanics into design criteria will bring significant benefits. It will make it possible to achieve the following :

a. Uniform margin of safety.

b. Introduction of new materials like HSC and Fiber Reinforced Concrete (FRC).

c. Improved structural reliability and economy.

The conventional design concepts are based on tensile strength, yield strength and buckling strength. These criterion are sufficient for flawless structures, but are insufficient when cracks are present. Fracture mechanics offers the methodology to compensate for the inadequacies of the design or strength concept. Fracture mechanics also takes the structural size and geometry effect into account. As seen in Figure 2.3, the classical strength theories, such as elastic analysis with allowable stress, plastic limit analysis, as well as any other theories which use some type of strength limit in terms of stresses (e.g., viscoelasticity, viscoplasticity) do not study any size effect. This is because the nominal stress σ_N which is defined as shown below :

$$\sigma_N = \frac{P_U}{bd} \tag{2.4}$$

(where , P_u = failure load , b and d are the dimensions of the structure) remains constant and equal to the tensile capacity 'f'_t' of the material (concrete). By contrast, failures governed by fracture mechanics exhibits a rather strong size effect which in Figure 2.3 is described by the dashed line of slope -1/2. But in reality, concrete structures exhibit transitional behavior illustrated by solid curve in Figure 2.3. This curve approaches horizontal line for the strength criterion if the structure is small (typical laboratory specimens), and approaches the inclined straight line for linear elastic fracture mechanics if the structure is very large. Although this size effect is obviously important in codes it is generally ignored by the current codes because these codes are usually based on theories and test results of standard sized structures.

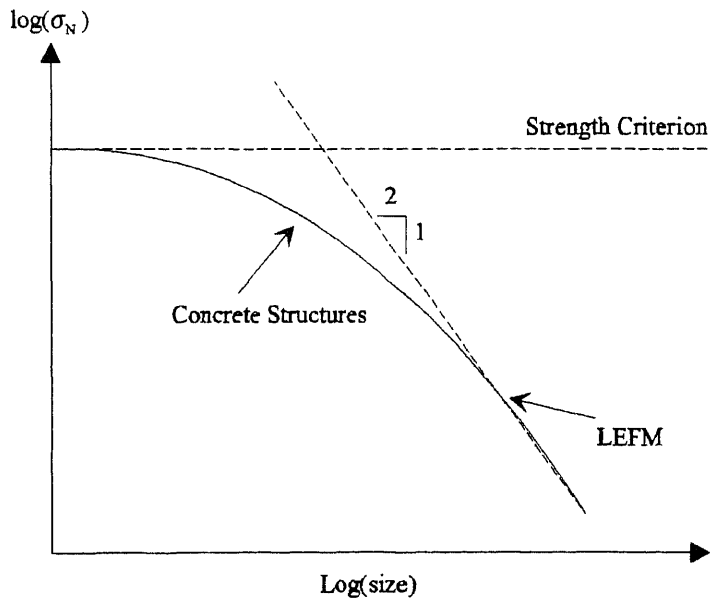

Figure 2.3 Fracture Mechanics Size Effect.

2.2 Recent Advances in Fracture Mechanics for Concrete

Due to the presence of a large micro-cracking process zone ahead of the crack tip in concrete, LEFM principles cannot be directly applied. A relationship which describes strain softening must therefore be included in the fracture analysis. Modeling this behavior can be done in two ways:

(1) In terms of Stress - Deformation (σ-ω) relationship.

(2) In terms of Stress -Strain (σ-ε) relationship.

In general, there are two types of non-linearity, ductile, as exhibited by metals, and non-ductile, as exhibited by ceramics, glass and concrete. Compared to the ductile fracture mechanics, in which, most of the non-linear zone undergoes plastic hardening, the fracture process zone in normal concrete is large and occupies nearly the entire non-linear zone.

Normal concrete, when subjected to tensile loads, behaves elastically until about 40%-60% of its tensile strength. Pre-critical crack growth and micro-cracking have been observed to be the cause of pre-peak non-linearity. When the maximum stress is reached, these microcracks coalesce to form one localized crack. In this local region of cracking after the peak stress, the crack is still able to transfer decreasing levels of stresses as the crack widens. In the other regions away from the region of localized cracking, the material simply unloads elastically. This localization of the deformation is referred to as the strain softening behavior of concrete. The post-peak tensile response of concrete can be incorporated into LEFM in a similar manner to the cohesive force

models of Dugdale (1960) and Barenblatt (Barenblatt 1962). To date there are three well known fracture models for concrete, they are :

(1) Fictitious Crack Model

(2) Crack Band Model

(3) Two Parameter Fracture Model

2.3 Non-Linear Fracture Mechanics for Concrete

Several fracture mechanics approaches have been proposed to characterize failure of concrete structures. These approaches primarily include the Fictitious Crack Model (FCM) by Hillerborg et. al., the size effect model by Bazant and Kazemi(1988), the two parameter fracture model by Jenq and Shah (1985a and 1985b). Each of these non-linear fracture models introduces some material fracture properties regardless of structural geometry and size. In order to use any of these models, material fracture parameters defined in the model must be experimentally determined.

The Fictitious Crack Model (FCM) by Hillerborg et. al. takes the softening stress separation curve as the material property. To completely determine the softening stress separation curve, one needs at least three fracture parameters such as the fracture toughness G_F, which is defined as the area under the curve, the tensile strength f'_t and the critical crack opening displacement ω_c. A given stress separation curve can be conveniently combined with a finite element code to predict fracture response of a concrete structure. Difficulty with FCM lies in being able to experimentally determine the values of G_F, f'_t and ω_c for a material. A method using three point bend beams has been proposed by RILEM to obtain the values of G_F. However, a round robin test has

shown that the values of G_F obtained are size dependent. No method for evaluating the other two parameters have been proposed. Additionally, some inconsistency may be introduced by separately measuring the values of f'_t and ω_c.

The size effect model (SEM) by Bazant and Kazemi(1988) introduces two material parameters G_F and c_f, where G_F and c_f are the critical energy release rate and the critical effective crack length extension for an infinite specimen, respectively. A method has been proposed by RILEM to measure the values of G_F and c_f by testing several three point bend beam specimens. These beams must be geometrically similar but must have at least three different sizes. Values of G_F and c_f are obtained from an extrapolation of the peak loads of the tested specimens by a statistical regression. In this case a slight error in the calculation of the extrapolation slope can significantly alter the values of G_F and c_f. Therefore, extreme care has to be exercised in determining the extrapolation slope. The beams should be of substantially different sizes for this method to yield accurate and reliable results.

The two parameter fracture model (TPFM) of Shah and Jenq proposes the stress intensity factor K_{IC}^S, and the critical crack tip opening displacement $CTOD_c$ as material fracture parameters. According to the RILEM proposal, only one single size three point bend beam is needed for measuring the values of K_{IC}^S and $CTOD_c$. However, the testing procedure commands an unloading when the load passes the maximum load but is not less than 95% of the peak load. To achieve a stable unloading after the peak load a closed-loop testing system is usually required. This requirement on testing facilities has somehow restricted the application of TPFM.

2.3.1 Fictitious Crack Model (FCM)

Hillerborg, Moodier and Petersson (1976) modified Dugdale (1960) and Barenblatt's (1962) model to incorporate the stress-softening behavior of concrete and called it the fictitious crack model (FCM). They proposed that on a certain length ahead of the crack tip, the yielded zone, cohesive forces must act such that the stresses from the fracture process zone cancel the stress singularity present ahead of an equivalent crack tip. In this model, which has been widely applied in finite element analysis of concrete fracture, the fracture properties are defined by the stress-deformation (σ-ω) relationships. The fracture energy, G_F, is defined as the area under the σ-ω curve.

$$G_F = \int_0^{\omega_f} \sigma d\omega \tag{2.5}$$

The FCM assumes the effect of microcracked zone to be confined to a narrow band of line crack where the total fracture energy is consumed. The material outside of the process zone behaves elastically based on the stress-strain relationships (see Figure 2.4a). The crack tip begins to open when the stress at the tip of the crack reaches the tensile strength, f'_t, of the concrete. As the crack opens, closing forces based on the amount of opening are introduced across the crack faces (see Figure 2.4b). When the crack opens more than the critical crack opening displacement ω_c, the closing traction across the crack face drops to zero. The length of crack over which the closing forces act is known as the fictitious crack. The fracture parameters are completely characterized by two parameters G_F and f'_t. The shape of the σ-ω curve has been shown

to have a profound influence on the results of the model. Linear, bilinear and even exponential σ-ω curves have been used.

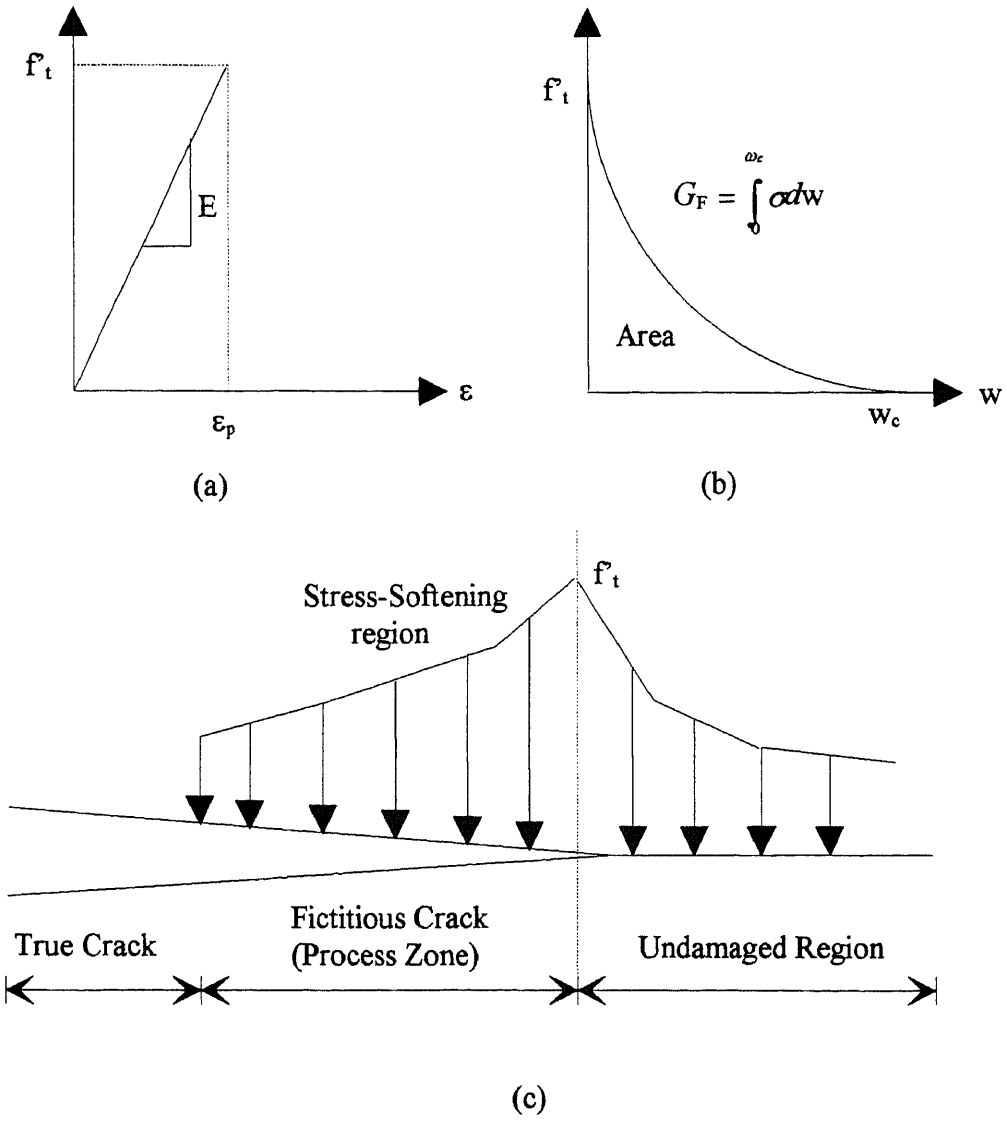

Figure 2.4 (a) Elastic Stress-Strain Relationship (Pre-Peak) (b) Stress-Separation Relationship (Post-Peak) (c) Distribution of Stresses Ahead of Crack Tip and in Process Zone

Hillerborg's fictitious crack model was verified and calibrated by various comparisons of test data. However, it seems that an exhaustive comparison with all the important concrete data from the literature has not yet been presented. But due to equivalence with the crack band model, the extensive comparisons of the latter with test data (Bazant and Oh 1983a, 1983b) indirectly validated the fictitious crack model.

2.3.2 Crack Band Model (CBM)

Inspired by the work of Hillerborg et. al., Bazant developed the crack band model (Bazant and Oh. 1983a, 1983b). In this model the fracture process zone is modeled as a system of parallel cracks that are continuously distributed (smeared) in the finite element. The material behavior is characterized by the constitutive stress strain relationship. The width of the fracture process zone (w_c) is assumed to be constant. For example, in concrete it is assumed to be three times the aggregate size. The width of the crack band is held constant in order to avoid spurious mesh sensitivity. This assures that the energy dissipation due to fracture per unit length of crack is a constant which is equal to the fracture energy of the material (G_F).

In this model, the crack is modeled by changing the isotropic elastic moduli matrix to an orthotropic one, thereby reducing the stiffness in the direction normal to the cracking plane. The softening behavior of concrete is modeled by superimposing the fracturing strain, ε_f, on the elastic strain.

A brief mathematical background (Bazant and Oh 1983a) of this model is given below by considering a system of Cartesian coordinates as shown in Figure 2.5. If

concrete is idealized as homogeneous material, the triaxial stress-strain relationship can be expressed as follows:

$$\begin{bmatrix} \varepsilon_x \\ \varepsilon_y \\ \varepsilon_z \end{bmatrix} = \frac{1}{E}\begin{bmatrix} 1 & -\upsilon & -\upsilon \\ -\upsilon & 1 & -\upsilon \\ -\upsilon & -\upsilon & 1 \end{bmatrix}\begin{bmatrix} \sigma_x \\ \sigma_y \\ \sigma_z \end{bmatrix} + \begin{bmatrix} 0 \\ 0 \\ \varepsilon_f \end{bmatrix} \tag{2.6}$$

where, ε_f , is the fracturing strain, i.e., additional strain caused by opening microcracks. ε_f is superimposed strain on the elastic strain ε_z, υ is Poisson's ratio and E is Young's Modulus of Elasticity. Since as the microcracks develop in the material the effect of these opening microcracks does not cause any effect on the strains in 'x' and 'y' directions ('y' axis perpendicular to the plane, see Figure 2.5).

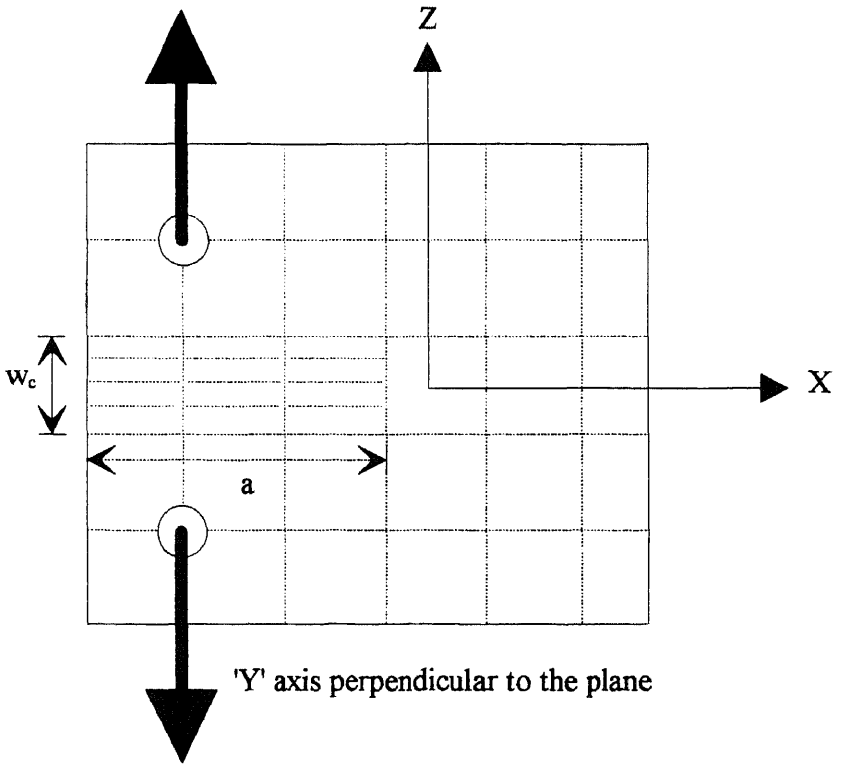

Figure 2.5 The Cartesian Coordinates for Crack Band Model.

The width of the fracture front ,w_c, is assumed to be a material constant which can be determined from experiments. w_c, is proportional to the aggregate size and for plain concrete it is equal to three times aggregate size.

The fracturing strain, ε_f, is determined by summing all the deformation or openings of individual microcracks, $\delta_f = \sum_i \delta_f^i$, intersecting 'z' axis over the width w_c.

$$\varepsilon_f = \delta_f w_c \tag{2.7}$$

The fracture starts when the stress at the crack tip reaches the tensile strength, at which point ε_f is still zero. As the crack opens, δ_f, starts to increase and σ_z starts to gradually decline. A simple choice for modeling this could be a linear function as shown in Figure 2.6.

Fracturing strain, ε_f, can be represented as a function of stress, σ_z, as follows:

$$\varepsilon_f = f(\sigma_z) = \frac{1}{C_f}(f'_t - \sigma_z) \tag{2.8}$$

where, $C_f = f'_t/\varepsilon_o$, slope of the softening curve.

Substituting equation (2.8) into (2.6), one obtains :

$$\begin{bmatrix} \varepsilon_x \\ \varepsilon_y \\ \varepsilon_z \end{bmatrix} = \frac{1}{E}\begin{bmatrix} 1 & -\upsilon & -\upsilon \\ -\upsilon & 1 & -\upsilon \\ -\upsilon & -\upsilon & 1 \end{bmatrix}\begin{bmatrix} \sigma_x \\ \sigma_y \\ \sigma_z \end{bmatrix} + \begin{bmatrix} 0 \\ 0 \\ \varepsilon_o \end{bmatrix} \tag{2.9}$$

where, ε_o, is the maximum fracturing strain, ε_f, at which the stress, σ_z, goes to zero and the microcrack forms a continuous crack.

The post-peak tensile stress-strain relationship is described by the tangent modulus, E_t, which is defined as:

$$\frac{1}{E_t} = \frac{1}{E} - \frac{1}{C_f} \tag{2.10}$$

The fracture energy, G_F, which is defined as the energy absorbed in creating (opening) of all cracks is given by:

$$G_F = w_c \int_0^{\varepsilon_0} \sigma_z(\varepsilon) d\varepsilon \tag{2.11}$$

The integral represents the area under the stress strain curve after the stress has reached f'_t (start of microcracking). If a linear relationship between stress-strain is assumed, then

$$G_F = w_c \frac{1}{2} f'_t \varepsilon_o \quad or \quad G_F = \frac{f'^2_t}{2C_f} w_c \tag{2.12}$$

If G_F, f'_t and w_c are known from experiments, then the basic parameters of the stress-strain relation can be calculated as follows :

$$C_f = \frac{f'^2_t w_c}{2G_F} \quad , \quad \varepsilon_o = \frac{f'_t}{C_f} = \frac{2G_F}{f'_t w_c} \tag{2.13}$$

Alternatively, it is also possible to express the fracture energy as the total area under the stress-strain relationship (see Figure 2.6). Using equation 2.10, it can be shown that :

$$G_F = \frac{1}{2}\left(\frac{1}{E} - \frac{1}{E_t}\right) f'^2_t w_c \tag{2.14}$$

Both the Fictitious Crack Model and the Crack Band Model require complete stress-deformation or stress-strain relationships. Such relationships can be obtained only by performing direct uniaxial tension tests. Both these models are well suited for numerical techniques such as finite elements.

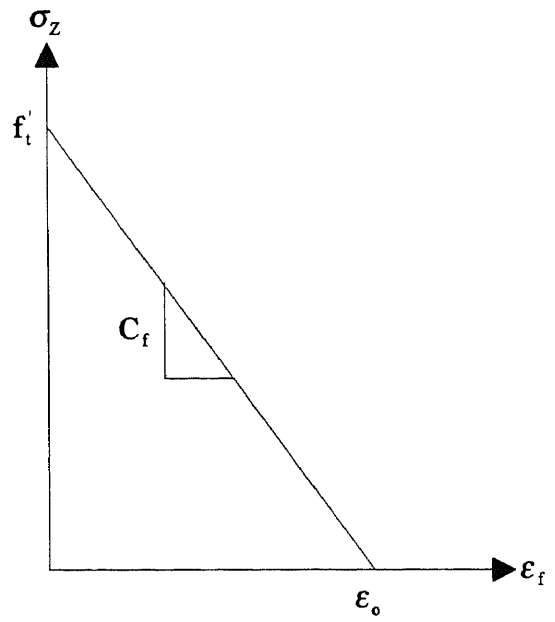

(a)

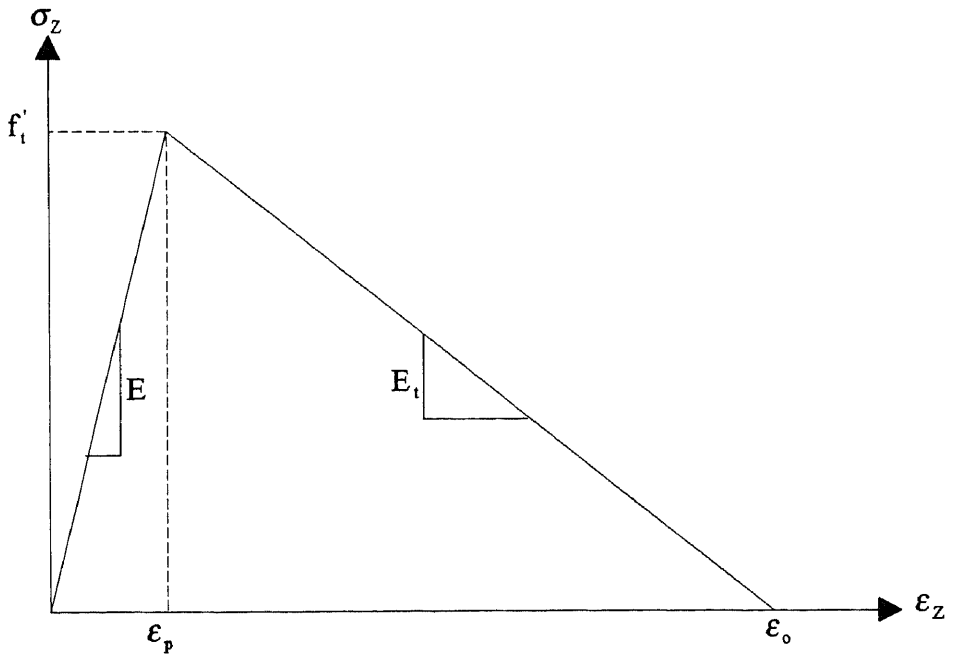

(b)

Figure 2.6 Stress-Strain Relationship for Crack Band Model.

2.3.3 Two Parameter Fracture Model (TPFM)

The two parameter fracture model was developed by Shah and Jenq (1985a, 1985b). This model was derived under the category of special non-linear fracture models without using the complete concrete stress-deformation (σ-ω) and stress-strain (σ-ε) softening relationships. It is based on the pre-peak nonlinear behavior of concrete. LEFM principles are modified to approximately reflect the fracture behavior of concrete.

Ever since the concept of LEFM has been applied to concrete testing (Kaplan, 1961), it was found that the fracture toughness or the stress intensity factor (K_{IC}) appeared to be size dependent. In recent years, it has been recognized that if K_{IC} is determined based on maximum load (P_u) and effective crack length (a_e), then the results are essentially independent of size and geometry effects. The effective crack length, a_e, is defined as the length over which all the pre-peak non-linear behavior of concrete takes place.

In general, the crack path in concrete is tedious. Furthermore cracks in concrete may not be traction free as a result of so called aggregate interlock. As a result, the experimental determination of effective crack length on surface extension is not useful for determining K_{IC}. An alternate method to determine effective crack length, a_e, is by the 'compliance' technique. Compliance is defined as the value of crack mouth opening displacement (CMOD) per unit load. The notched beam specimen is unloaded (see Figure 2.7) just after the peak load, and the compliance C_u is determined. Comparing this compliance C_u with C_i and using LEFM readily available relationships between compliance and crack lengths, one can determine the effective crack length. If K_{IC}, is calculated based on peak load and the corresponding effective crack length, then, K_{IC},

and a_c become the two parameters that characterize the fracture toughness of concrete. However, it was found that the value of a_c depends on the material properties and on the specimen's geometry. Therefore the value of a_c determined from one particular size cannot be used to predict fracture behavior of other sizes. To overcome this problem, Shah and Jenq proposed to use the critical crack tip opening displacement, $CTOD_c$, as a fracture parameter. Their measurements showed that $CTOD_c$ was essentially independent of the size and geometry of specimens. They calculated CTOD from the compliance measurements and the available LEFM equations. The brief procedure involved in the calculation of the two parameters K_{IC} and $CTOD_c$ for three point bend specimens is as follows.

The Young's modulus 'E' is determined from the initial slope C_i (compliance) by using the formula :

$$E = \frac{6Sa_o V(\alpha)}{C_i d^2 b} \tag{2.15}$$

where, C_i = Initial compliance from the load-CMOD, $V(\alpha)$ = Size correction factor obtained from handbooks (Tada, Paris and Irwin 1985) for different (S/d) ratios.

$\alpha = a_o/d$, S = Testing Span, d = depth of the beam, b = width of the beam,

and a_o = initial notch.

The effective crack length, a_e, is calculated by using 'E' calculated by equation 2.16 and by knowing the unloading compliance C_u. Using an iterative procedure 'a_e' is found such that the following equation is satisfied:

$$E = \frac{6Sa_e V(\alpha)}{C_u d^2 b} \tag{2.16}$$

where, a_e is the effective crack length and $\alpha = a_e/d$ and the rest of the terms are as described before. Once a_e is determined K_{IC} is calculated by using the following relationships:

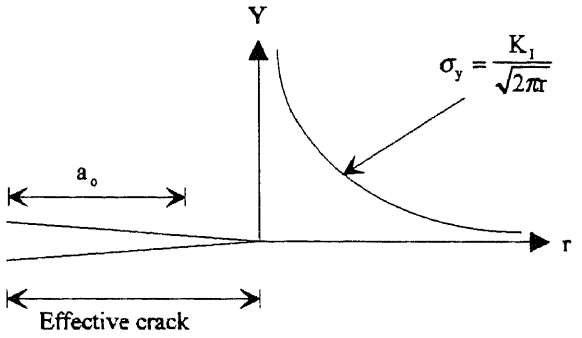

(a)

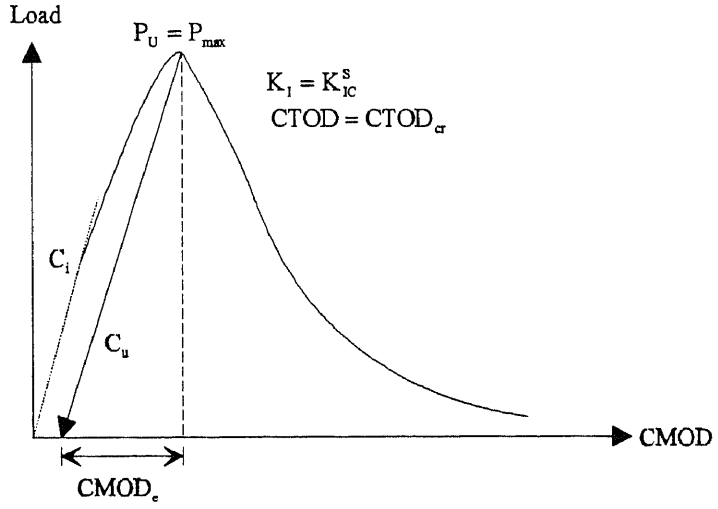

(b)

Figure 2.7 (a) Effective Griffith Crack (b) Typical Load-CMOD Curve.

$$K_{IC} = \frac{3(P_u + 0.5W)S\sqrt{\pi a_e}}{2d^2 b} F(\alpha) \qquad (2.17)$$

where,

$F(\alpha)$ = Size correction factor obtained from handbooks (Tada, Paris and Irwin 1985) for different (S/d) ratios.

$\alpha = a_o/d$

$W = w_o S/L$, where w_o is the self weight of the beam , L is the length and S is the testing span.

Next the critical crack tip opening displacement $CTOD_c$ is calculated using the following equation.

$$CTOD_c = \frac{6P_{max}Sa_e V(\alpha)}{Ed^2 b} f(\alpha, \beta) \qquad (2.18)$$

where $f(\alpha,\beta)$ = Size correction factor obtained from in handbooks (Tada, Paris and Irwin 1985) for different (S/d) ratios and where $\alpha = a_o/d$ and $\beta = a_o/a_c$.

In the two parameter model the maximum applied load and the corresponding $CMOD_e$ (used to calculate C_u) are experimentally determined. With known specimen geometries and Young's modulus, the effective crack a_c can be determined using the LEFM formulae. It should be noted that the an iterative procedure is needed to calculate a_c. Once a_c is calculated, K_{IC} and $CTOD_c$ can be obtained.

2.4 Direct Uniaxial Tension Tests

The direct tension test for concrete is not commonly performed despite the fact that the test is of considerable theoretical and practical significance for understanding the

structural behavior of concrete. Although not recommended as a standard test, its validity and general characteristics have been studied by numerous investigators.

The non-linear fracture models, such as the fictitious crack model and the crack band model, used an assumed portion of the post peak tensile softening since no data were available from these tension tests. Therefore the accuracy of the assumptions made in order to arrive at such models cannot really be ascertained without uniaxial tension test results. The reasons for lack of information on this subject at the time when the models were developed are the brittleness of the material and unavailability of closed loop control systems which are sensitive enough to conduct tension tests.

Evans and Marathe (1968) tested a number of plain concrete specimens in direct tension and their results indicated that the stress-strain curves did not contain any appreciable inelastic deformation. Sudden failures at the peak stresses resulted in collecting information only till the peak load. To resolve this problem, they tried to increase the stiffness of the equipment by testing four steel rods in parallel with the concrete specimen. This effort also failed to yield complete stress strain curves since they could only obtain information in the post peak region to about one fifth of the peak stress after which abrupt failure occurred. Petersson (1981), also used the approach by externally increasing the stiffness of the testing system. This was done by placing aluminum columns parallel to the concrete test specimen. These aluminum columns were then electrically heated causing them to expand. This made the cross head of the machine move upwards and thereby applying tensile force to the specimen. However, these tests were not carried out far enough to yield complete stress-strain curves. They obtained only the peak stresses. No information on the descending part of the stress-

strain was available until Rusch and Hilsdorf (1963) demonstrated the existence of a complete stress-strain relationship for concrete in direct tension. Hughes and Chapman (1966) further supplemented the findings.

It is accepted now that the shape of the stress-strain curve is a property of the material. But it can be affected by the experimental conditions, namely, alignment of the specimen and gage length over which the deformation or strains are measured. Blackley and Beresford (1970) studied some of these aspects.

Testing of brittle materials in tension posed two main problems. In addition to the higher stiffness requirements for the testing machine and closed-loop control capability, tests had to be carried out at relatively slower deformation rates for stable control. Other problems are associated with the possibility of specimen failures at or near the grips due to possible stress concentration effects and improper alignment of the specimen in the test setup.

To overcome the problems associated with specimen grips, Reinhardt and Cornelissen (1984) tried gluing the top and bottom of the test specimen to metal plates, which in turn were bonded to bearing blocks allowing for free lateral movement of the specimen and better alignment. Shah and Gopalaratnam (1985) designed special wedge type frictional grips made out of aluminum and they used serrated rubber padding between the grips and specimen surface to more evenly transfer the load. This method proved to be restrictive. If the size of the specimen was increased beyond that which they used, the friction force would not be sufficient to hold the specimen in order to avoid slippage.

Although some of these researchers had the capabilities for conducting the uniaxial tensile tests to its entirety, they did not, however. Shah and Goparatnum (1985) terminated their tests at 1600 micro-inch or at 2400 micro-inch deformation. They assumed that after this value of deformation the behavior of concrete is asymptotic. They also assumed that the addition to the fracture energy, G_F, which is defined as the area under the total stress-deformation curve, from the untested part of the stress-deformation curve would be insignificant. This assumption is questionable since the stress level at a value of 1600 micro-inch or at a 2400 micro-inch deformation is still relatively high. To obtain a correct value of G_f, tension tests should be conducted to complete separation of the specimen.

All these researchers, as mentioned above, have carried out their tensile tests on normal strength concrete. There is not much information available at present on the softening response of high strength concrete.

A few models are available which describe the softening response of normal concrete under uniaxial tension. These are mentioned below.

1. Reinhardt (1984)

$$\left[\frac{\sigma}{f_t'}\right]+\left[\frac{\omega}{\omega_c}\right]^k = 1.0 \qquad (2.19)$$

where, σ = Tensile stress, f'_t = Tensile strength (Peak), ω = Crack opening displacement, ω_c = Critical crack opening displacement, and k = empirical constant for concrete = 0.248.

2. Cornelissen (1985)

$$\frac{\sigma}{f_t'} = \{1 + c_1(\frac{\omega}{\omega_c})^3\} \exp(-c_2 \frac{\omega}{\omega_c}) - \frac{\omega}{\omega_c}(1 + c_1^3)\exp(-c_2) \qquad (2.20)$$

where, σ = Tensile stress, f'_t = Tensile strength (Peak), ω = Crack opening displacement, ω_c = Critical crack opening displacement, c_1, c_2 = empirical constants, c_1= 3.981 and c_2 = 8.359 respectively.

3. Hillerborg (1978)

$$\frac{\sigma}{f_t'} = \exp(-p_1 \omega^{p_2}) \qquad (2.21)$$

σ = Tensile stress, f'_t = Tensile strength (Peak), ω = Crack opening displacement, and p_1, p_2 = empirical constants, p_1= 0.074 and p_2 = 0.756 respectively.

4. Shah (1985)

$$\frac{\sigma}{f_t'} = \exp(-k\,\omega\lambda) \qquad (2.22)$$

σ = Tensile stress, f'_t = Tensile strength (Peak), ω = Crack opening displacement measured in micro-inch and k, λ = empirical constants, k = 1.544×10^{-3} and λ = 1.01 respectively.

Note : The above equation is valid only till 2400 micro-inch.

5. Wecharatana and Chou (1986)

$$\frac{\sigma}{f_t'} = \frac{A}{\xi}\left(1 - e^{-B\xi^C}\right)(1 - \xi)^D \qquad (2.23)$$

where, σ = Tensile stress, f'_t = Tensile strength (Peak), ξ = ratio of crack opening displacement to critical crack opening displacement ω_c, and A, B, C and D are empirical constants, A = 0.052, B = 400, C = 1,75 and D = 0.5 respectively. The above equation holds for mortar as well as for normal concrete.

2.5 Need for a Standard Test for Determination of Fracture Parameters

No study has been reported in the literature which has evaluated the existing fracture models predictions for the behavior of high strength concrete. But it is felt that among the models discussed above, the most promising model for high strength concrete is the Hillerborg's Fictitious Crack Model. To model the fracture behavior of HSC, one must realize this model has been used in the past with assumed portions of the stress softening curves which mostly were determined by a trial and error method. The prime reason for using beam tests is the unavailability of direct tension tests on concrete. In recent years, however, some researchers have been successful in measuring the softening behavior of normal strength concrete and the need for assuming the shape of softening curves is no longer necessary. One of the objectives of this study has been to experimentally determine the softening characteristics for high strength concrete and to incorporate such relationships into ABAQUS finite element program to numerically study the behavior of high strength concrete members. Another aspect of the present study is concerned with the experimental determination of the fracture parameter G_F. As mentioned, G_F values have been known to be size dependent (test results based on 700 beams, (Hillerborg 1985c)). The main reasons for this size dependency are believed to be:

- Experimental errors (incomplete record of Load-Deflection measurements, support crushing)
- Energy dissipation in the bulk of the specimen.
- Crack propagation into a high compressive stresses regions (at ultimate failure loads), thereby requiring higher energy for crack propagation

It has been observed in fracture tests that the load point deflection measurements are strongly affected by the support conditions. The crack mouth opening displacements on the other hand are not to be affected by the test setups in any way. Based on this fact, it is realized that if there was a way to relate the "true deflection" measurements to the crack mouth measurements then it would be possible to use load-crack mouth opening measurements for evaluations of the fracture energy of concrete. In this study, a methodology will be developed which will allow the use of the load-crack mouth opening displacements responses to determine the fracture energy of concrete.

The next chapter deals with the experimental program designed in this study for the evaluation of fracture and mechanical properties of high strength concrete. Chapter 4 deals with the finite element modeling of high strength concrete members and parametric study. The theoretical background for deflection-CMOD relationships are presented in Chapter 5. Also in Chapter 5, important fracture parameters and fracture energy of high strength concrete are developed.

CHAPTER 3

EXPERIMENTAL PROGRAM AND RESULTS

3.1 Introduction

In this chapter the details of the experimental program developed to evaluate the mechanical as well as the fracture parameters of high strength concrete are presented. High strength concrete of compressive strengths ranging between 6000 psi to 12000 psi were tested. The experimental program (Table 3.2) was designed so as to yield the various material properties required by the proposed finite element model, such as the tensile strength f'_t, fracture energy G_F and the complete tension softening curve of high strength concrete. An improved experimental setup for conducting three point bend beam tests was developed. Test data comprising of Load Point Displacement (LPD) and Crack Mouth Opening Displacement (CMOD) were used in developing a method for the determination of the fracture energy G_F (Beam Test - RILEM) based on the load and crack mouth opening displacement response. The relationship between CMOD and LPD is established for that purpose. The number of specimens tested are listed in Table 3.2. The types of tests that were included in the experimental study are:

- Direct uniaxial tension test
- Compression test
- Beam bending test

3.2 Details of Concrete Mix and Materials Used

Details of the mix design used for the concrete mixtures are presented in Table 3.1. Coarse aggregates chosen for this study were 3/8th" basalt. Fine aggregates were river sand conforming to ASTM C 33. Type 1 Portland Cement (Hercules Brand) conforming to ASTM C 150 was used.

Table 3.1 Details of Mix Proportions

Concrete Designation	Mix Proportions (by Weight) C:S:A:W:SF	Expected Compressive Strength (psi)
HSC - A	1.0:2.0:3.0:0.5:0.11	6,000
HSC - B	1.0:1.1:2.0:0.33:0.11	9,000
HSC - C	1.0:0.64:1:61:0.26:0.11	12,000

where, C = Cement, S = Fine Aggregates, A = Coarse Aggregates, W = Water Cementitious Ratio, SF = Silica Fume. Superplasticizer (Master Builders - Rheobuild 1000) was used at the rate of 1.0 liter per 100 kg of Cementitious material (cement+silica fume)

Table 3.2 Experimental Program

Type of Test	6000 psi	9000 psi	12000 psi	Total
Tension	6	6	6	18
Compression	3	3	4	10
Beam Test HSC -C Concrete	Size A S/D=4 a_o/D=0.25,0.5	Size B S/D=6 a_o/D=0.25,0.5	Size C S/D=8 a_o/D=0.25,0.5	Total #
BxDxSxa_o	3x4.5x18x1.125 3x4.5x18x2.25	3x3x18x0.75 3x3x18x1.50	4x4x32x1.0 4x4x32x2.0	9 9

* All dimensions indicated are in inches, actual Length of the beams 2" longer than the span length.

3.3 Direct Uniaxial Tension Tests

In the past decade extensive attention has been focused on the strain softening behavior of concrete in tension. There are two alternate approaches to determine the tensile fracture energy of concrete: the direct tension test (Reinhardt, 1984, Gopalaratnam, et. al. 1984, Wecharatana, et. al 1986, Navalurkar, et. al. 1994) and the notched beam test - RILEM (Hillerborg and Peterson, 1980). The tests available in the literature are mainly on low to normal strength concrete. At the present time no such test results of uniaxial tensile properties on high strength concrete are available.

In this study direct uniaxial tension tests were specifically undertaken for understanding the general tensile behavior of high strength concrete and for the determination of the following properties:

(1) The uniaxial tensile strength (f'_t).

(2) Fracture Energy (G_F), which is defined as the amount of energy absorbed for total failure i.e. area under the stress-separation curve.

(3) Critical Crack Opening Displacement (w_c), where w_c, is defined as the crack opening displacement at which the tensile stress attains a value of zero.

Due to its highly brittle nature, testing of high strength concrete in tension poses two main problems. In addition to the higher stiffness requirements of the testing machine, and closed-loop control capability, tests have to be carried out at relatively slower deformation rates for stable control. Other problems are associated with the possibility of specimens failures at or near grips due to possible stress concentration effects and improper alignment of the specimen in the test setup.

3.3.1 Design of Test Specimen and Testing Setup

To overcome these problems, end tapered specimens were designed. A typical specimen is shown in Figure 3.1. The cross section in the constant width zone has a rectangular cross section of 3.25"× 1.75", the height of the specimen is 12". The tapered slope of the specimen ends is 0.4166. PVC shims were employed to fit the specimen within the metal grips. The load was transferred to the grip via a universal joint connected through the top. Loads were transferred from the metal grips to the specimen through PVC shims. Another universal joint was used at the bottom end to allow for free rotation of the specimen. Tests were performed in an MTS closed loop system under deformation control. The test setup used in the present study was modified from the work of earlier researchers at NJIT (Wecharatana 1986). Details of the complete test setup are shown in Figure 3.2 and Figure 3.3. The average rate of crack tip opening displacements across the notches was employed as the feedback signal for the closed-loop testing system. Deformations were measured across the notches using clip gages, the signal was then electronically averaged for the feedback control. In the pre-peak region, specimens were loaded under deformation control at the rate of 6.7×10^{-8} inch per second. Past the peak load the deformation rate was gradually increased at regular intervals depending on the load level. Typically, it took approximately 35 to 40 minutes to reach the peak load and around 3 hours to complete the entire test. A data acquisition board was employed for storage and processing of data via a microcomputer.

For every batch of concrete and strength type, a total of four tension specimens were cast in plexi-glass molds. The specimens were demolded after 24 hours and

transferred to lime saturated water for curing. Notches of 0.5" were cut using a circular diamond saw just prior to testing. All tension tests were performed between the ages of 28 to 35 days.

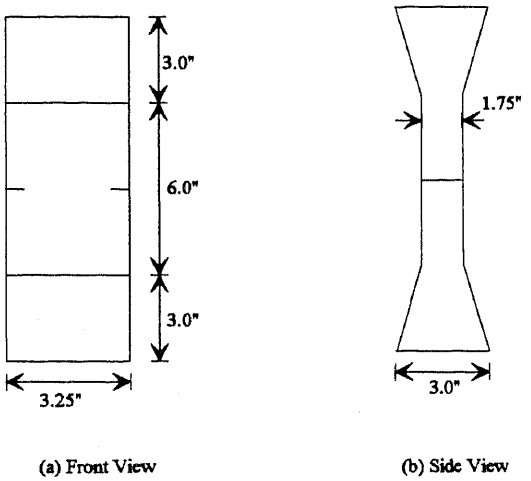

Figure 3.1 Dimension of the Tension Test Specimen.

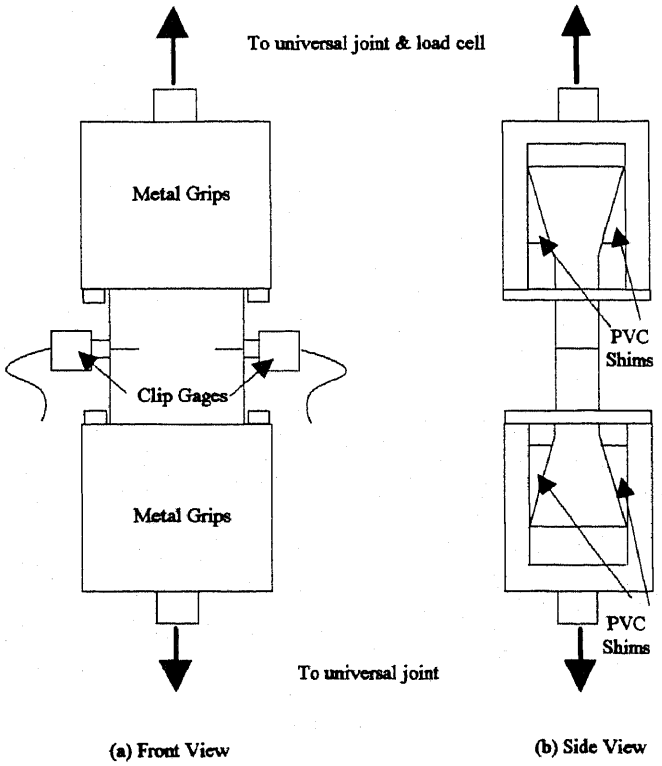

Figure 3.2 Schematic Diagram of Test Specimen Within the Metal Grips and PVC Shims

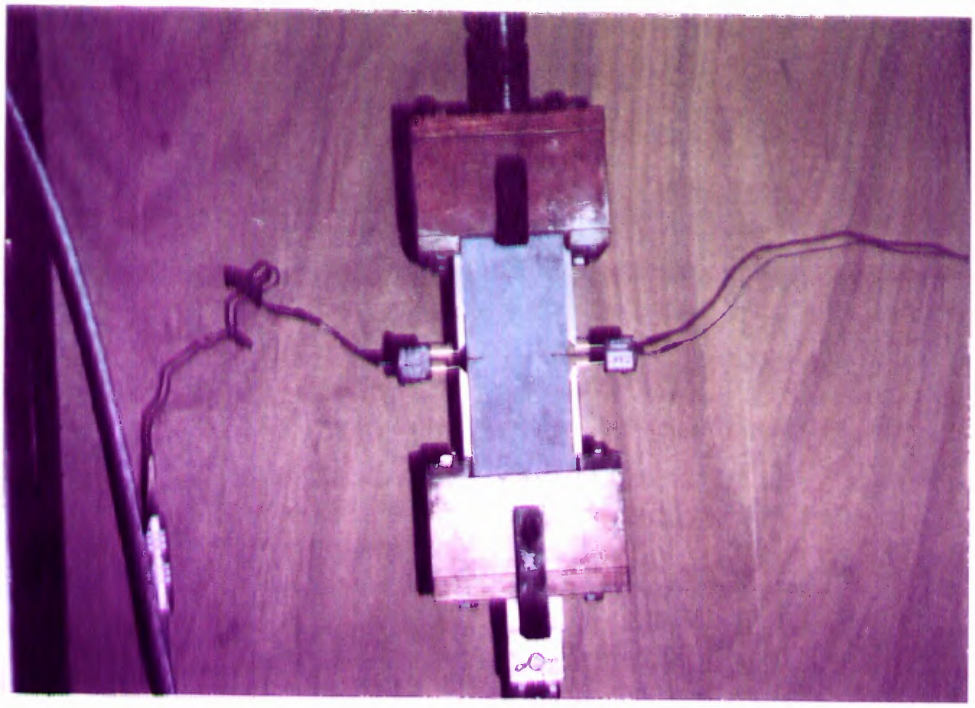

(a) Front View

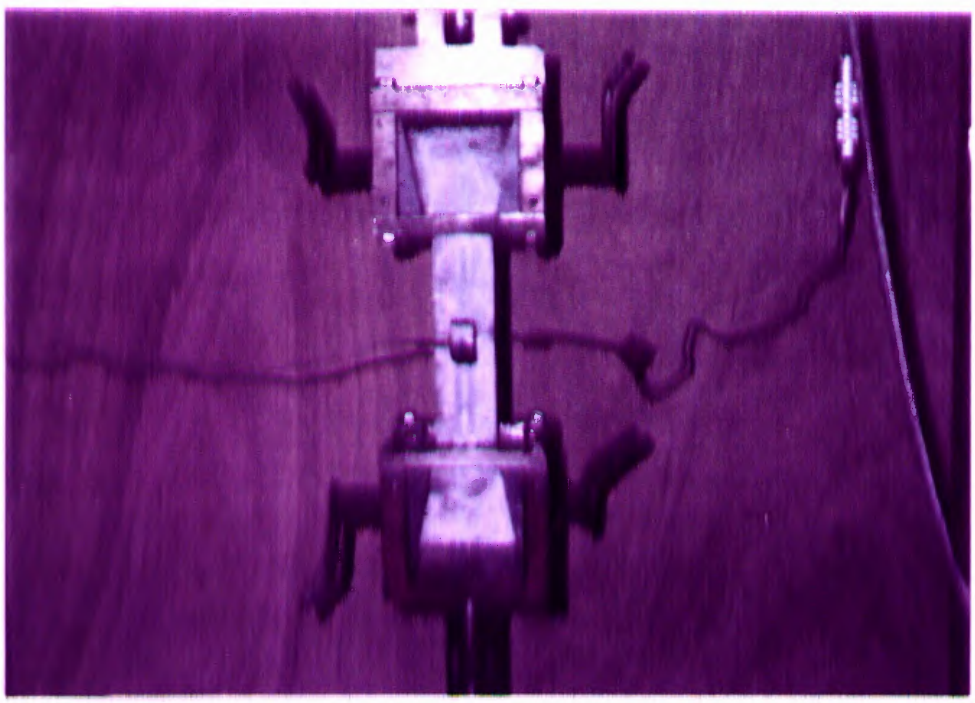

(b) Side View

Figure 3.3 Photograph of the Tension Test Showing the Specimen Within the Metal Grips and PVC Shims

3.3.2 Results of Direct Uniaxial Tests

The test results are summarized and are presented in Tables 3.4 through 3.6. To calculate the fracture energy, the complete stress-deformation curves were transformed to stress-separation (σ-ω) curves. The separation deformation is defined as the total deformation minus the elastic deformation and an irreversible deformation represented by an unloading line from the top of the σ-δ_{total} curve parallel to the first loading branch below the stress level of σ=0.6f'_t. Figures 3.4 through 3.12 presents typical stress deformation and σ-w relationships for the three different strength concrete tested in the present study. The corresponding G_f-ω curves are also shown. As seen from Figures 3.4 through 3.12, for increasing compressive strengths, the σ-ω curves become more steeper in the initial region with correspondingly lower ω_c values. For HSC-C concrete, the cracks always propagated through the cement matrix and through the aggregate particles whereas in HSC-A and HSC-B concretes, the cracks were observed to propagate through the cement matrix, along the grain surfaces (bond phase) and sporadically through the aggregates.

Based on the experimental data the following model which describes the softening portion of tensile stress separation curve was developed. It should be noted that other types of mathematical equations were tried and were found to be inadequate to model the behavior of HSC softening characteristics.

$$\left(\frac{\sigma}{f'_t}\right)^m + \left(\frac{\omega}{\omega_c}\right)^n = 1.0 \qquad (3.1)$$

where, σ = Tensile stress, f'_t = Tensile strength (Peak), ω = Crack opening displacement, and m, n are empirical constants and are listed in Table 3.3 below:

Table 3.3 Empirical Constants for Softening Curves of High Strength Concrete

Concrete Type	m	n
HSC - A	0.400	0.535
HSC - B	0.440	0.473
HSC - C	0.420	0.454

Table 3.4 Tension Test Results for HSC- A Concrete

Specimen Name	Tensile Strength f'_t (psi)	Critical Crack Opening ω_c (in)	Fracture Energy G_F (lb./in)
A1	439	0.0082	0.666
A2	466	0.0105	0.624
A3	460	0.0090	0.677
A4	427	0.0117	0.654
A5	430	0.0098	0.636
A6	426	0.0109	0.698
AVERAGE	**441**	**0.0100**	**0.659**

Table 3.5 Tension Test Results for HSC- B Concrete

Specimen Name	Tensile Strength f'_t (psi)	Critical Crack Opening ω_c (in)	Fracture Energy G_F (lb./in)
B1	496	0.0096	0.677
B2	497	0.0113	0.652
B3	529	0.0099	0.727
B4	513	0.0091	0.723
B5	496	0.0082	0.756
B6	517	0.0101	0.773
AVERAGE	**508**	**0.0097**	**0.718**

Table 3.6 Tension Test Results for HSC- C Concrete

Specimen Name	Tensile Strength f'_t (psi)	Critical Crack Opening ω_c (in)	Fracture Energy G_F (lb./in)
C1	649	0.0092	0.769
C2	645	0.0090	0.622
C3	605	0.0097	0.707
C4	624	0.0104	0.699
C5	593	0.0093	0.747
C6	676	0.0094	0.570*
AVERAGE	**632**	**0.0095**	**0.709**

- *not included in the average for G_F.

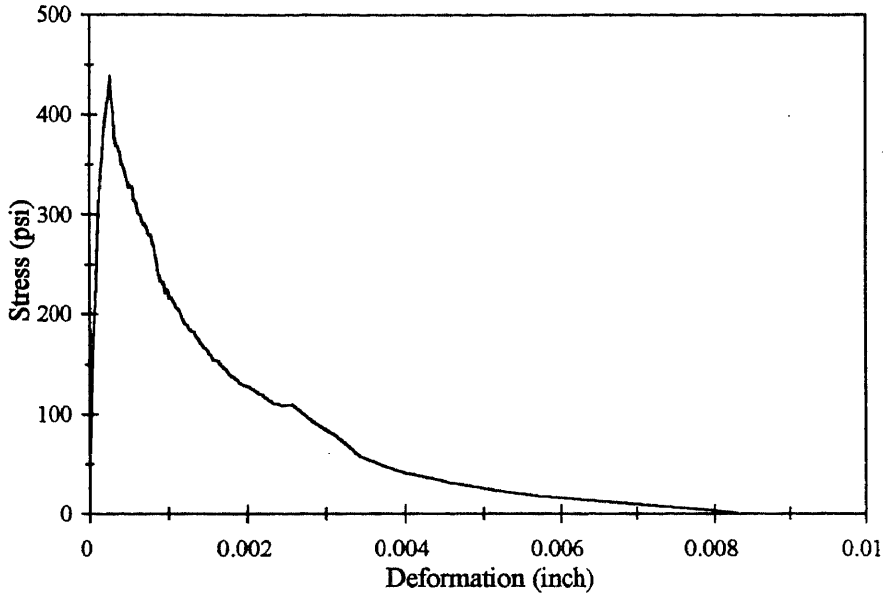

Figure 3.4 Typical Stress-Deformation Curve for HSC-A Concrete (Specimen - A1)

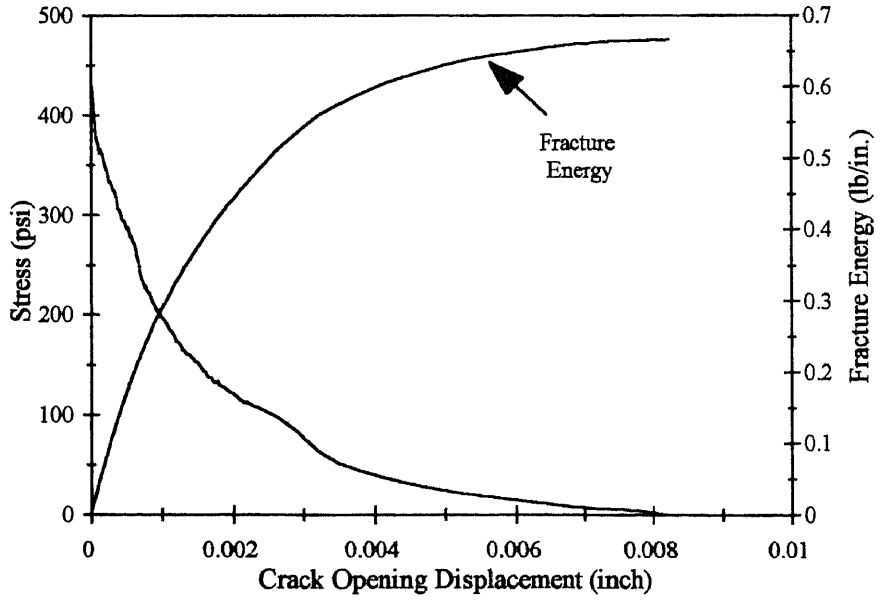

Figure 3.5 Typical Stress-Crack Opening Displacement Curve and Fracture Energy G_F for HSC-A Concrete (Specimen - A1)

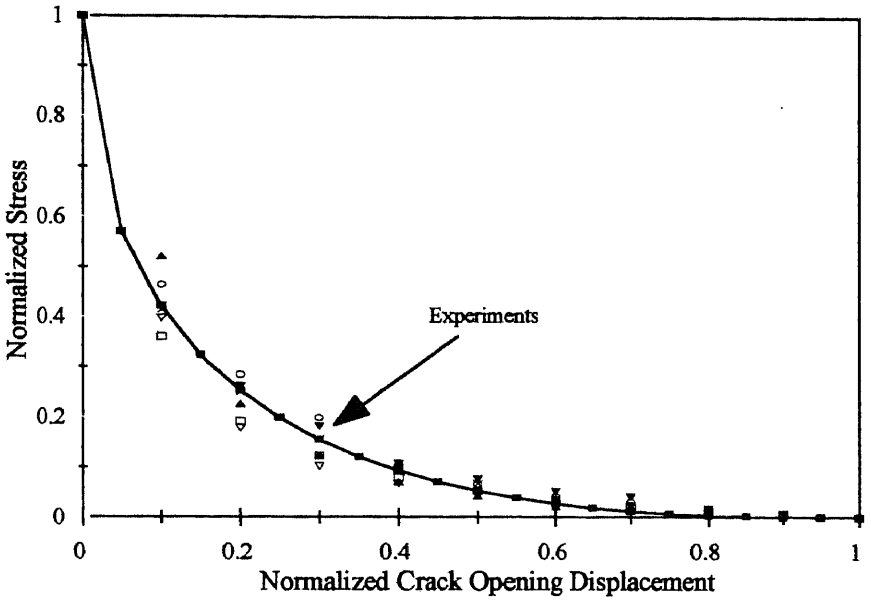

Figure 3.6 Normalized Stress-Crack Opening Displacement Curves of HSC -A Concrete with Regressed Curve Fit (equation 3.1)

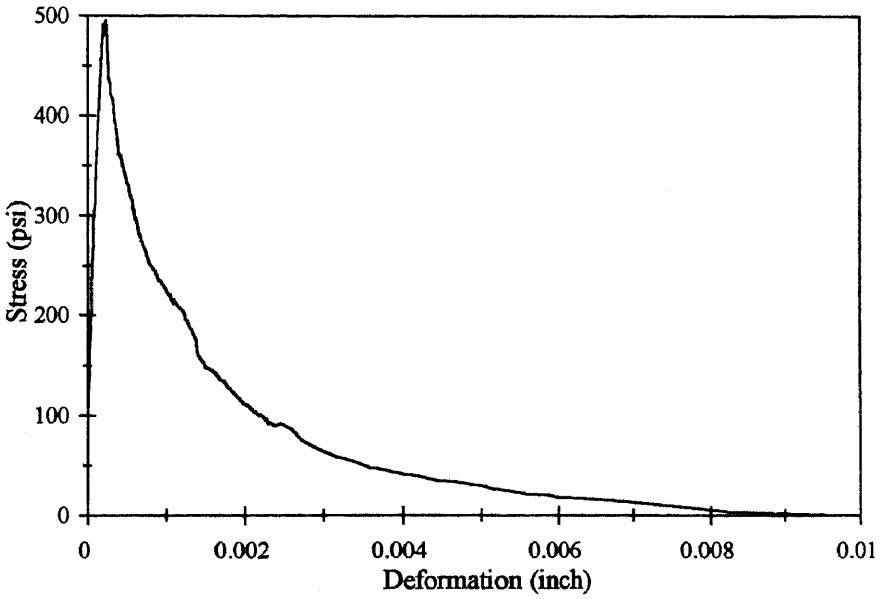

Figure 3.7 Typical Stress-Deformation Curve for HSC-B Concrete (Specimen - B1)

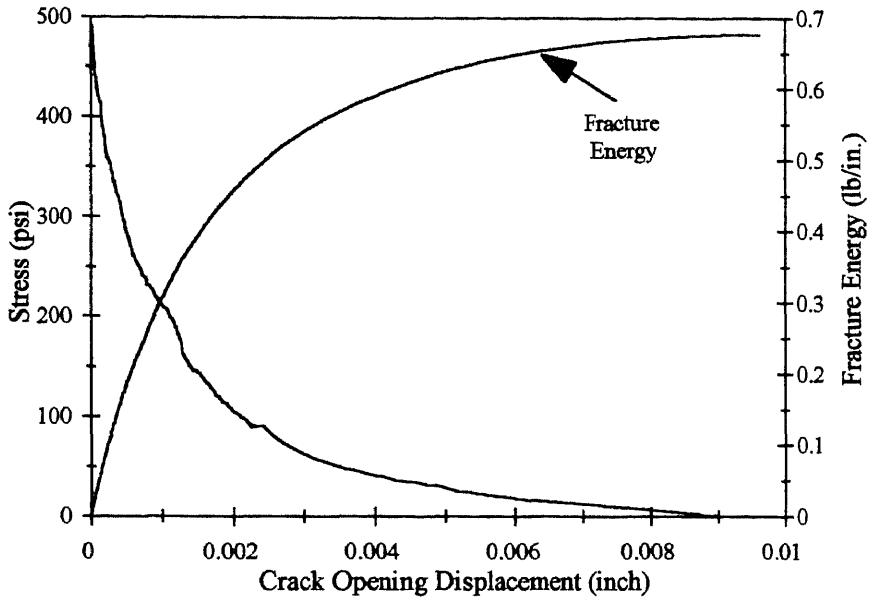

Figure 3.8 Typical Stress-Crack Opening Displacement Curve and Fracture Energy G_F for HSC - B Concrete (Specimen - B1)

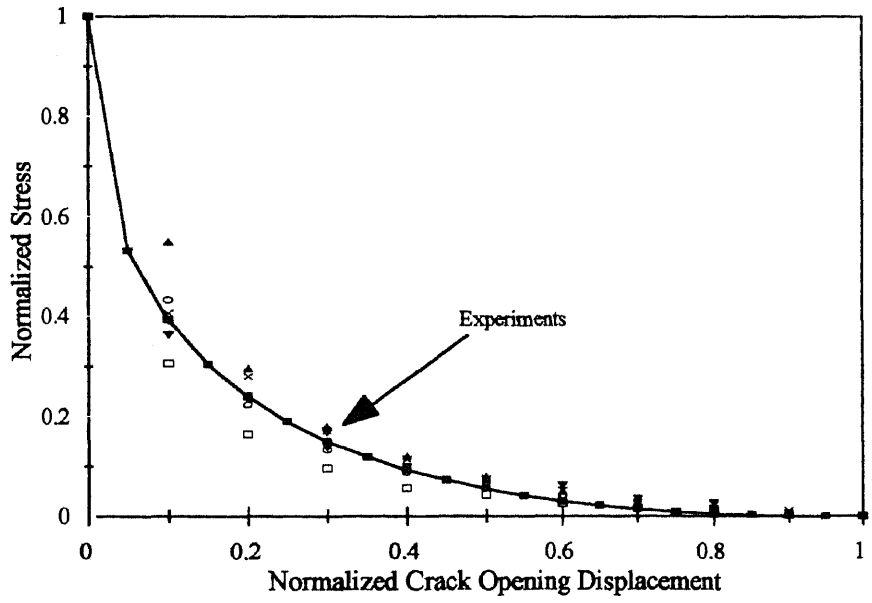

Figure 3.9 Normalized Stress-Crack Opening Displacement Curves of HSC -B Concrete with Regressed Curve Fit (equation 3.1)

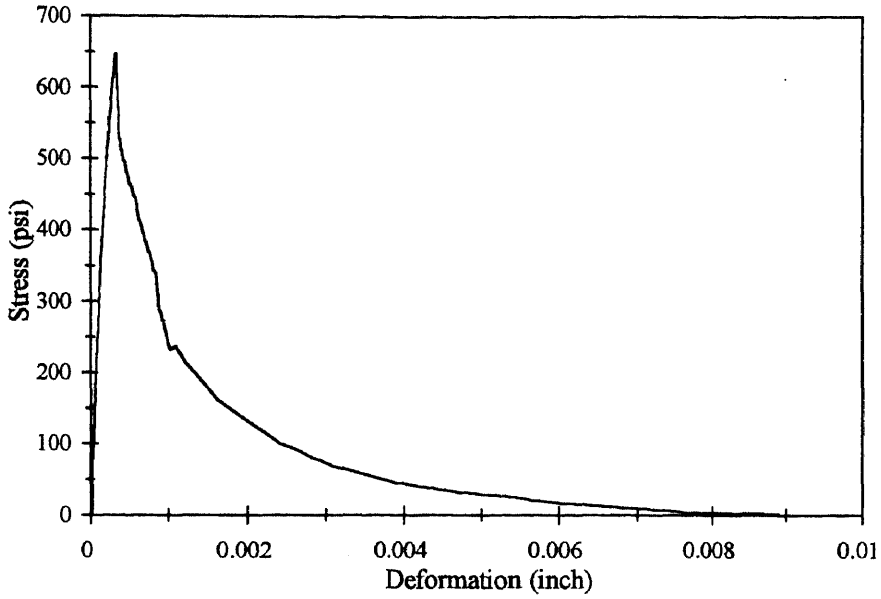

Figure 3.10 Typical Stress-Deformation Curve for HSC-C Concrete (Specimen - C1)

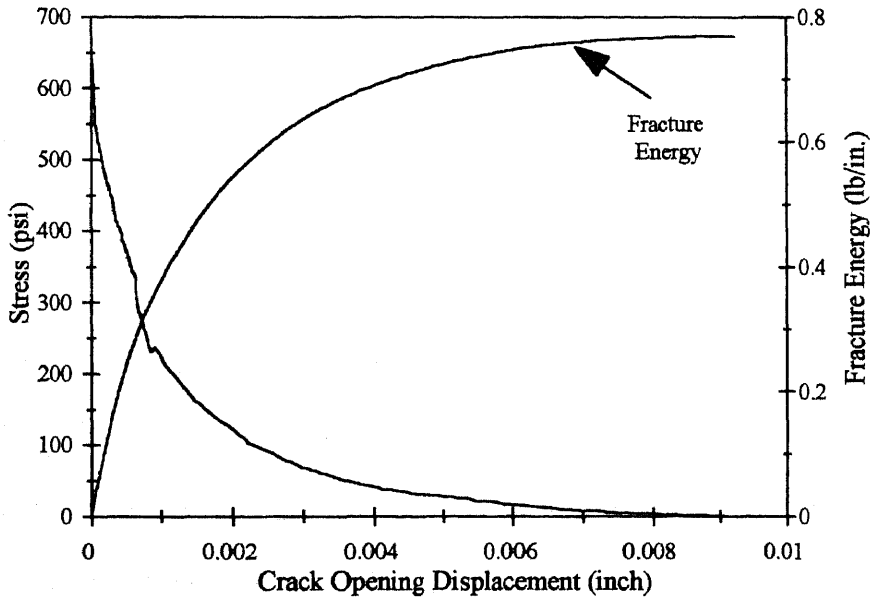

Figure 3.11 Typical Stress-Crack Opening Displacement Curve and Fracture Energy G_F for HSC-C Concrete (Specimen - C1)

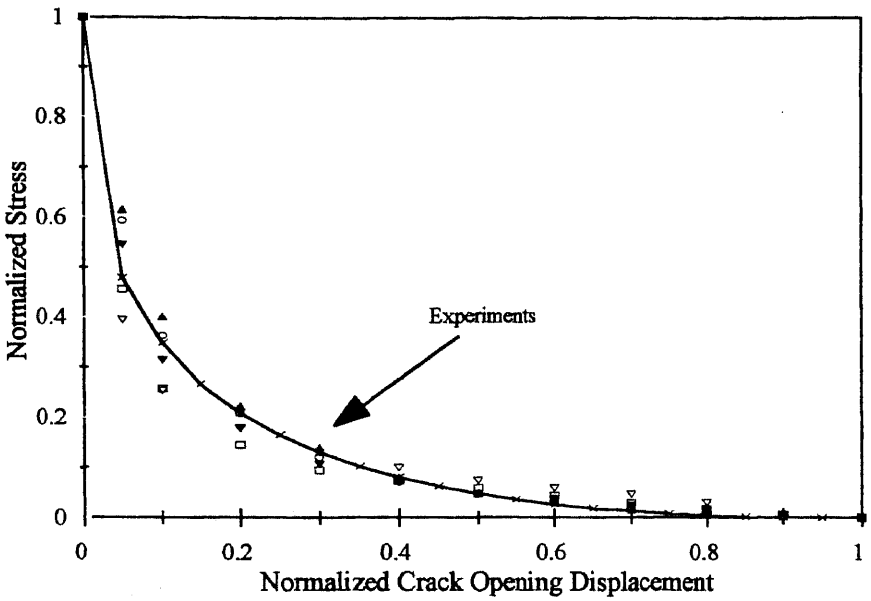

Figure 3.12 Normalized Stress-Crack Opening Displacement Curves of HSC -C Concrete with Regressed Curve Fit (equation 3.1)

In Chapter 4, wherein the finite element analysis is performed, softening curve for HSC-A concrete is referred to as curve A and for HSC-B and HSC-C as curve B and curve C respectively.

3.4 Compression Tests

Information about compressive stress strain response is of direct practical interest in the design of reinforced concrete structures. The primary objective of conducting compressive tests on high strength concrete was to determine the following properties:

1. The uniaxial compressive strength (f'_c)
2. The Modulus of Elasticity (E_c), and
3. The peak strain (ε_p)

Due to the brittle nature of high strength concrete, compression tests were performed at a relatively slower rate compared to the testing rate for normal strength concrete. The details of the actual method used for testing differed depending upon the type of high strength concrete. For HSC-A and HSC-B concrete the tests were performed in an 100 kip capacity MTS closed loop system under deformation (axial strain) control. The details of the test setup is as shown in Figure 3.13

The average rate of axial deformation was measured by the two clip gages. The signal was then electronically averaged and used as the feedback control. The uniaxial deformations were converted to strains by dividing the deformation by the gage length. In this setup the gage length was 6.0 inches (height of the specimen). Strains were employed to calculate the Modulus of Elasticity (E_c) of concrete in compression. In the pre-peak region, specimens were loaded under deformation (axial strain) control at the rate of 4.167×10^{-7} in./in. per second Past the peak load the deformation rate was gradually increased at regular intervals depending on the load level. It took approximately 10 to 15 minutes to reach the peak load and around 45 minutes to complete the entire test.

For HSC-C concrete tests, using the above test setup it was found to be extremely difficult to obtain a stable post-peak response. Sudden failure at peak loads caused by loss of feedback control of the machine often resulted in explosive failure of the test sample and termination of the test at the peak level stresses. To overcome this problem, HSC - C cylinders were tested using circumferential strain (displacement) control. A high resolution MTS circumferential gage (range 0.3 in.) was utilized. The

average rate of axial deformation was also measured by the two strain gages (4 in. gage). The specimens were loaded initially under load control until around 40 kip (7000 psi) and then switched to circumferential control at the rate of 2 $\times 10^{-4}$ in. per second. Past the peak load, when the circumferential gage ran out of its range, the test was continued by switching to axial displacement control mode. Availability of such a unique capability in the 1000 kip MTS (model 815) testing system made the testing of HSC-C concrete possible. It took approximately 2 to 3 minutes to reach the peak load and around 45 minutes to complete the entire test. Details of the test setup is shown in the Figure 3.14 and photograph of the test setup is shown in the Figure 3.15.

At least 3 cylinders (3 $\times$ 6) for every strength (Table 3.2) were cast in plastic molds from the same batch of concrete that was used for casting the tension specimens. and beam specimens. After 24 hours the cylinders were demolded and transferred into lime saturated water for curing until the testing age of 28-35 days.

3.4.1 Results of Compression Tests

Typical stress-strain curves are shown in Figures 3.16 through 3.18. As can be seen from these graphs, the stress-strain curves for HSC-A and HSC-B are very much consistent as far as the post peak behavior is concerned. For HSC -C the post peak response is highly unpredictable. The descending part of stress-strain curves become steeper for HSC-B and HSC-C type of concrete because of increased compressive strengths. For HSC-C the post peak is most dynamic. This could be due to the difference in failure mode of each type of concrete. For HSC-A the failure mode was the usual cone type. This is probably because of lesser influence of the restraining effect (end effects) at the ends of the sample

and the loading platens. In HSC - C, the end effects are more evident, owing to higher rigidity of the samples and the larger effect of lateral restraint, the mode of failure was major splitting along the length which caused the load (stresses) to drop whenever splitting occurred and to build up again whenever splitting occurred again. The compressive stress-circumferential strain is shown in Figure 3.19. There are no similarities in the peak values of circumferential strains. One possible explanation is the failure (bulging) of the specimen may or may not occur at the location of the circumferential gage. Nonetheless, the complete stress strain curve can be captured only if circumferential deformation control is used. Furthermore, the Modulus of Elasticity values obtained for HSC-A concrete and HSC-B concrete are significantly lower than expected. The reason for that is due to the extraneous strain measured during the tests. As seen in Figure 3.13, the deformation of the specimen was measured by the two clip gages. Since these gages were mounted on the top of the metal platen, it is possible that the deformations included not only the true strains of the specimen but also the end effect and the deformation of the metal platens causing higher strain readings to be recorded. To overcome such errors, while testing HSC-C concrete, the axial strains were measured away from the end effects and the platens as is shown in Figure 3.14. The strain measurements were made over a gage length of 4". The calculated values of Modulus of Elasticity are more realistic and were used in the finite element calculations presented in the next chapter and in Chapter 5. Similar conclusions regarding low values of Modulus of Elasticity obtained due to extraneous deformations if the strains are measured including the full depth of the sample and the machine platen were also

observed by Hsu et. al. (Hsu and Hsu, 1994) and Mansur et. al. (Mansur, Wee and Chin, 1995).

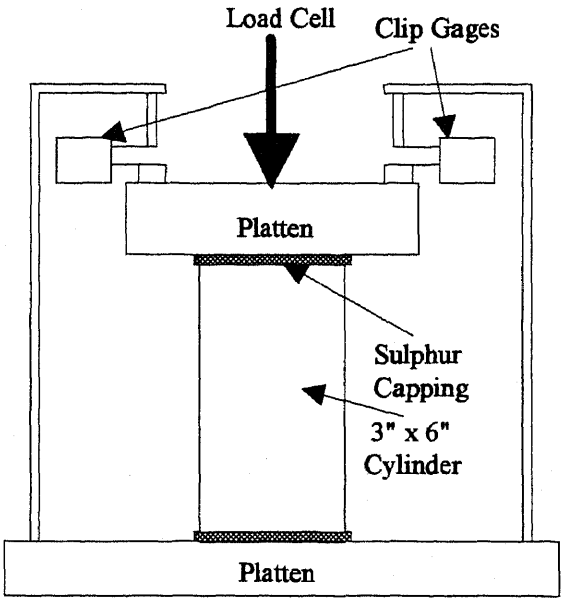

Figure 3.13 Compression test setup used for testing HSC-A and HSC-B concrete

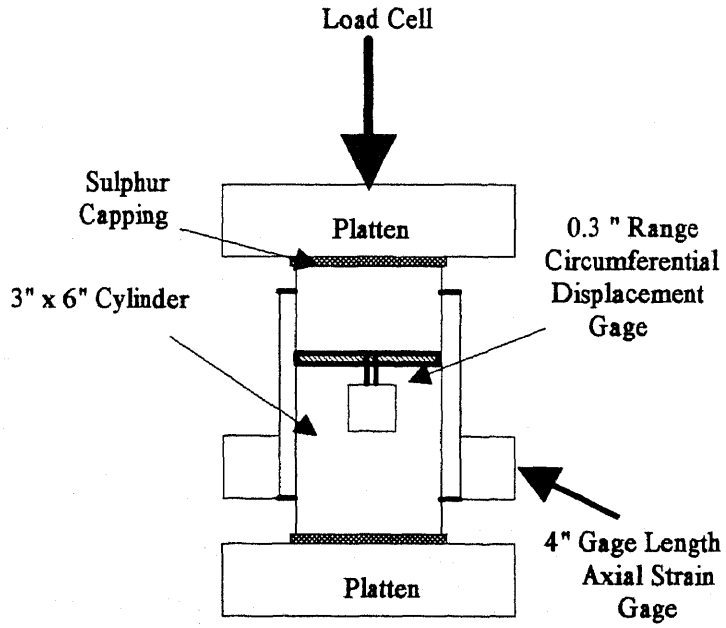

Figure 3.14 Compression test setup used for testing HSC-C concrete

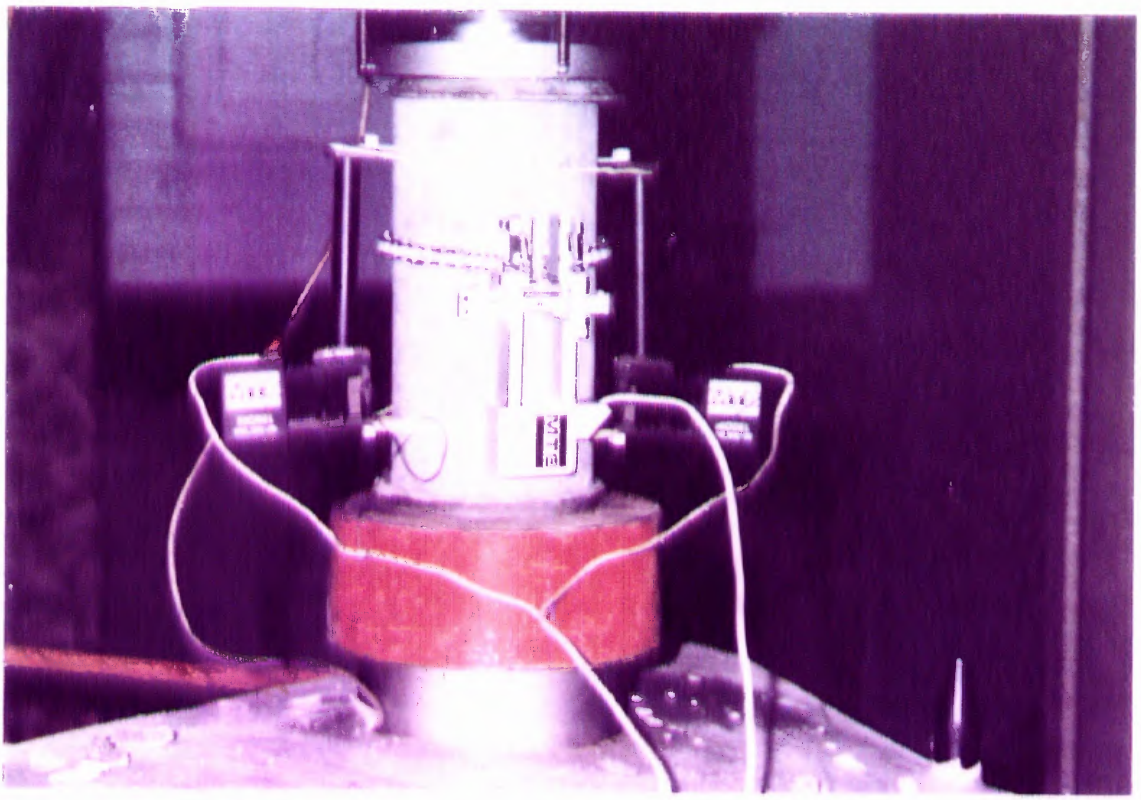

Figure 3.15 Photograph of the Compression Test Setup for HSC-C Concrete

Table 3.7 Compression Test Results

Specimen Name	Compressive Strength f'_c (ksi)	Peak Strain ε_p (in/in)	Modulus of Elasticity E (ksi)
A1	6.570	0.002669	2644
A2	6.528	0.002433	2856
A3	6.653	0.002425	2992
AVERAGE	**6.583**	**0.002509**	**2831**
B1	9.112	0.003044	3160
B2	9.506	0.003345	3409
B3	9.230	0.003003	3345
AVERAGE	**9.283**	**0.003131**	**3305**
C1	11.602	0.003204	5167
C2	11.885	0.002618	4961
C3	12.169	0.002641	5407
C4	12.392	0.002901	5331
AVERAGE	**12.012**	**0.002795**	**5216**

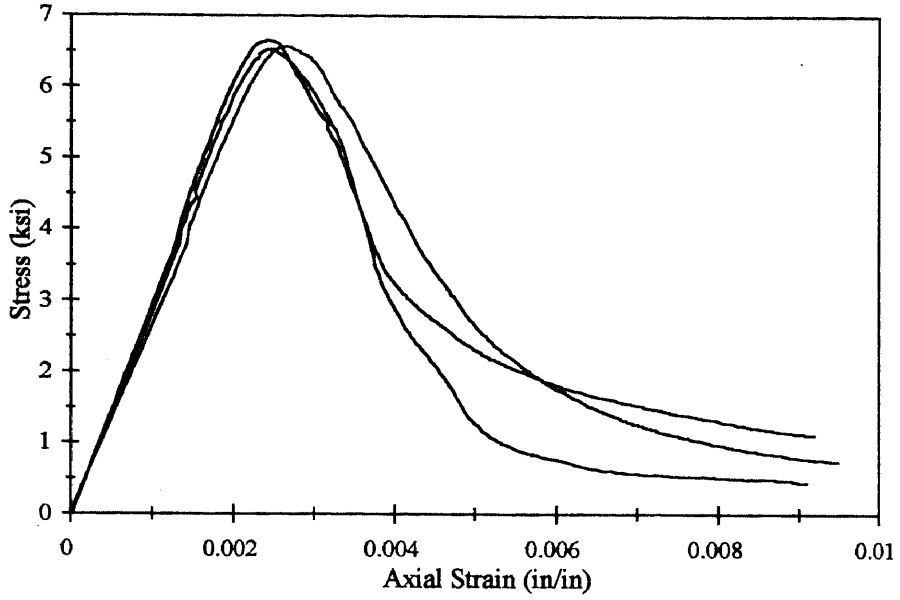

Figure 3.16 Compressive Stress-Strain Curve for HSC-A Concrete

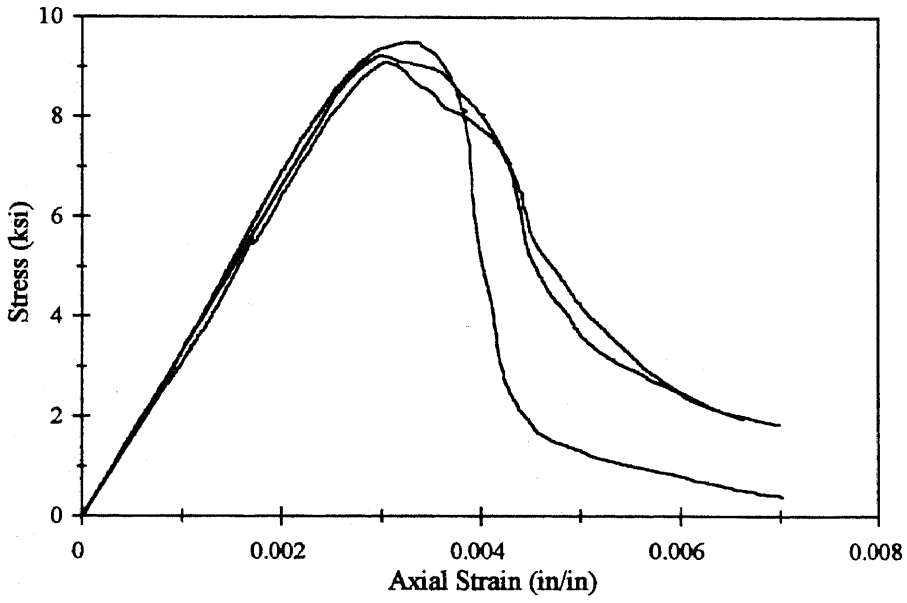

Figure 3.17 Compressive Stress-Strain Curve for HSC-B Concrete

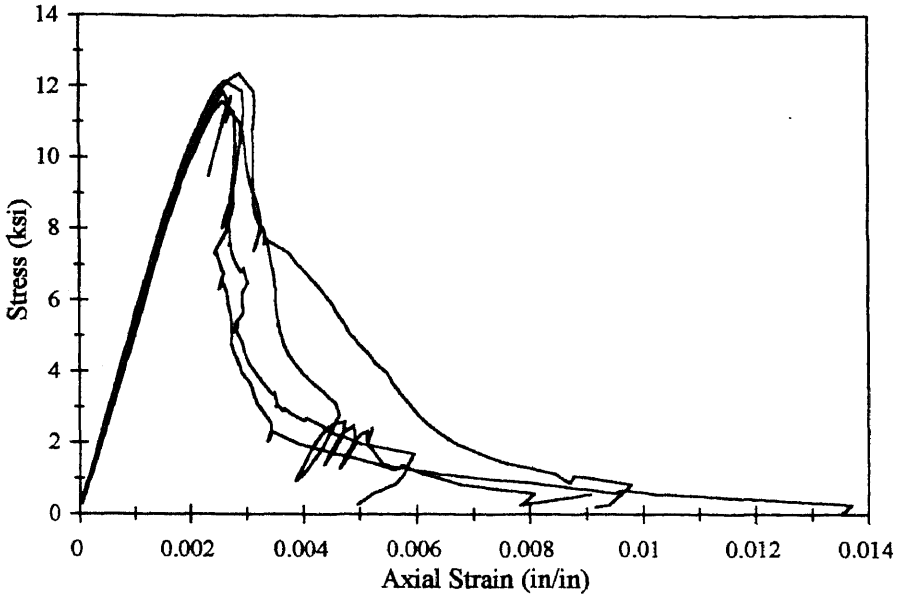

Figure 3.18 Compressive Stress-Strain Curve for HSC-C Concrete

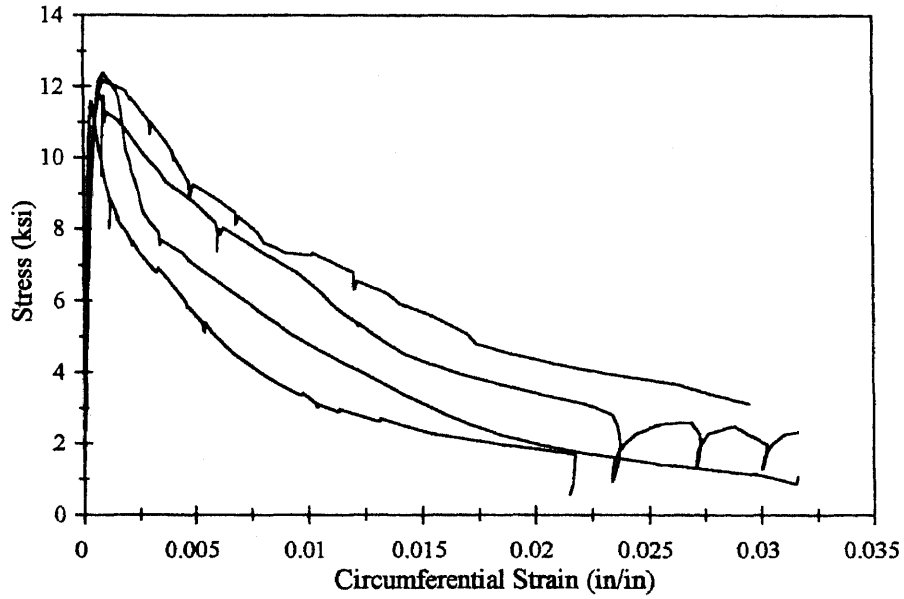

Figure 3.19 Compressive Stress-Circumferential Strain Curve for HSC-C Concrete

3.5 Beam Tests

Three point beam bending tests were performed to evaluate the following parameters:

1. The fracture Energy G_F, which according to the RILEM recommendation, is defined as the area under the load and load point displacement curve divided by the uncracked ligament length. The G_F values from the tension tests will be compared with the RILEM G_F obtained from the beam tests.
2. To develop a relationship between the crack mouth opening displacement and load point displacement.

All beam tests were performed using crack mouth opening displacement (CMOD) control in a MTS closed loop system at a deformation rate of 5×10^{-5} in/sec. Along with the load point displacement measurements off a reference frame (bar), deflection measurements off the beam were also recorded in selected tests. The test data consisting of load, crack mouth opening displacement and the two measurements of deflections were recorded using DAS 8 PGH data acquisition board and Labtech Notebook program. A total of 18 beam tests were performed. The dimension of the test specimen and the details of the test setup are shown in Table 3.2 and Figure 3.20. Actual photograph of the test setup is shown in Figure 3.21. The dimensions of the size C beams were chosen based on the RILEM recommendation. The beam specimens were cast in plexi-glass molds in the direction shown (see Figure 3.20). After 24 hours they were demolded and transferred into lime-saturated water for curing. Prior to testing the beams were notched using a circular diamond saw. All beams were tested at the age of 28 -35 days.

3.5.1 Results of the Beam Tests

Typical load-deflection and load-crack mouth opening displacement curves are shown in Figures 3.22 and 3.23. All other graphs are presented in the appendix. In chapter 5, a method is developed that uses load and crack mouth opening displacement responses to calculate the fracture energy of concrete. Relationship between the crack mouth opening displacement and load point displacement is shown in Figure 3.24. Such a relationship is utilized for calculating fracture energy of concrete and will be presented after the theoretical background is developed in Chapter 5. Tables 3.8 through 3.10 summarize the test data.

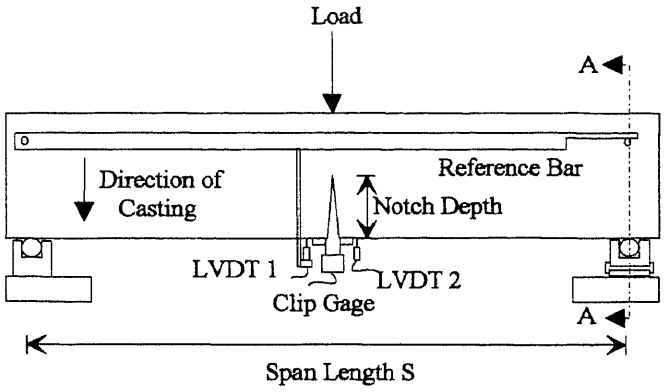

(a) Front View

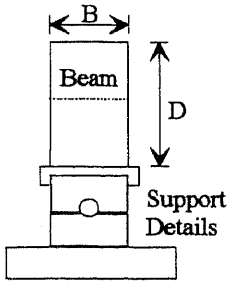

Section A - A

(b) Side View

Figure 3.20 Beam Test Setup Details

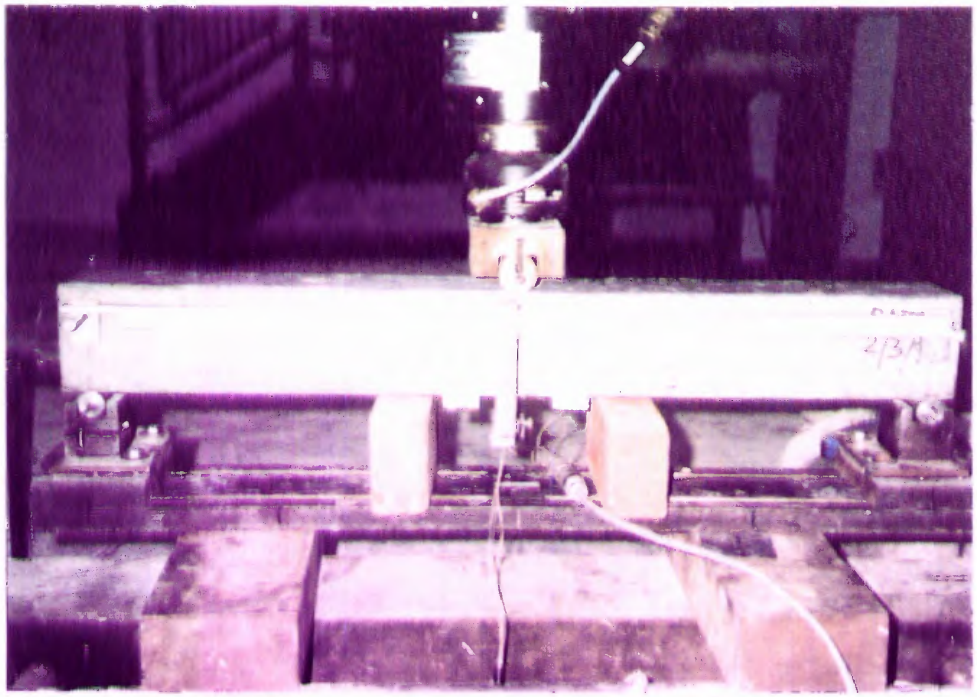

(a) Front View

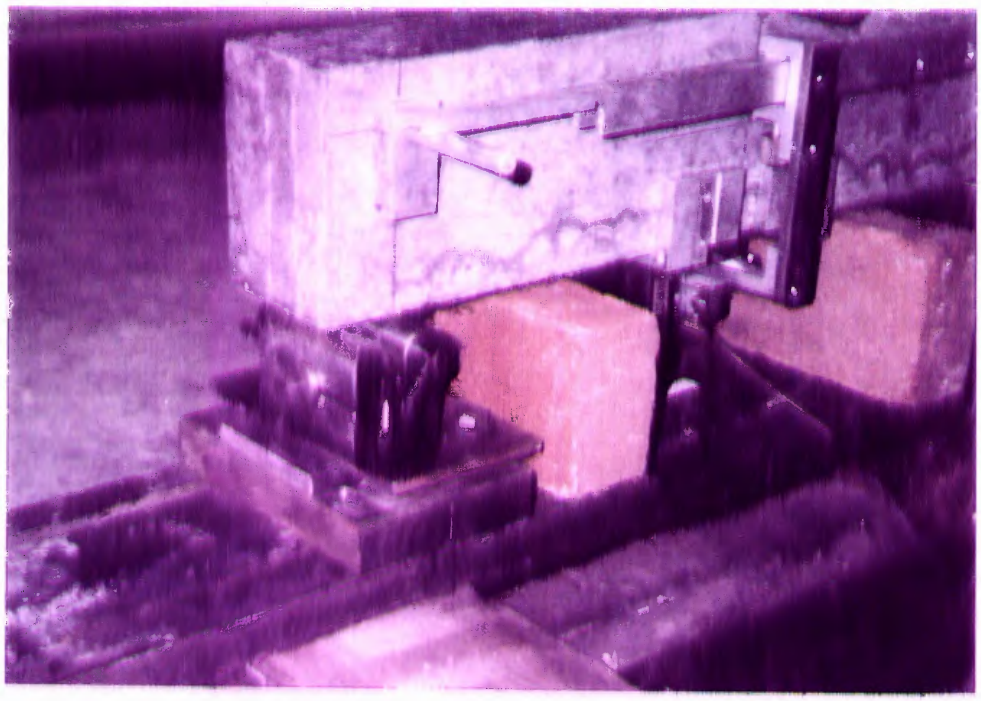

(b) Close-up View

Figure 3. 21 Photograph of the Beam Test Setup

Table 3.8a Test Results Size A -a_o/D = 0.25 Beams (A = Area of ligament = 10.125 in^2)

Specimen Name	Peak Load (pounds)	Peak CMOD (inch)	Peak Deflection (inch)	Fracture Energy (lb./in) $\frac{1}{A}\int_0^{\delta} P d\delta$
A11	1320	0.001816	0.004345	(0.615) 0.655
A12	1143	0.001445	0.002148	(0.685) 0.758
A13	1101	0.001621	0.002295	(0.625) 0.695
AVERAGE	**1188**	**0.001627**	**0.002929**	**(0.642) 0.703**

( ) indicates fracture energy without considering self wt.

Table 3.8b Test Results Size A -a_o/D = 0.50 Beams (A = Area of ligament = 6.75 in^2)

Specimen Name	Peak Load (pounds)	Peak CMOD (inch)	Peak Deflection (inch)	Fracture Energy (lb./in) $\frac{1}{A}\int_0^{\delta} P d\delta$
A21	548	0.002715	0.003027	(0.622) 0.707
A22	551	0.002324	0.003076	(0.700) 0.803
A23	589	0.002891	0.002637	(0.625) 0.719
AVERAGE	**563**	**0.002643**	**0.002913**	**(0.649) 0.743**

( ) indicates fracture energy without considering self wt.

Table 3.9a Test Results Size B -a_o/D = 0.25 Beams (A = Area of ligament = 6.75 in^2)

Specimen Name	Peak Load (pounds)	Peak CMOD (inch)	Peak Deflection (inch)	Fracture Energy (lb./in) $\frac{1}{A}\int_0^{\delta} P d\delta$
B11	437	0.001640	0.003320	(0.587) 0.659
B12	480	0.002402	0.005127	(0.724) 0.808
B13	472	0.001738	0.003418	(0.642) 0.715
AVERAGE	**463**	**0.001926**	**0.003955**	**(0.651) 0.727**

( ) indicates fracture energy without considering self wt.

Table 3.9b Test Results Size B -a_o/D = 0.50 Beams (A = Area of ligament = 4.5 in^2)

Specimen Name	Peak Load (pounds)	Peak CMOD (inch)	Peak Deflection (inch)	Fracture Energy (lb./in) $\frac{1}{A}\int_0^{\delta} P d\delta$
B21	251	0.001914	0.003223	(0.578) 0.724
B22	271	0.001934	0.003613	(0.652) 0.770
B23	258	0.001621	0.002832	(0.547) 0.667
AVERAGE	**260**	**0.001823**	**0.003223**	**(0.592) 0.720**

( ) indicates fracture energy without considering self wt.

Table 3.10a Test Results Size C -a_o/D = 0.25 Beams (A = Area of ligament = 12.0 in^2)

Specimen Name	Peak Load (pounds)	Peak CMOD (inch)	Peak Deflection (inch)	Fracture Energy (lb./in) $\frac{1}{A}\int_0^{\delta} P d\delta$
C11	485	0.001836	0.006445	(0.756) 0.933*
C12	512	0.002402	0.007520	(0.639) 0.818
C13	539	0.001484	0.005908	(0.643) 0.798
AVERAGE	**512**	**0.001907**	**0.006624**	**(0.641) 0.808**

( ) indicates fracture energy without considering self wt.
* Not included in average for G_F. - Cracked outside of the straight line path.

Table 3.10b Test Results Size C -a_o/D = 0.50 Beams (A = Area of ligament = 8.0 in^2)

Specimen Name	Peak Load (pounds)	Peak CMOD (inch)	Peak Deflection (inch)	Fracture Energy (lb./in) $\frac{1}{A}\int_0^{\delta} P d\delta$
C21	344	0.002129	0.005859	(0.494) 0.691
C22	329	0.002246	0.005664	(0.486) 0.693
C23	345	0.002910	0.007519	(0.796) 1.074*
AVERAGE	**339**	**0.002428**	**0.006347**	**(0.490) 0.692**

( ) indicates fracture energy without considering self wt.
* Not included in average for G_F - Cracked outside of the straight line path.

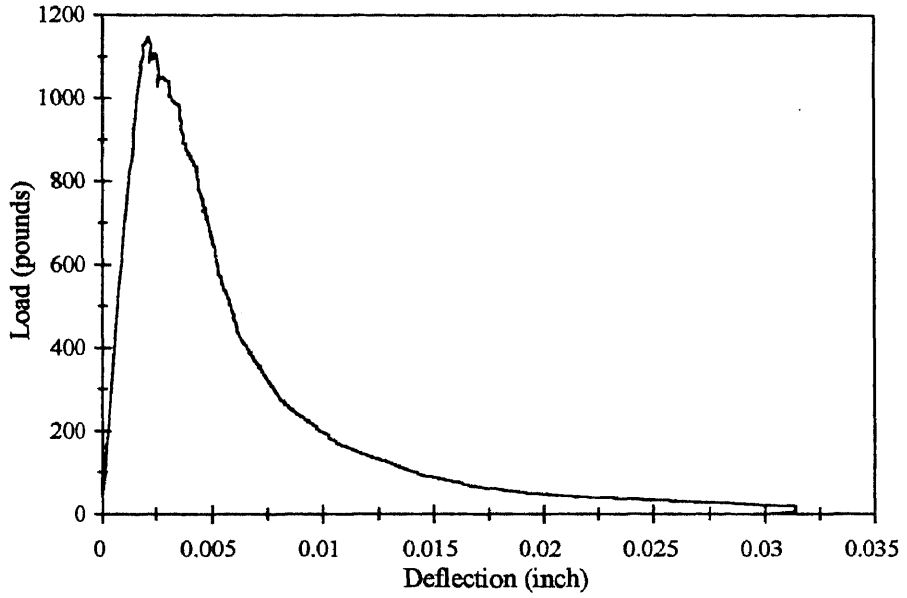

Figure 3.22 Typical Load-Deflection (LPD) Response of Size A Beam - HSC-C Concrete

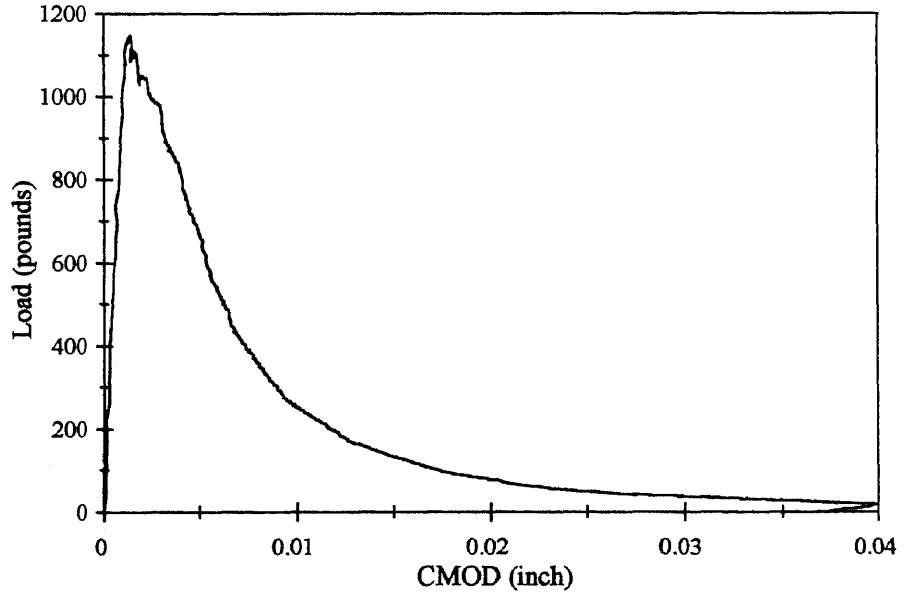

Figure 3.23 Typical Load-Crack Mouth Opening Displacement (CMOD) Response of Size A Beam - HSC-C Concrete

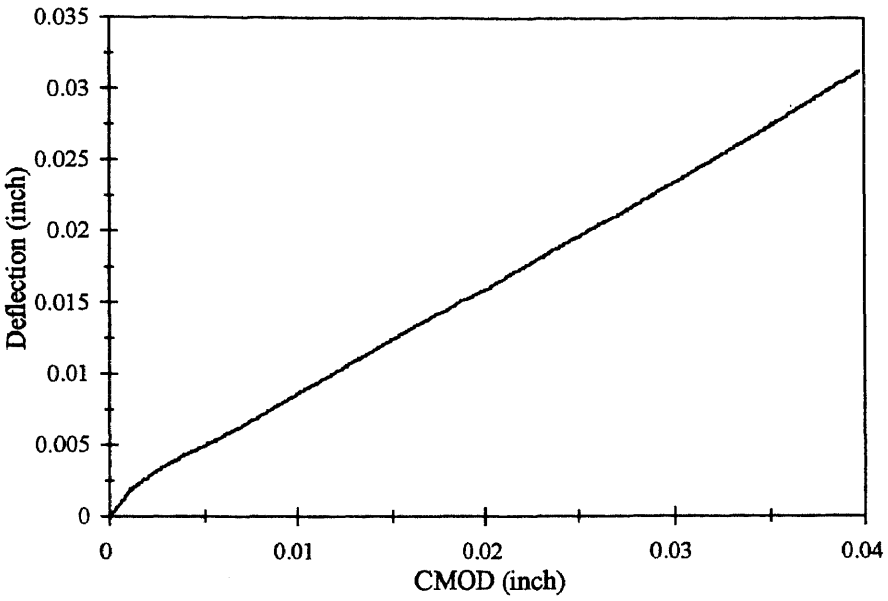

Figure 3.24 Typical CMOD-LPD Relationship of Size A Beam - HSC-C Concrete

CHAPTER 4

FINITE ELEMENT ANALYSIS

4.1 Introduction

The major part of this chapter deals with the method of finite element calculations used in the present study for fictitious crack analysis of concrete members. Alternate methods of calculations are also discussed briefly.

The present approach of modeling the crack and its propagation is based on the fictitious crack model developed by Hillerborg (Hillerborg, Modeer and Petersson 1976). Spring elements with softening characteristics located along the crack path are employed in modeling the crack opening during the load-deflection analysis of unreinforced concrete members. The details of the modeling approach are explained in this chapter. It should be noted that the purpose of the present study has been to only utilize the finite element method for performing parametric study on the behavior of concrete members (normal and high strengths) and not for the evaluation or development of a new finite element method.

It is appropriate to mention that different methods and types of calculations may be utilized during the fictitious crack analysis. To mention a few: the finite element method, the boundary element method, the finite difference method and if special problems are to be studied, other less general methods such as modified linear elastic fracture mechanics concepts may be utilized. It seems that the finite element method is the most flexible and most well known. These reasons made finite element method an obvious choice for the present study.

Finite element computer programs are readily available such as ANSYS, ADINA, ABAQUS etc. The FEM program chosen in this study is ABAQUS ver. 5.4. Such a choice was necessary because of the capability of ABAQUS in treating "a negative stiffness" in the modeling of non-linear spring elements in the fracture zone. A brief description of ABAQUS is shown in Section 4.2 and details of the algorithm used in the solution phase is discussed in section 4.3.

4.2 ABAQUS

ABAQUS is a general purpose finite element program which was developed by Hibbitt, Karlsson & Sorensen, Inc. 1994. The ABAQUS/Standard version 5.4 has been installed on the UNIX based Spark workstation at the New Jersey Institute of Technology computer facilities.

In this thesis, ABAQUS finite element program was used for developing a model which will simulate the crack propagation and other characteristics of concrete behavior in tension. As crack propagates in concrete, the stresses acting around the crack still transfer across the interface of the crack. To simulate such behavior, spring elements with decreasing stiffness as the crack widens are utilized. ABAQUS offers a non-linear spring element which can be defined with negative stiffness. In the following sections, details of this FEM model are presented.

4.3 Modeling Inside and Outside the Fracture Region

The material outside of the fracture zone is assumed to be linear elastic and has been modeled by using 4-node rectangular and quadrilateral shaped plane stress elements. In

the transition regions from a coarser mesh to a finer mesh, 3-node plane stress triangular elements were utilized. Higher order elements were not utilized. This has partly to do with the presently adopted simple approach of modeling of the fracture zone and partly to do with the possibility of an irregular displacement distribution close to the fracture zone, which may not fit smooth displacement distribution of the high order polynomial shape functions. Where the modeling of the fracture zone is concerned, two approaches have been debated for more than two decades: the discrete method and the smeared method. The fictitious crack model is a material model and it clearly belongs to the discrete models. The present study is based on the fictitious crack material model and hence belongs to the discrete modeling category.

The smeared method approach in the sense of a material model is defined with a descending branch in the stress - strain curve without attention being paid to the strain localization during fracture process. The smeared cracking model was first introduced by Rashid (1968) and has prevailed in finite element analysis of concrete since the 1970's. The popular applications are attributed mainly to two computational conveniences: They are (1) automatic generation of cracks without the redefinition of the finite element topology and (2) complete generality in possible crack direction. In spite of all the conveniences and widespread use of the smeared approach, there is no consensus as to its superiority relative to the discrete approach. Furthermore, in recent years the use of smeared approach has declined rapidly, this is probably because of increasing awareness of the phenomena of strain instability and strain localization and the knowledge of the unfortunate influence of the size of the finite elements.

In Figure 4.1, few examples of different methods or possibilities for the finite element modeling of a fracture zone with a known crack propagation path are shown. The approach denoted in Figure 4.1(d) is used in the present analysis. Figure 4.1(a) corresponds to the method used by Hillerborg et. al. (Hillerborg, Modeer and Petersson, 1976). Similar approach, but more modulated modeling, is shown in Figure 4.1(b). This type of modeling has been used by Ingraffea and Gerstle (1985). Alternative approach shown in figure 4.1(c) is smeared based approach and has been used extensively by Bazant and Oh (1983a and 1983b) and Rots (Rots and Blaauwendraad 1989) and many other researchers. During the application of this alternative, the absolute size of the finite element is taken into account in the assumed part of the descending stress-strain curves. A major advantage in the proposed method of modeling is that during incremental load-deflection analysis, the topology of the finite elements does not need to be updated.

4.4 Properties of the Fracture Process Zone (Spring elements)

As described in chapter 2, presence of a fracture process zone and post cracking softening are the characteristics of concrete. These characteristics also dominate the modeling methods of finite element analysis of concrete cracking. As a result, implementing the post cracking softening relationships into analytical procedure becomes an essential part of finite element analysis of concrete structures.

In smeared crack analysis, the softening relationship is realized through the stress-strain relations at the integration points inside the solid element. In the discrete approach (present case), the crack is simulated by splitting the nodes along a common boundary between the two elements (see Figure 4.1(d)).

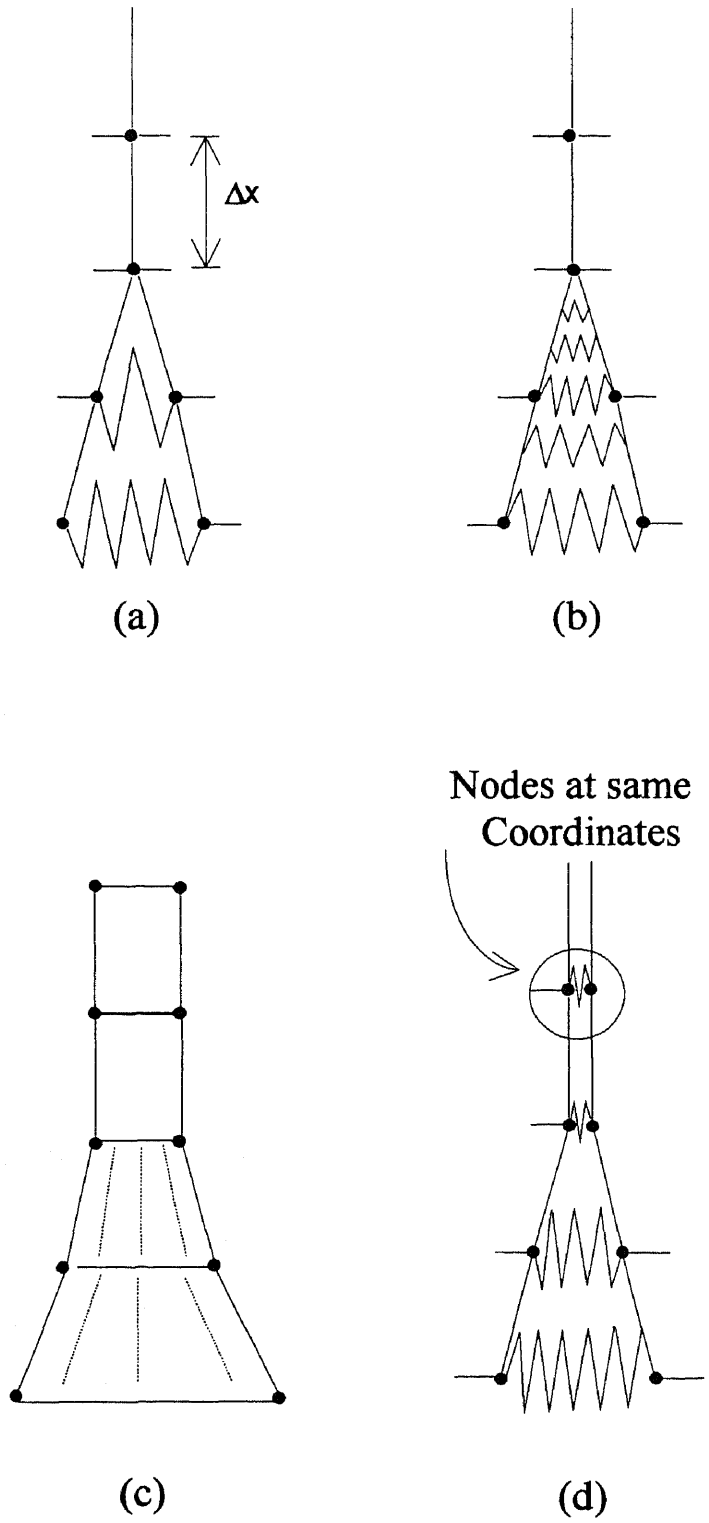

Figure 4.1 Finite Element Models with a Known Crack Path (a) Hillerborg, Modeer et. al. (b) Ingrafea, Gerstle et, al, (c) Bazant and Oh et. al. (d) Present Approach

In this study, force displacement relationships (spring properties) at discrete crack faces are assigned based on the direct uniaxial tension test data obtained from experimental investigation. The normal stress across the cracks is assumed to be related to the crack width. Shear stresses, which might be transferred across the interfaces have been neglected.

As described in Figure 4.1(d), a pair of unsplit nodes represent a material point in a structure. The node pair is allowed to split when the force or the stress within the element equals or exceeds the tensile strength of concrete. The magnitude of the tensile force across the section where a crack is forming reduces or decreases as the crack width increases or widens. This is achieved by defining the non-linear spring element properties in accordance with the stress-separation curves obtained from direct tension tests and are declared in the input parameters in model definition module of ABAQUS. In order to have zero displacement across the crack path before the tensile strength is reached at the nodes, the spring elements are assigned a very high initial stiffness. The value of the initial stiffness was calculated such that the stiffness (initial) of the beam model without the spring elements located along the crack path deflects the same amount for a given load as the beam model with spring elements assigned along the pre-defined crack path (see Figure 4.2 (a) and (b) and Figure 4.3). In this study a value of 1×10^{10} lb./in was found suitable. By defining a high initial stiffness, the overlapping of elements in the compression region is also prevented. The non-linear properties of the springs are shown in Figure 4.2 (c).

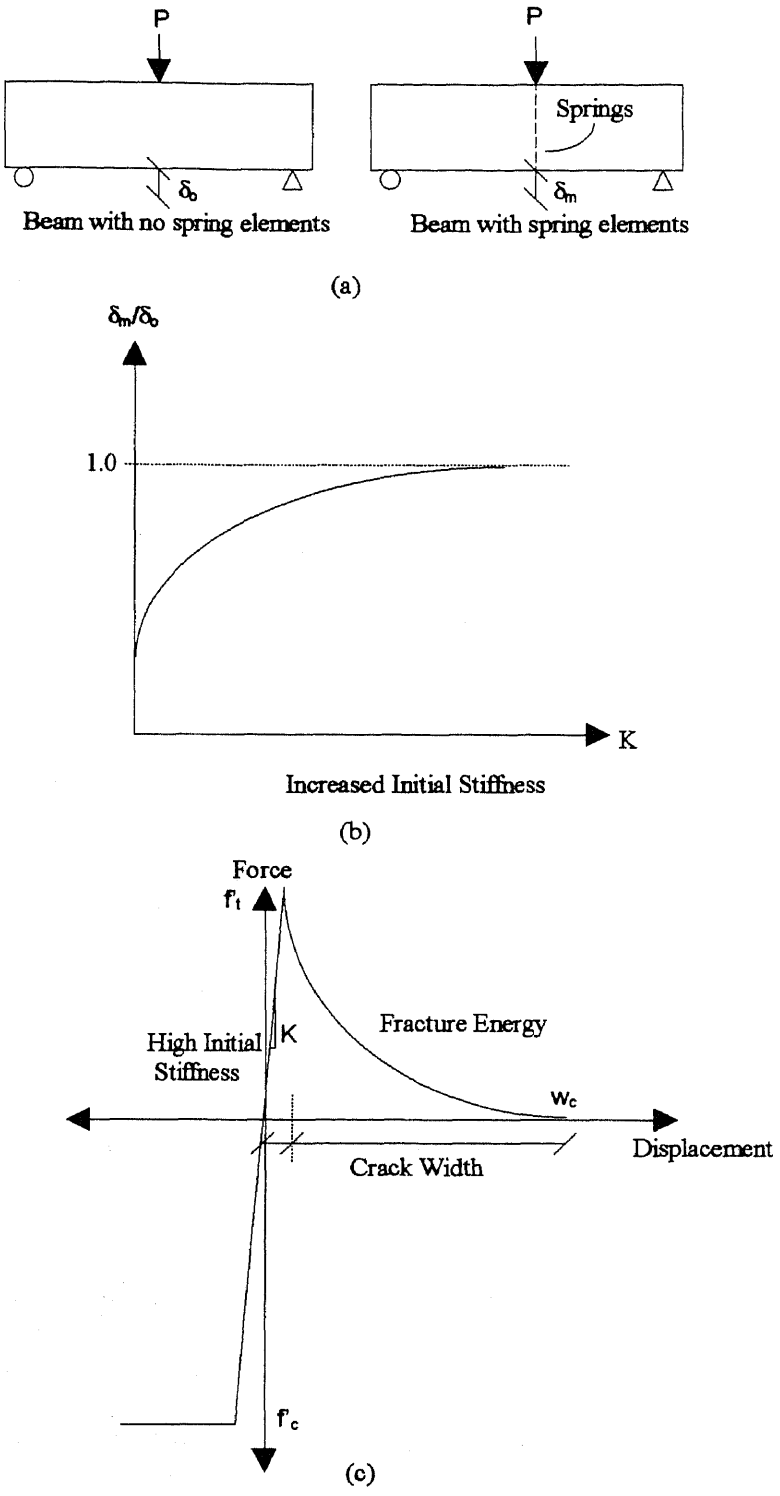

Figure 4.2 (a) Method used for Determination of Initial Stiffness of the Spring Elements (b) Convergence of the Model Deflection Compared to Actual Deflection as Initial Spring Stiffness is Increased (c) Material Properties of the Spring Element

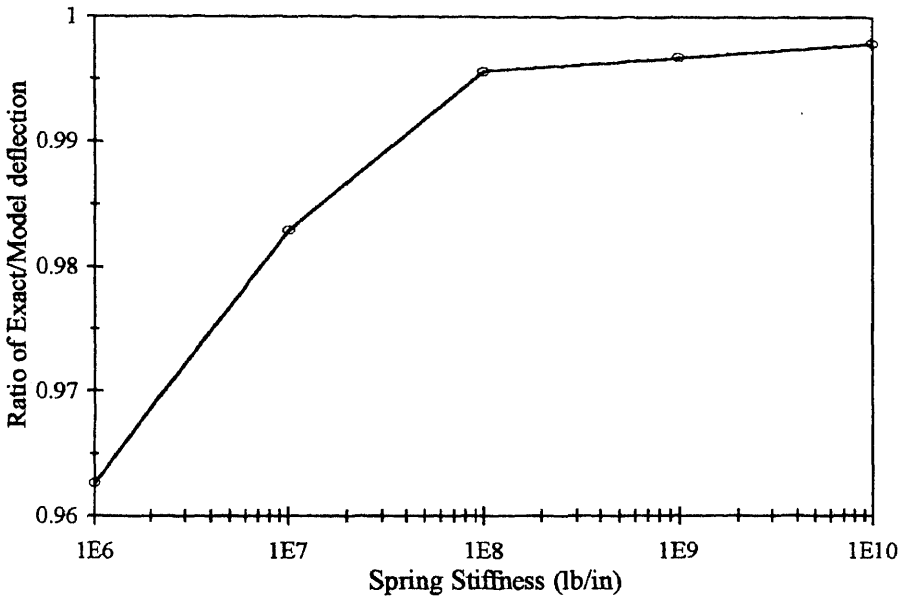

Figure 4.3 Convergence of Beam Deflection as Spring Stiffness is Increased

4.5 Modified RIKS Solution Algorithm Used in the FEM Analysis

4.5.1 General Background

It is often necessary to obtain nonlinear static equilibrium solutions for unstable problems where the load-displacement may exhibit the type of behavior shown in the Figure 4.4 below. During the periods of the response, the load and/or the displacement may decrease as the solution evolves. The modified RIKS method is an algorithm which allows an effective solution of such cases.

It is assumed that the loading is proportional, that is, that the load magnitudes vary with a single scalar parameter. Also, it is assumed that the response is reasonably smooth, that is, sudden bifurcations do not occur. Several methods have been proposed and applied to such problems. Of these, the most successful seems to be the modified

RIKS method (Crisfield 1981; Ramm 1981; Powell and Simons 1981) and a version of this has been implemented in ABAQUS. The essence of this method is that the solution is viewed as the discovery of a single equilibrium path in the space defined by the nodal variables and the loading parameter. Development of the solution requires traversing this path as far as required. The basic algorithm remains the Newton method, and therefore at any time there will be finite radius of convergence. Further, many of the materials of interest will have path dependent responses. For these reasons, it is essential to limit the increment size. In the modified RIKS method (as implemented in ABAQUS) this is done by moving a given distance (determined by ABAQUS' standard, convergence rate dependent, automatic incrementation algorithm for the static cases) along the tangent line to the current solution point, and then searching for equilibrium in the plane that passes through the point thus obtained and is orthogonal to the same tangent line. Here the geometry referred to is the space of displacements, rotations and load parameters mentioned above.

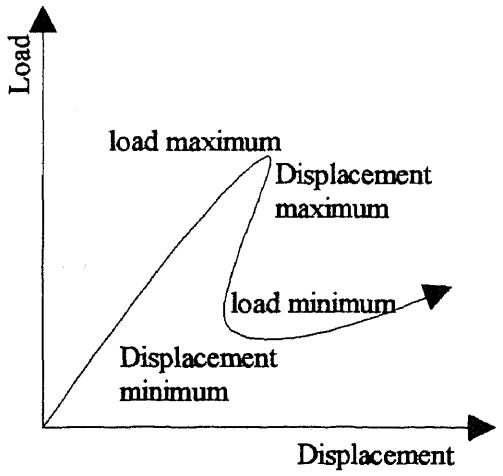

Figure 4.4 Typical Unstable Static Response

4.5.2 Basic Variable Definitions

Let P^N , where N is the degree of freedom of the model and P is the variable used for control, for instance the using CMOD control or the load-point displacement control as defined in the model. Let λ be the load magnitude parameter, so that at any time the actual load state is λP^N, and let u^N be the displacement at that time.

The solution space is scaled to make the dimensions of approximately the same magnitude on each axis. In ABAQUS, this is done by measuring the maximum absolute value of all displacement variables, u_o, in the initial linear iteration. Also define $P_o = (P^N P^N)^{1/2}$. Then the scaled space is spanned by:

$$\text{load} = \lambda \, \widetilde{P}^N, \widetilde{P}^N = P^N / P_o, \tag{4.1a}$$

$$\text{displacements} = \widetilde{u}^N = \left(u^N / u_o \right), \tag{4.1b}$$

and the solution path is then continuous set of equilibrium points as described by the vector $(\widetilde{u}_o^N ; \lambda)$ in this scaled space. All components of this vector will be of order unity. The algorithm for this is shown in Figure 4.5 and is described below.

Suppose the solution has developed to the point $A^o = (\widetilde{u}_N^o; \lambda_o)$. The tangent stiffness, K_o^{NM}, is formed, and solved in the following equation:

$$K_o^{NM} v_o^M = P^N \tag{4.2}$$

The increment size A^o to A^1 in Figure 4.5 is chosen from a specified path length, Δl, in the solution space, so that:

$$\Delta\lambda_o^2(\tilde{v}_o^N;1):(\tilde{v}_o^N;1)=\Delta l^2 \tag{4.3}$$

and hence

$$\Delta\lambda_o=\pm\frac{\Delta l}{(\tilde{v}_o^N\tilde{v}_o^N+1)^{1/2}} \tag{4.4}$$

The value of Δl is initially suggested by the user and is adjusted by the ABAQUS automatic load incrementation algorithm for the static problems, based on the convergence rate. The sign of $\Delta\lambda_o$ — the direction of response along the tangent line — is chosen so that the dot product of $\Delta\lambda_o^2(\tilde{v}_o^N;1)$ on the solution to the previous increment $(\Delta\tilde{u}_{-1}^N;\Delta\lambda_{-1})$, is positive:

$$\Delta\lambda_o^2(\tilde{v}_o^N;1):(\Delta\tilde{u}_{-1}^N;\Delta\lambda_{-1})>0, \tag{4.5}$$

that is

$$\Delta\lambda_o^2(\tilde{v}_o^N\Delta\tilde{u}_{-1}^N+\Delta\lambda_{-1})>0 \tag{4.6}$$

It is possible that in some cases, where the response shows very high curvature in the $(\tilde{u}^N;\lambda)$ space, this criterion will cause the wrong sign to be chosen. This rarely happens in practical cases, unless the increment size is too large, or the solution bifurcates sharply. For further details regarding the theoretical background of the RIKS method the reader is referred to ABAQUS theoretical manual.

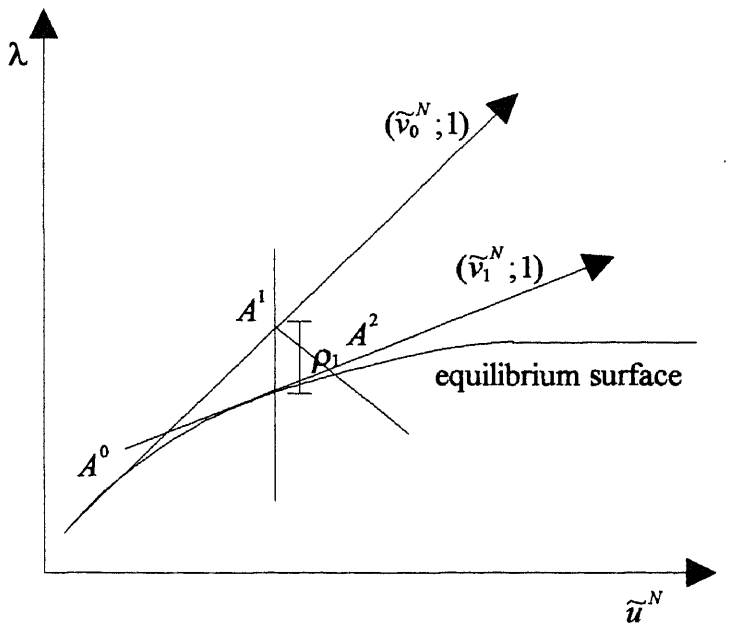

Figure 4.5 Modified RIKS Algorithm Method

4.6 Convergence

To develop an understanding of the convergence rate and the influence of the mesh refinement on the predicted outputs of the model, the following conditions were investigated.

1. The minimum number of elements required to converge to exact elastic load point deflection in un-notched beams and to exact load point deflection and crack mouth opening displacements in the notched beams.
2. The effect of mesh refinement along the crack path on the calculated ultimate load values for both notched and unnotched beams.

For unnotched beams, the number of 4-node plane stress elements along the crack path were equal to 12, 24, 48 and 96, correspondingly 13, 25, 49 and 97 spring elements were used. For notched beams (ratio a/D=0.5), the number of spring elements

were 7, 13 ,25 and 49, respectively. In other parts of the beam, similar 4-node coarser mesh was defined. Triangular (3-node) elements were used in the transition regions. A fairly coarse mesh (12 elements along the crack path) and a very fine mesh (96 elements) are shown in Figure 4.6.

The elastic deflection and CMOD were calculated for different mesh spacing using ABAQUS ver. 5.4 computer program. A beam size of 6.0" depth with width of 3.0" and span length of 24" was analyzed using the material properties of high strength concrete (HSC -C , f'_c = 12,000 psi). The results are tabulated in Table 4.1. The values of K_1 and K_2 represent the stiffness of the beam with respect to the load point displacement and crack mouth opening displacement. These results seem to suggest a parabolic type of convergence of the elastic deflection and CMOD values. It is interesting to note that the effect of mesh spacing has considerable effect on the crack mouth opening displacement values.

In concrete, the development of process zone in front of the crack tip plays an important role and affects the peak load calculations considerably. The influence of mesh spacing on the computed peak loads was studied. It was found that the minimum number of elements required to get within engineering accuracy in predicting peak load values depended on the effect of the process zone length development, i.e., the number of nodes opened due to stress equaling or exceeding the tensile strength limit at the peak load. The size of process zone development depends on the size or the depth of the beam, hence it is not the number of elements required but the influence of the size (depth of beam / total number of elements) of elements defined along the crack path that affects the accuracy of the predicted peak loads. This is because the stresses across the crack

path is represented in parts in which they are constant. The finer the mesh the more accurate is the profile of stress distribution along the crack path. A very important result observed is that the load converges to a certain values when the size of element is decreased. For instance, for a beam depth of 3.0" (B = 3.0" and S = 12.0") as compared to beam depth of 6.0" (B = 3.0" and S = 24.0"), the size of process zone at peak load is expected to be higher (% of depth of the section) in the smaller beam. This implies that the length over which non-linear stress distribution is occurring in smaller beam is larger (% wise) in small depth beams as compared to that in larger depth beams. Also, it must be mentioned that this will also depend on the shape of the stress-separation curves used in the analysis. The above reason help explain why the error or difference in the computed peak loads of smaller beams is higher as compared to that of larger beams. This indicates that to achieve a reasonable degree of accuracy in peak loads in small depth beams, it is necessary to use smaller size of elements as compared to that in larger beams or specimens. However there is a minimum size (largest size) of element that should be used beyond which there can be considerable difficulties in convergence and achieving stable post-peak responses. Computational results are presented in Table 4.2 and in Figures 4.7 through 4.9. In this study it was found that for a range of depth of beams studied an element size of 0.125" with aspect ratio of 1:1 to 1:2 is sufficient.

In this study, the number of elements used and the size of elements for the various size of specimens studied are listed in Table 4.3.

In the next chapter, the application of the proposed finite element model is presented. Finite element solutions are used there to develop the background for

proposing the use of load - crack mouth opening displacement response of three point bend specimens in computing fracture energy of concrete.

Table 4.1 Effect of Mesh Refinement on Load Point Deflection (δ) and Crack Mouth Opening Displacements (CMOD).

Number of Elements	Span Depth Ratio =4.0					
Across Crack Path	Un-Notched Beam a/d=0.0		Notched Beam a/d=0.5			
	$K_1 = P_e/\delta$	% Diff.	$K_1 = P_e/\delta$	% Diff.	$K_2 = P_e/CMOD$	% Diff.
12	8.296×10^5	3.80%	3.068×10^5	11.93%	5.353×10^5	15.62%
24	8.100×10^5	1.35%	2.905×10^5	5.98%	5.011×10^5	8.23%
48	7.996×10^5	0.05%	2.745×10^5	0.15%	4.640×10^5	0.22%
96	7.992×10^5	0.00%	2.741×10^5	0.00%	4.63×10^5	0.00%
Number of Elements	Span Depth Ratio =6.0					
Across Crack Path	Un-Notched Beam a/d=0.0		Notched Beam a/d=0.5			
	$K_1 = P_e/\delta$	% Diff.	$K_1 = P_e/\delta$	% Diff.	$K_2 = P_e/CMOD$	% Diff.
12	2.740×10^5	3.10%	1.222×10^5	9.83%	3.613×10^5	13.89%
24	2.680×10^5	0.85%	1.155×10^5	3.81%	3.347×10^5	5.53%
48	2.661×10^5	0.13%	1.125×10^5	1.11%	3.228×10^5	1.77%
96	2.657×10^5	0.00%	1.113×10^5	0.00%	3.172×10^5	0.00%
Number of Elements	Span Depth Ratio =8.0					
Across Crack Path	Un-Notched Beam a/d=0.0		Notched Beam a/d=0.5			
	$K_1 = P_e/\delta$	% Diff.	$K_1 = P_e/\delta$	% Diff.	$K_2 = P_e/CMOD$	% Diff.
12	1.215×10^5	4.11%	0.623×10^5	11.12%	2.773×10^5	16.76%
24	1.177×10^5	0.86%	0.584×10^5	4.19%	2.534×10^5	6.69%
48	1.170×10^5	0.26%	0.568×10^5	1.30%	2.428×10^5	2.22%
96	1.167×10^5	0.00%	0.560×10^5	0.00%	2.375×10^5	0.00%

Table 4.2 Influence of Mesh Refinement on the Convergence and Accuracy of the Computed Peak Load Values.

Beam Depth (in.)	Notch Depth (in.)	Number of Elements	Size of Elements Δx (in.)	Computed Peak Load (lb.)	Predicted Peak Load (lb.)	Error (%) $(P - P_e)/P_e$
3.0	0.0	6	0.5000	1253	1253	3.18%
		12	0.2500	1230	1230	1.24%
		24	0.1250	1220	1221	0.53%
		48	0.0625	1218	1217	0.24%
			0.0000		1214[a]	0.00%
	1.5	6	0.5000	388	388	14.72%
		12	0.2500	351	351	3.90%
		24	0.1250	341	342	1.03%
		48	0.0625	340	339	0.50%
			0.0000		338[a]	0.00%
6.0	0.0	12	0.5000	2131	2131	0.81%
		24	0.2500	2120	2120	0.29%
		48	0.1250	2116	2116	0.11%
		96	0.0625	2115	2115	0.05%
			0.0000		2113[a]	0.00%
	3.0	12	0.5000	610	610	4.42%
		24	0.2500	590	590	1.00%
		48	0.1250	585	585	0.20%
		96	0.0625	584	584	0.02%
			0.0000		584[a]	0.00%

[a] Extrapolated peak load for element size of $\Delta x = 0.0$.

Material data used in the analysis: High Strength Concrete - $E = 5.2 \times 10^6$ psi, $f'_t = 650$ psi and $f'_c = 12000$ psi, tensile softening curve C as defined in Chapter 3.

Table 4.3 List of Number of Elements Used in the Finite Element Analysis

Beam Depth	Total No. of elements*	No. of element across the crack path and size
1.5"	768	24 (0.0625")
3.0"	2928	48 (0.0625")
6.0"	3960	96 (0.0625")
9.0"	3960	96 (0.09375")
12.0"	3960	96 (0.1250")
18"	3960	96 (0.1875")

* Plane stress 4-node and 3-node elements, Number of spring elements depend on the notch depth.

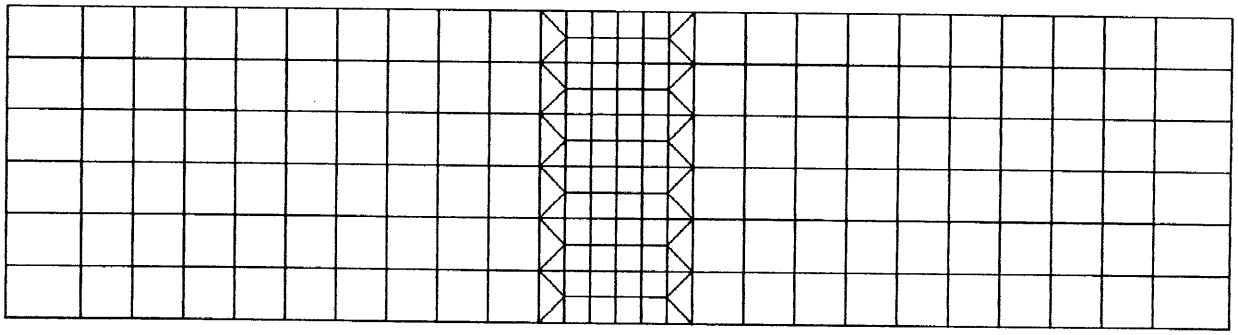

Figure 4.6(a) Finite Element Mesh - Coarse Mesh (12 Elements Along the Crack Path)

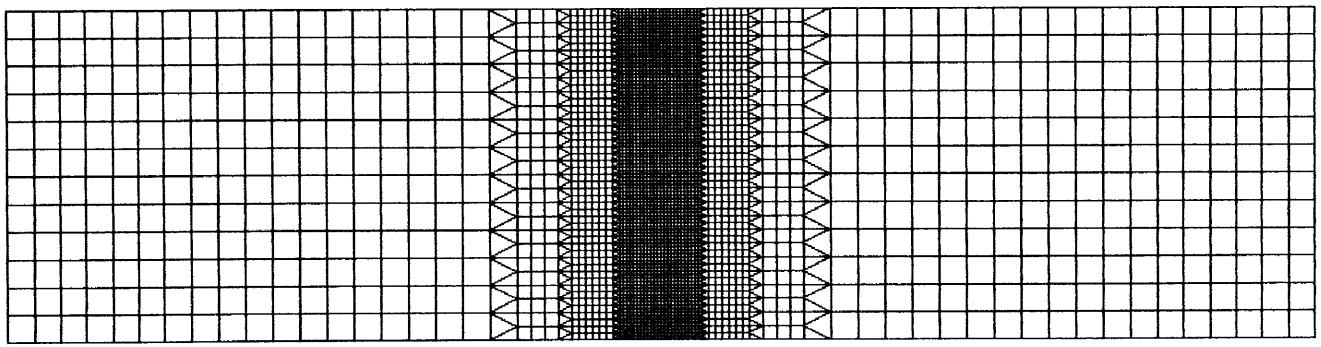

Figure 4.6(b) Finite Element Mesh - Fine Mesh (96 Elements Along the Crack Path)

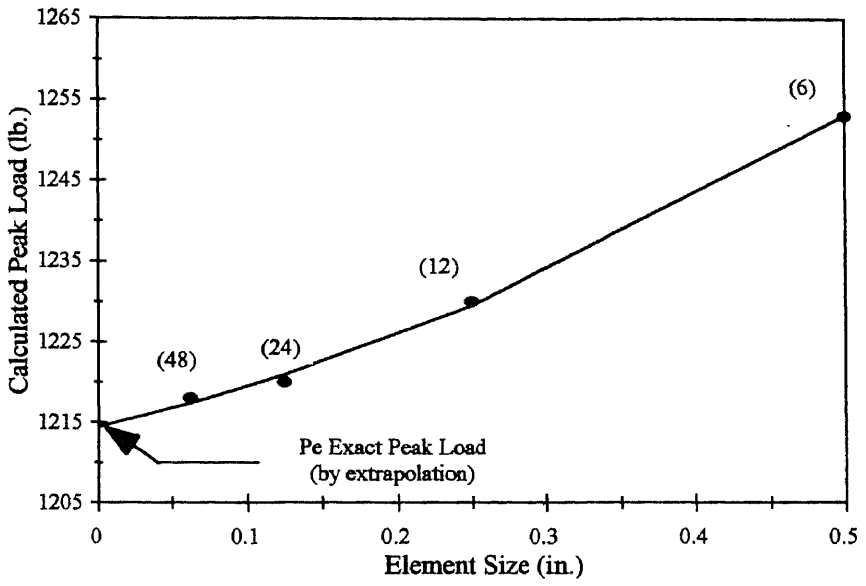

(a)

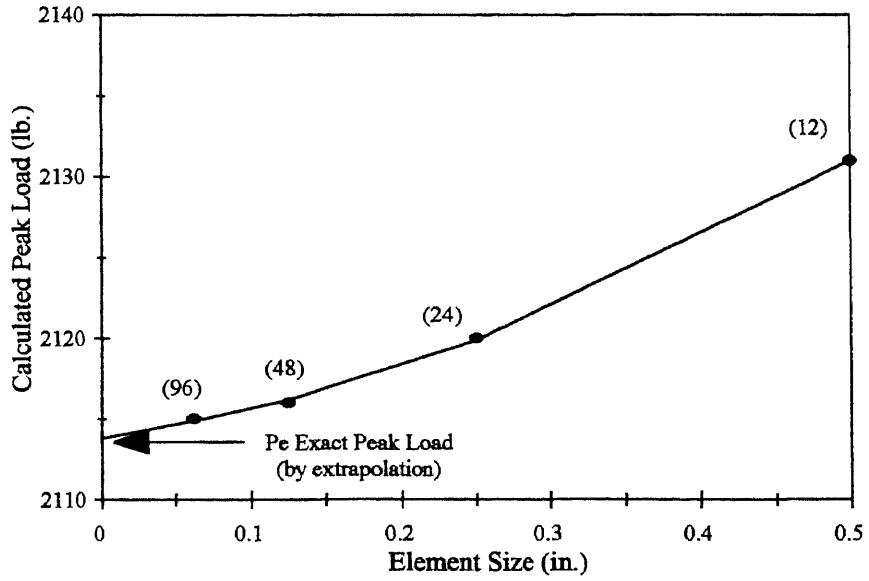

(b)

Figure 4.7 Influence of Mesh Refinement on Peak Load Calculations (a) D = 3.0" and (b) D = 6.0" Un-notched Beam a/D = 0.0

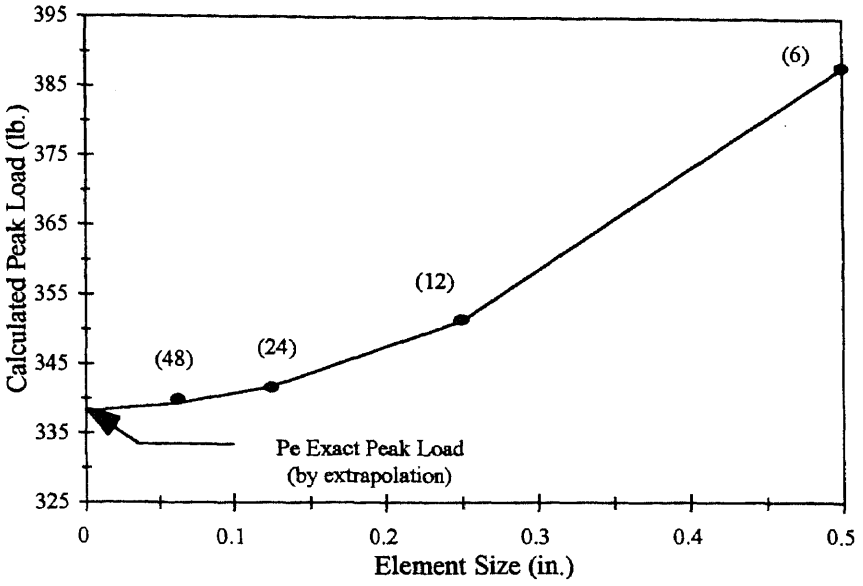

(a)

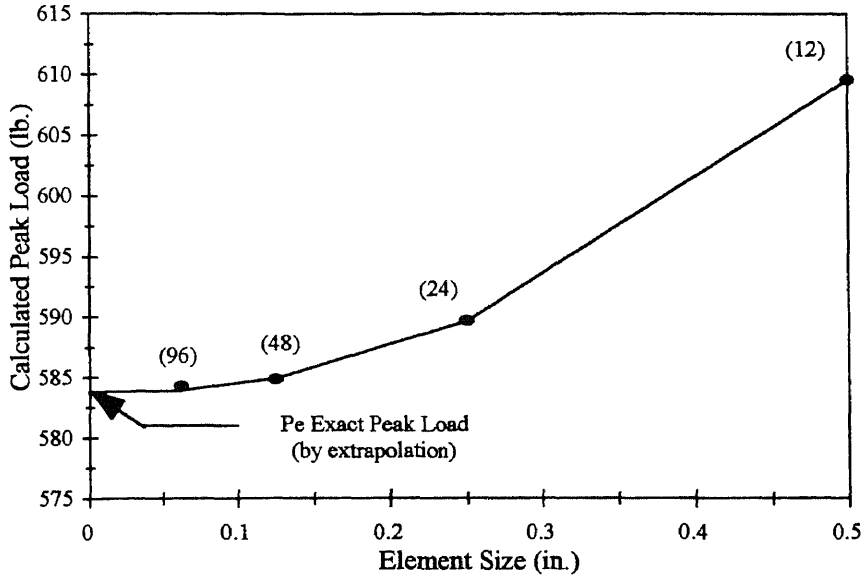

(b)

Figure 4.8 Influence of Mesh Refinement on Peak Load Calculations (a) D = 3.0" and (b) D = 6.0" Notched Beam a/D = 0.5

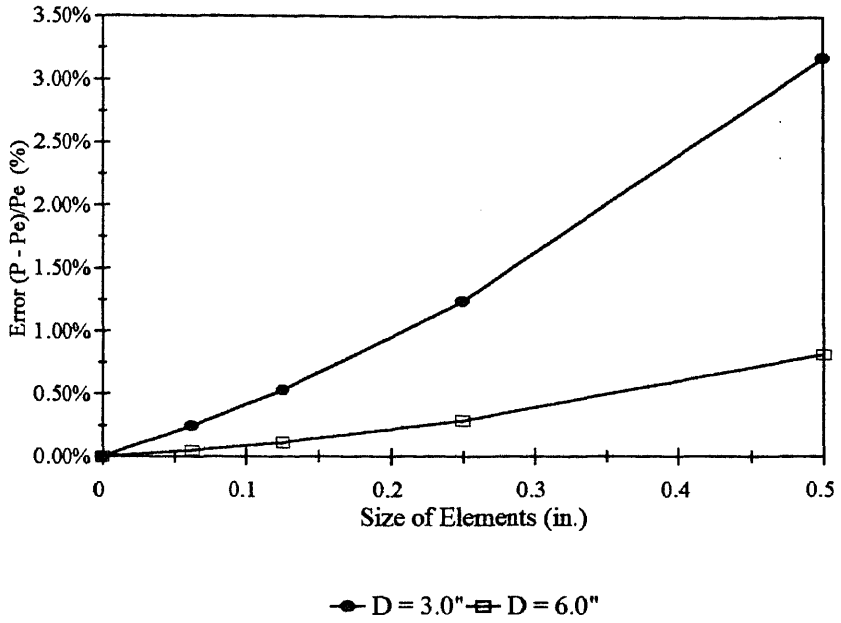

(a)

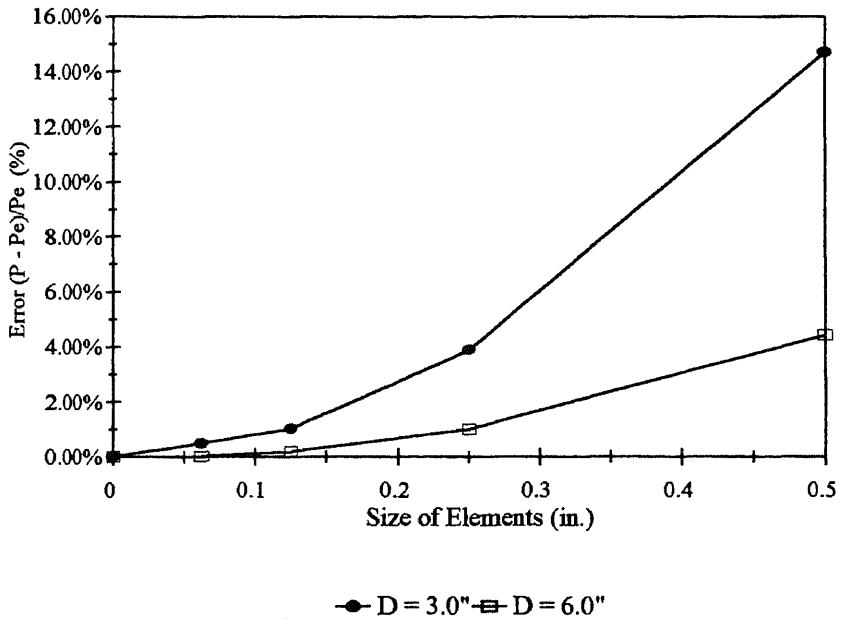

(b)

Figure 4.9 Error in Peak Load Calculations vs. Element Size
(a) Un-notched Beam a/D = 0.0 and (b) Notched Beam a/D = 0.5

CHAPTER 5

FRACTURE PARAMETERS AND FRACTURE ENERGY OF NORMAL AND HIGH STRENGTH CONCRETE

5.1 Introduction

In this chapter, the results of the proposed finite element model for predicting the flexural strengths, calculation of size of process zone in beams of different depths and calculation of nominal strengths are presented. A discussion on the effect of deflection measurements on fracture energy computations and development of the methodology that uses crack mouth opening displacements instead of load point deflections in calculating the fracture energy are also described. In this study, Finite Element Analysis was used to study the fracture properties of normal and high strength concrete and, for determination of various fracture parameters. The following parameters have been studied.

- Calculation of peak loads (flexural strength) and size of process zone of high strength and normal strength concrete beams of rectangular cross sections subjected to three point bending.
- Effect of size and effect of increased compressive strength on the fracture behavior of notched concrete beams.
- Effect of approximate stress separation relation on the predicted load deflection and load CMOD responses.
- Establishing a relationship between crack mouth opening displacements (CMOD) and load point displacements (LPD) for the purpose of calculating fracture energy, G_F, of concrete.

- Establishing relationship between fracture energies obtained from three point bending tests and uniaxial tension tests.

Concrete structural members subjected to bending are usually reinforced. In spite of this, analysis of unreinforced concrete beams has been the subject of many experimental and theoretical investigations. One reason for this is that the flexural, or bending test conveniently provides information about a very important property of concrete, namely the tensile strength of concrete and hence the modulus of rupture. Another reason that bending specimens are often used for experimental research is the determination of the flexural strength for different materials. Flexural strength of unreinforced concrete is of direct practical importance to some mass produced concrete structures, such as in dams, pavements, airfield runways. In reinforced concrete structures, flexural strength of concrete is used in calculating the cracking, yielding and ultimate loads and, for strength design.

The flexural test is one of the three standard tension tests. The first two are the direct uniaxial tension test and the indirect tension test (or spitting tension test). It is well known that the flexural strength of concrete in general does not equal the tensile strength of concrete. Experimental evidence also supports the fact that flexural strength is not constant but depends on the depth of the beam or, more general, it depends on the geometry of the specimen. It is also accepted that the fracture energy determined from the RILEM recommended notched beam tests is not the true fracture energy (assumed to be the fracture energy determined from the tensile test). Tension tests are more difficult to carry out so beam tests are usually used for the determination of fracture energy instead.

In this study, a correlation between the fracture energies determined from the above mentioned first two tests was developed. Another aspect of the present study was the development of a method to correct the errors involved in beam tests, particularly errors in load-line deflection measurements, which cause appreciable errors in the experimentally measured fracture energy. In section 5.3, the effect of improper or erroneous deflection measurement on fracture energy is investigated.

5.2 Fracture Analysis of Unreinforced Structural Members (Beams) - Size Effect

The first published study of flexural strength analysis of unreinforced concrete beams using the fictitious crack model was presented by Hillerborg, Modeer and Petersson, 1976). Computational results regarding the effect of beam depth on flexural strength were presented and the results indicated that the flexural strength decreases with increased beam depth. During these analysis, the shape of the stress separation curves was assumed. Indirectly obtained tensile strengths from splitting cylinder tests were combined with the fracture energy obtained from the RILEM beam tests, to define the stress separation curves.

In this study, a three point bend beam, as shown in Figure 5.1, with the length to depth ratios varying between 4 to 8 were studied. Plane stress, with Poisson's' ratio ν = 0.2, was assumed. The exact non-linear stress separation curves determined from the experimental investigation (Chapter 3) were used in defining the non-linear properties of the spring elements. The rest of the beam was modeled by using regular 4 node linear elastic plane stress elements as explained in Chapter 4.

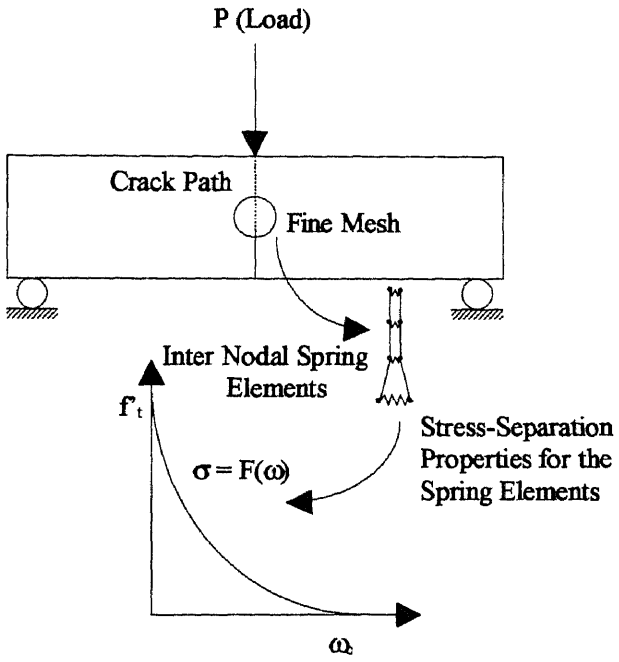

Figure 5.1 Three Point Bend Specimen Finite Element Model

The flexural strengths were calculated using equation 5.1 given below for beams with varying depths ranging from 1.5" to 18". The flexural strength was calculated by dividing the maximum moment (M_u) by the section modulus.

$$f_f = \frac{6M_u}{BD^2}, M_u = \frac{P_u L}{4} \tag{5.1}$$

where, P_u = peak load, B, D and L are (width, depth and length) dimensions of the beam

The finite element computational results are shown in Table 5.1. The numerical results are plotted in Figure 5.2. For both the high strength concrete and normal strength concrete, a relationship between the flexural strength as a function of the depth of the beam is shown in the Figure 5.2. As can be seen from Figure 5.2, the flexural strength of normal strength concrete is about 1.6 times the tensile strength for smaller depth beams (D = 3.0") and the flexural strength gradually approaches the tensile strength as the depth of the beam increases. This was found to occur for a beam depth of 18.0" for

normal strength concrete. For high strength concrete, the flexural strength is about 1.4 times the tensile strength for smaller depth beams (D = 3.0"). The flexural strength approaches very rapidly and equals the tensile strength for a beam depth of 9.0". This observation indicates that high strength concrete behaves much more like a linear elastic material.

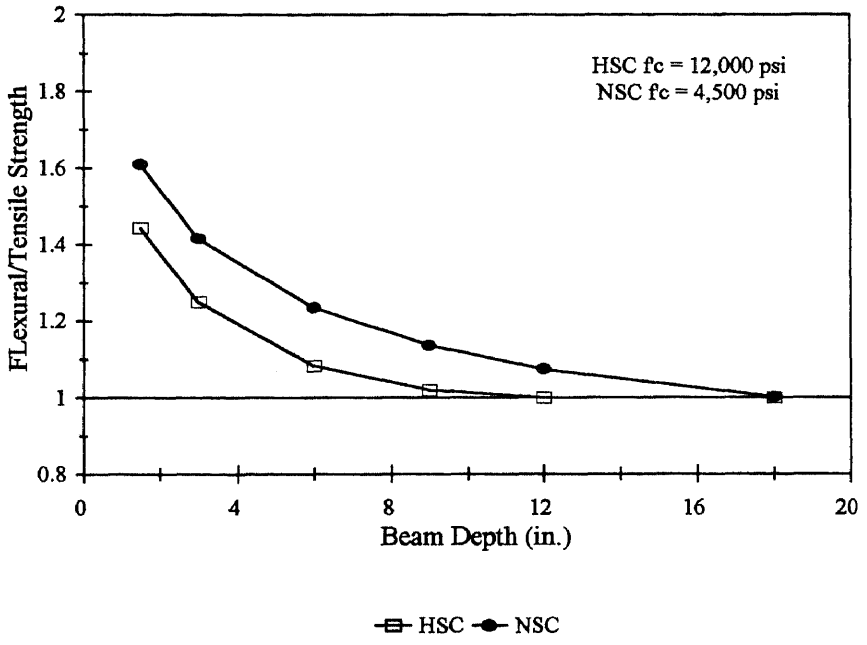

Figure 5.2 Theoretical variations of Flexural Strength Versus Depth Of The Beam. (Beam Dimensions -Width : B=3.0", Span : S = 4×Depth, Depth as indicated above)

The reason for this can be explained on the basis of the stress softening characteristics of concrete. In concrete, even when a crack propagates (stress level exceeds its tensile strength), the crack continues to transfer stresses due to an effect of aggregate interlock. This zone, in which the stress transfer is taking place, is known as the process zone. In Figure 5.3 the size of process zone at peak load is shown for different depth of beams. The size of the process zone decreases as the beam depth

increases. As the size of process zone decreases, the region of non-linear stress distribution decreases and it approaches a stress distribution of linear elastic brittle material (small or no process zone). This is predicted to occur for normal strength beams of greater than 18" depth. For high strength concrete beams, due to their brittleness, the size of the process zone is significantly smaller than that as compared to the same depth beam of normal concrete. Hence, the ratio of flexural strength and tensile strength is lower for high strength concrete. The initial slope of the post peak stress-separation curve for high strength concrete is very steep compared to normal strength concrete. This steepness drops after the tensile stress is reached greatly influences the development of the size of the process zone and the of peak load and thence the flexural strength. The stress distribution along the crack path of normal and high strength concrete for un-notched beams is shown in Figure 5.5a and 5.5b.

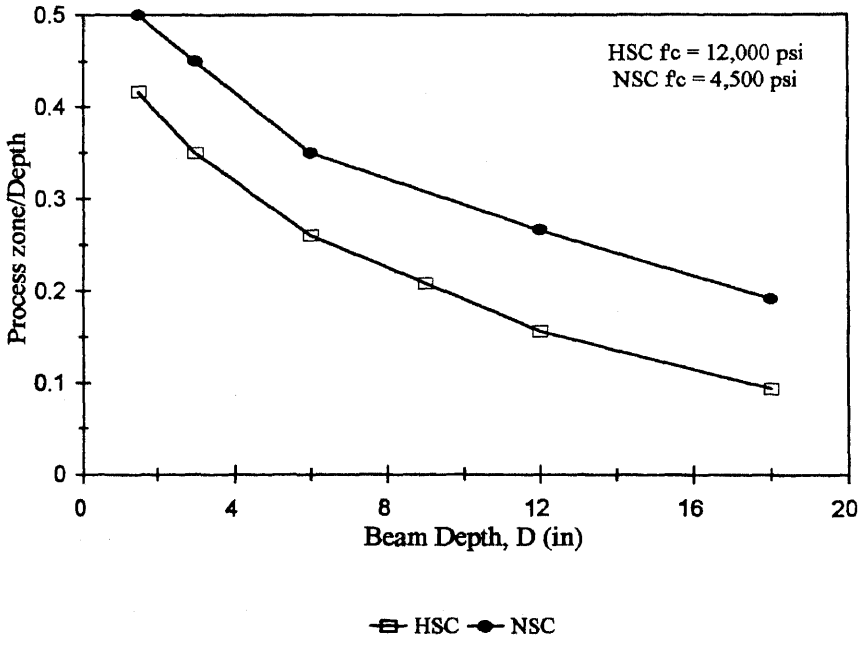

Figure 5.3 Size Of Process Zone (A_c) At Peak Load As A Function Of The Depth Of The Beam For High Strength And Normal Strength Concrete

Table 5.1a Flexural Strength Results For Normal And High Strength Concrete Beams (Finite Element Analysis)

Span/Depth = 4.0		
Beam Depth D (in)	Normal Strength Concrete f_f/f'_t	High Strength Concrete f_f/f'_t
1.5	1.612	1.443
3.0	1.416 (1.833*, 1.643**)	1.250 (1.660*, 1.450**)
6.0	1.236	1.083
9.0	1.136 (1.445*, 1.308**)	1.0034 (1.322*, 1.159**)
12.0	1.074	1.002
18.0	1.020	1.000

Calculations performed using ()* linear and ()** bi-linear stress-separation curves (Beam Dimensions -Width : B=3.0", Span : S = 4×Depth, Depth as indicated above)

Overestimation of flexural strength between 15-30% can occur in analysis performed considering linear or bi-linear stress softening curves. This variation is due to the fact that the initial slope (segment) of stress softening curve plays an important role in the stress distribution at the peak load and therefore affects the peak load calculations. Most of the bi-linear and linear stress softening curves used by researchers (Hillerborg 1981, Gustaffson 1985) are defined in terms of the fracture energy of concrete. Figure 5.4 presents a comparison between an exact stress softening relationship (present finite element analysis) and approximate relations. Note that in this figure the fracture energy G_F has been maintained constant (the area under stress-separation curve). Use of inflated values of G_F in defining the stress separation curve will result in further errors in the results of the finite element models. To illustrate the over prediction, the flexural strengths (see Table 5.1) were calculated for two beam depths of 3 and 9 inches, the stress softenings were assumed to be linear (constant G_F) and bi-linear. The effect of approximate stress-separation curves on the predicted load-deflection and load-CMOD

is shown in Figures 5.6a and 5.6b. As can be seen from these figures, the shape of the stress-separation curves has a profound influence on the predictions of the peak load as well on the post peak behavior.

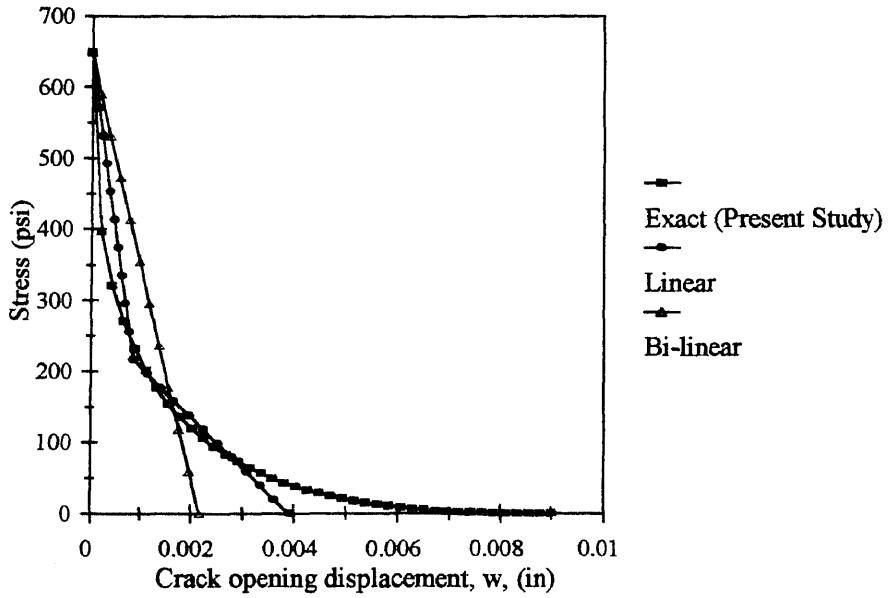

Figure 5.4 Different Shapes Of Stress Separation Curves Commonly Employed (Note: The Area Under the Curves are same)

To study the effect of notch depth on peak load capacity of beams with varying depths was undertaken. Nominal strength as defined in equation 5.2 was used to plot a stress contour for normal and high strength concrete beams. The notch to depth ratio was varied between 0.0 to 0.5. The results are presented in Table 5.1b and are plotted in Figures 5.7a and 5.7b.

$$\sigma_N = c_N \frac{P_u}{BD}, c_N = \frac{3L}{2D} \tag{5.2}$$

where, P_u = peak load, B, D and L are (width, depth and length) dimensions of the beam.

Interesting observation from this study concerns the computed lengths of the process zone. Hillerborg introduced a length parameter known as the characteristic length, l_{ch}, as a measure of the process zone size or of the ductility of the material. This parameter l_{ch} , as defined in equation 5.3 , is calculated for the present employed material properties.

$$l_{ch} = \frac{EG_F}{f'^{2}_{t}} \tag{5.3}$$

For normal strength concrete, the material properties used were: f'_t = 400 psi, G_F =0.55 lb/in. and E = 3.8 × 10^6 psi, shape of stress-separation curve is curve A (see Chapter 3). Substituting in equation 5.3, yields the characteristic length l_{ch} = 13.0625 in. Whereas for high strength concrete, using the material properties of f'_t = 650 psi , G_F = 0.73 lb/in. and E = 5.25 × 10^6,. shape of stress-separation curve is curve C (see Chapter 3), yields l_{ch} = 9.07 in.. Both results are significantly higher than the process zone size calculated in this study. In this study it was found that the size of the process zone reaches its maximum extent at the peak load and varies for different depths of the beam. This clearly means that the process zone is not a material constant. The parameter l_{ch}, can only be used for characterizing the ductility of the material.

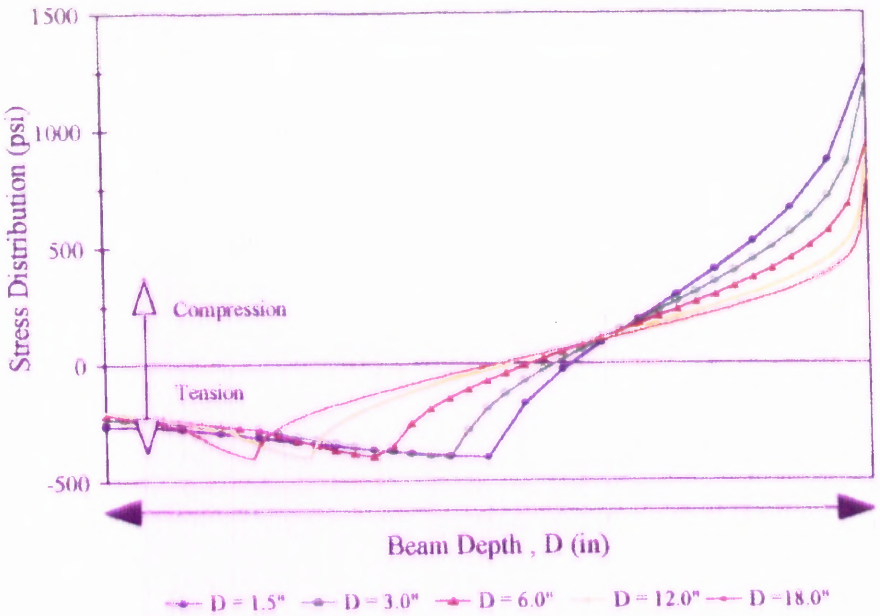

Figure 5.5a Stress Distribution At Peak Load For Normal Strength Concrete (f'_c = 4,500 psi - Unnotched Beams)

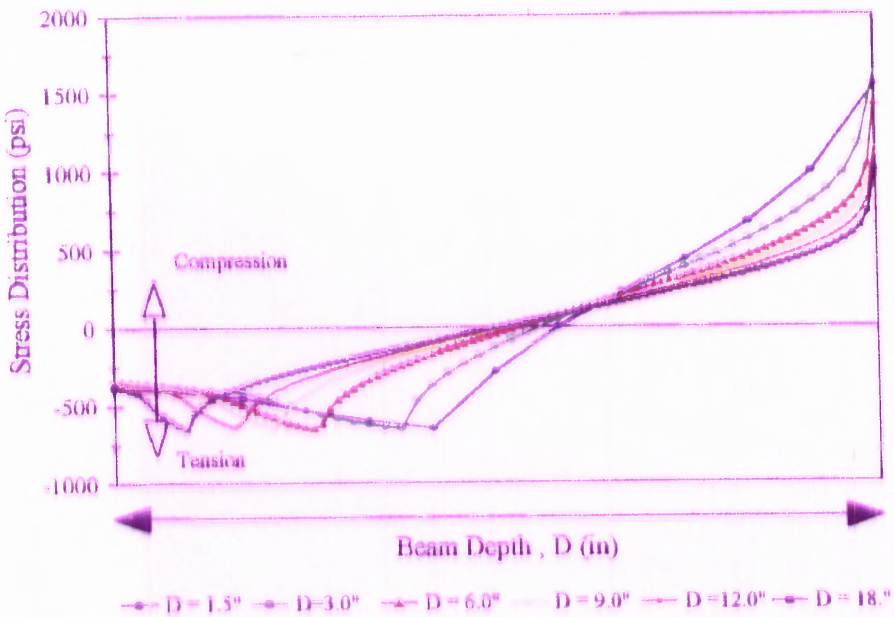

Figure 5.5b Stress Distribution At Peak Load For High Strength Concrete (f'_c =12,000 psi - Unnotched Beams)

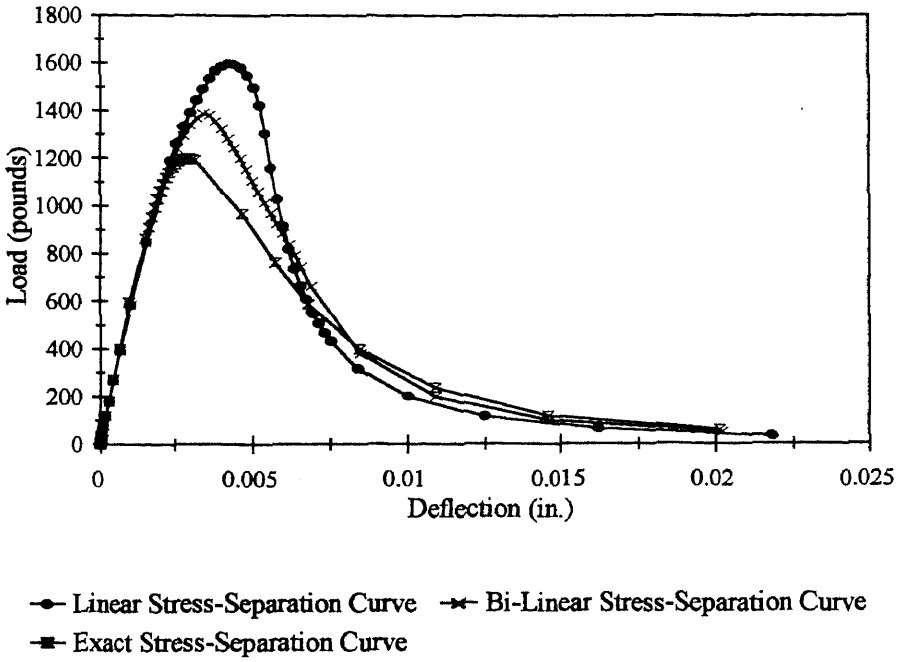

Figure 5.6a Comparison of Predicted Load-Deflection Behavior Depending Upon the Employed Stress-Separation Curves. (Beam Dimensions - Width: B=3.0",Depth D =6.0", Notch Depth Ratio a/D=0.25 and Span = 4×D)

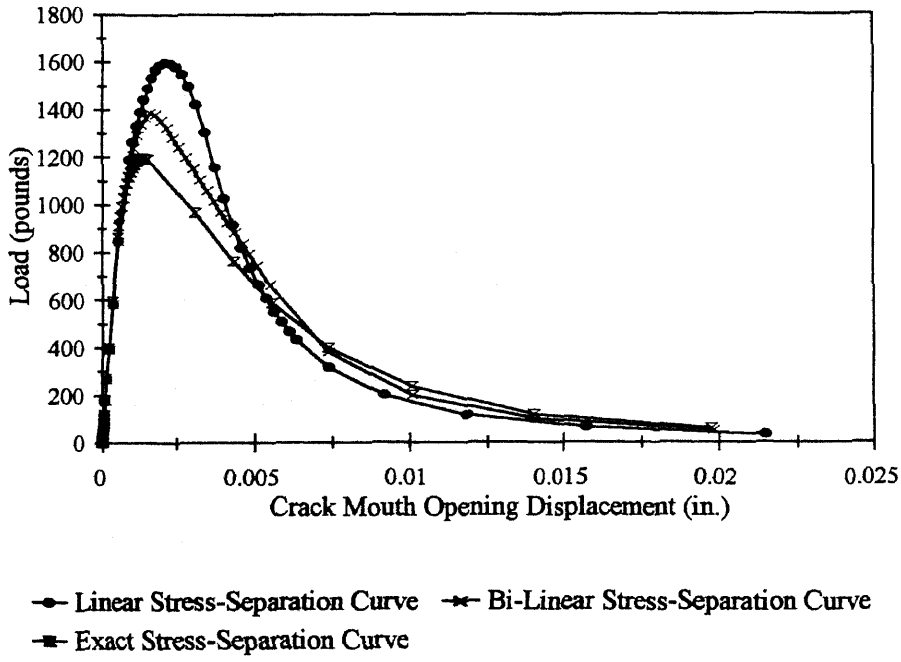

Figure 5.6b Comparison of Predicted Load-CMOD Behavior Depending Upon the Employed Stress-Separation Curves. (Beam Dimensions - Width: B=3.0",Depth D =6.0", Notch Depth Ratio a/D=0.25 and Span = 4×D)

Table 5.1b Nominal Strength Results For Normal And High Strength Concrete Beams (Finite Element Analysis)

(a) Normal Strength Concrete (f'_c = 4,500 psi)

Depth D (in.)	σ_n/f'_t				
	a/D=0.0	a/D=0.25	a/D=0.25	a/D=0.416	a/D=0.5
1.5"	1.61	1.148	0.940	0.608	0.451
3"	1.416	0.998	0.822	0.525	0.396
6"	1.236	0.860	0.710	0.454	0.344
12"	1.075	0.728	0.602	0.386	0.295
18"	1.02	0.654	0.541	0.348	0.266

(b) High Strength Concrete (f'_c = 12,000 psi)

Depth D (in.)	σ_n/f'_t				
	a/D=0.0	a/D=0.25	a/D=0.25	a/D=0.416	a/D=0.5
1.5"	1.44	1.019	0.8394	0.5378	0.4133
3"	1.249	0.86	0.71	0.461	0.35
6"	1.085	0.7446	0.6148	0.394	0.3
9"	1.02	0.6745	0.556	0.357	0.273
12"	1	0.625	0.516	0.3318	0.253
18"	1	0.559	0.392	0.2977	0.227

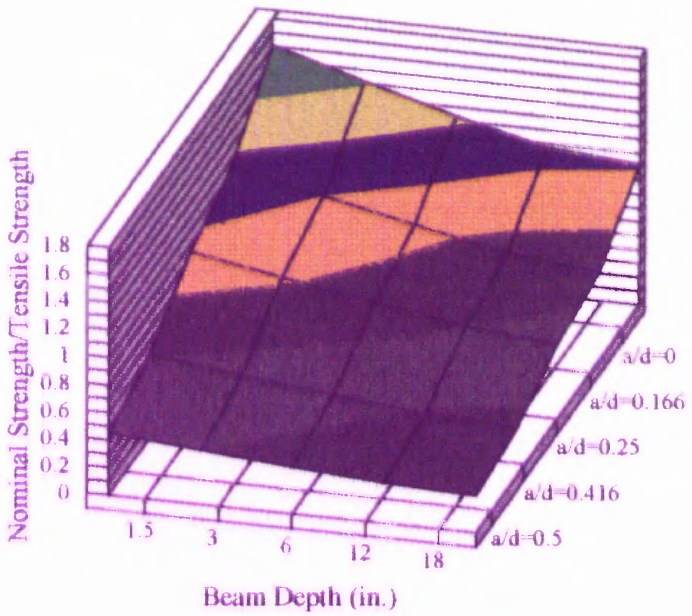

Figure 5.7a Theoretical Variations of Nominal Strength of Normal Strength Concrete Beams Versus Depth of the Beam.
(Beam Dimensions -Width: B=3.0", Span: S = 4×Depth, Depth as indicated above)

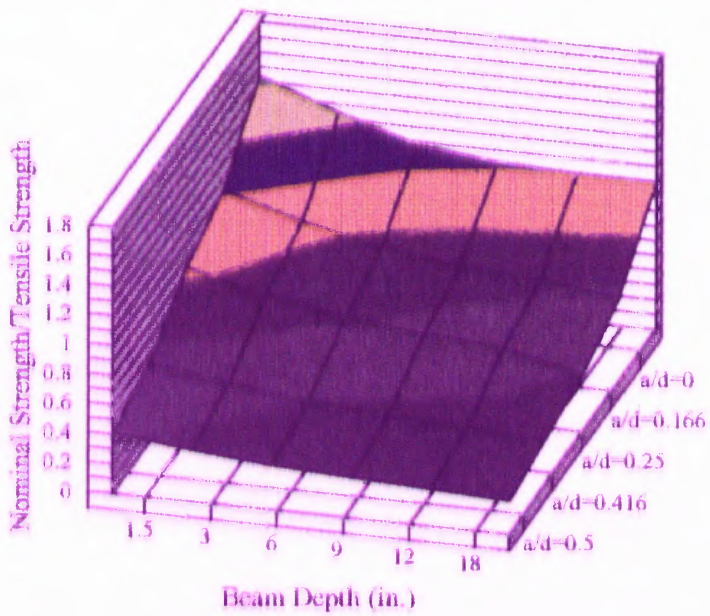

Figure 5.7b Theoretical Variations of Nominal Strength of High Strength Concrete Beams Versus Depth of the Beam.
(Beam Dimensions -Width : B=3.0", Span : S = 4×Depth, Depth as indicated above)

Based on the finite element solutions of this study, the following conclusions can be made regarding the behavior of normal and high strength concrete beams.

1. Flexural strength of beam does not equal the tensile strength of concrete.
2. As the depth of the beam increases, the flexural strength decreases and it approaches the tensile strength.
3. The ratio of flexural to tensile strength depends on the compressive strength of concrete. The ratio is lower for high strength concrete than for normal strength concrete.
4. The shape of the stress-separation curve affects the predicted peak load values as well as the post peak behavior.

5.3 Effect Of Load Point Displacement Measurements On Fracture Energy (G_F) As Measured From Beam Tests (RILEM)

The Fracture Energy (G_F) determined from the notched beam test as recommended by RILEM can be significantly higher than its true value due to inaccurate load-point deflection measurements. Erroneous deflection measurement can occur due to crushing of the specimen over the supports, support settlement, machine deformation to mention a few (see Figure 5.8). Another possible factor that causes errors in G_F is negligence of tail portion of the load deflection data.

Based on the RILEM recommendations, G_F is determined by computing the area under the load deflection curve and by using the following formula:

$$G_F^R = \frac{\int_0^{\delta_o} P d\delta + mg\delta_o}{A_{lig}} \tag{5.4}$$

where, P = load, δ = load line deflection and δ_o the final deflection at termination of the test, mg = self weight of the beam and A_{lig} = cross section area of the ligament = B (D-a_o), B = width, D= depth and a_o is the initial notch depth. The main restrictions of the RILEM method are the use of a span to depth ratio of eight, and a notch depth ratio of 0.5. Lower notch depth ratios have been reported to yield higher G_F.

In this study, the various possible reasons for the problems associated with experimentally determined G_F values are analyzed. Among all causes, the main reason for a higher value of G_F is inaccurate measurement of the load-line deflections. A procedure for using crack mouth opening displacement instead of load point deflection is developed in the present study for calculating fracture energy from the load-CMOD data. The use of CMOD responses is preferable because the CMOD measurements are generally not affected by any settlements, crushing of the beam specimens or deformations of the test setup.

In this study, the methodology that calculates the fracture energy, G_F, from load - CMOD data is developed in the following two ways:

- Relating accurately measured load point displacement (LPD) to crack mouth open displacements (CMOD) of the beam.
- Establishing a relationship between the plastic components of the load point displacement (LPD) and crack mouth opening displacement (CMOD) of the beam

The above two mentioned relationships can also be experimentally determined.

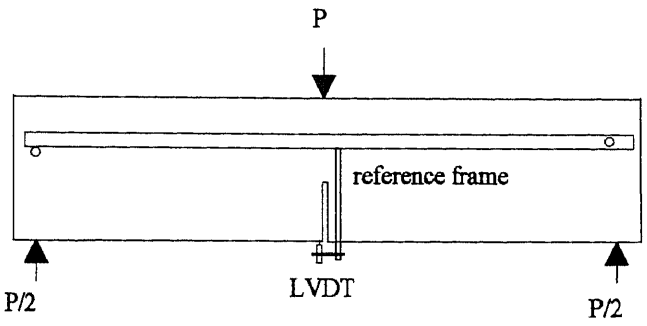

(a) Proper method of measuring deflections

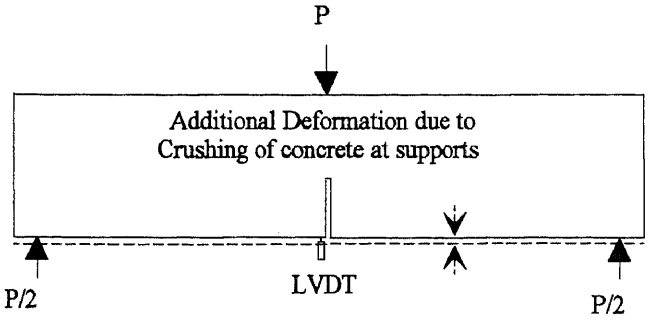

(b) Improper method of measuring deflections

Figure 5.8 Methods Of Measuring Load-Line Deflection

In the following sections, the theoretical basis for such relationships is presented. The theoretical analysis is obtained using the solutions of the present finite element model.

The effect of inaccurate deflection measurements on the computed fracture energy is demonstrated by means of an idealized load-deflection response. In Figure 5.9 the curve represented by the solid line represents an accurately measured load-line deflection versus load response, the dashed line represents the load-deflection response of the same specimen, which includes extraneous deformations. The pre-peak non-linearity has been ignored. Post peak responses are described in terms of the normalized

values of the peak load and displacement. The brittleness index, β, defines the shape of the post peak curve. Values between 0.2 to 0.8 were considered to investigate the effect of the "steepness" of the post peak curve on the fracture energy. Typically, β, is approximately equal to 0.2 for fiber reinforced concrete and 0.8 for high strength concrete. These values of β were found by evaluating a number of experiments, see Figure 5.10. The parameter 'n' represents the end point of the load deflection curve (displacement at which the load is negligible). Usually for normal concrete, n is 8 to 12 times the peak displacement. As shown in Figures 5.9 and 5.10, most of the extraneous deformations occur prior to the peak load. The parameter, γ, relates the extraneous peak deflection to the actual true deflection at peak load (experiments reported in the literature indicate the possibility of γ being as high as 3 to 4). Based on experimental evidence (Kim, 1991), the end point on the erroneous load-deflection response curve seems to lie somewhere in between the true end point (n) and the point which would correspond to a point where the erroneous load deflection curve is parallel to the true load deflection curve (n + γ -1). To account for this the end point of the erroneous load deflection curve is defined by using a parameter ξ as shown in the Figure 5.9. The post peak response of the true load-deflection curve can be written as

$$P = P_e e^{\beta(1-m)}, 1 < m < n \tag{5.5}$$

where P_e is the peak load, and m varies between 1 and n.

Based on this load-deflection curve the true fracture energy (area under the load-deflection curve, cross sectional area of the beam considered as a unit area for simplicity) can be written as:

$$E = \frac{1}{2} P_e \delta_e + \frac{P_e \delta_e}{\beta}(1 - e^{\beta(1-n)}) \tag{5.6}$$

The erroneous load deflection response similarly can be described as:

$$P = P_e e^{\beta(\gamma - m)} \;,\; \gamma < m < n + \xi(\gamma - 1) \tag{5.7}$$

where, ξ, can be assumed to vary between 0 and 1.0. The area under the erroneous curve can be determined by integrating the above equation between the limits of m to yield:

$$E_r = \frac{\gamma}{2} P_e \delta_e + \frac{P_e \delta_e}{\beta}(1 - e^{\beta(1-n+\gamma(1-\xi))}) \tag{5.8}$$

Therefore the error in the measured fracture energy because of erroneous deflection measurement can be obtained by:

$$Error(\%) = \frac{E_r - E}{E} \cdot 100 \tag{5.9}$$

$$Error(\%) = \frac{\gamma\beta - 2e^{\beta(\gamma - n + \zeta(1-\gamma))} - \beta + 2e^{\beta(1-n)}}{\beta - 2e^{\beta(1-n)} + 2} \tag{5.10}$$

Using the above formula, the error in fracture energy due to erroneous deflection measurements was found to be in the order of 1.5 - 4 times the accurate (true)

deflections. The results are shown in Figure 5.11 and tabulated in Table 5.2, which clearly demonstrates the importance of measuring the load-line displacements accurately.

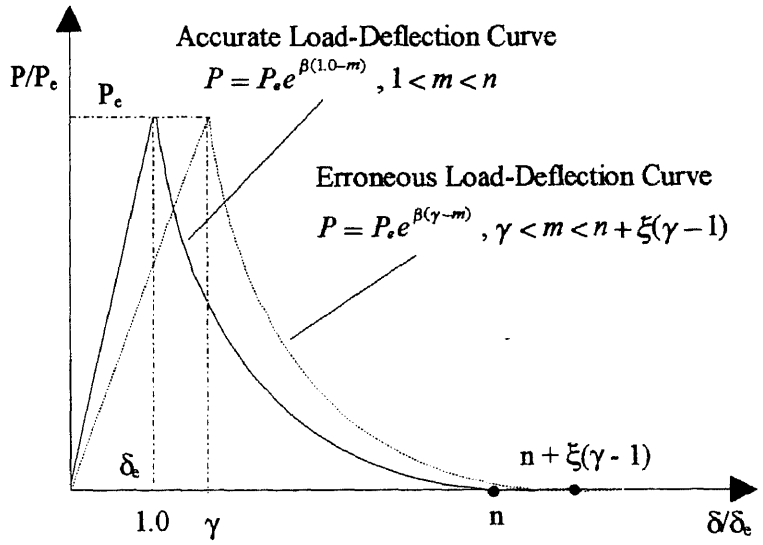

Figure 5.9 Idealized Load-Deflection Curves

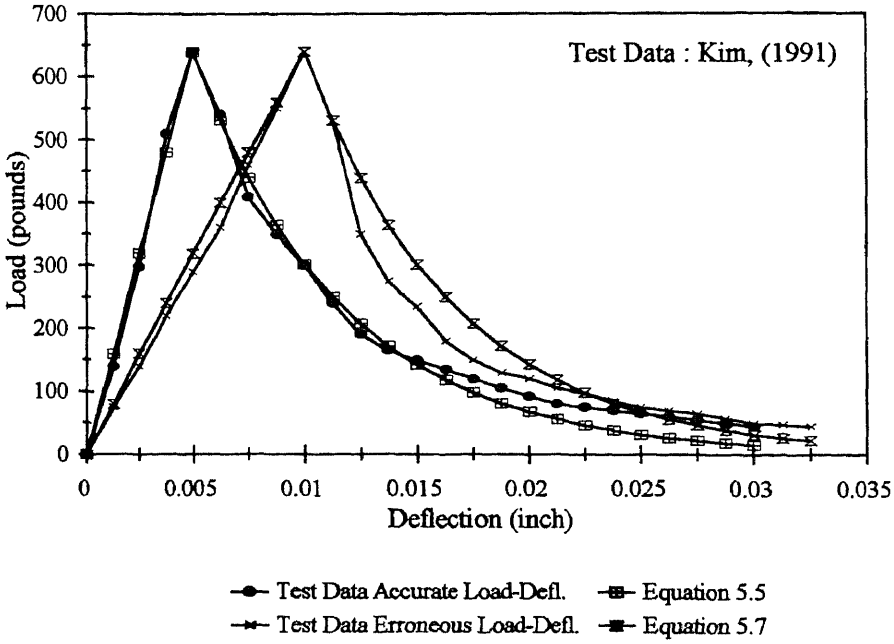

Figure 5.10 Comparison Of The Idealized Load-Deflection Curves With Actual Test Data($\beta = 0.75$, $\gamma=2.0$, $\xi=0.5$ And $n = 6$)

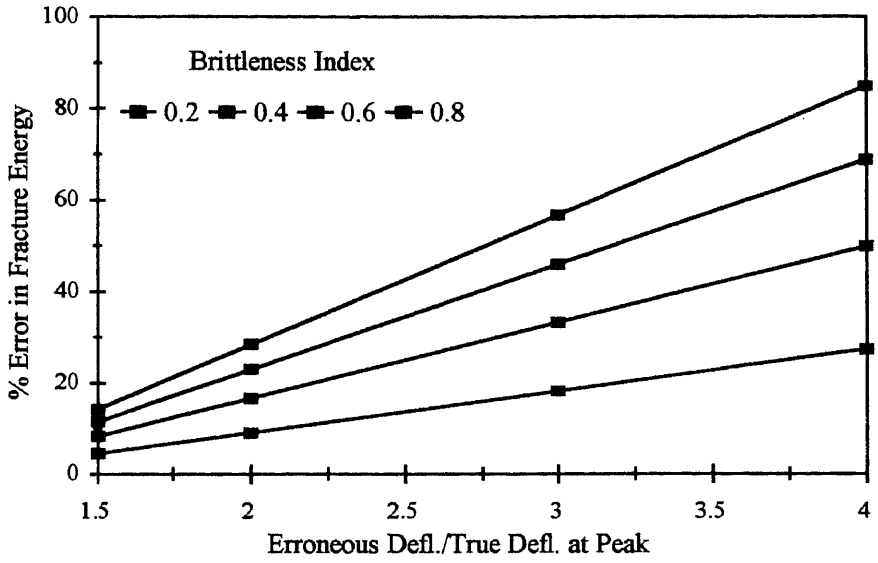

Figure 5.11 Effect Of Erroneous Displacement Values On Fracture Energy

Table 5.2 Error In Fracture Energy As A Function Of Erroneous Displacement Measurements

End point	Brittleness Index	Value of γ (erroneous displ./true displ.)			
n	β	1.5	2.0	3.0	4.0
		Error in Fracture Energy (%)			
25	0.2	4.54	9.08	18.22	27.22
13	0.4	8.32	16.63	33.22	49.78
9	0.6	11.51	23.00	45.92	68.74
7	0.8	14.28	28.45	56.76	84.85

5.4 Determination of Fracture Energy Based on Load and CMOD Relationships

5.4.1 Relationship Between Load Point Deflection (LPD) and Crack Mouth Opening Displacement (CMOD)

The first study to report a relationship between the two quantities LPD and CMOD was by Kim (Kim, 1991). In Kim's study only specimens of span to depth ratio of 4 were analyzed. In this study, the concept is extended to different span to depth ratios. Span depth ratios varying between 4 to 8 were studied. Figure 5.12a illustrates a typical load deflection response of the beam. As seen in Figure 5.12b, a typical relationship between accurately measured LPD and CMOD is bi-linear in shape. The initial slope S_1 is valid in the linear portion of the load-deflection response (Figure 5.12b). The slope S_1 then gradually changes to S_2 during the formation of the process zone in the viscinity of the crack tip. Around the peak load the process zone reaches a certain size after which the specimen exhibits a linear relationship between LPD and CMOD with a constant slope S_2. The values of S_1 and S_2 can be experimentally evaluated. In Kim's study the value of S_2 was reported to be 0.875.

Using ABAQUS computer analysis, the values of S_1 and S_2 were computed by combining the predicted finite element solutions of deflection, load and crack mouth opening displacements. It was found in this study that the values of S_1 are dependent on the initial notch depth and, the values of S_2 depend on the span to depth ratio. The results of the numerical analysis are presented in the Table 5.3. The relationship of S_1, S_2 and notch depth for different span-depth ratios is shown in Figures 5.13 and 5.14.

To calculate the fracture energy from the P-CMOD curves, the following equation is used:

$$G_F \cdot B(D-a_o) = \int_0^{\delta_u} Pd\delta = \beta \int_0^{CMOD_1} PdCMOD + \gamma \int_{CMOD_1}^{CMOD} PdCMOD \qquad (5.11)$$

where $\beta = S_1$ in the linear elastic range and $\gamma = S_2$ in the post peak region. The region between the elastic region and post peak is approximated by extending the slope S_1 and S_2 till they intersect. Such approximations cause negligible errors since this transition region is very small.

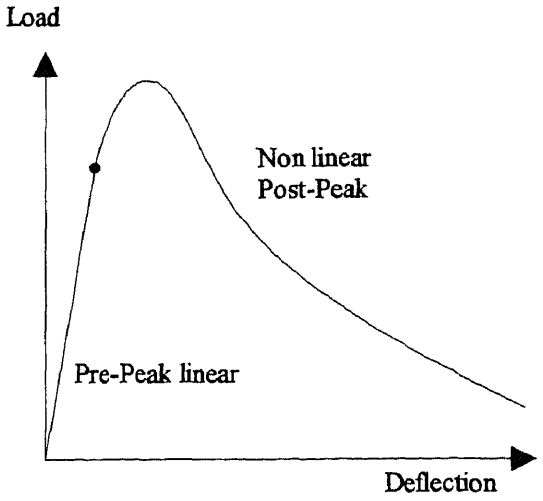

Figure 5.12a Typical Load Deflection Response

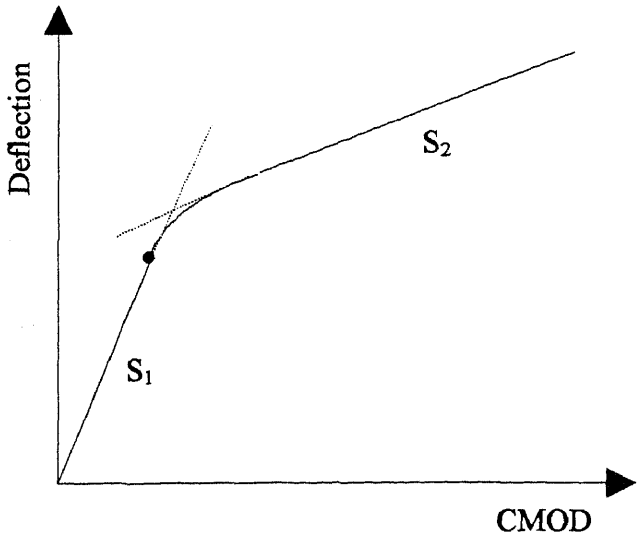

Figure 5.12b Relationship between Crack Mouth Opening Displacement and Load Line Deflection (Kim, 1991)

Table 5.3 Values Of S_1 And S_2 Obtained From Finite Element Analysis

Span/Depth Ratio	Notch/Depth Ratio a/D = 0	
S/D	S_1	S_2
4.0	∞	0.911
6.0	∞	1.342
8.0	∞	1.634
Span/Depth Ratio	Notch/Depth Ratio a/D = 0.25	
S/D	S_1	S_2
4.0	3.061	0.910
6.0	5.746	1.354
8.0	9.420	1.710
Span/Depth Ratio	Notch/Depth Ratio a/D = 0.5	
S/D	S_1	S_2
4.0	1.716	0.957
6.0	2.869	1.418
8.0	4.278	1.849

Beam Dimensions- Width: B = 3.0", Depth as given above, Span-Depth ratio and Notch depth ratio as given in the table. Material properties used were of HSC - f'_t =650 psi, E=5.2 $\times 10^6$ psi, f'_c = 12,000 psi and tensile softening curve C.

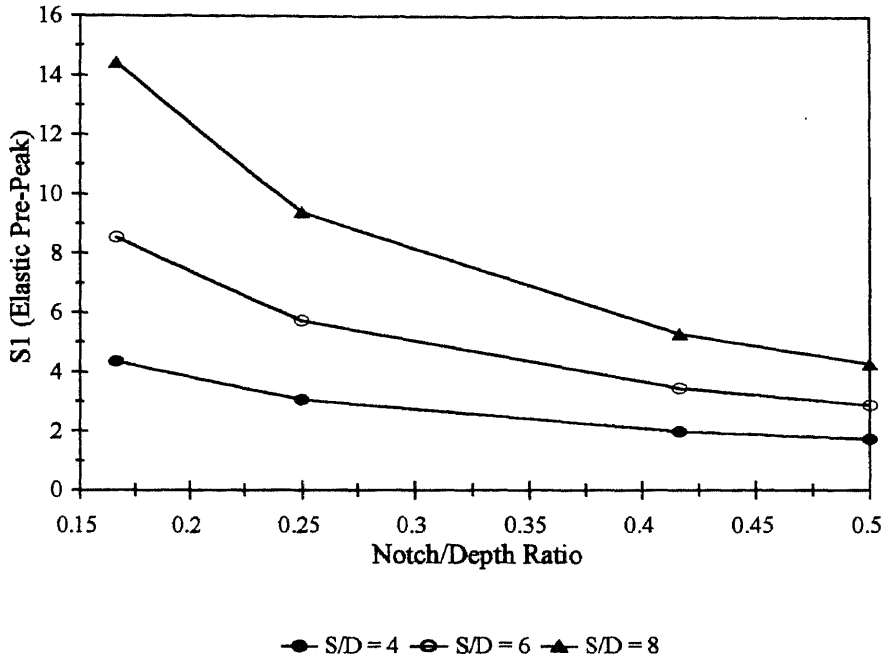

Figure 5.13 S_1 versus Notch/Depth Ratio

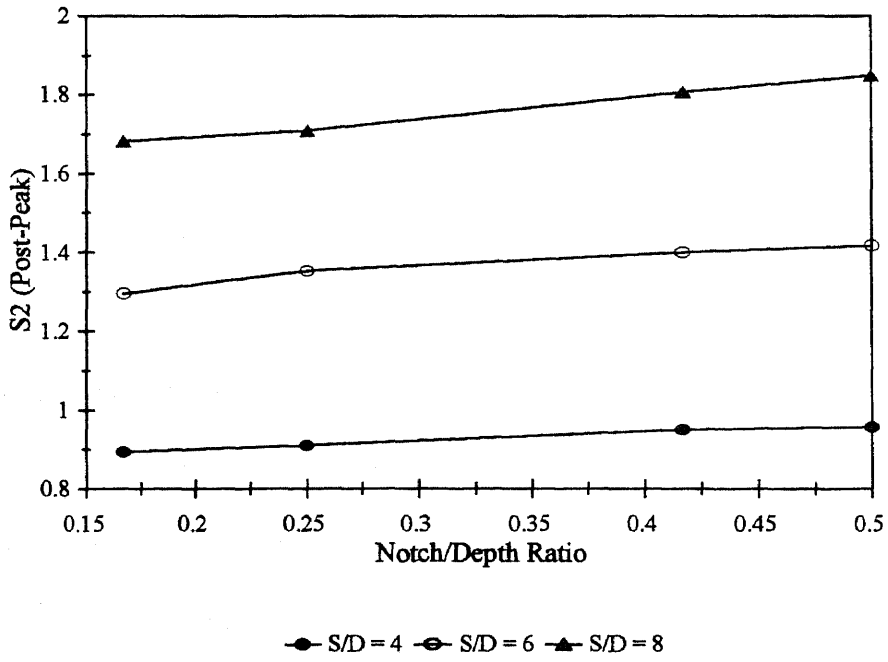

Figure 5.14 S_2 versus Notch/Depth Ratio

5.4.2 Relationship Between Plastic Components of Load Point Deflection (LPD_p) and Crack Mouth Opening Displacement ($CMOD_p$)

Similar to the method developed above, it is possible to eliminate the initial slope S_1 by considering only the plastic components of the displacements (load point deflection and CMOD). To derive a relationship for determining the fracture energy from Load-CMOD responses of a beam test, the following assumptions are utilized:

1. The elastic components of both the load point displacement and crack mouth opening displacement (δ, CMOD) can be calculated (estimated) at any instant of load by considering:

   (a) Material unloads-reloads elastically with constant initial stiffness K - see Figure 5.15a

   (b) Material unloads-reloads with stiffness degradation, and the rate of stiffness degradation is assumed to be linearly dependent on the displacements - see Figure 5.15b

2. Fracture Energy can be defined as the accumulation of the plastic energy which reaches a steady state value as the beam specimen finally separates in two halves.
3. The ratio of the plastic components of load point displacement and crack mouth opening displacements is a constant.

The beam displacement, u, (load line deflection and CMOD) can be separated into two components, namely the elastic component and the plastic component which occurs due to crack propagation.

$$u_T = u_e + u_p \tag{5.12}$$

where, u_p = plastic component of the displacements (either deflection or CMOD) due to crack propagation, u_T and u_e are the total and elastic component of the displacement respectively.

The elastic component of the displacement as a function of total displacement can be determined by using either assumption number 1 above or, by performing cyclic tests. It was shown by Jenq and Shah (1985) that the elastic components of both load point displacement and crack mouth opening displacements as a function of total displacement is a material property. Using assumption 1(a), the elastic component of displacements can be written as:

$$\delta_e = \frac{P}{K_1}, \; CMOD_e = \frac{P}{K_2} \tag{5.13}$$

where K_1 and K_2 are the stiffness of the beam with respect to load point and crack mouth opening displacements before the start of the fracture process growth.

Knowing the elastic component of the displacement, the plastic component of displacement can be estimated by subtracting from total displacements the elastic part as determined from Equation (5.13). The relation between plastic component of displacement and fracture energy can be obtained by considering the energy equilibrium of beam under bending at any instant of time, Δt. The external energy (or work) of load and deflection is equated to the strain energy and the energy absorbed in the fracture process zone.

External Work = Plastic Energy (Fracture) + Elastic Energy (Strain) (5.14a)

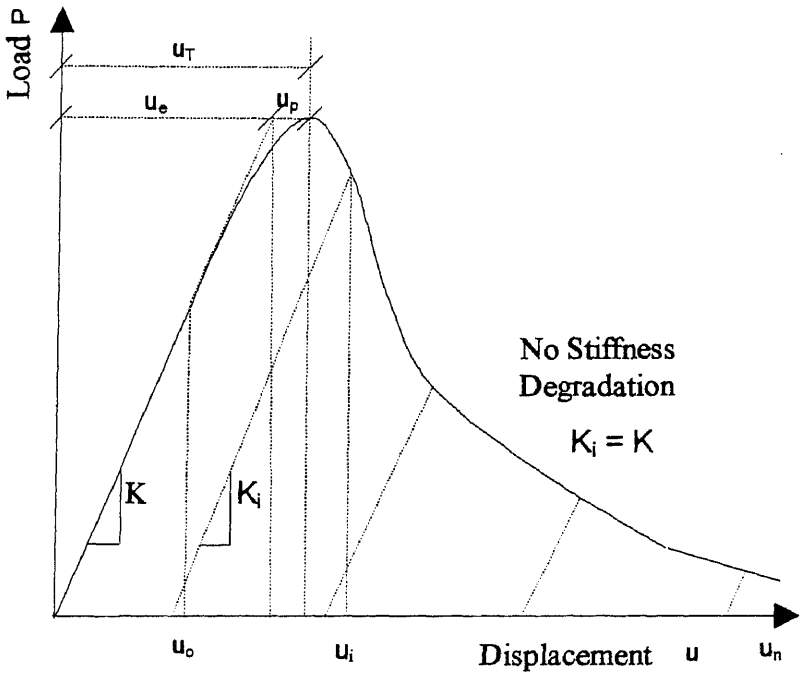

(a)

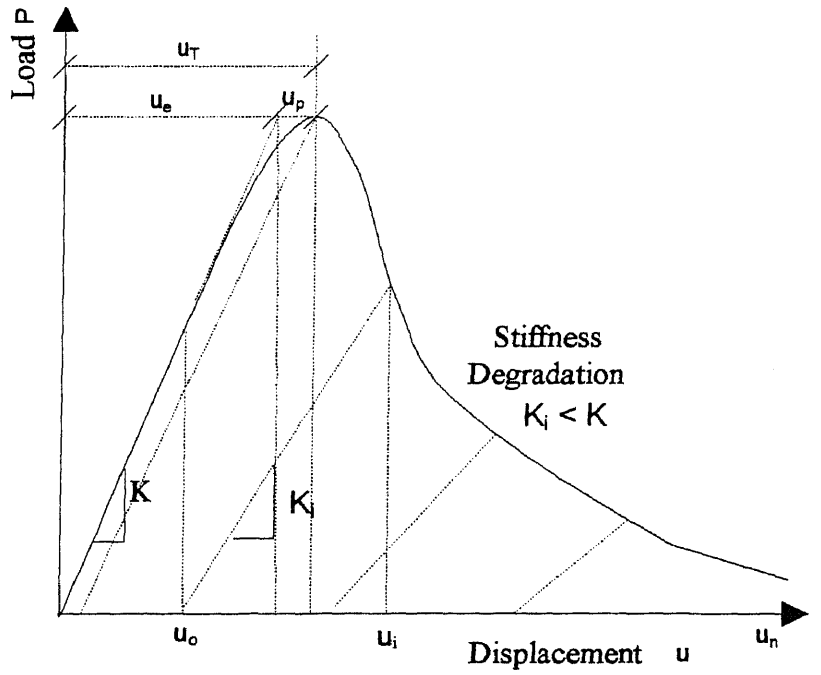

(b)

Figure 5.15 (a) Assumption Of Elastic Unloading-Reloading Behavior (B) Inelastic Stiffness Degradation Assumption

$$\int_0^{\delta} P d\delta = \int_A \int_{\omega} \sigma_p d\omega dA + \int_V \int_{\varepsilon} \sigma_e d\varepsilon dV \qquad (5.14b)$$

where P is the load acting on the beam, dδ is the incremental deflection at the considered time Δt, σ_p is the stress in the fracture process zone, dω is the amount of displacement in the fracture process zone, σ_e is the stress in the elastic region, dε is the amount of change of strain, A is the area of the fracture process zone and V is the volume of the specimen. If during the studied instant of time, the fracture process has not started, then the first term in the right hand side of the equation is still zero. In this case, the external energy is balanced by the elastic strain energy alone. As the specimen fractures the external energy is divided into two components, viz. the elastic strain energy and the plastic energy that is dissipated in the fracture process. Integrating the left hand side of the Equation (5.14b) between δ=0 and δ=δ_∞ and using the relationship between the total deflection (δ) and its elastic and plastic components:

$$\int_{\delta=0}^{\delta=\infty} P d\delta = \int_0^{\delta=\infty} P d\delta_p + \frac{1}{K_1} \int_{P(\delta=0)}^{P(\delta=\infty)} P dP = \int_0^{\delta=\infty} P d\delta_p + \left[\frac{P^2}{2K_1} \right]_{P(\delta=0)}^{P(\delta=\infty)} \cong \int_{\delta_p=0}^{\delta_p=\infty} P d\delta_p \qquad (5.15)$$

Refer to Figure 5.16 which illustrates the energy participation during beam bending. As seen in the Figure 5.16, the plastic energy is zero till the elastic limit after which the elastic as well as the plastic energy increase. The elastic energy reaches its maximum value at the peak load after which it starts to reduce and eventually vanishes when the load attains a value of zero. This leads to an important conclusion that the area under the load-plastic component of deflection also yields the fracture energy of concrete. As shown in Figure 5.16, the elastic external work is small compared to the

plastic external work, therefore as a simplification, it may be assumed that the total external work is equal to the plastic external work as indicated in Equation (5.15).

Integration of the two terms on right hand side of Equation (5.14b) over the entire displacement response (between δ=0 and δ=∞) can be dealt with individually. The first term by definition is G_F which yields:

$$\int_A \int_0^{w_f} \sigma_p dw dA = G_F B(D - a_o) \tag{5.16}$$

For the second term, the integration gives:

$$\int_V \int_\varepsilon \sigma_e d\varepsilon dV = \frac{1}{2}\int_V \sigma_e \cdot \varepsilon \, dV|_{\varepsilon(\delta=\infty)} - \frac{1}{2}\int_V \sigma_e \cdot \varepsilon \, dV|_{\varepsilon(\delta=0)} \tag{5.17}$$

The sum of $\sigma_e \varepsilon dV$ is zero at δ = 0 (since P = 0). As no external forces act on either of the two halves of the beam, considered individually, either at δ = 0 or at δ = ∞. Furthermore no plastic deformations are assumed to occur outside of the fracture zone, thus the sum of $\sigma_e \varepsilon dV$ is zero at δ = ∞ (since at δ = ∞, P = 0). For any other situation a closed form solution for the strain energy cannot be easily made.

In reality, the stiffness 'K' of the beam specimen for concrete like material will decrease as the crack propagates. To account for this, a simplified assumption is utilized and the stiffness K (both K_1 and K_2) is assumed to be linearly degrading as the displacement of the specimen increases. The stiffness at any value of displacement is calculated by using the equation given below:

$$K_i = K_o\left(\frac{u_n - u_i}{u_n - u_o}\right) \tag{5.18}$$

where, K_o is the initial stiffness, u_o = displacement prior to start of fracture process, u_n is the final displacement (load, $P \approx 0$), u_i is the current total displacement and K_i is the stiffness at the displacement value of u_i.

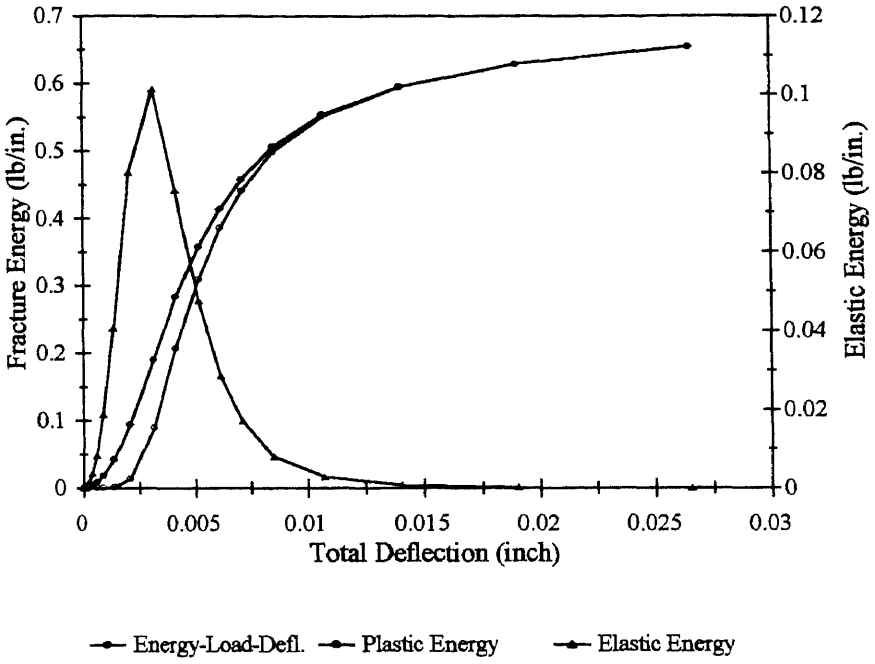

Figure 5.16 Energy Participation During Fracturing Of Beam

Relation between the plastic part of CMOD and fracture energy G_F can be developed by utilizing assumption no. 3. Using the finite element solutions for load, deflection and crack mouth opening displacements for the various sizes of beam studied, the plastic components of deflection and crack mouth opening displacements were calculated. They were found to have a linear relationship for any given S/D. In Figure 5.17, a typical linear relationship between plastic component of load-line deflection and plastic component of crack mouth opening displacement is presented. Using the constant S_3, the relationship between G_F and plastic CMOD is developed.

$$G_F \cdot B(D-a_o) = \int_0^{\delta_p} P d\delta_p = S_3 \int_0^{CMOD_p} P dCMOD_p \qquad (5.19)$$

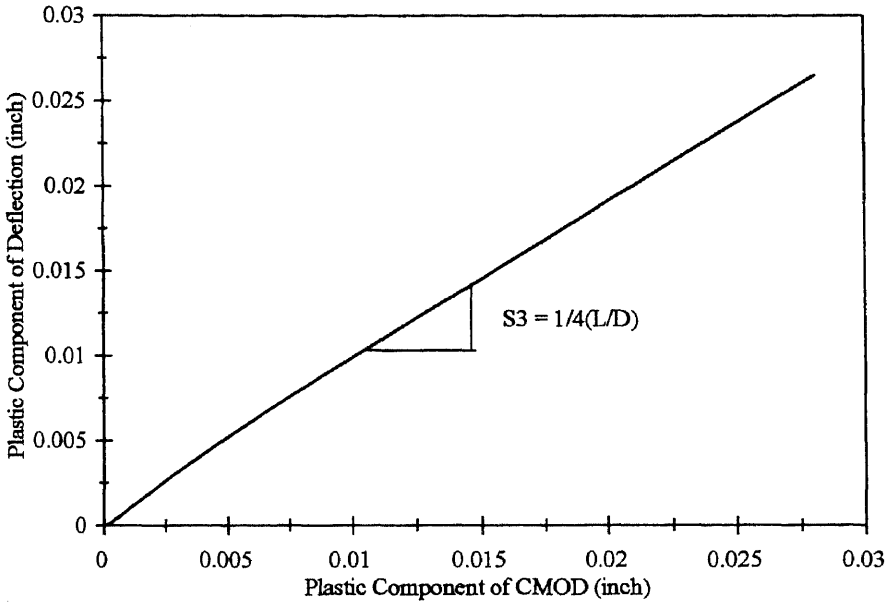

Figure 5.17 Typical Relationship Between Plastic Components Of Deflection And CMOD (FEM Solution)

Alternatively, an upper bound solution for the constant S_3 can also be developed by considering the collapse mechanism of the beam specimen at failure stage (see Figure 5.18). Since the relationship between the plastic component of displacement and CMOD is linear, only the final displacement (total displacement = plastic displacement) is considered. At initial position, i.e., when no cracking (elastic stage) has occurred, both the plastic components of load-line deflection and crack mouth opening displacement are zero. At the failure stage, this constant is found to be equal to:

$$CMOD = D\theta \,, \delta = \frac{L\theta}{4} \qquad (5.20)$$

Solving for $\delta/CMOD \approx S_3$:

$$S_3 = \frac{1}{4}\left(\frac{L}{D}\right) or\ \delta = S_3 \cdot CMOD \tag{5.21}$$

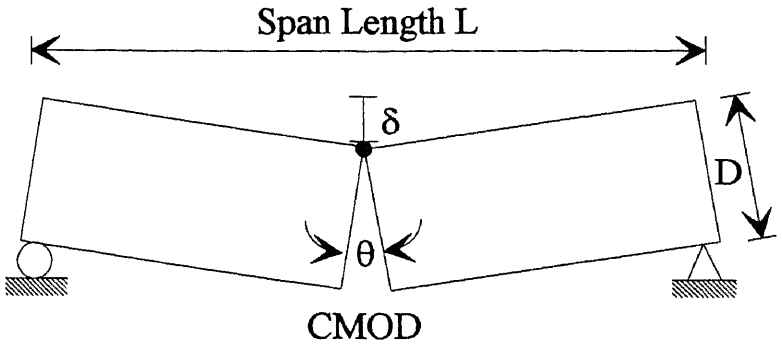

Figure 5.18 Collapse Mechanism of Beam at Failure Stage

In the next section, prediction of load-CMOD and load-deflection responses of other researchers as well as of the present study are given.

5.5 Performance of Present Finite Element Model - Comparison with Test Data of Other Researchers

In this section, comparisons of test data of few researchers with the predictions of the present finite element model are presented. Although a large number of fracture test data is available in the literature, they are mainly for normal strength concrete. Reliable and exhaustive test data on high strength concrete is lacking and very limited. Test data referred in this section were specifically chosen to highlight the importance of the correct measurement of load point deflections. As mentioned previously, error in deflection measurement greatly affects the fracture energy G_F. The test data referred to are from:

1. Kim (1991), Medium strength concrete f'_c = 7000 to 8000 psi

2. Gettu et. al. (Gettu, Bazant and Karr 1990), High strength concrete $f'_c > 12000$ psi
3. Xie et. al. (Xie, Elwi and MacGregor 1994), High strength concrete $f'_c = 12000$ psi

Figures 5.19 through 5.21 present the test data adapted from Kim's study (1991). As seen from these figures, larger discrepancies are seen to be associated with the load-deflection curves compared to the load-CMOD responses. The finite element model (material properties used: Curve B softening curve, $f'_t = 550$ psi and $E = 4.7 \times 10^6$ psi, $G_F = 0.65$ lb./in) generally compares favorably with the load-CMOD responses. The variations in the load-deflection responses are associated with the measurement technique employed in the tests. The deflections were measured from a reference frame, and the LVDT (deflection measuring transducer) was attached to a roller (used for transmitting the load) placed under the load application point and the deflection was measured as the movement of the roller with reference to the frame (bar). In Kim's study, independent deflections (off the beam) measurement were also recorded. It was shown that the deflections measured independently were higher in magnitude as compared to the measurement from the reference frame.

The reason the observed deflection (reference frame measurements) values were higher than the finite element prediction, and tests on the same size of beams done for this study is probably due to concrete crushing that took place under the load application point. Even though the deflections were measured off a "floating" reference frame, the deflections did not totally exclude the effect due to crushing of concrete. It is interesting to note that if it is assumed that this was the cause, then the concrete crushing that takes place at the supports is higher in magnitude (independent deflection measurements were higher) than that occurring at the load application point.

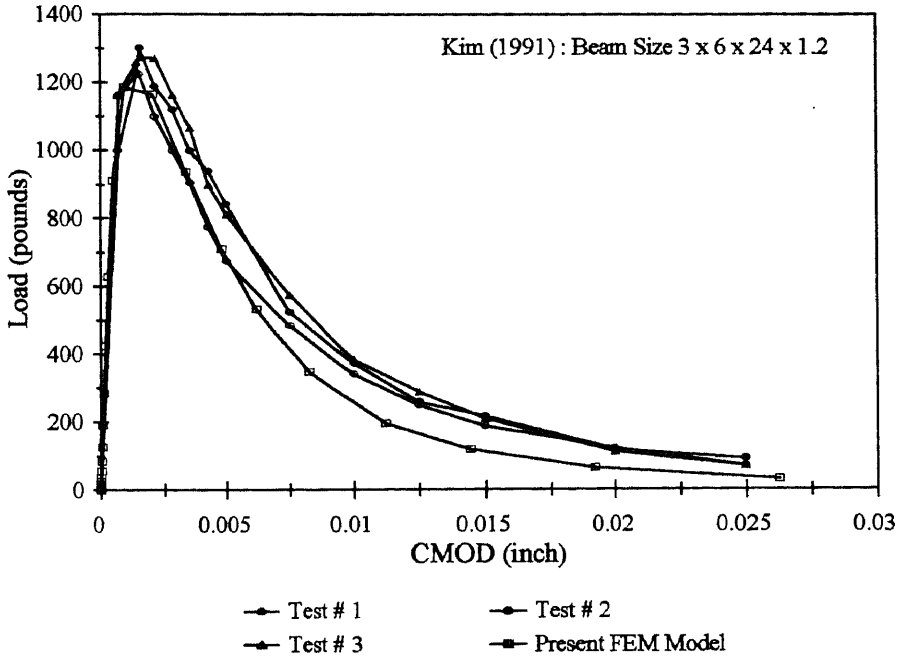

Figure 5.19a Load - CMOD Response of Kim (1991) test data

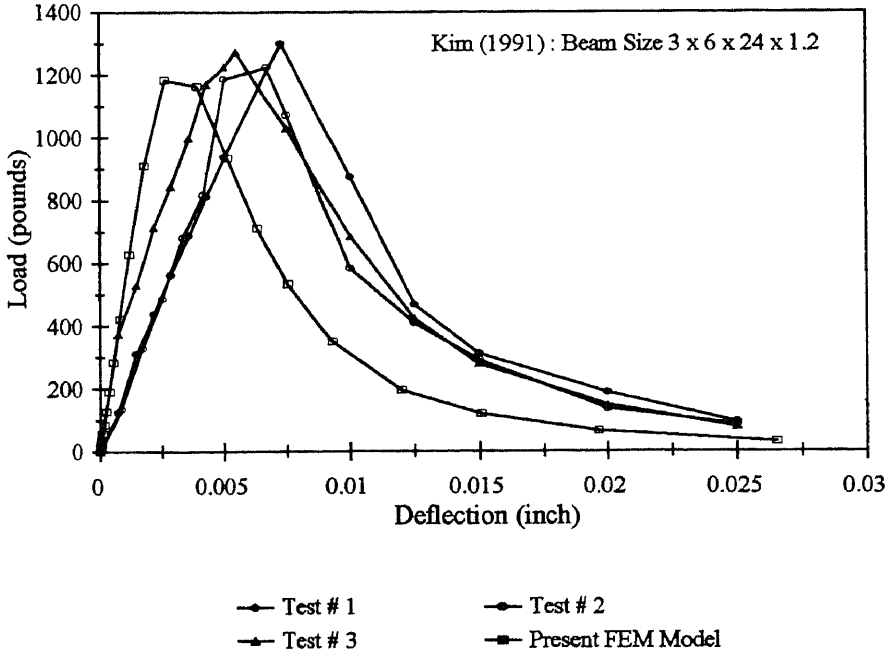

Figure 5.19b Load - Deflection Responses of Kim (1991) test data

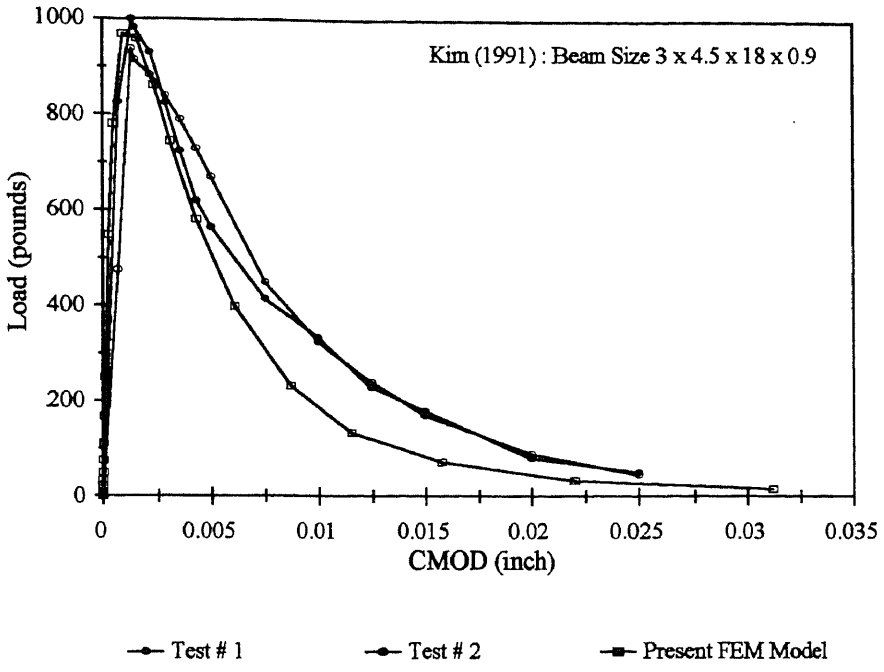

Figure 5.20a Load - CMOD Responses of Kim (1991) test data

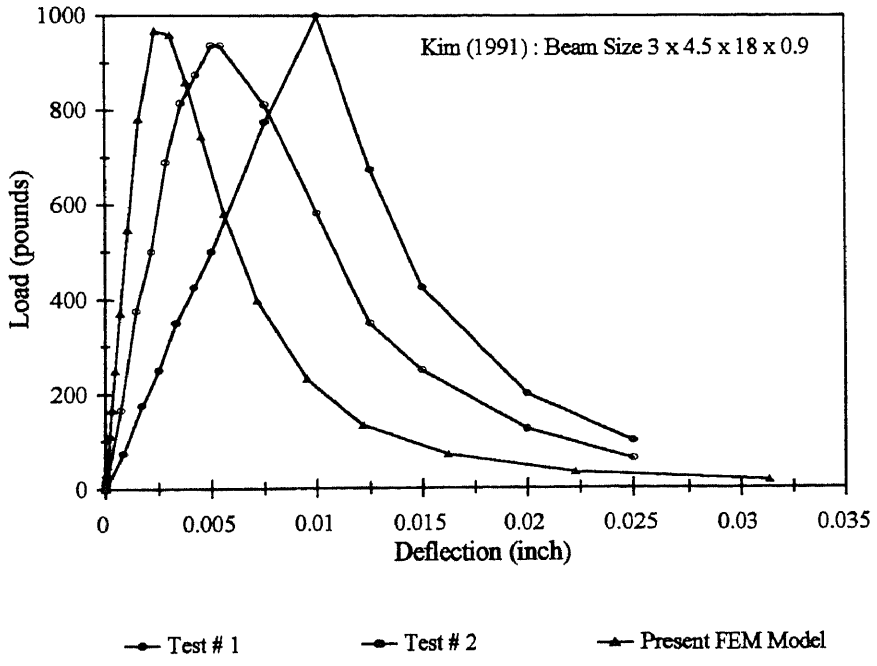

Figure 5.20b Load - Deflection Responses of Kim (1991) test data

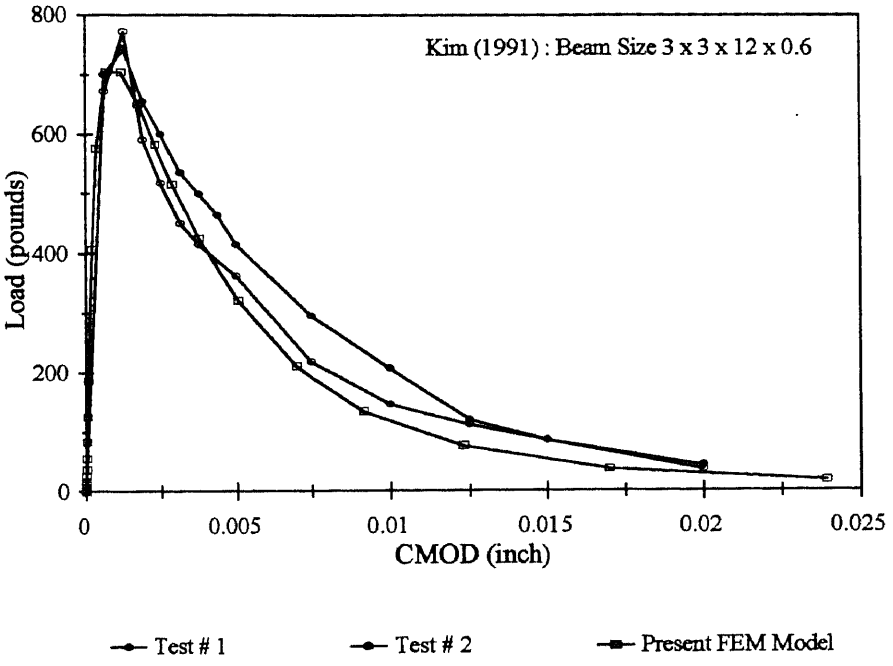

Figure 5.21a Load - CMOD Responses of Kim (1991) test data

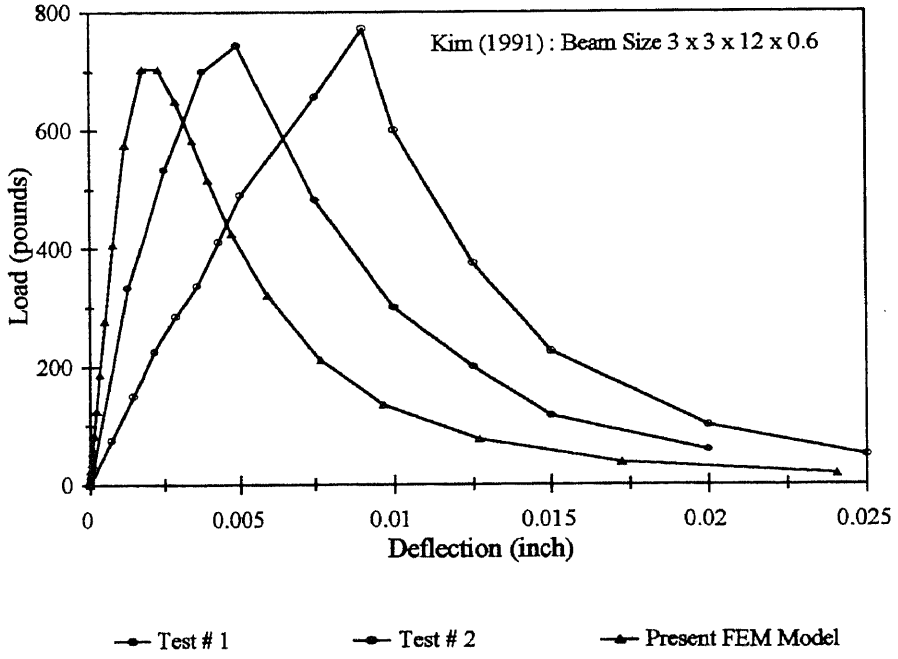

Figure 5.21b Load - Deflection Responses of Kim (1991) test data

In Figure 5.22a and 5.22b, test data adapted from the study of Gettu et. al. (Gettu, Bazant and Karr 1990) are presented. In the tests the deflections were measured totally independent of the beam. It is obvious that the deflection measurements included the erroneous deflections caused by concrete crushing at the supports. It is interesting to note that the difference in the measured peak deflection of the tests compared to the present finite element model predictions is almost four times. Since the high strength concrete tested was of higher strength than those studied in the present study (> 12000 psi), the tensile strength was assumed to be 700 psi, $E = 5.5 \times 10^6$ psi and Curve C softening curve was employed during the present finite element analysis.

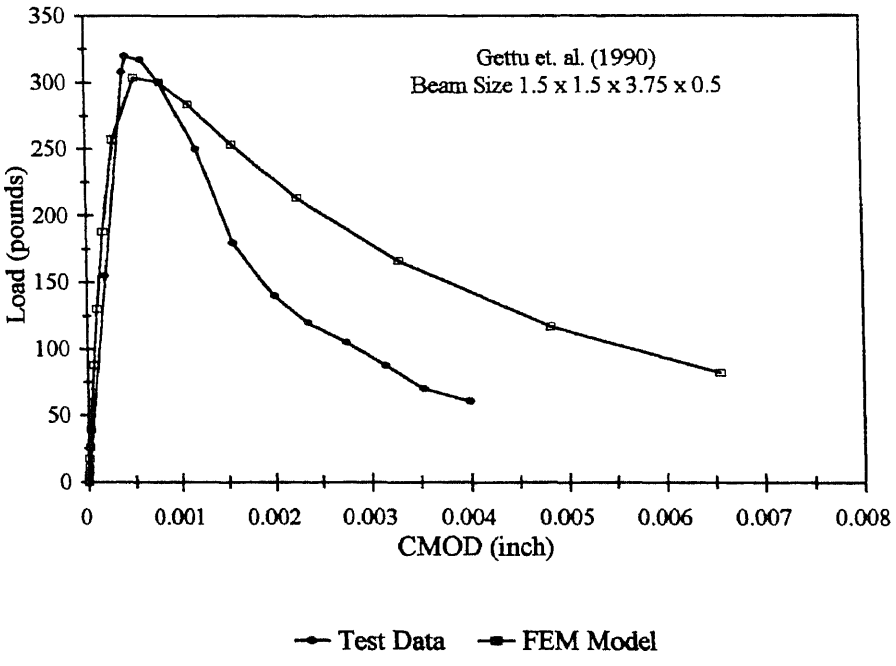

Figure 5.22a Load - CMOD Response of Gettu et. al. (1990) test data

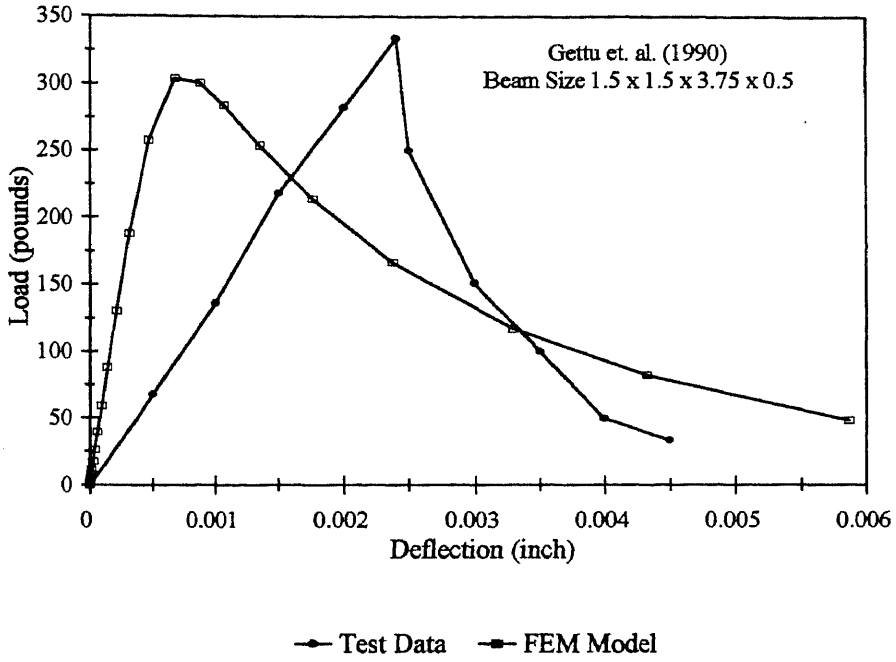

Figure 5.22b Load - Deflection Response of Gettu et. al. (1990) test data

Test data (Figure 5.23) reported by Xie et. al. (Xie, Elwi and MacGregor 1994) consists of fracture energy determination from beam tests as per RILEM specifications. The load point deflection was measured or recorded as the movement of the steel platen (Stroke) attached to the load cell. The calculated fracture energy reported in their study was 0.98 lb./in, which is about 35% higher than the value obtained in the present study for a similar compressive strength concrete (12000 psi). In their study, recording of load-CMOD measurements was not undertaken.

Based on the discussions above it is clear that the deflection measurement is very sensitive to the technique used. In this study, the load point deflection was measured with reference to a frame mounted on the beam "floating" with the beam, at the level of the initial neutral axis, on pivots attached over the supports (see Figure

3.20). Deflection measurements were also monitored independently of the beam. In Figure 5.24, a typical response of load-deflection is shown. As can be seen, there is a profound effect on the deflection from the crushing of concrete. It is picked up by the deflection measured independent of the beam (LVDT 2, Figure 3.20). In Figures 5.25 through 5.30, the results of the beam tests (present study) with the finite element predictions are shown. Note the consistency in both the deflection and CMOD measurements. Also the finite element predictions are found to be in good agreement with the tests.

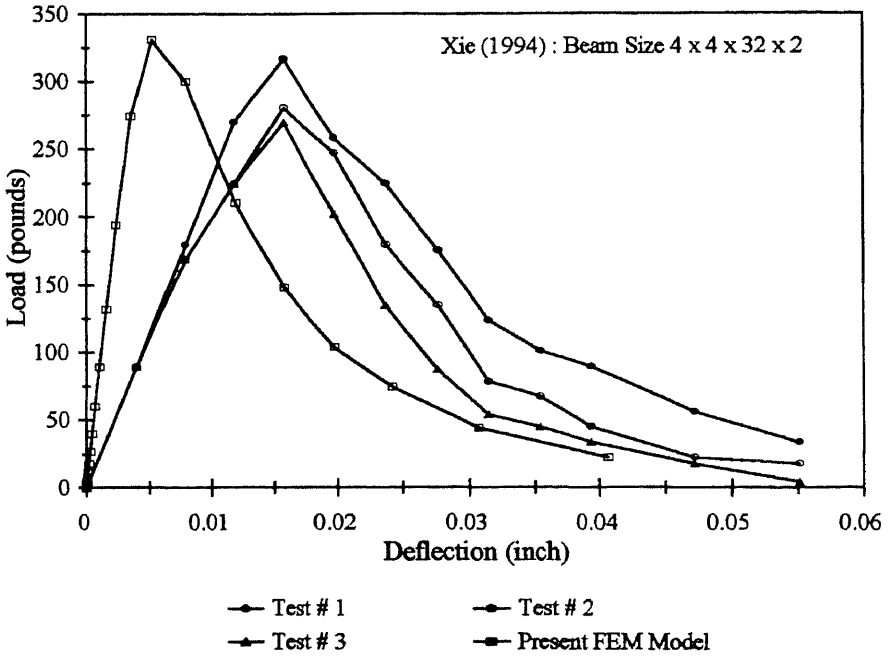

Figure 5.23 Load - Deflection Responses of Xie et. al. (1994) test data

In the next section, calculation of fracture energy from the load-CMOD data is presented. The purpose for developing a correlation between CMOD and accurately measured load point displacement will help accomplish the following:

- To improve experimental determination of G_F, from load-CMOD data. Since the CMOD measurements are generally unaffected by any movement of the specimen or crushing of concrete at the supports. This will result in less variation in G_F.
- To offer a method to correct the fracture test data available in the literature by using the relationship between CMOD-Deflection to re-calculated G_F from the load and newly obtained deflection measurement.

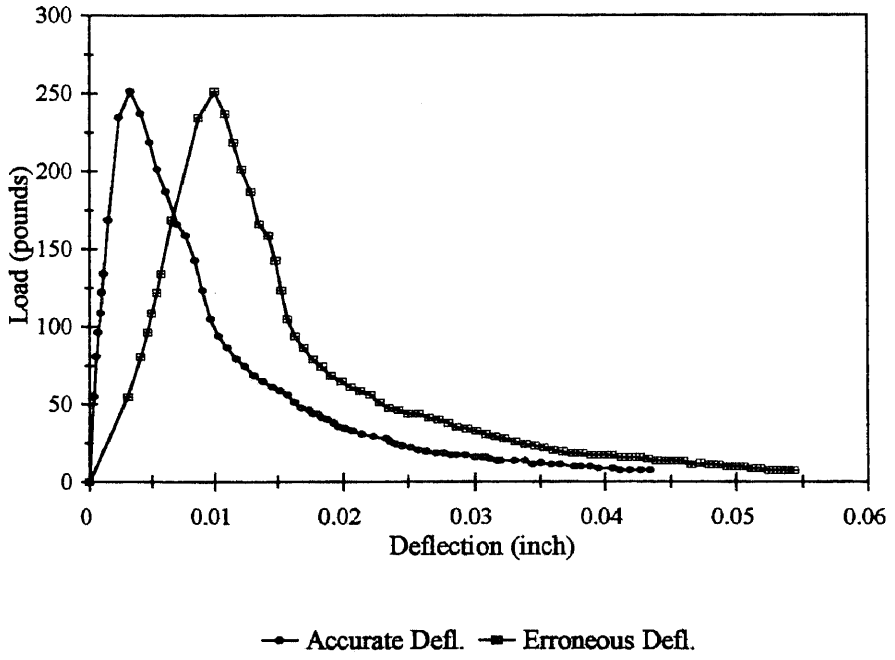

Figure 5.24 Effect of Crushing of Concrete at Supports as Shown By Measuring the Load Point Deflections at Two Locations. (a) With reference to the frame (Accurate Defl.) (b) Independent of the Frame (Erroneous Defl.).

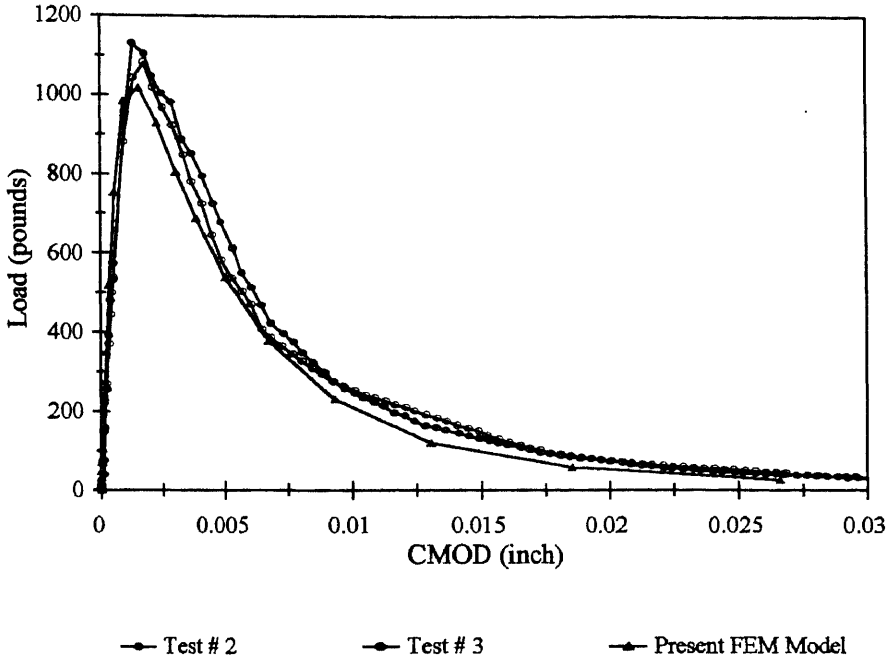

Figure 5.25a Comparison with Load-CMOD Responses
(Present Study - Size A specimen, A12 through A13)

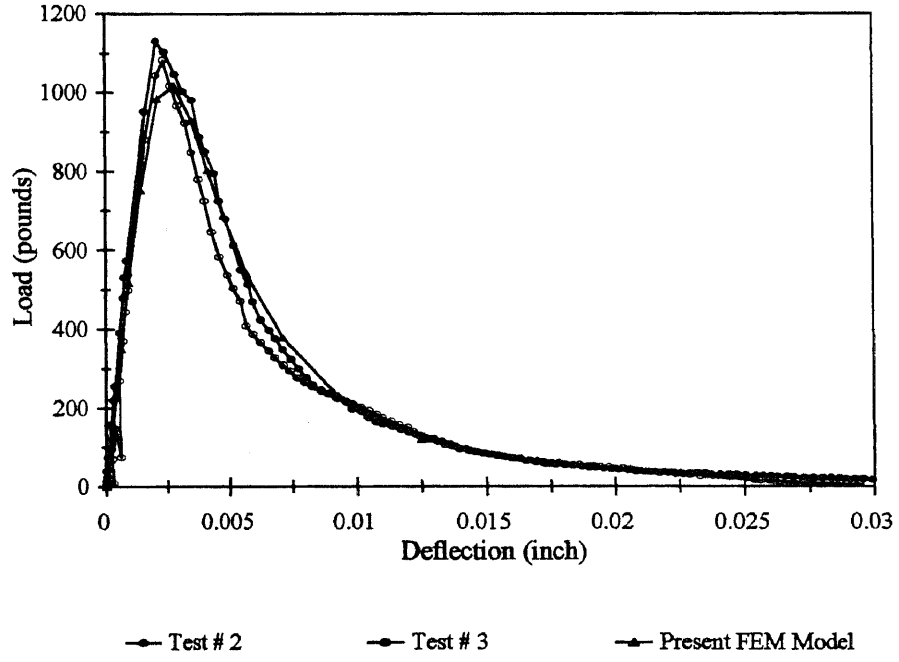

Figure 5.25b Comparison with Load-Deflection Responses
(Present Study - Size A specimen, A12 through A13)

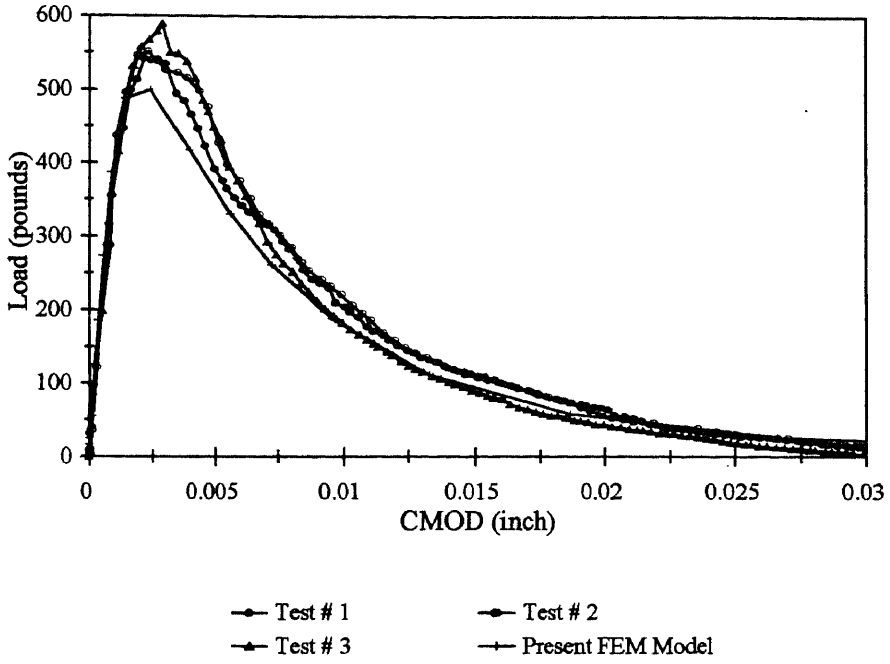

Figure 5.26a Comparison with Load-CMOD Responses
(Present Study - Size A specimen, A21 through A23)

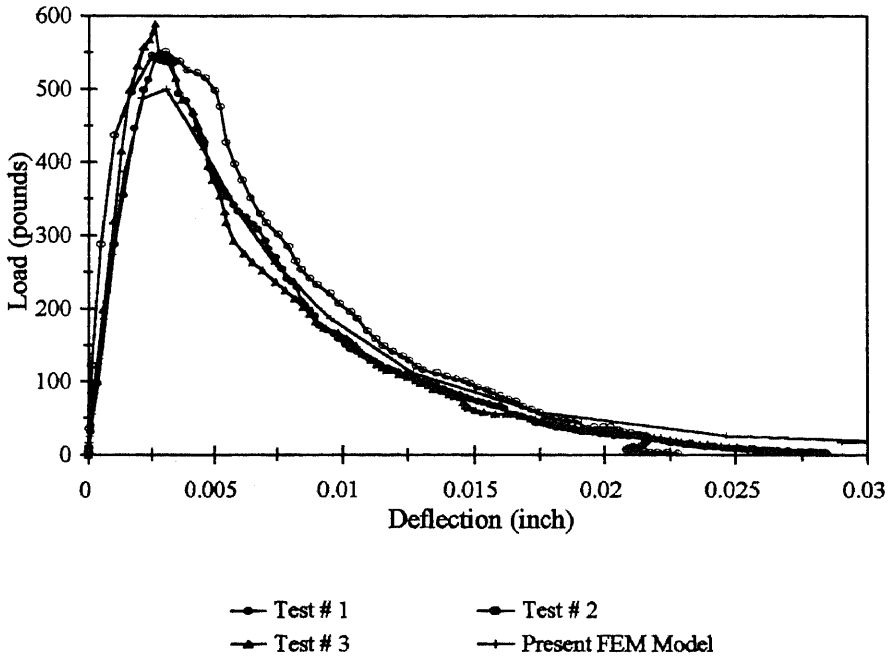

Figure 5.26b Comparison with Load-Deflection Responses
(Present Study - Size A specimen, A21 through A23)

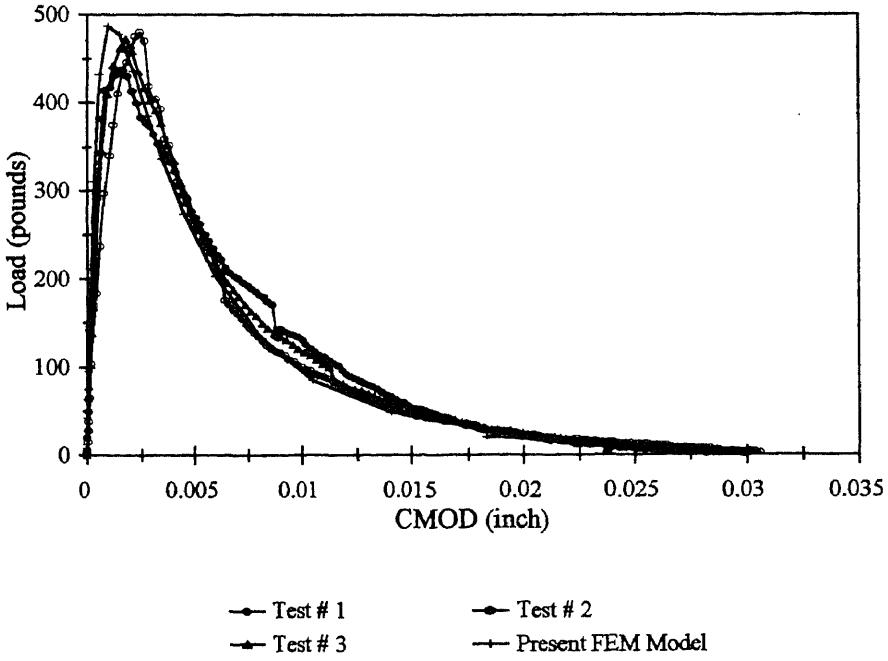

Figure 5.27a Comparison with Load-CMOD Responses
(Present Study - Size B specimen, B11 through B13)

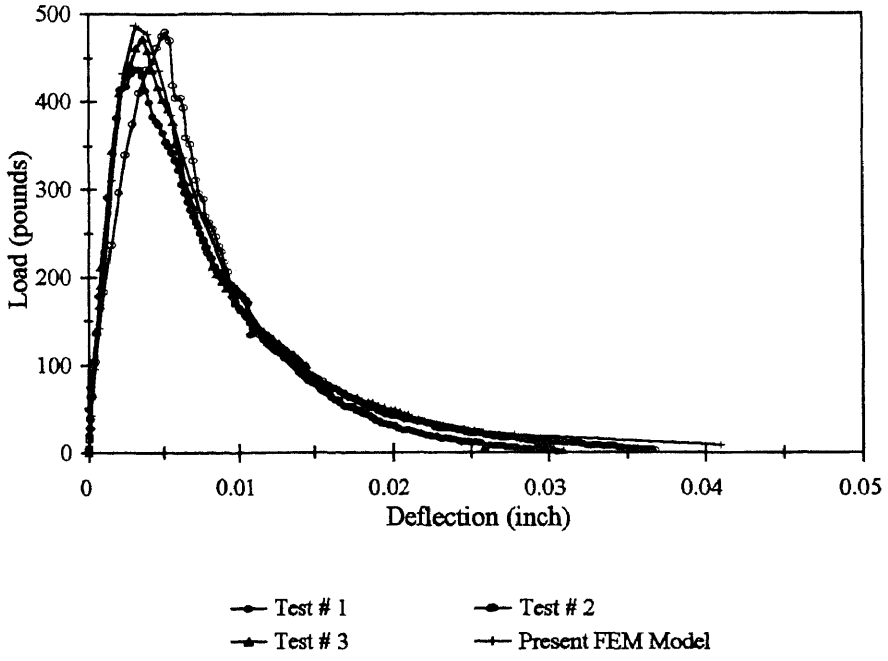

Figure 5.27b Comparison with Load-Deflection Responses
(Present Study - Size B specimen, B11 through B13)

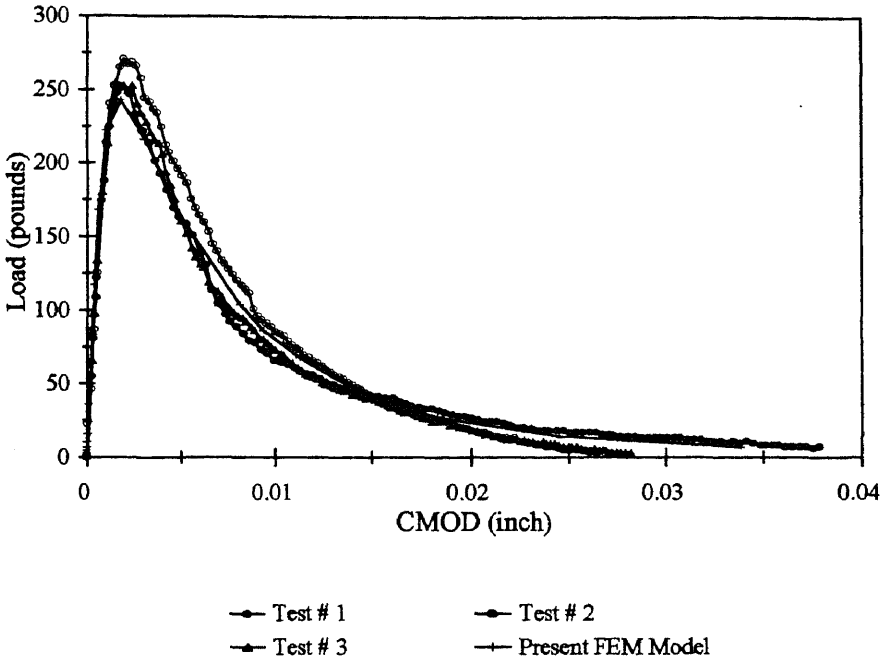

Figure 5.28a Comparison with Load-CMOD Responses
(Present Study - Size B specimen, B21 through B23)

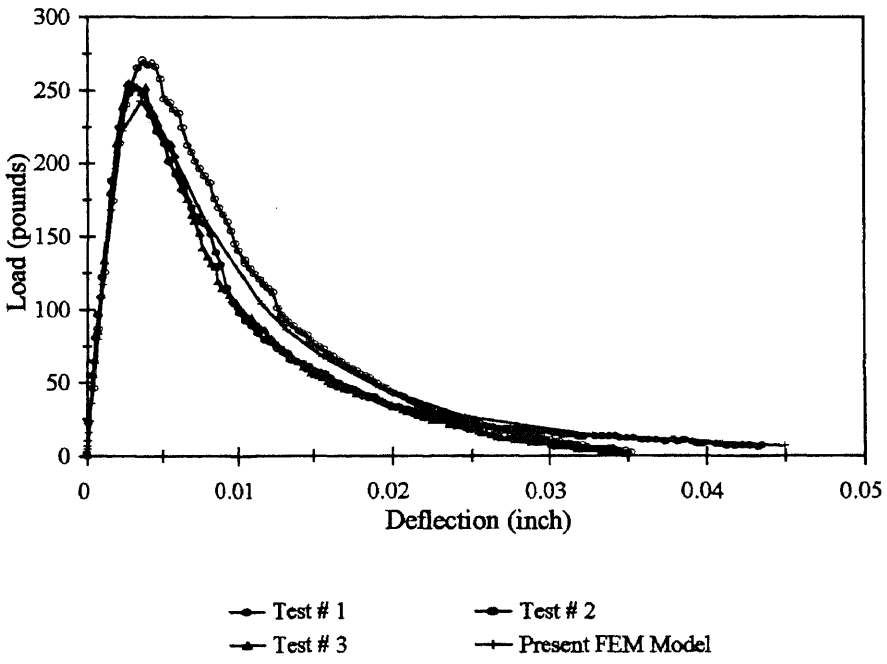

Figure 5.28b Comparison with Load-Deflection Responses
(Present Study - Size B specimen, B21 through B23)

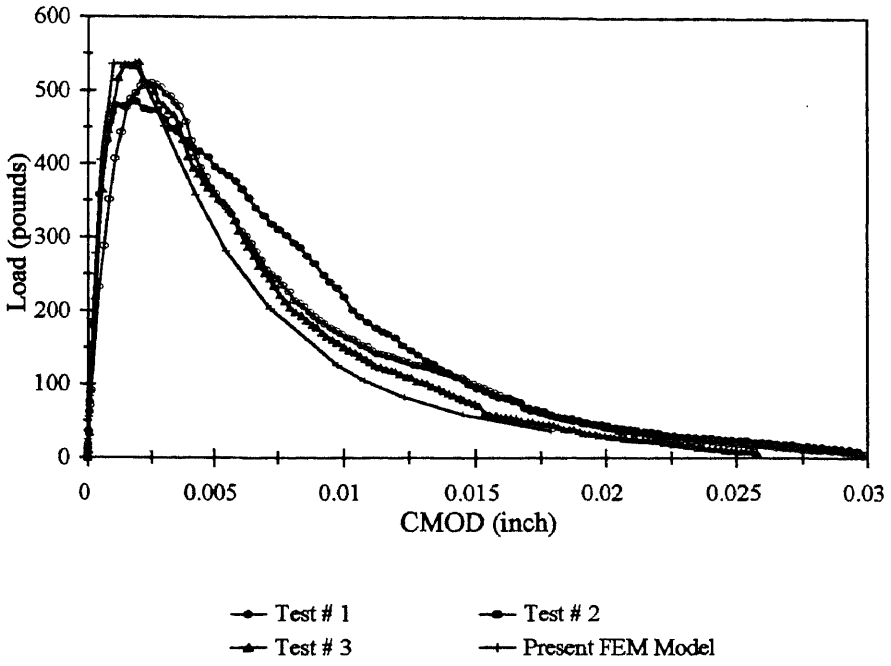

Figure 5.29a Comparison with Load-CMOD Responses
(Present Study - Size C specimen, C11 through C13)

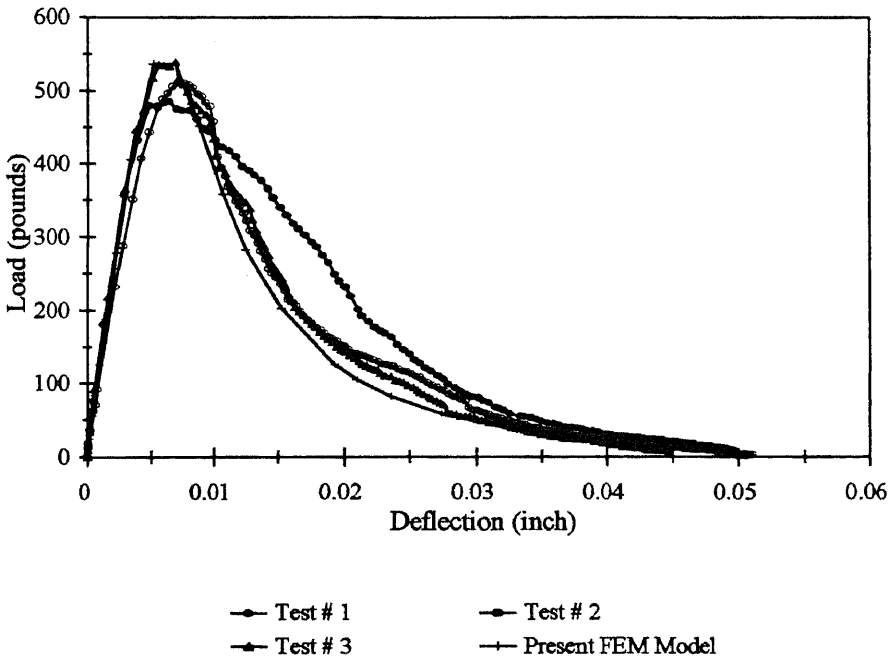

Figure 5.29b Comparison with Load-Deflection Responses
(Present Study - Size C specimen, C11 through C13)

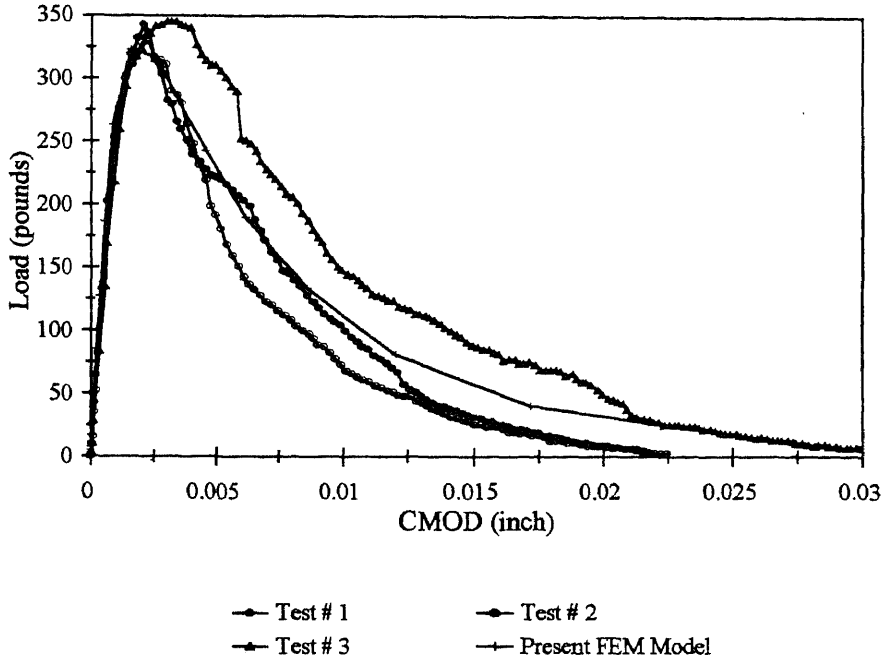

Figure 5.30a Comparison with Load-CMOD Responses
(Present Study - Size C specimen, C21 through C23)

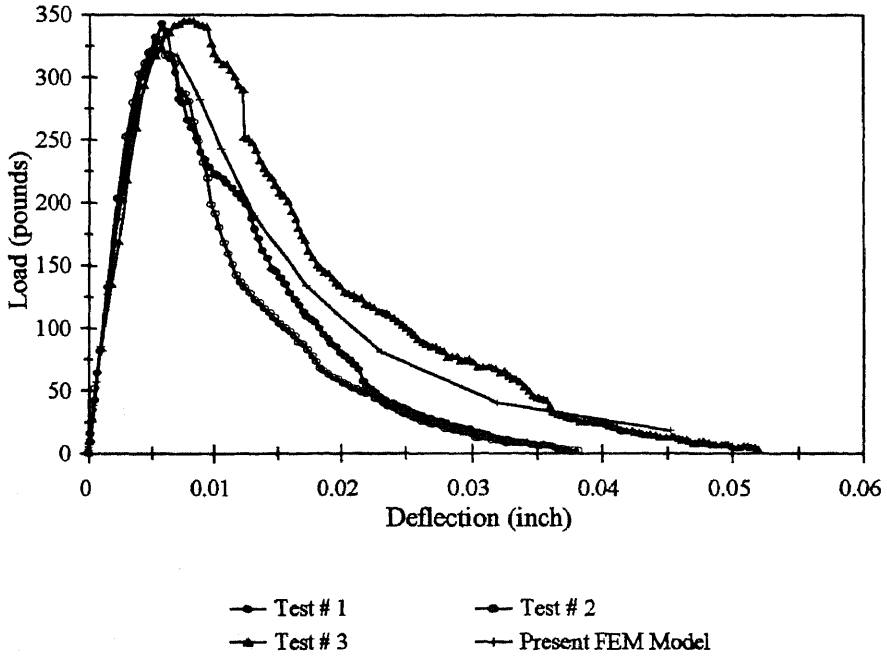

Figure 5.30b Comparison with Load-Deflection Responses
(Present Study - Size C specimen, C21 through C23)

5.6 Evaluation Of Fracture Energy G_F From Load-CMOD Test Data

In this section the evaluation of fracture energy (G_F) from the Load-CMOD data is presented. The correlated constants S_1, S_2 and S_3 were experimentally evaluated as discussed in sections 5.4.1 and 5.4.2. The present test and FEM results are summarized in Table 5.4.

Table 5.4 Correlated Constants (average values - 3 tests)

Specimen Details	Experimental			Finite Elements*			LEFM*
	S_1	S_2	S_3	S_1	S_2	S_3	S_1
A - $a_o/D = 0.25$ 3x4.5x18x1.125	1.790	0.735	0.800	2.610	0.882	0.912	2.470
A - $a_o/D = 0.5$ 3x4.5x18x2.25	1.215	0.79	0.815	1.550	0.928	0.949	1.314
B - $a_o/D = 0.25$ 3x3x18x0.75	3.073	1.11	1.148	4.910	1.276	1.323	4.45
B - $a_o/D = 0.5$ 3x3x18x1.50	1.954	1.223	1.256	2.598	1.331	1.368	2.093
C -$a_o/D = 0.25$ 4x4x32x1.0	6.663	1.558	1.661	8.087	1.607	1.752	7.666
C - $a_o/D = 0.5$ 4x4x32x2.0	3.204	1.603	1.687	3.875	1.737	1.809	3.300

* After applying correction $\Delta h = 0.3$"

As can be seen from the above table, S_1, S_2 and S_3 obtained experimentally are somewhat different from the FEM and LEFM values. The difference is even higher when compared with the values presented in Table 5.3. One of the reason for this is that in FEM and LEFM analysis, crack mouth opening displacements (CMOD) was calculated exactly at the beam's crack mouth (see Figure 5.31). However, in experiments, CMOD is always measured at a small distance below the beam bottom face (see Figure 5.31). If this distance is taken into account i.e., CMOD is calculated at a small distance below the beam's bottom fiber, the difference in the constants S_1, S_2 and S_3 gets smaller. Also, in theoretical analysis (present FEM model) the crack path was

assumed along a straight line. In reality, i.e. in experiments, the crack path is not necessarily along a straight line. Slight deviations in the crack path (see photograph in Figure 5.32) can also contribute to the observed differences between theoretically calculated constants and experimentally obtained values. Using LEFM, an equation which relates CMOD and Load and takes into account the location of the measurements of CMOD in the elastic portion was proposed by Shah et. al. (Shah 1990). This equation is given below:

$$\frac{P_e}{CMOD} = K_2 = \frac{EBD^2}{6Sa_oV(\alpha)} \tag{5.22}$$

where, P_e = Elastic Load, E = Young's Modulus, B , D , S and a_o are the width, depth span and initial notch depth. The factor $V(\alpha)$ is given by:

$$V(\alpha) = 0.76 - 2.28\alpha + 3.87\alpha^2 - 2.04\alpha^3 + \frac{0.66}{(1-\alpha)^2} \quad , \quad \alpha = \frac{a_o + \Delta h}{D + \Delta h} \tag{5.23}$$

In the present experimental study, the CMOD was measured at a distance of 0.3"-0.4" below the bottom of the beam. Substituting Δh = 0.3" in the above equations, it can be shown that the stiffness (K_2) of the beam with respect to CMOD can change by more than 10% to 25% depending on the initial notch depth. In computing S_3, K_1 and K_2 are both used, and the values of S_2 and S_3 are significantly affected if K_2 changes. To determine the extent of influence of Δh on the values of S_1, S_2 and S_3, finite element analysis was performed by defining a pair of stiff elements on either side of the crack path at the bottom face of the beam. The height of the element was varied between 0.1" to 0.4" and the corresponding changes in K_2 (P_e/$CMOD_e$) were computed. The influences on S_1, S_2 and S_3 were then determined. The following equation which is valid

for a_o/D (notch depth ratio) of 0.1 to 0.5 and for Δh of 0.1" to 0.4" was developed from the numerical results.

$$K_2^c = K_2 \cdot \left[1 - r\left(\frac{a_o}{D}\right)^s \Delta h\right] \tag{5.24}$$

where, K_2 = Stiffness with respect to CMOD (initial notch depth), K_2^c = corrected stiffness after taking into account Δh. r and s are constants, r= 0.15 and s =-0.622.

The above equation is valid for span to depth ratios of 4 to 8. Figures 5.33 through 5.35 show the effect of Δh on the values of S_1, S_2 and S_3 for span to depth ratio of 4 beams.

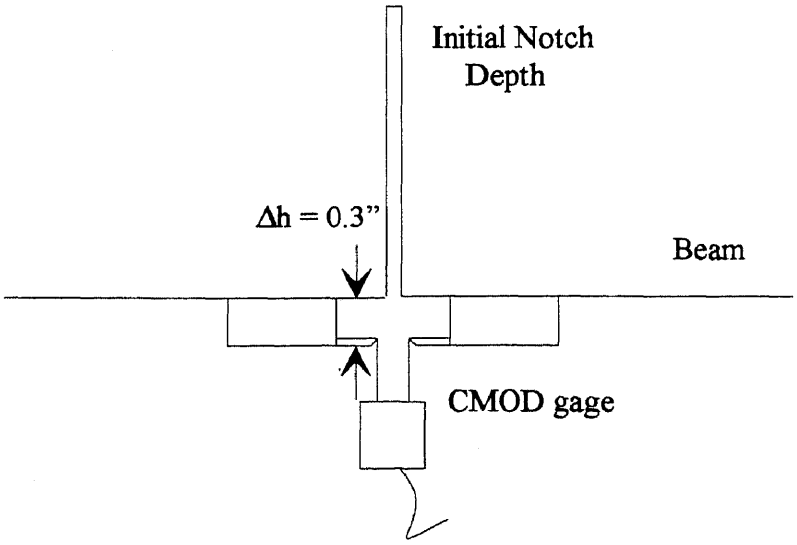

Figure 5.31 Location of the CMOD Gage Below the Beam Bottom Surface

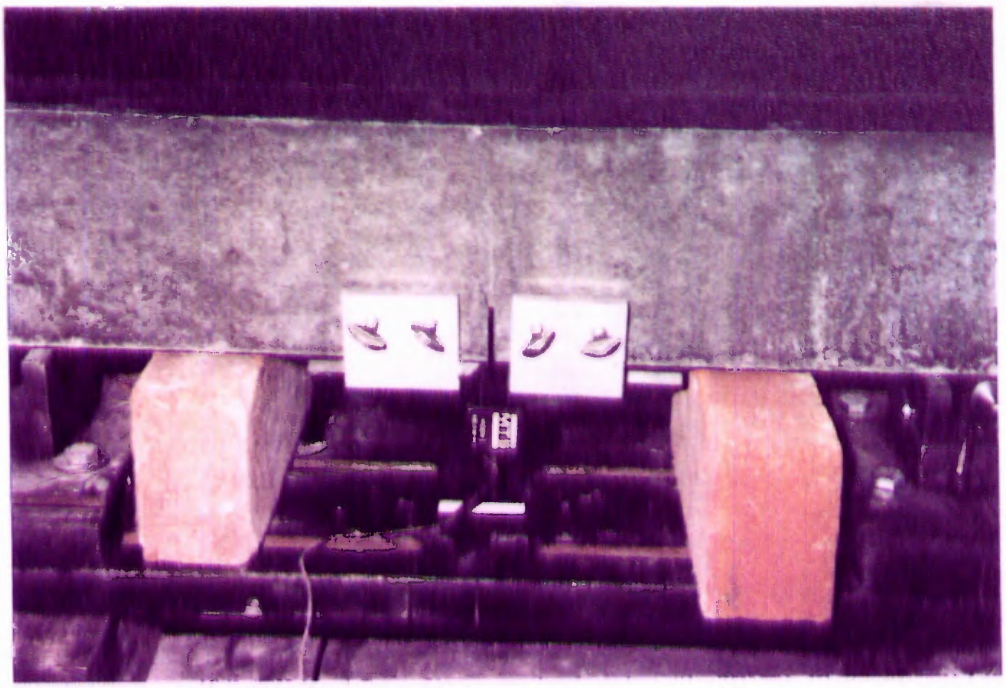

Figure 5.32 Photograph of a Cracked Beam Showing the Tendency for the Crack Path to Deviate From a Straight Line.

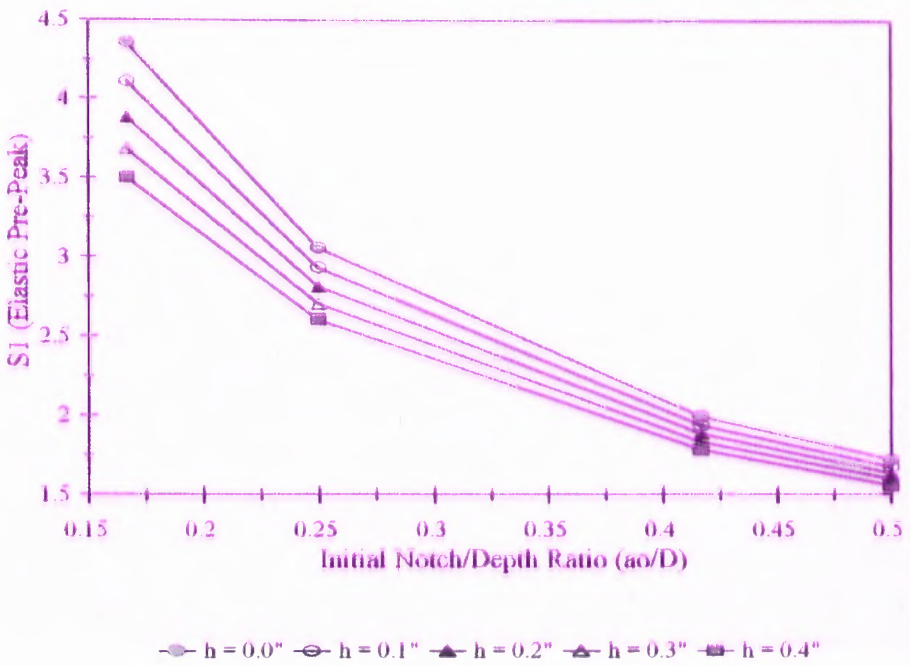

Figure 5.33 Influence of Δh on the Pre-Peak S_1 Constant
(h = Location of the CMOD Gage)

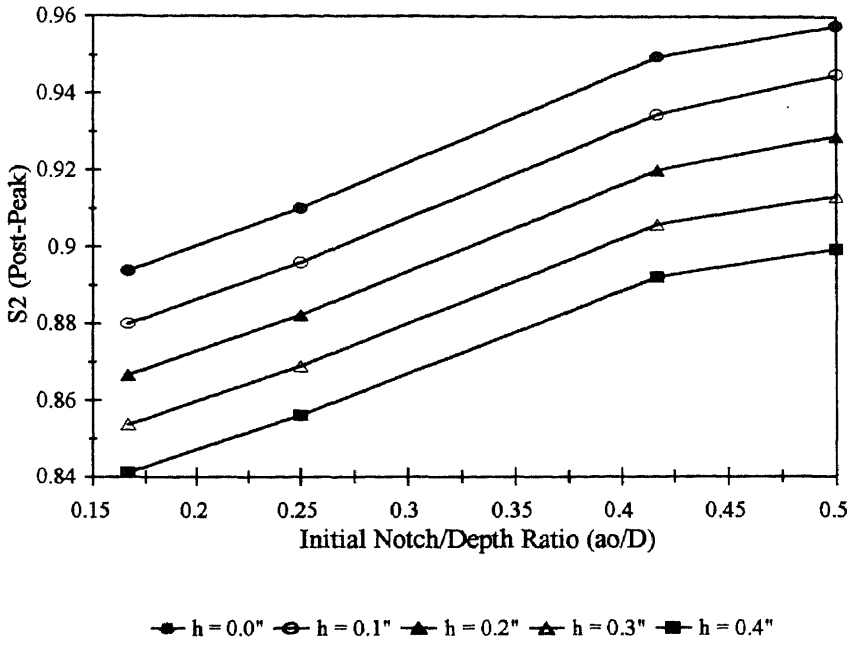

Figure 5.34 Influence of Δh on the Post-Peak S_2 Constant
(h = Location of the CMOD Gage)

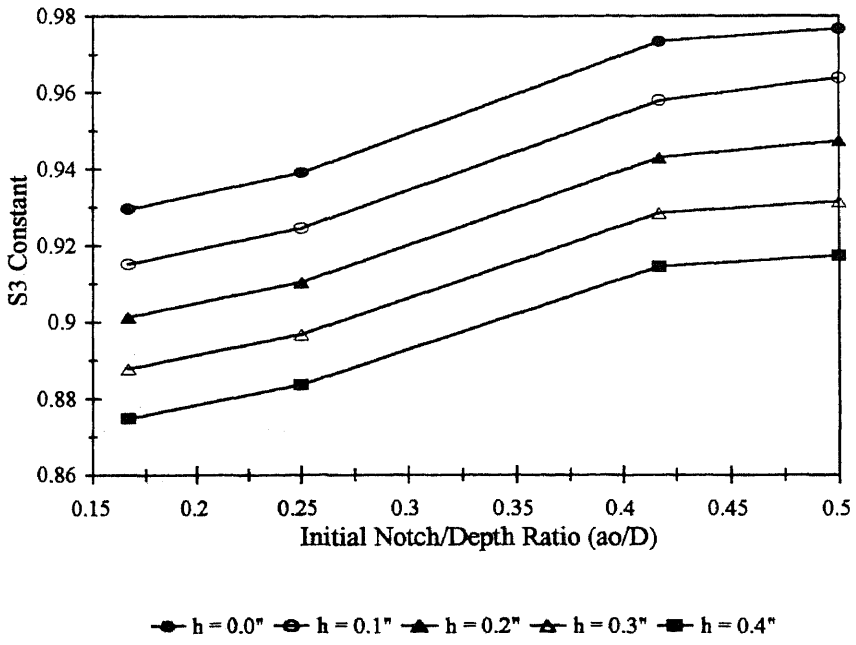

Figure 5.35 Influence of Δh on the S_3 Constant
(h = Location of the CMOD Gage)

As discussed in sections 5.4.1 and 5.4.2, the fracture energy G_F was determined using the correlated constants S_1, S_2 and S_3 and the results are presented in Table 5.5. As can be seen the G_F values evaluated based on the load-CMOD data compare favorably with the fracture energy calculated using the conventional load-deflection basis. In this study, the beam deflections were recorded accurately, i.e., excluded the effect of crushing of concrete at the supports.

Although all precautions were observed, during some tests there were some erroneous measurements of deflection. Such data was not used in computing the constants S_1, S_2 and S_3. In Figure 5.36, comparison of G_F values obtained from load-CMOD data, load-deflection results and also the G_F obtained from tension tests is presented.

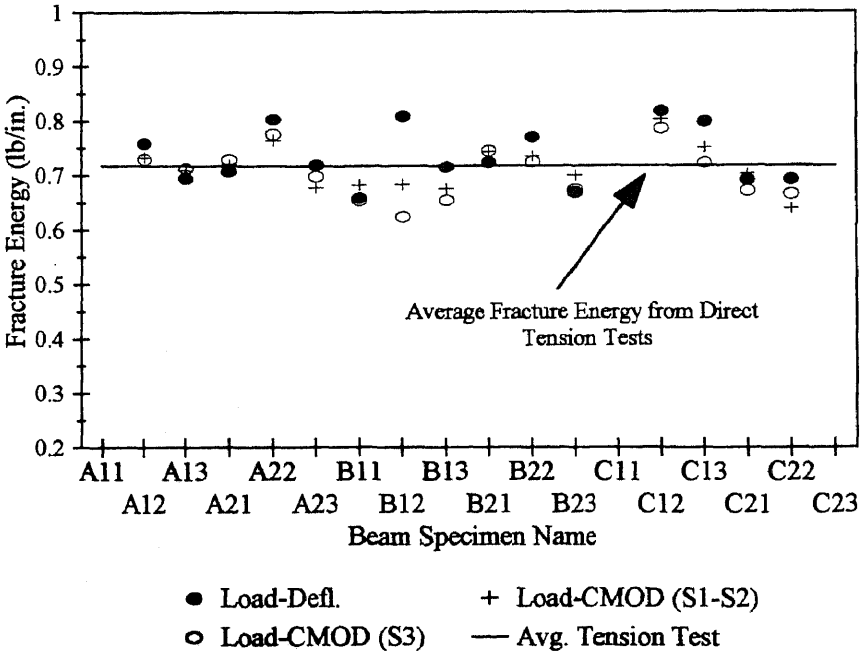

Figure 5.36 Comparison of Fracture Energy obtained from Load-CMOD data and Load-Deflection Data.

As seen from the results, the G_F obtained from the beam tests compare very well with the G_F obtained from the tension tests indicating that the G_F obtained from the experimental study should be considered as a material property and since it is found to be independent of the type of test used for evaluating as well as the specimen size (beams) used further validates G_F as a true material property.

Table 5.5 Computed Values of G_F from Load-CMOD Data (Experimental)

Specimen Name	G_F using Load-Defl.(lb./in)	G_F using Load-CMOD S_1- S_2 method (lb./in)	G_F using Load-CMOD S_3 method (lb./in)
A11	N/A	0.655	0.660
A12	0.758	0.733	0.730
A13	0.695	0.710	0.713
A21	0.707	0.721	0.729
A22	0.803	0.765	0.775
A23	0.719	0.678	0.698
B11	0.659	0.683	0.654
B12	0.808	0.684	0.624
B13	0.715	0.675	0.654
B21	0.724	0.743	0.745
B22	0.770	0.735	0.725
B23	0.668	0.699	0.673
C11	N/A	0.878	0.849
C12	0.817	0.802	0.785
C13	0.798	0.751	0.722
C21	0.691	0.702	0.671
C22	0.692	0.639	0.665
C23	N/A	0.991	0.943

N/A : Erroneous deflection measurement. G_F values cannot be determined based on Load-Deflection data.

CHAPTER 6

SUMMARY, CONCLUSIONS AND RECOMMENDATIONS

6.1 Summary and Conclusions

A test program designed for determination of the mechanical and fracture properties of high strength concrete is proposed herein. High strength concretes with compressive strengths ranging from 6000 psi to 12000 psi were used. Important material properties such as Young's Modulus, tensile strength and complete softening curve, fracture energy are some of the parameters studied.

In testing high strength concrete, the interaction of the testing machine and the specimen is critical due to high brittleness of high strength concrete. To obtain stable post peak responses during compression, tension and beam tests, suitable rates of loading as well as a good choice of feedback control are very crucial. In this study, better testing techniques, such as use of special grips for tension test, and use of a circumferential extensometer gage in compression tests enabled successful determination of the material's softening properties.

The complete post peak response obtained from direct uniaxial tension tests for high strength concrete reveals significant drops in the compliance of stress-crack opening curves as the compressive strength increases. It is observed that the fracture energy and tensile strength of high strength concrete increases as the compressive strength increases, but the increase is not proportional. Fracture energy obtained in this study is found to be about 35% higher than that in normal strength concrete and, is seen to reach a constant value for f'_c = 9000 to 12000 psi range concrete (see Figure 6.1). It will be of interest to

study whether or not the fracture energy will change for a much higher compressive strength concrete than those studied here (i.e., higher than 12,000 psi)

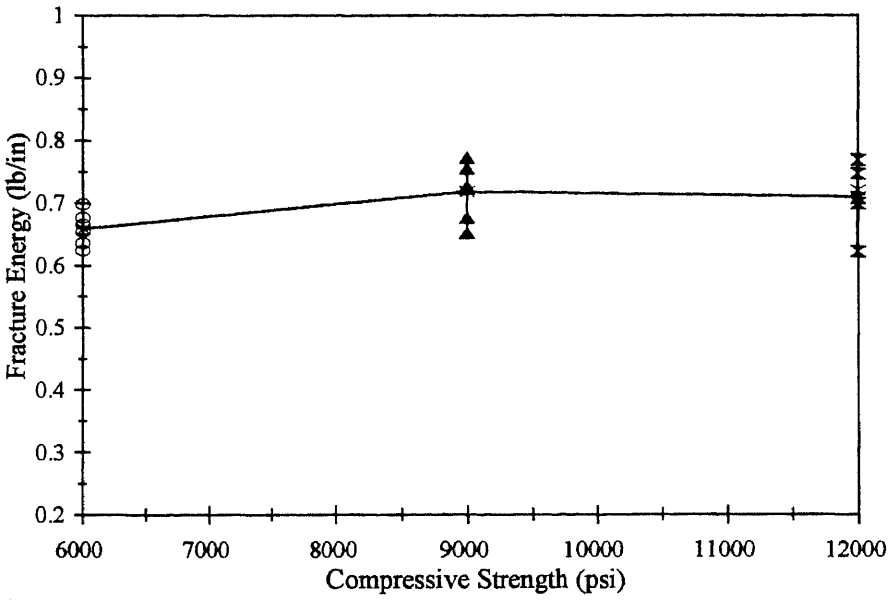

Figure 6.1 Fracture Energy of Concrete versus Compressive Strength

Using the experimental results, a new relationship for tensile stress as a function of crack opening displacement is developed. In Figure 6.2, the new relationships for the three different compressive strengths HSC is shown. Existing models developed mainly for normal strength concretes are also shown for comparison.

A simpler and efficient finite element model based on the Fictitious Crack Model concept (discrete method) is developed using commercially available ABAQUS computer program. To model the crack propagation and frictional effects at the tip of initial crack, non-linear spring elements are defined (pre-inserted). The spring element properties are defined with high initial stiffness with post tensile strength-crack width

properties as per the exact shape of the tensile softening curve obtained from experiments. It is shown that this model is able to predict successfully the test data of load-deflection and load-CMOD of beam tests with good accuracy. Test data of other researchers are also matched satisfactorily. A key observation from this study is that the shape of the softening curve plays a significant role affecting the flexural strength, size of process zone, the shapes of post peak load-deflection and, load-CMOD responses. The FEM model is capable of handling an intermediate size beam (2500+ elements) efficiently. The complete analysis takes only about 20 minutes. This is attributed to the superior method of solution strategy used in the FEM analysis. RIKS modified algorithm is found to be very efficient. Also, this FEM model does not require any topology updating.

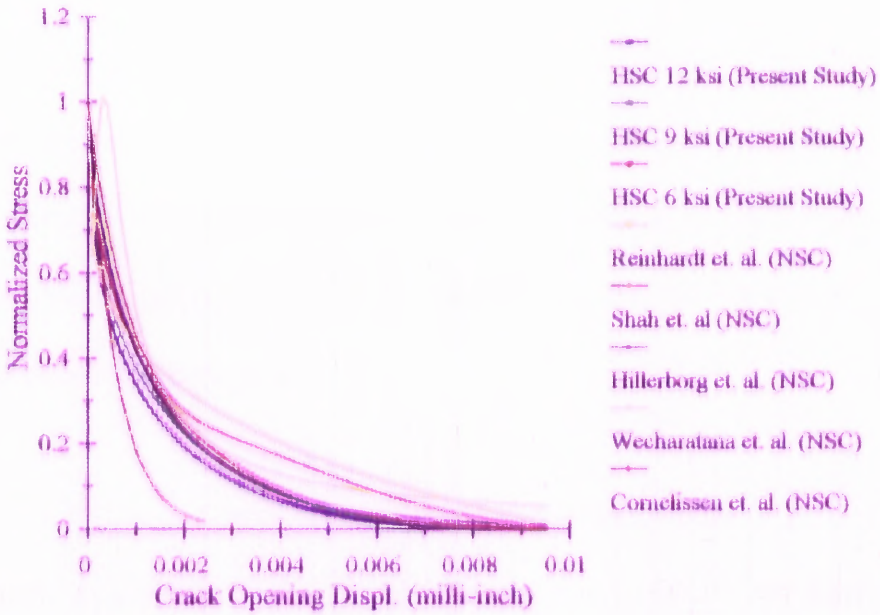

Figure 6.2 Comparison of the Tension Softening Model of Present Study with Existing Softening Models developed for Normal Strength Concrete.

Survey of experimental results available in literature on fracture tests reveals that a large number of tests have been carried out in which the deflection measurements have often included the crushing of concrete at supports (includes extraneous deformation). This problem although not recently discovered, has not been taken into consideration. In this study, an alternative means of calculating the fracture energy of concrete based on the load-CMOD response is developed. It is found that better estimates of the fracture energy can be obtained by using the load-CMOD response. Based on the experimental results of this study, it is found that sizes of test specimen is important when considering suitable beam size for testing. It is also found that specimens with span to depth ratio of four are easy to handle and produce more accurate results. The test results also have lesser scatter (in particular shape of load-CMOD and load -deflection responses) as compared to the RILEM beam test results. The RILEM beam, having a span to depth ratio of eight, is found to be difficult to handle especially due to its relatively high self weight. In this study, the fracture energy of high strength concrete was obtained from two test methods. It is important to note that in both cases, all data consist of complete load-deflection responses. Incomplete information on the responses affects the computed fracture energy values.

6.2 Recommendation for Future Work

1. Influence of shear stresses on crack propagation in beams are often neglected in many models (including the present model). It will be an interesting investigation to determine the relationship of normal and shear stresses as a function of crack opening displacement experimentally.

2. It was found in this study, that the finite element models based on fictitious crack model concepts are more successful predicting load-deflection than the load-CMOD responses. A more detailed investigation of this issue may help resolve the matter and improve modeling.
3. The experimental setups developed in this study can be easily be extended to test higher compressive strength concrete such as $f'_c > 12{,}000$ psi.

APPENDIX

EXPERIMENTAL DATA

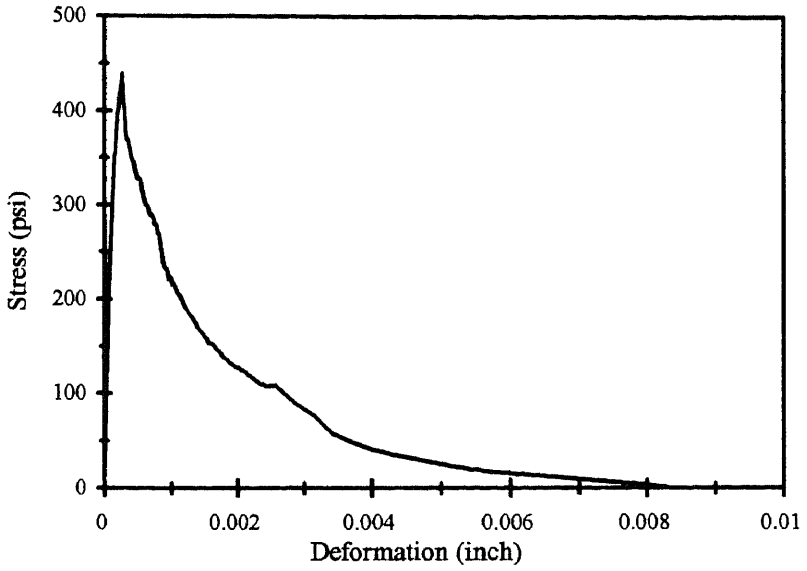

Figure A.1a Stress - Deformation Curve for HSC -A (Specimen A1)

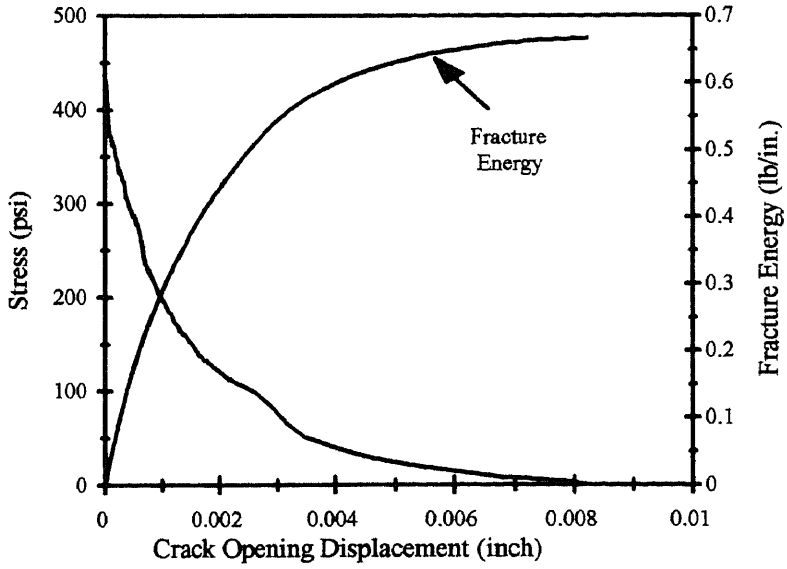

Figure A.1b Stress - Separation Curve and Fracture Energy for HSC-A (Specimen A1)

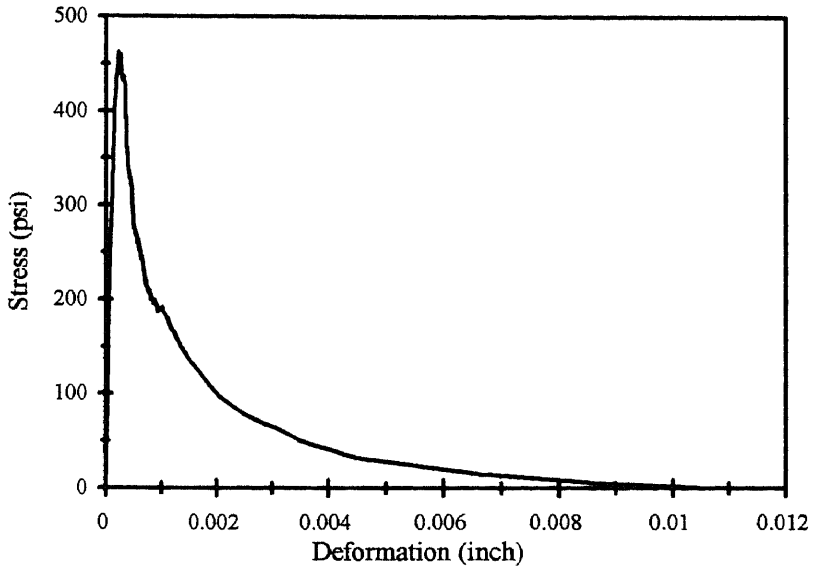

Figure A.2a Stress - Deformation Curve for HSC -A (Specimen A2)

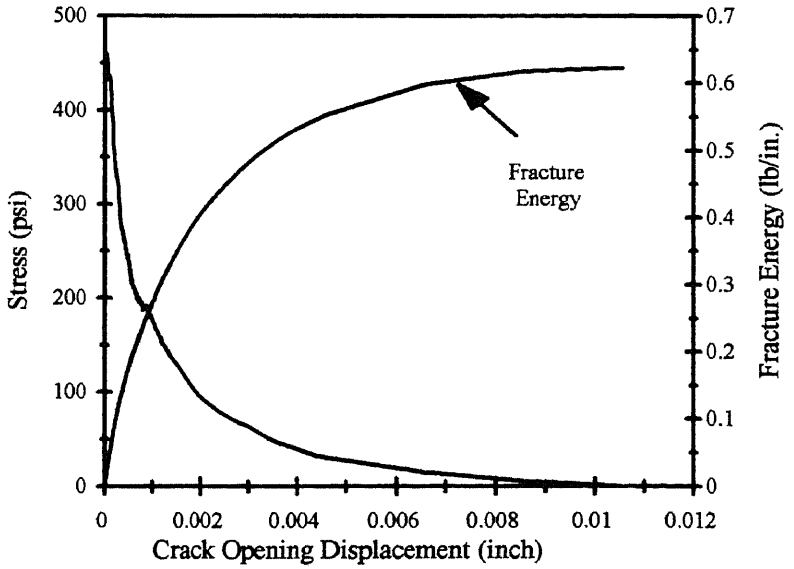

Figure A.2b Stress - Separation Curve and Fracture Energy for HSC-A (Specimen A2)

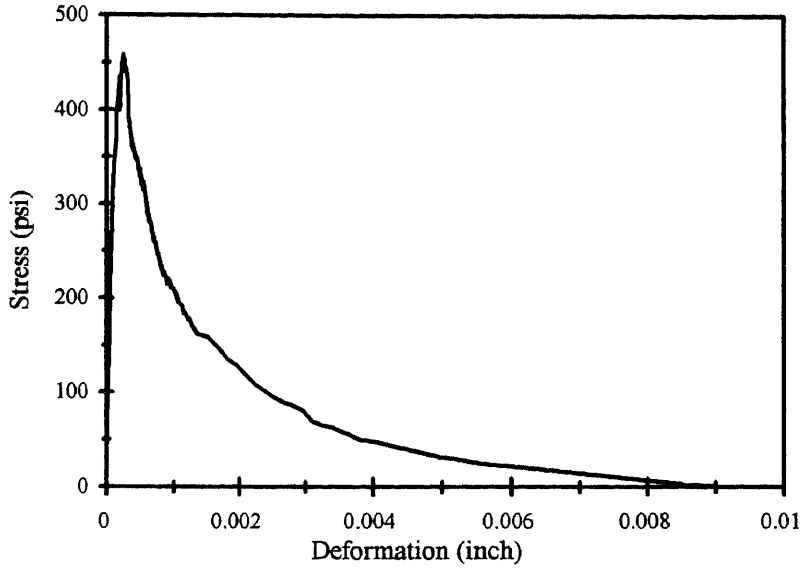

Figure A.3a Stress - Deformation Curve for HSC -A (Specimen A3)

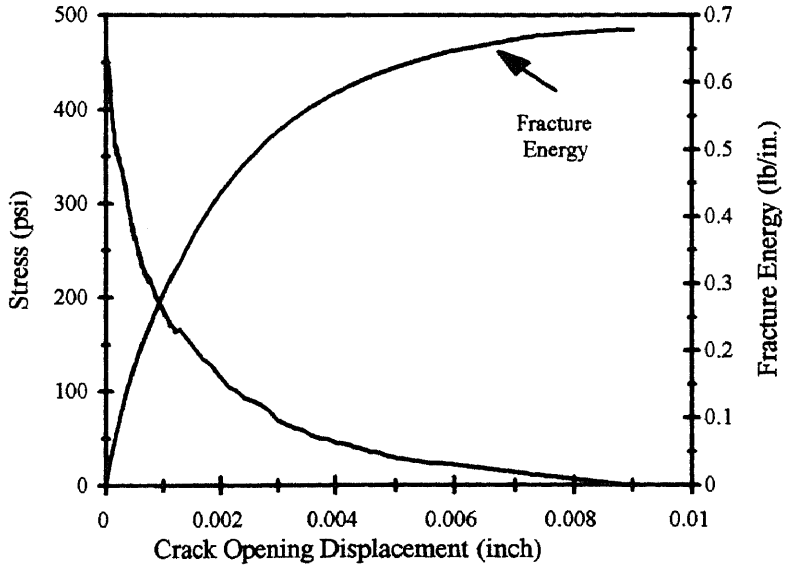

Figure A.3b Stress - Separation Curve and Fracture Energy for HSC-A (Specimen A3)

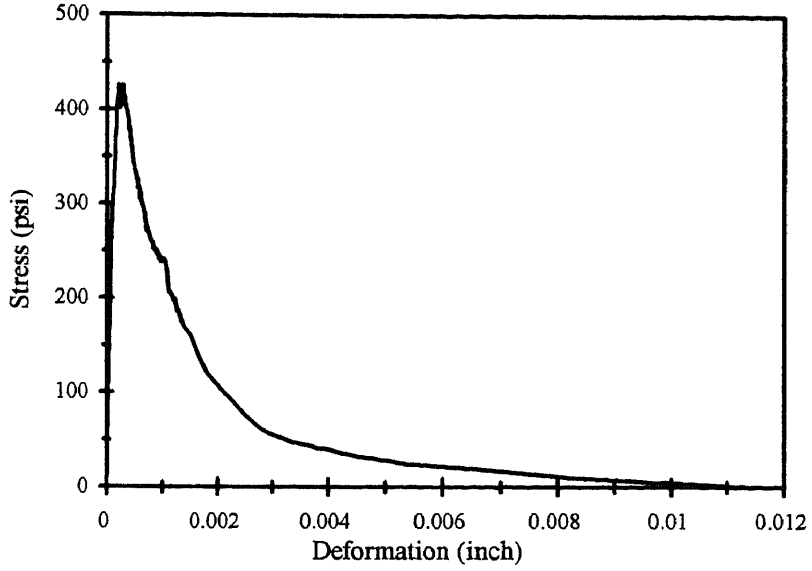

Figure A.4a Stress - Deformation Curve for HSC -A (Specimen A4)

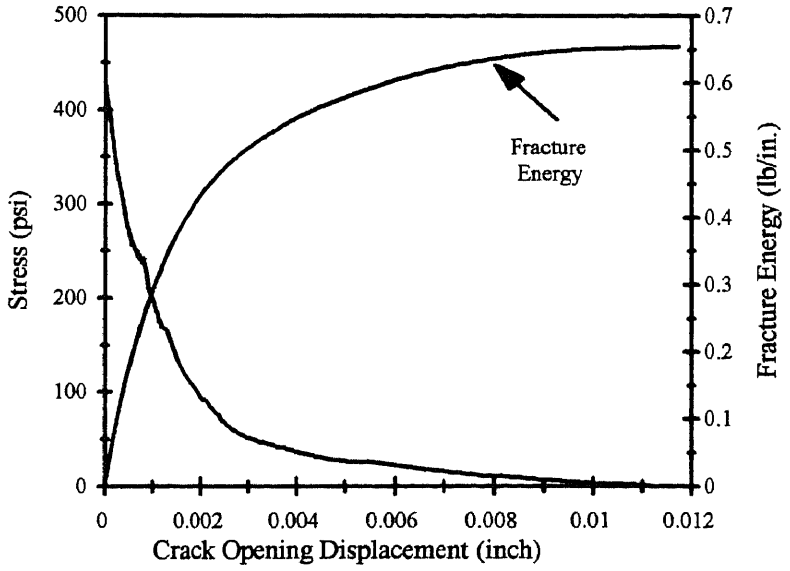

Figure A.4b Stress - Separation Curve and Fracture Energy for HSC-A (Specimen A4)

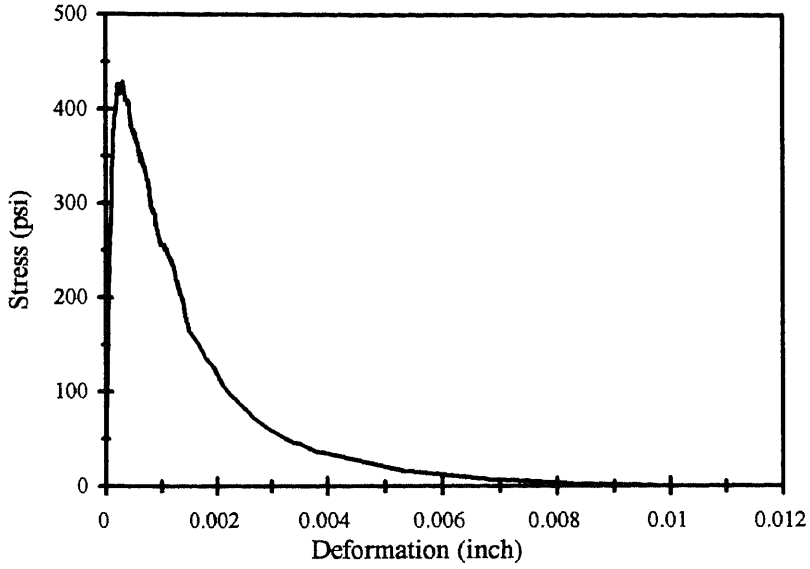

Figure A.5a Stress - Deformation Curve for HSC -A (Specimen A5)

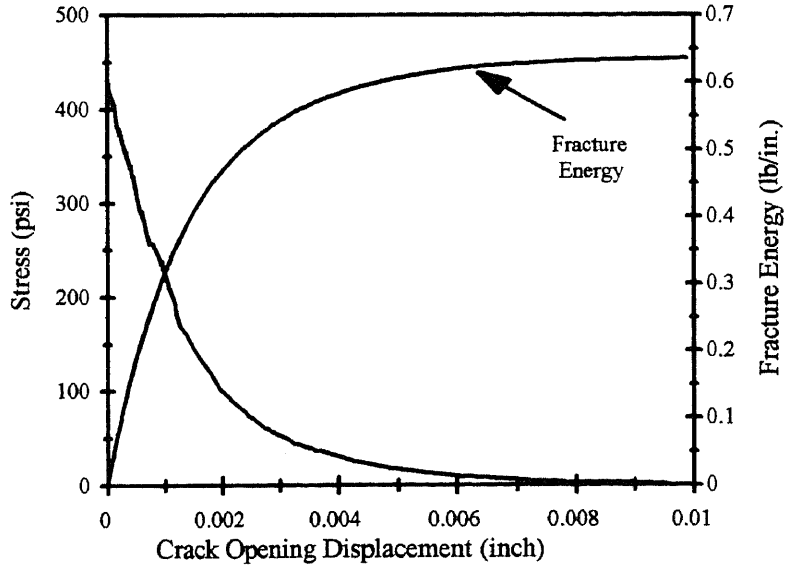

Figure A.5b Stress - Separation Curve and Fracture Energy for HSC-A (Specimen A5)

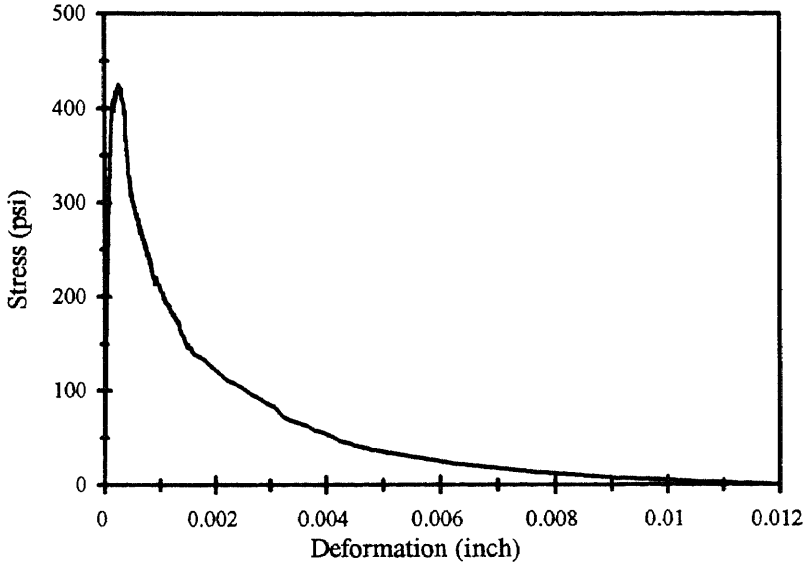

Figure A.6a Stress - Deformation Curve for HSC -A (Specimen A6)

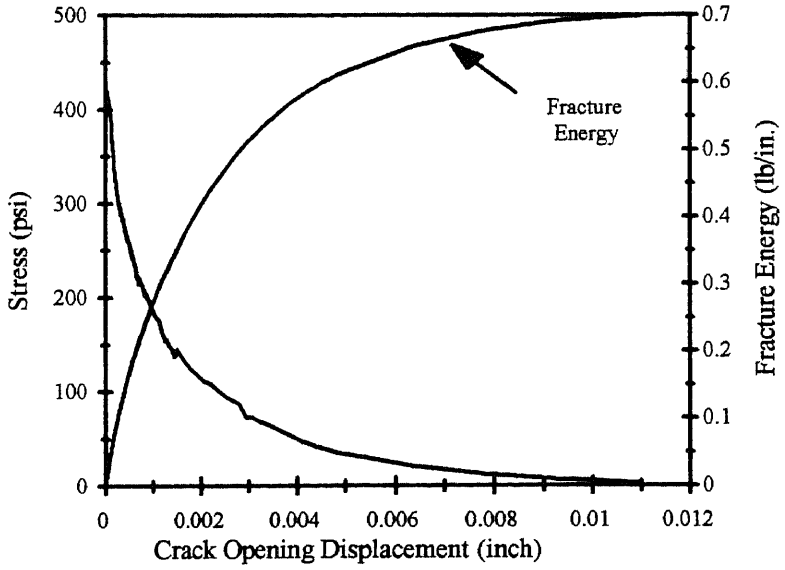

Figure A.6b Stress - Separation Curve and Fracture Energy for HSC-A (Specimen A6)

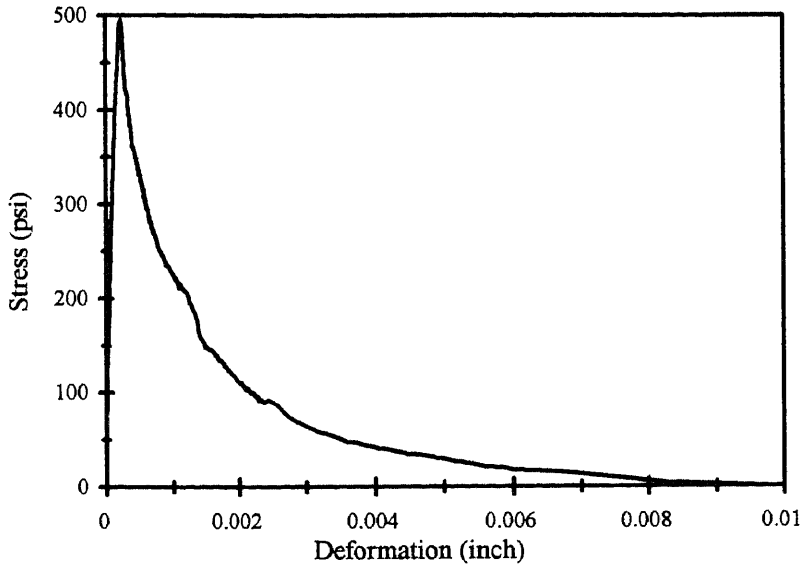

Figure B.1a Stress - Deformation Curve for HSC -B (Specimen B1)

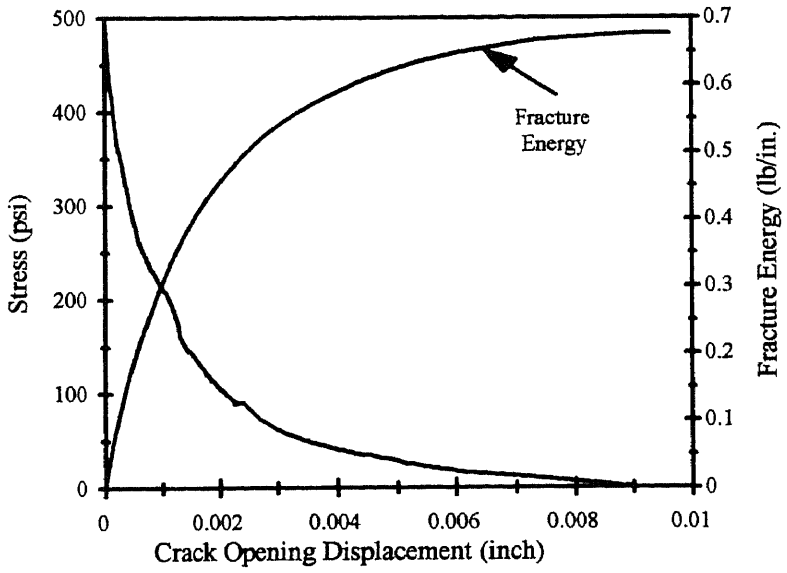

Figure B.1b Stress - Separation Curve and Fracture Energy for HSC-B (Specimen B1)

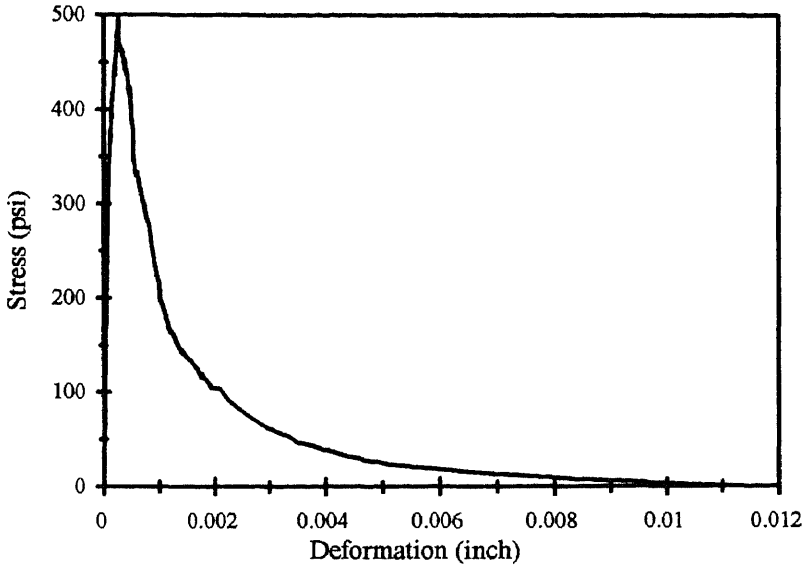

Figure B.2a Stress - Deformation Curve for HSC -B (Specimen B2)

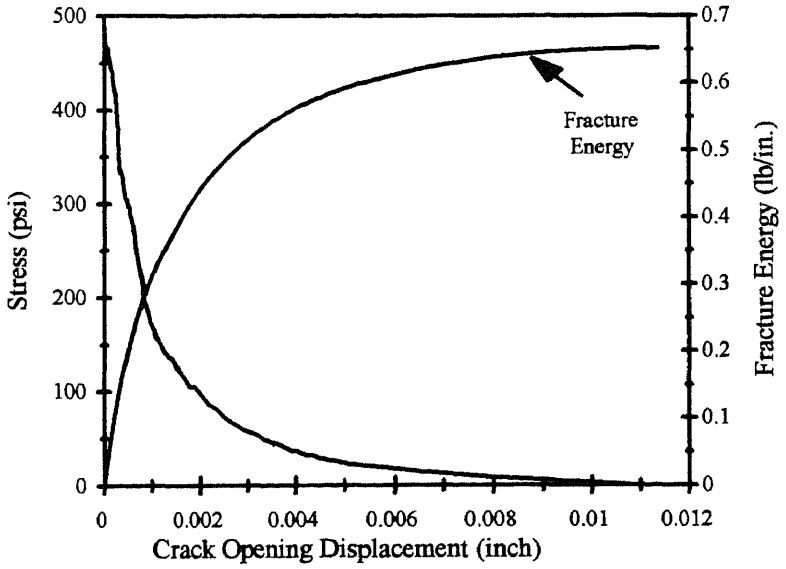

Figure B.2b Stress - Separation Curve and Fracture Energy for HSC-B (Specimen B2)

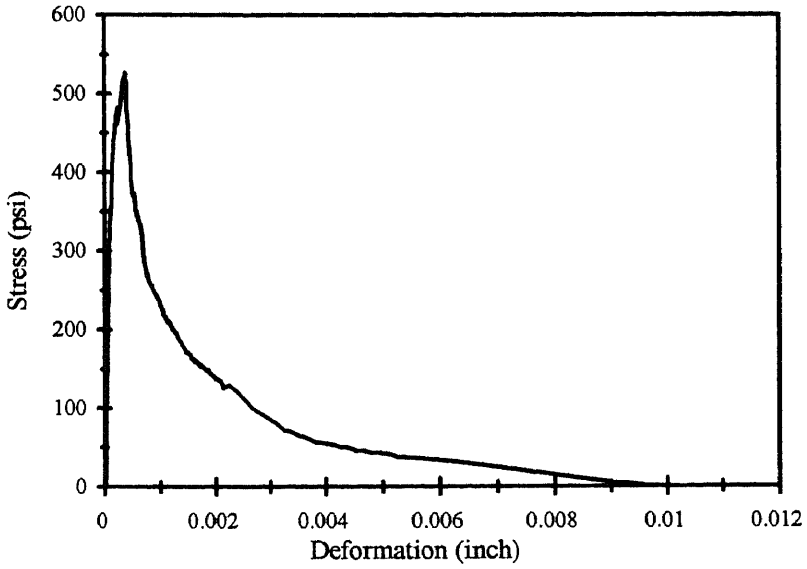

Figure B.3a Stress - Deformation Curve for HSC -B (Specimen B3)

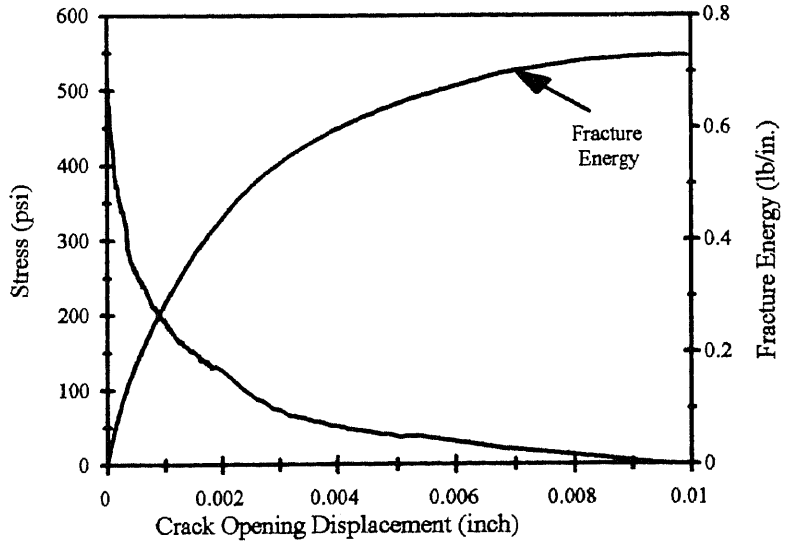

Figure B.3b Stress - Separation Curve and Fracture Energy for HSC-B (Specimen B3)

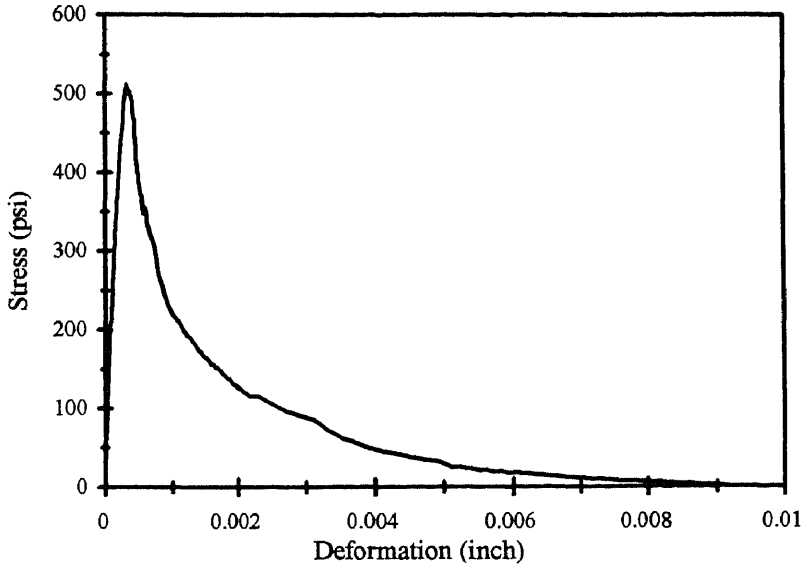

Figure B.4a Stress - Deformation Curve for HSC -B (Specimen B4)

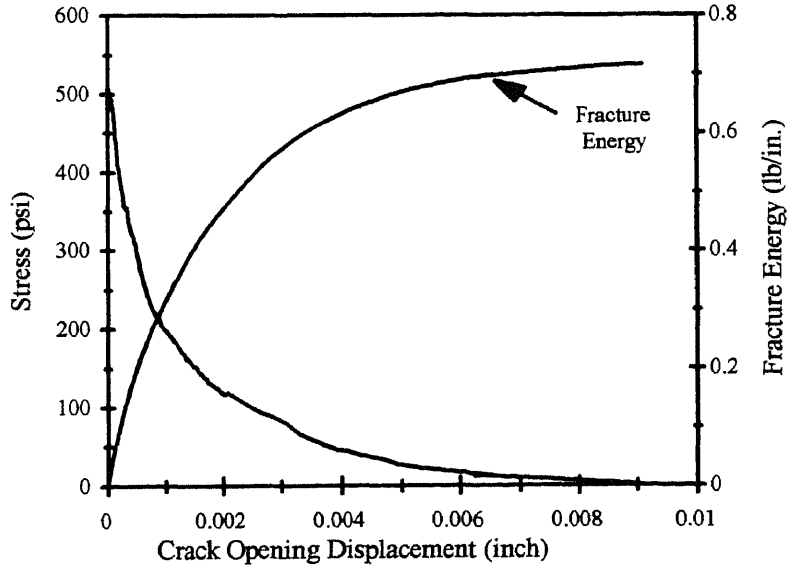

Figure B.4b Stress - Separation Curve and Fracture Energy for HSC-B (Specimen B4)

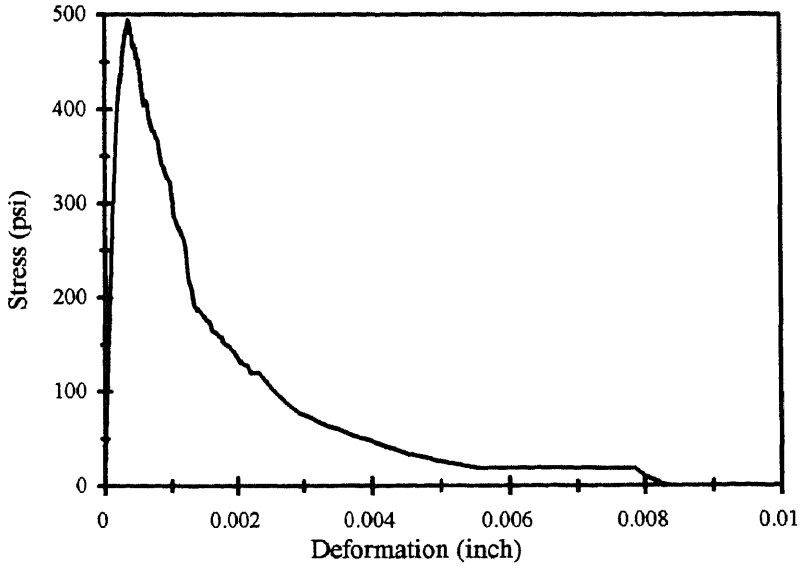

Figure B.5a Stress - Deformation Curve for HSC -B (Specimen B5)

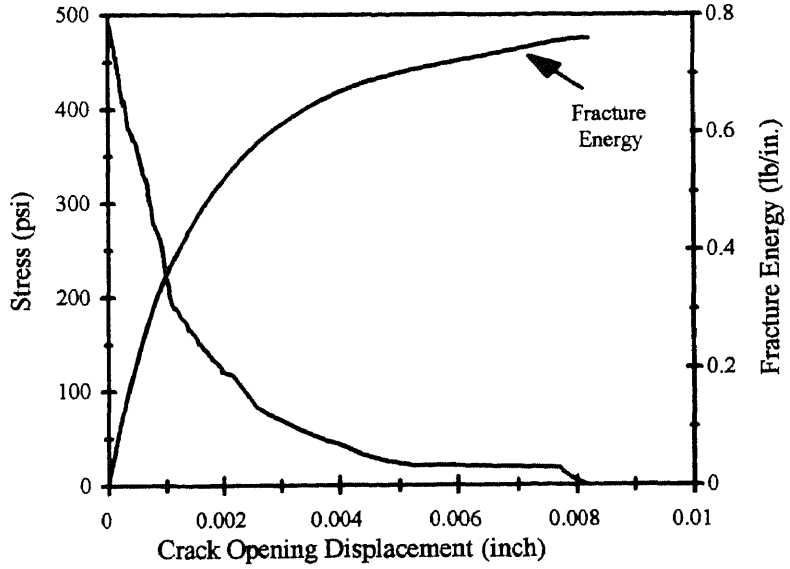

Figure B.5b Stress - Separation Curve and Fracture Energy for HSC-B (Specimen B5)

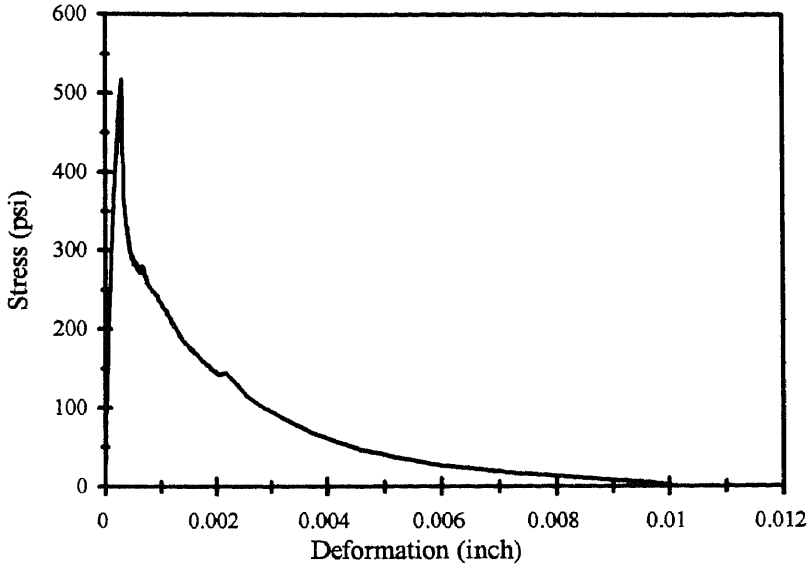

Figure B.6a Stress - Deformation Curve for HSC -B (Specimen B6)

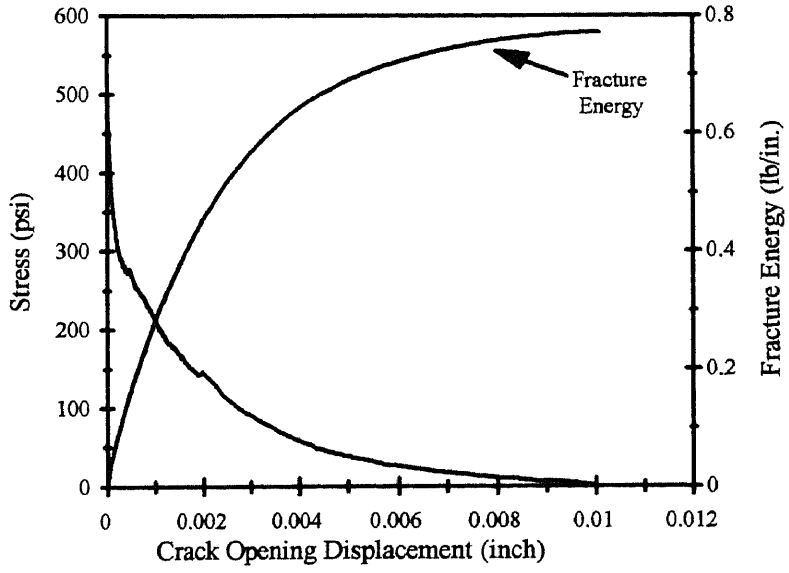

Figure B.6b Stress - Separation Curve and Fracture Energy for HSC-B (Specimen B6)

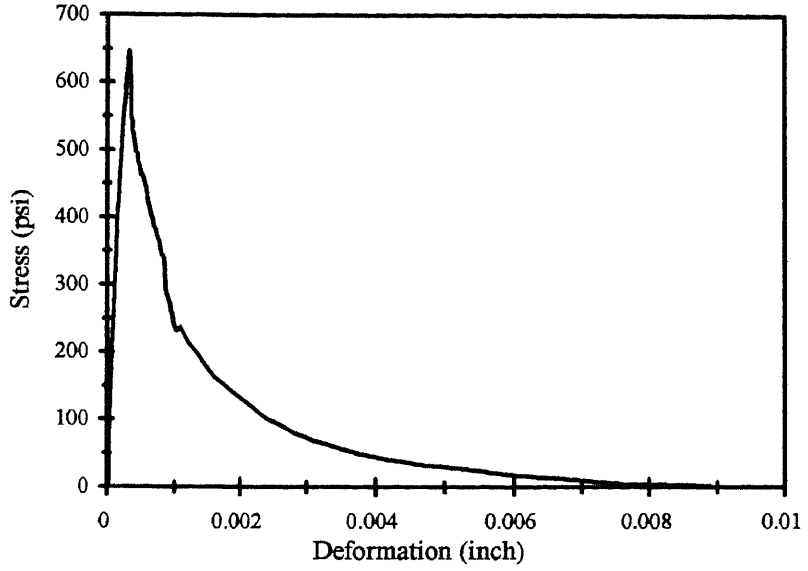

Figure C.1a Stress - Deformation Curve for HSC - C (Specimen C1)

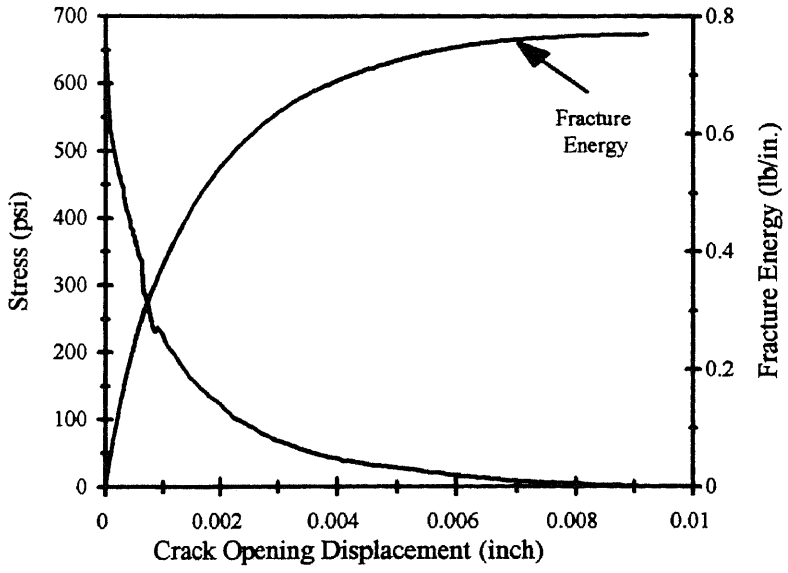

Figure C.1b Stress - Separation Curve and Fracture Energy for HSC-C (Specimen C1)

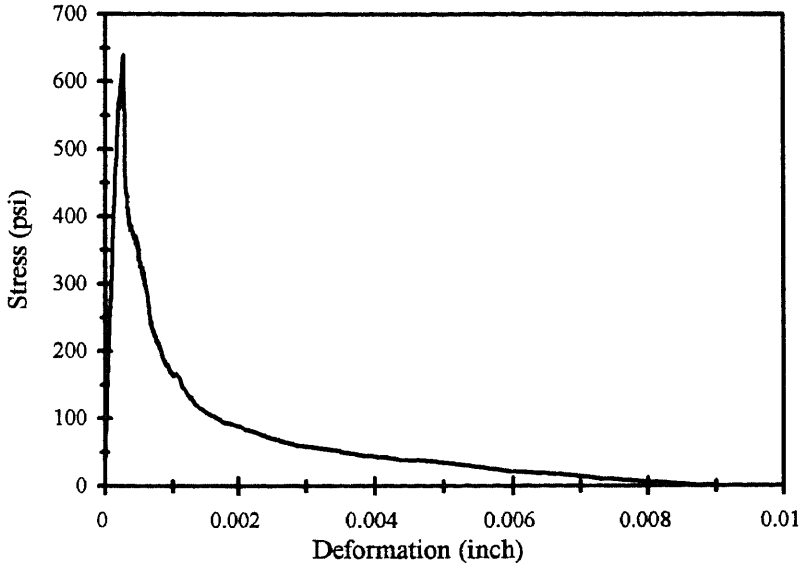

Figure C.2a Stress - Deformation Curve for HSC - C (Specimen C2)

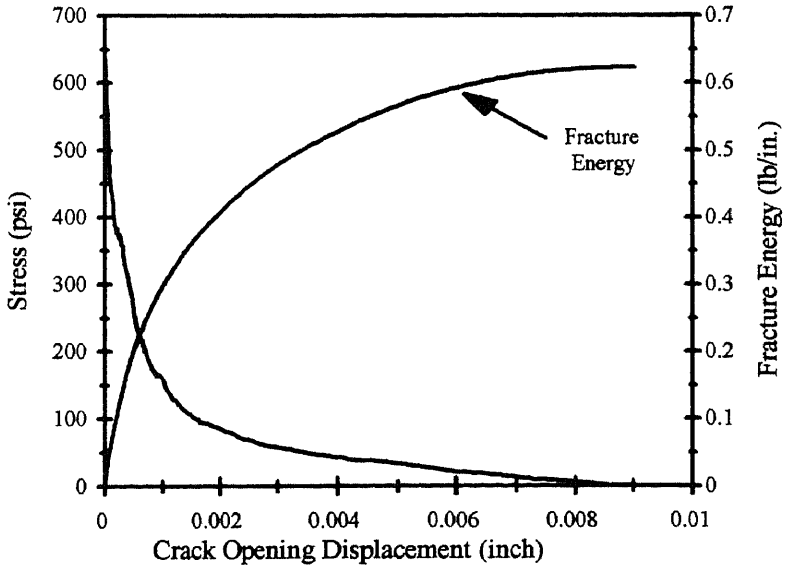

Figure C.2b Stress - Separation Curve and Fracture Energy for HSC-C (Specimen C2)

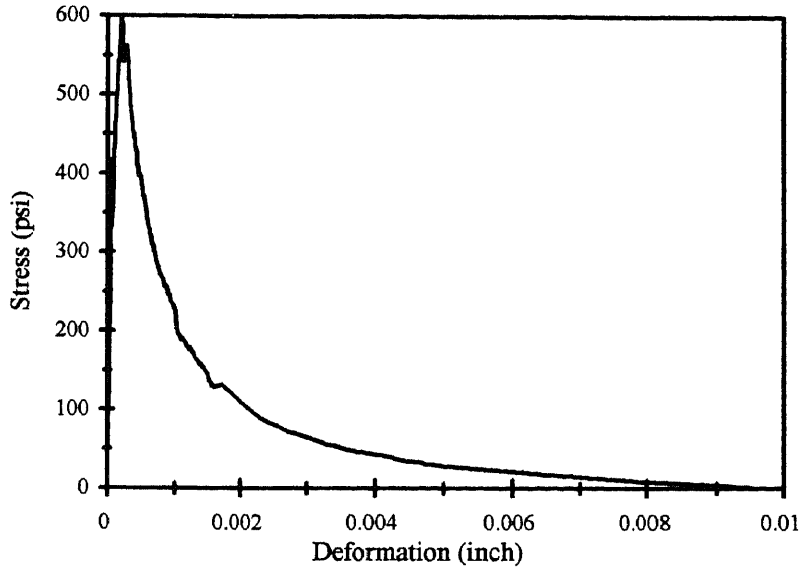

Figure C.3a Stress - Deformation Curve for HSC - C (Specimen C3)

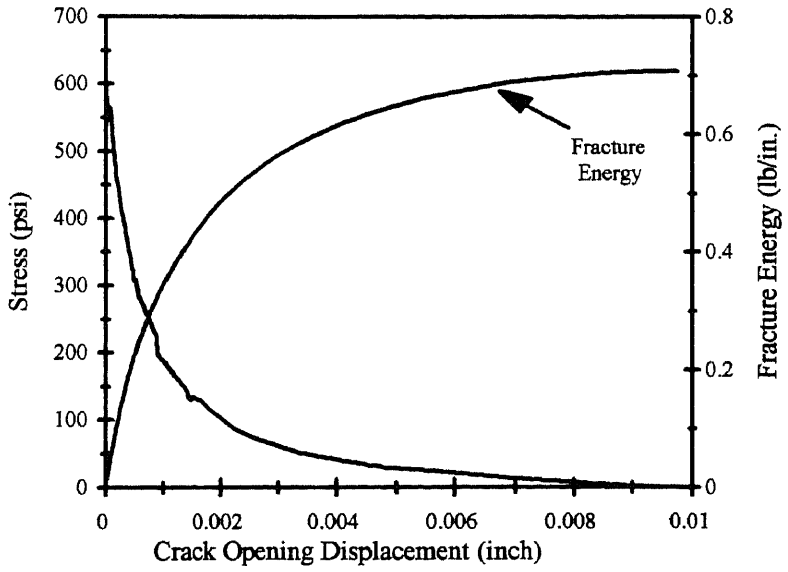

Figure C.3b Stress - Separation Curve and Fracture Energy for HSC-C (Specimen C3)

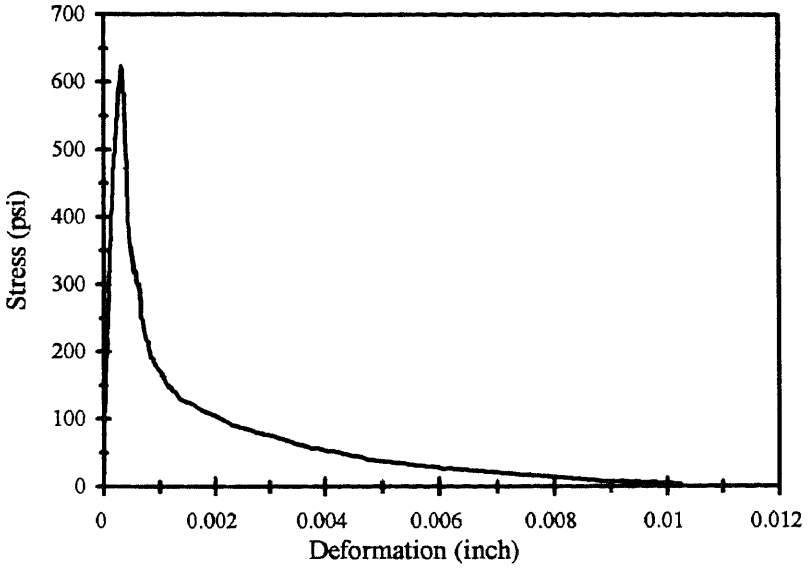

Figure C.4a Stress - Deformation Curve for HSC - C (Specimen C4)

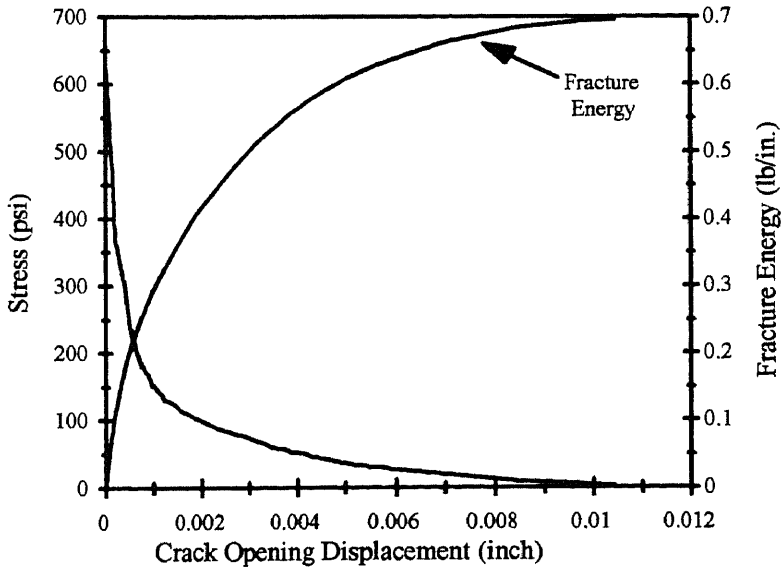

Figure C.4b Stress - Separation Curve and Fracture Energy for HSC-C (Specimen C4)

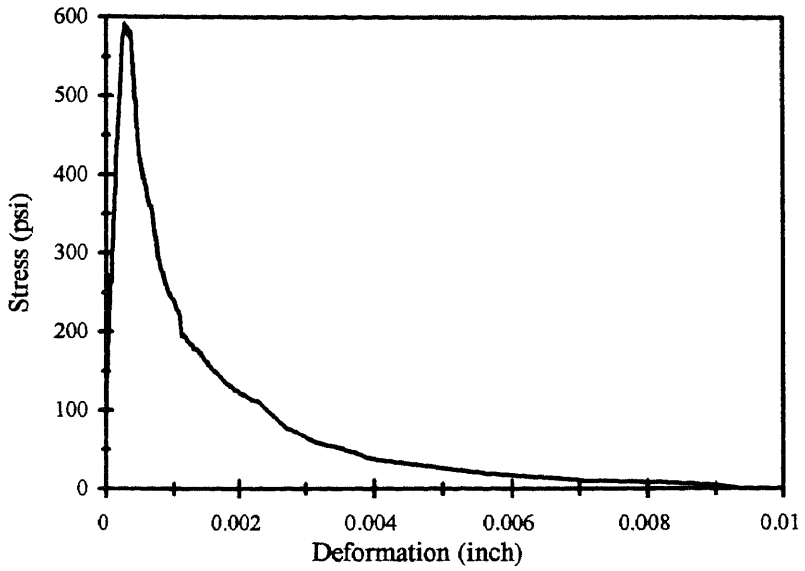

Figure C.5a Stress - Deformation Curve for HSC - C (Specimen C5)

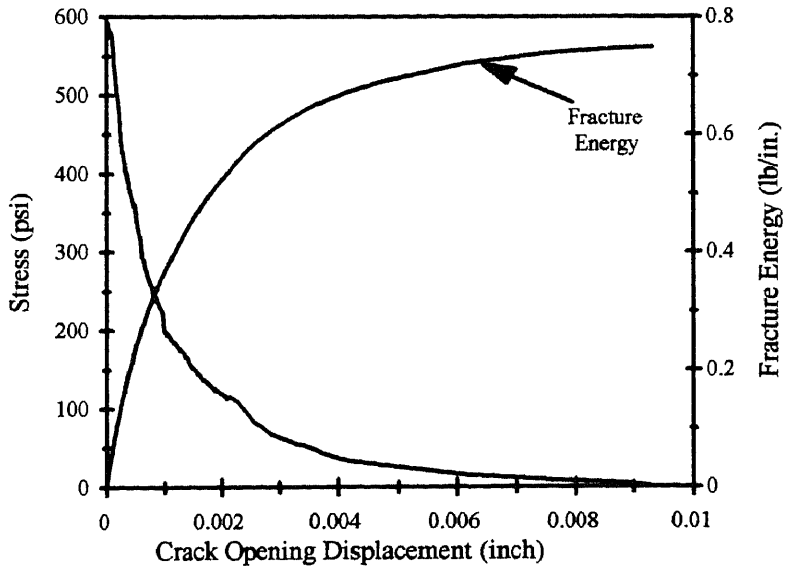

Figure C.5b Stress - Separation Curve and Fracture Energy for HSC-C (Specimen C5)

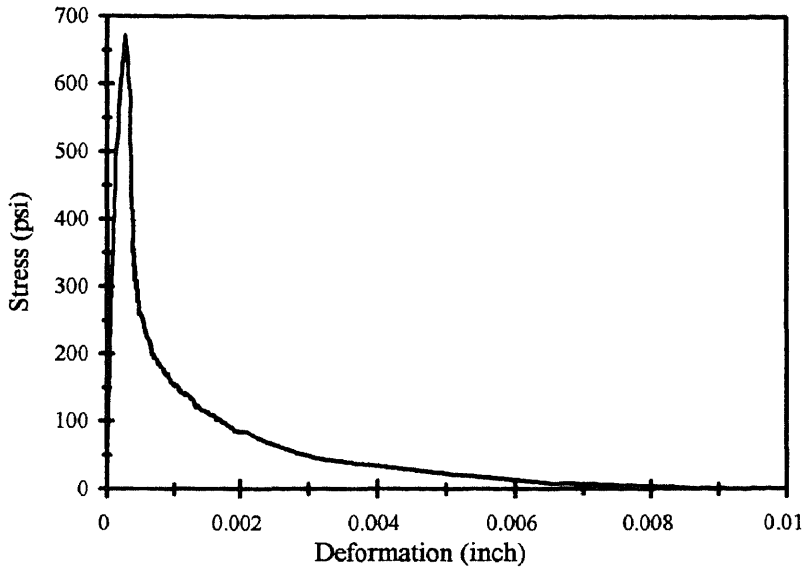

Figure C.6a Stress - Deformation Curve for HSC - C (Specimen C6)

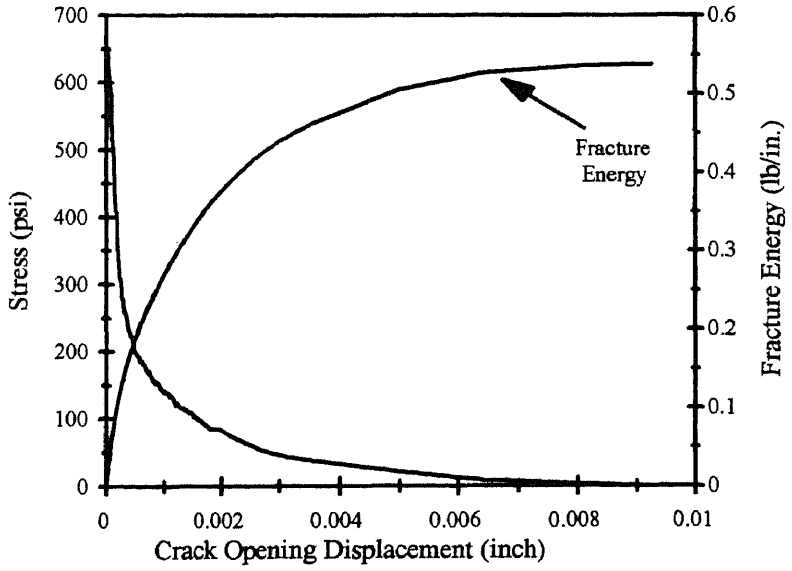

Figure C.6b Stress - Separation Curve and Fracture Energy for HSC-C (Specimen C6)

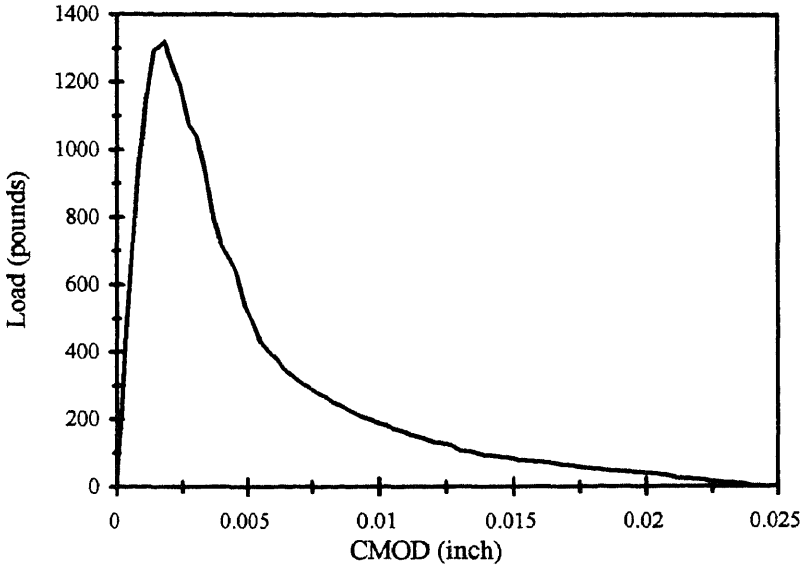

Figure D.1a Load-CMOD Response (Size A beam, Specimen A11)

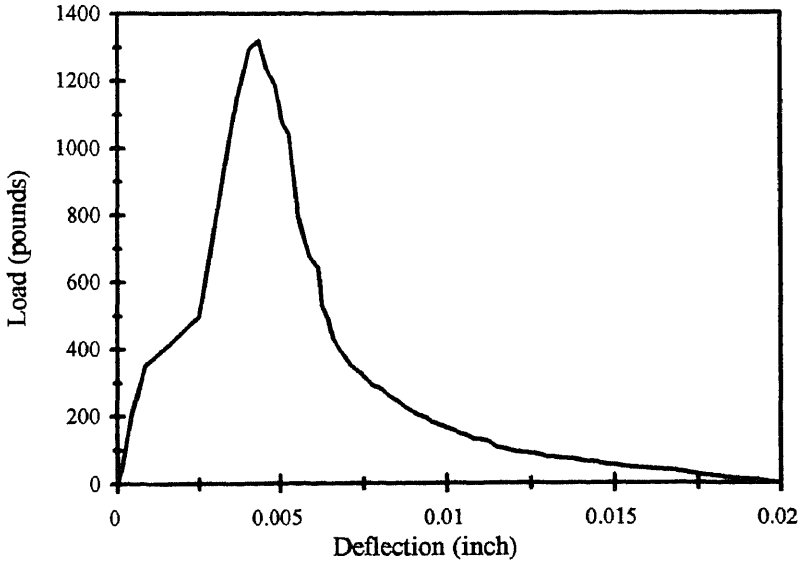

Figure D.1b Load -Deflection Response (Size A beam, Specimen A11)

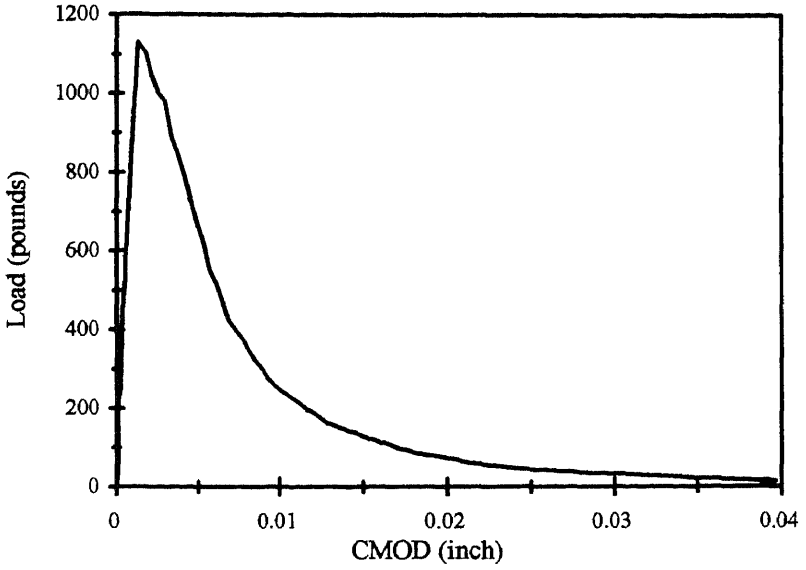

Figure D.2a Load-CMOD Response (Size A beam , Specimen A12)

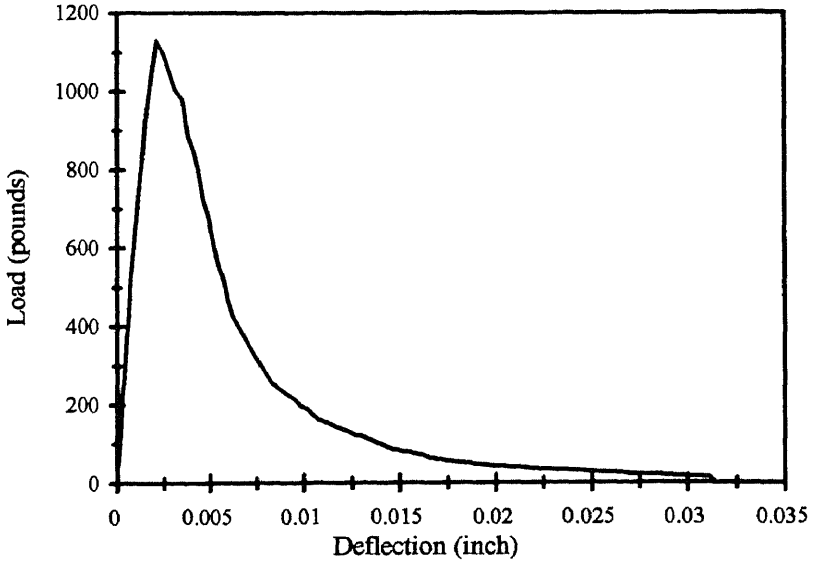

Figure D.2b Load -Deflection Response (Size A beam, Specimen A12)

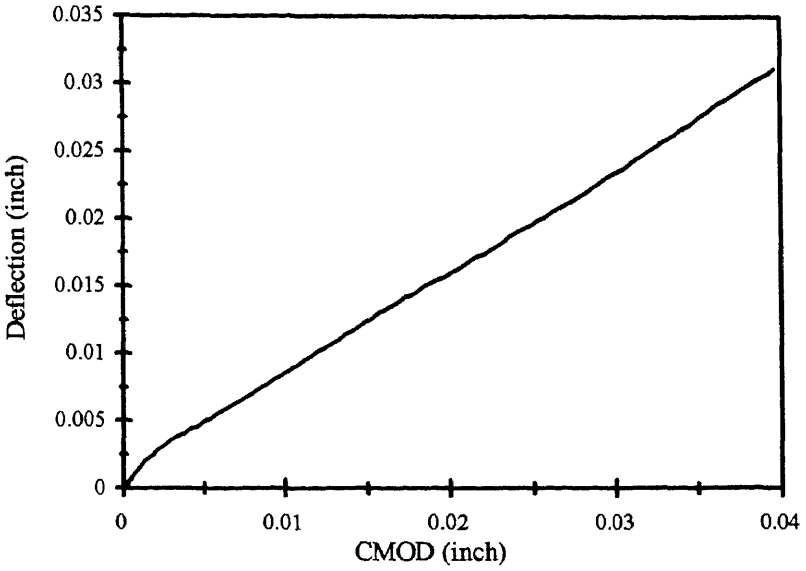

Figure D.2c CMOD-Deflection Response (Size A beam, Specimen A12)

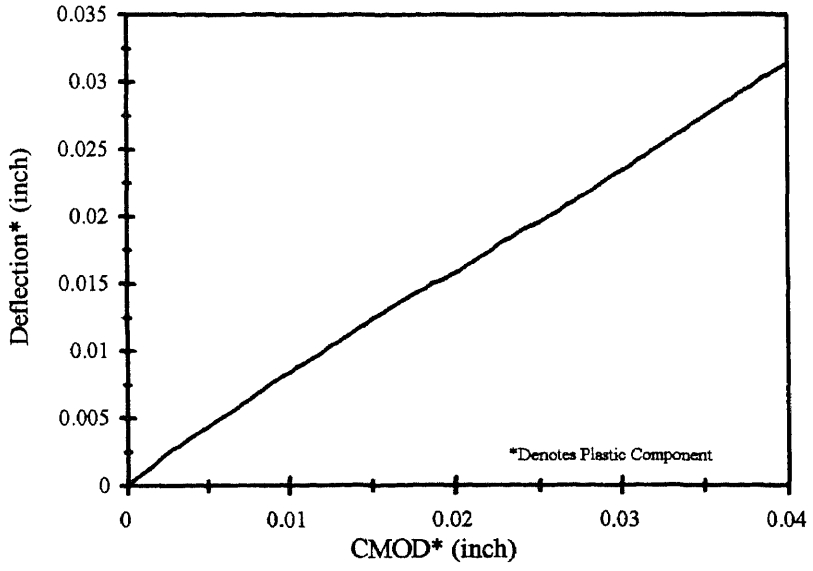

Figure D.2d Plastic Components of CMOD-Deflection Response (Size A beam, Specimen A12)

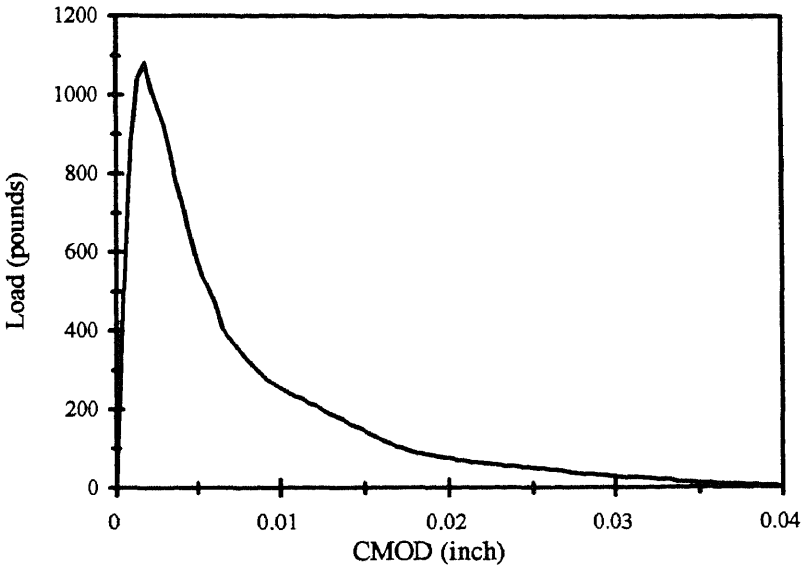

Figure D.3a Load-CMOD Response (Size A beam, Specimen A13)

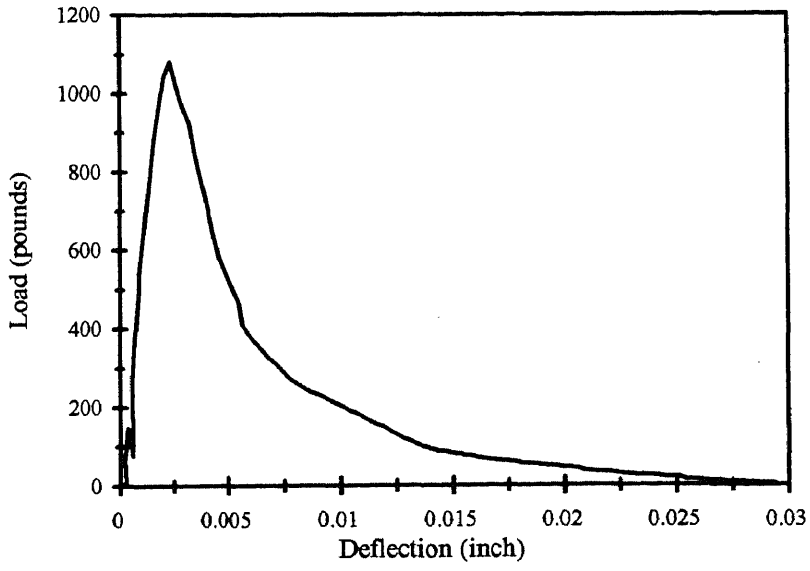

Figure D.3b CMOD-Deflection Response (Size A beam, Specimen A13)

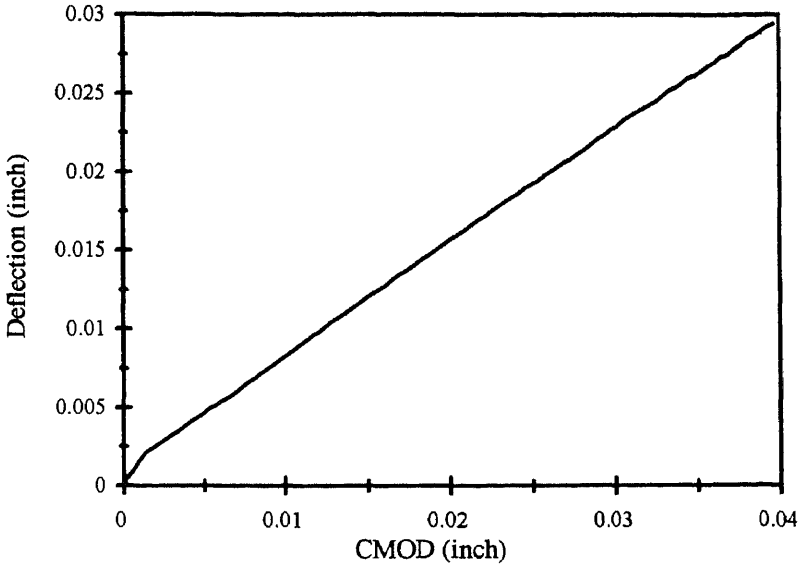

Figure D.3c CMOD-Deflection Response (Size A beam, Specimen A13)

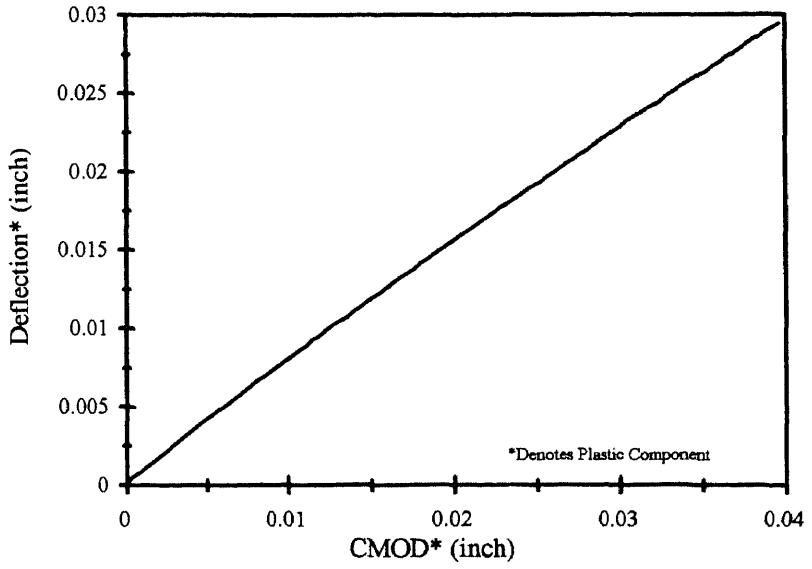

Figure D.3d Plastic Components of CMOD-Deflection Response (Size A beam, Specimen A13)

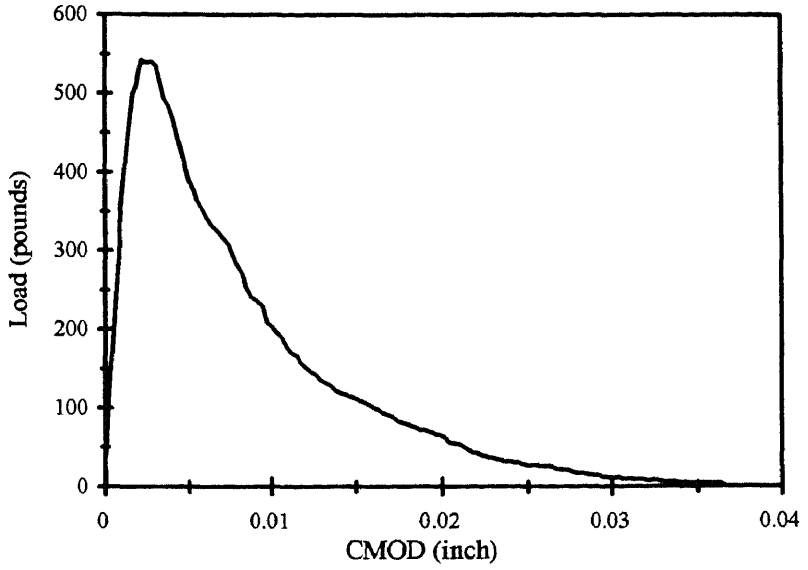

Figure D.4a Load - CMOD Response (Size A beam, Specimen A21)

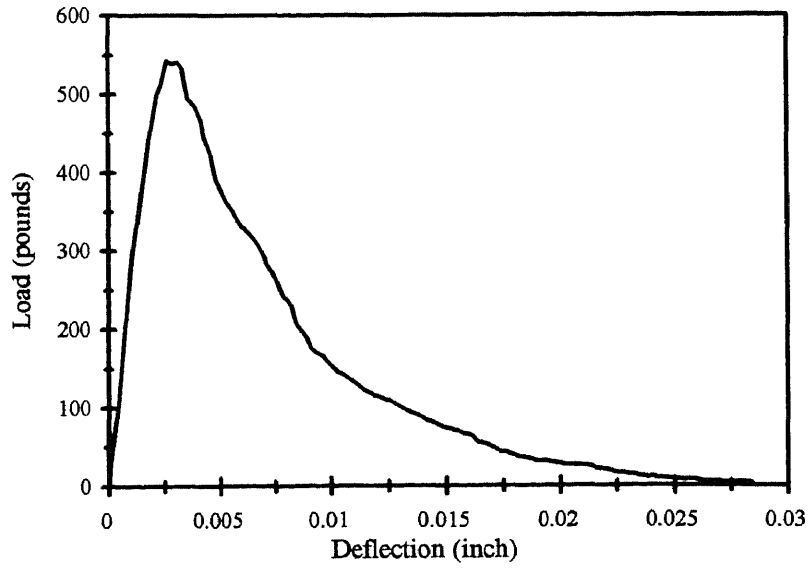

Figure D.4b Load - Deflection Response (Size A beam, Specimen A21)

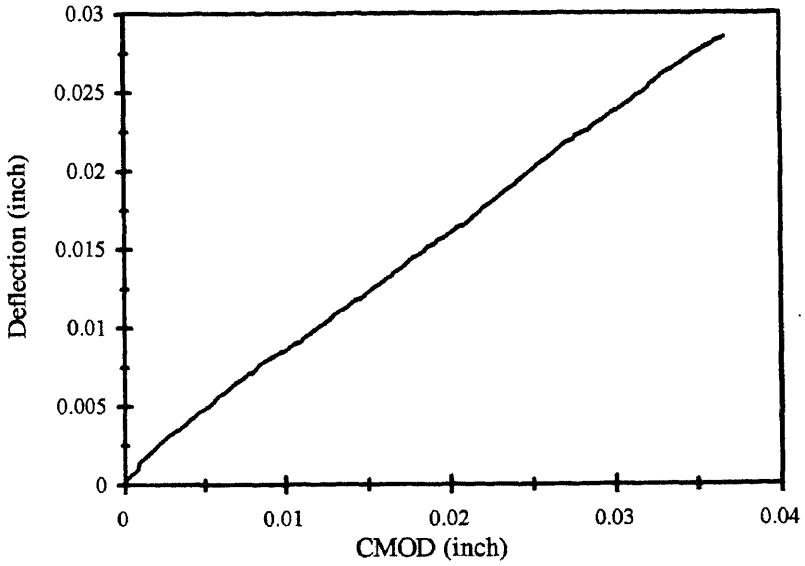

Figure D.4c CMOD-Deflection Response (Size A beam, Specimen A21)

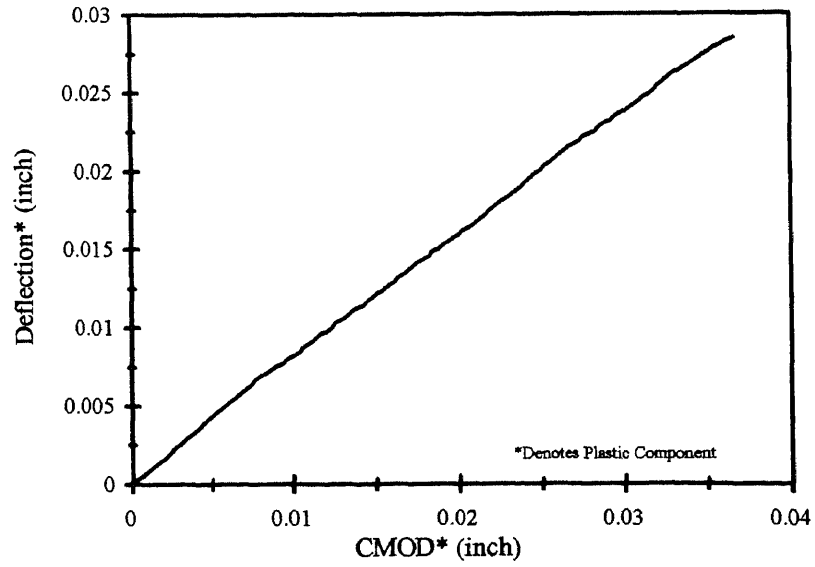

Figure D.4d: Plastic Components of CMOD-Deflection Response (Size A beam, Specimen A21)

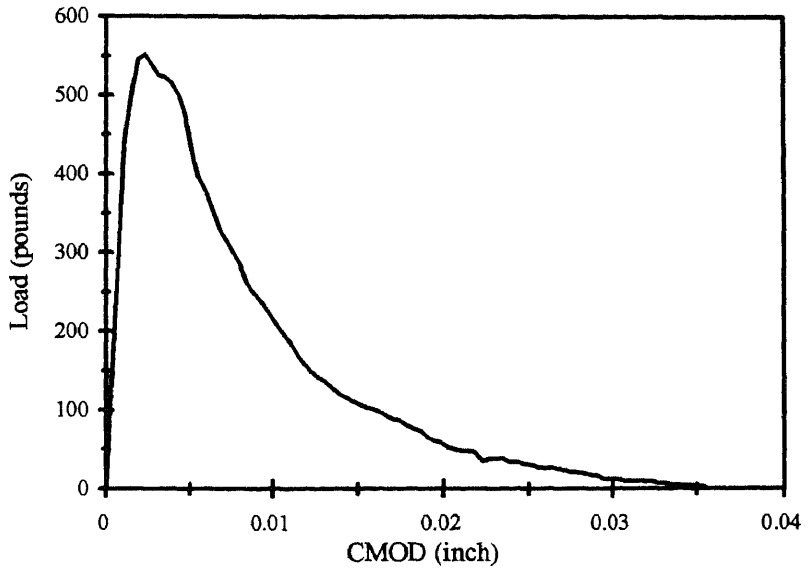

Figure D.5a Load - CMOD Response (Size A beam, Specimen A22)

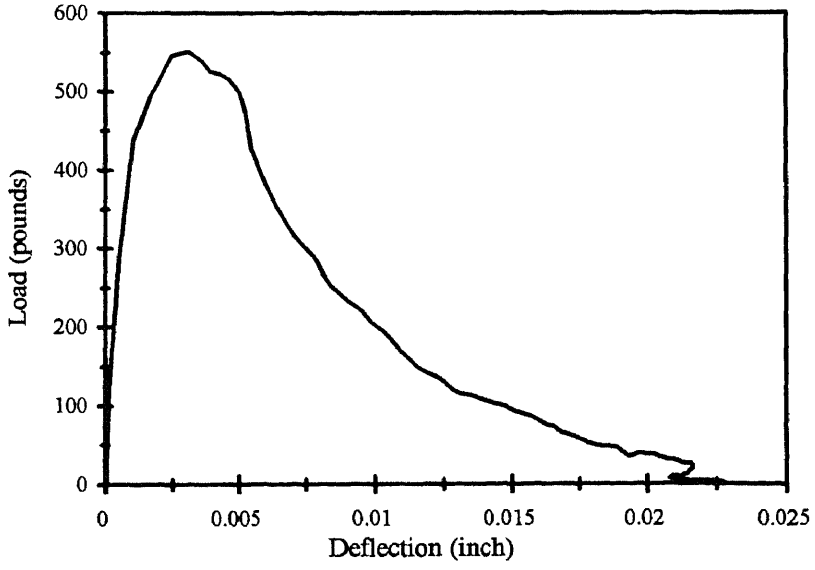

Figure D.5b Load - Deflection Response (Size A beam, Specimen A22)

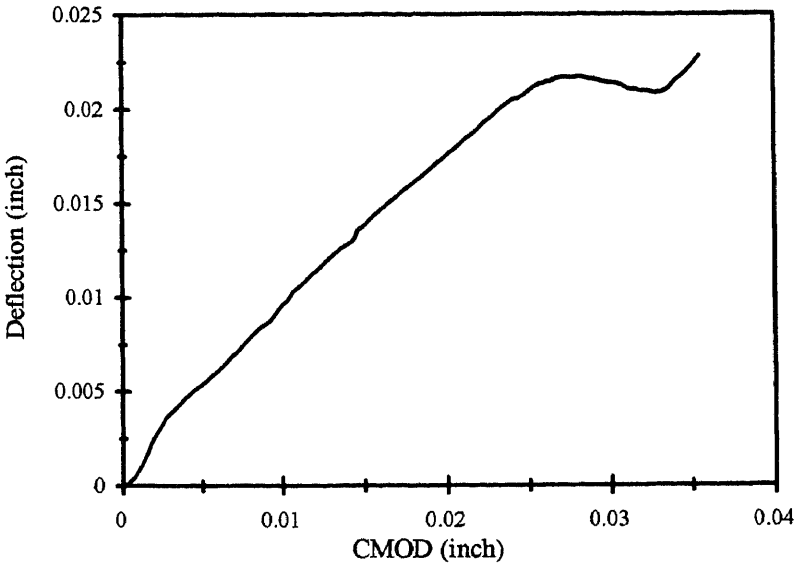

Figure D.5c CMOD-Deflection Response (Size A beam, Specimen A22)

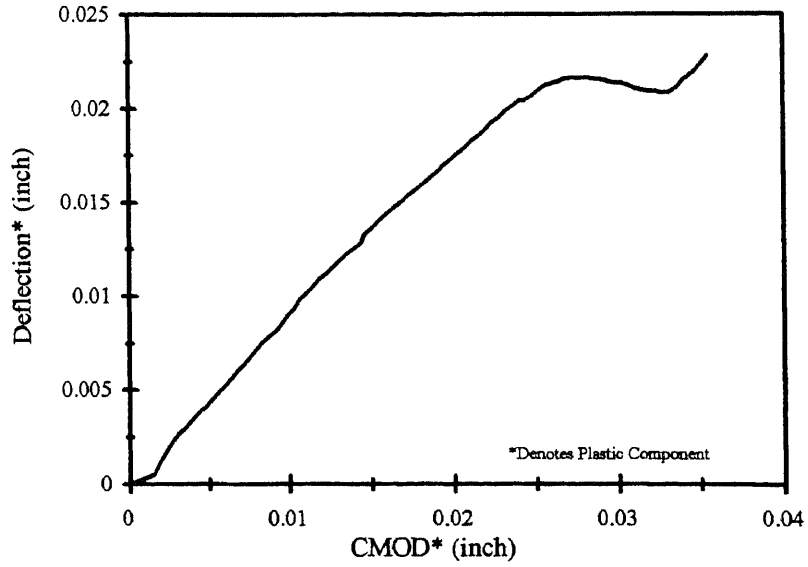

Figure D.5d Plastic Components of CMOD-Deflection Response (Size A beam, Specimen A22)

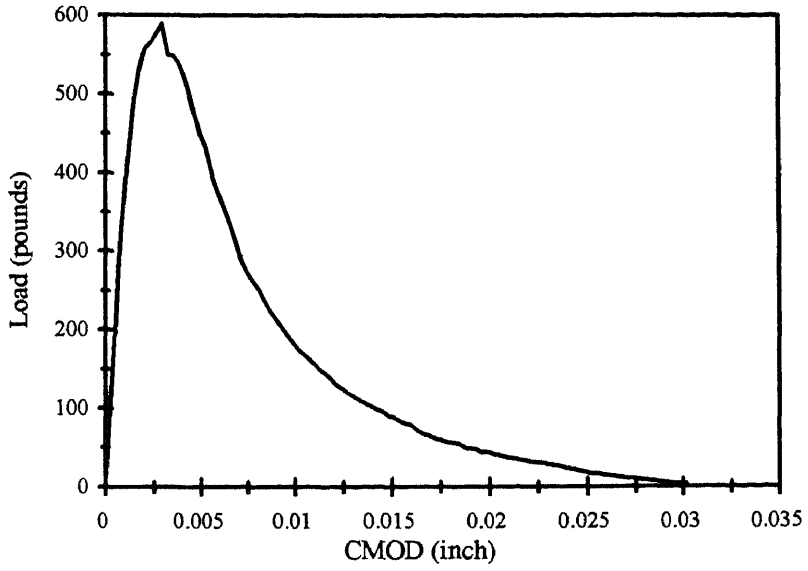

Figure D.6a Load - CMOD Response (Size A beam, Specimen A23)

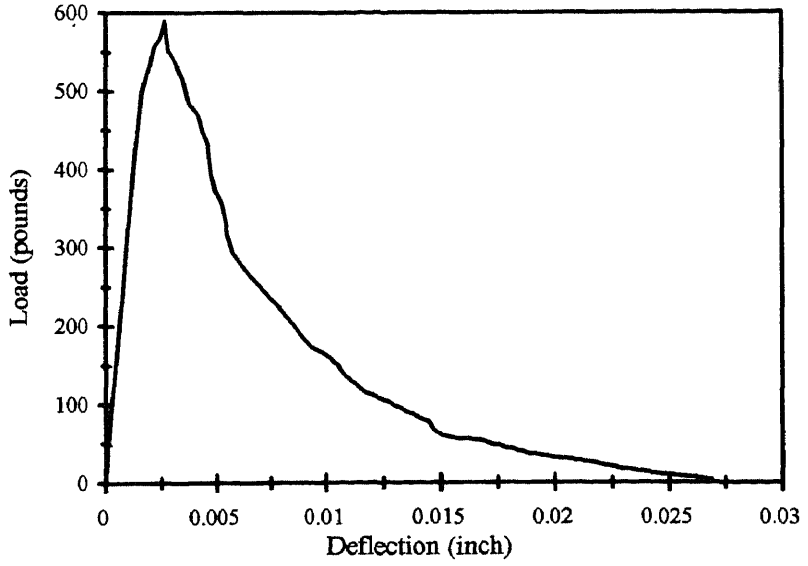

Figure D.6b Load - Deflection Response (Size A beam, Specimen A23)

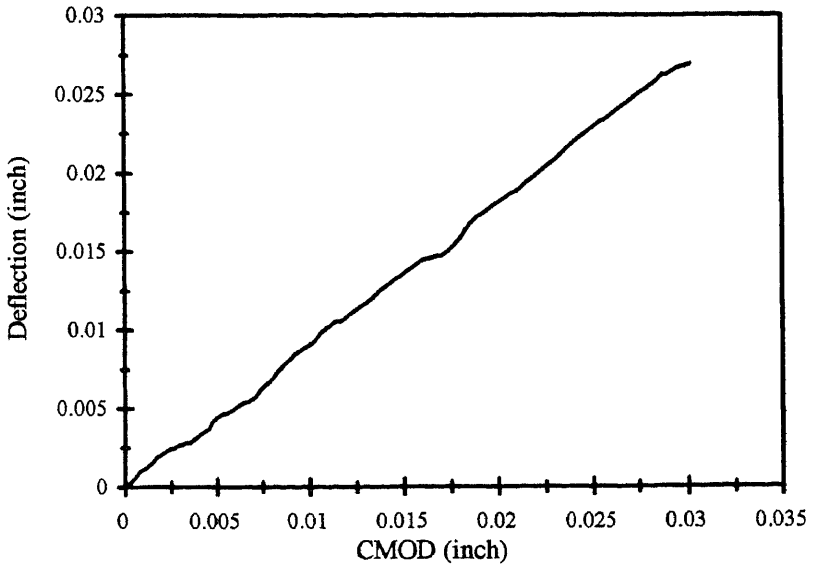

Figure D.6c: CMOD-Deflection Response (Size A beam, Specimen A23)

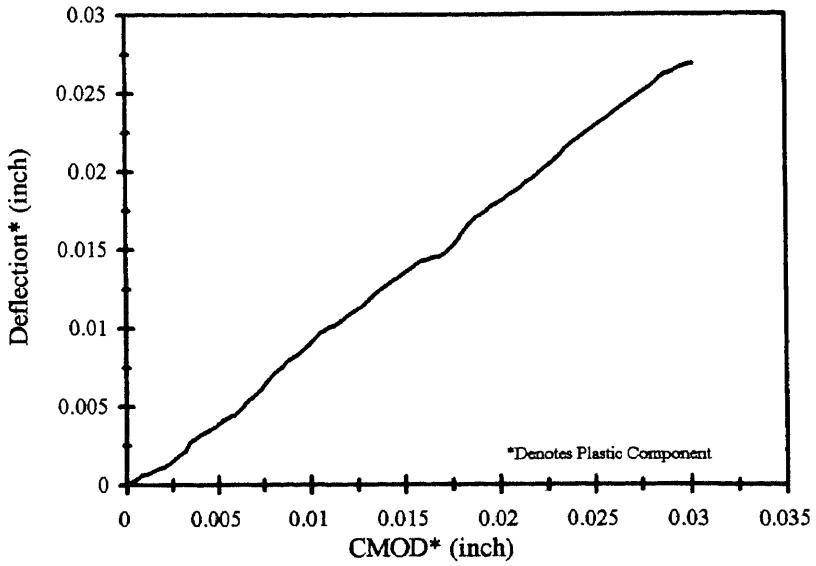

Figure D.6d Plastic Components of CMOD-Deflection Response
(Size A beam, Specimen A23)

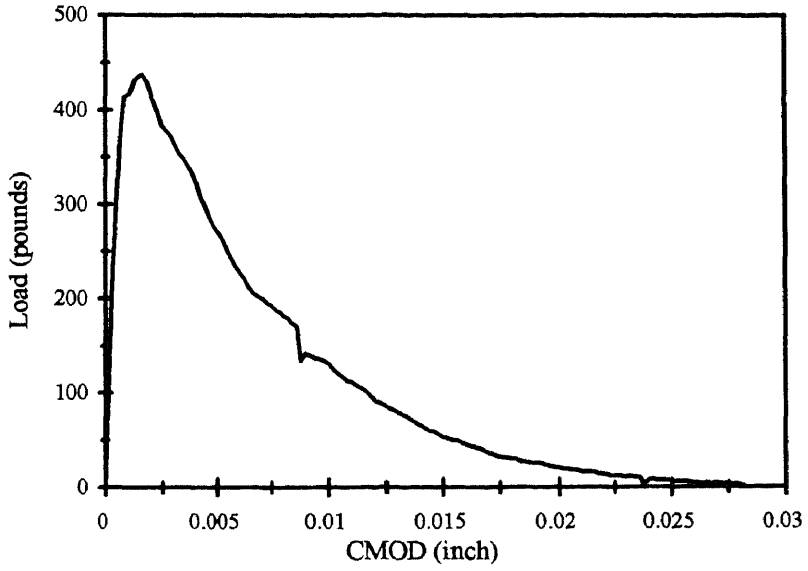

Figure E.1a Load - CMOD Response (Size B beam, Specimen B11)

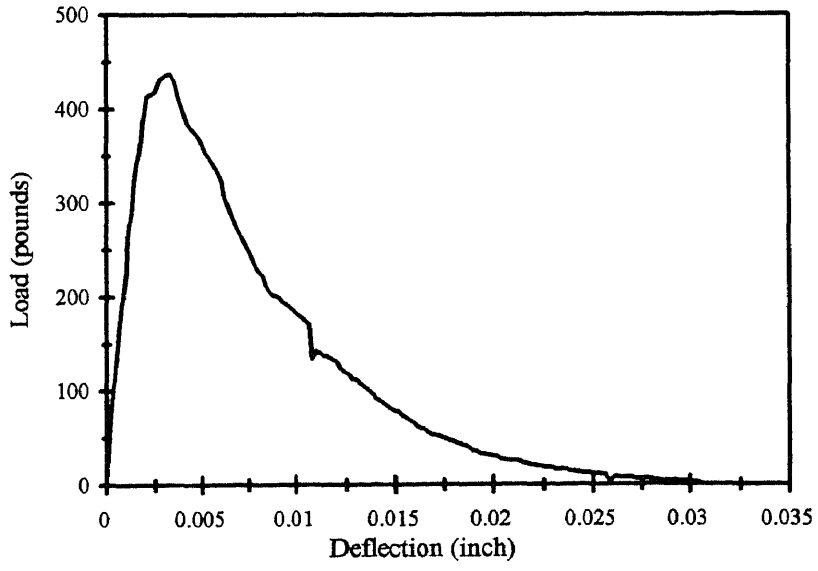

Figure E.1b Load - Deflection Response (Size B beam, Specimen B11)

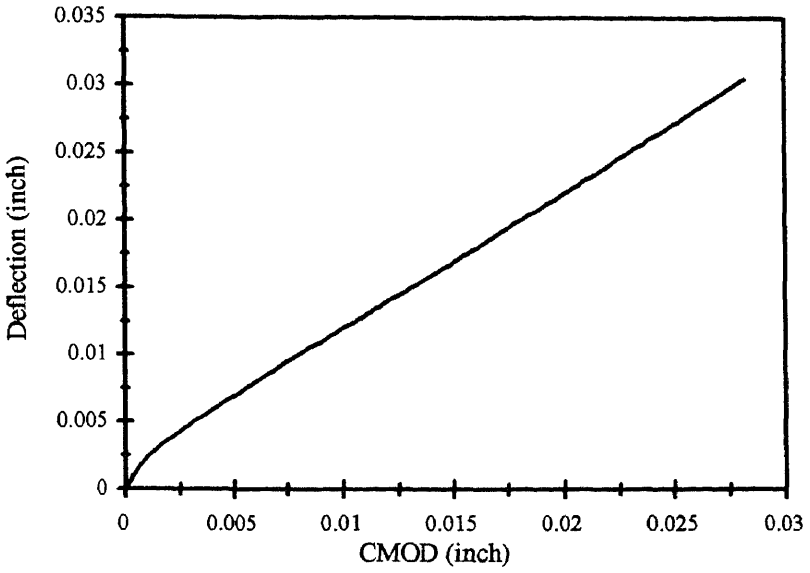

Figure E.1c CMOD-Deflection Response (Size B beam, Specimen B11)

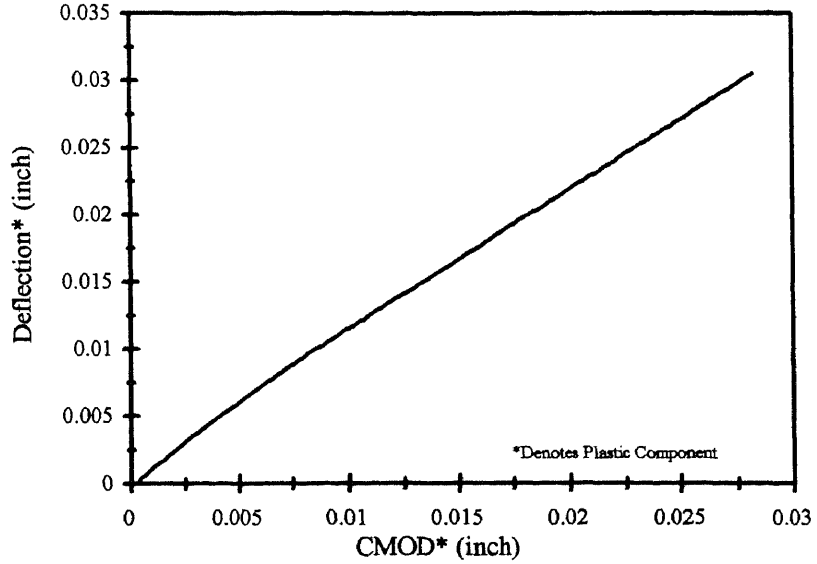

Figure E.1d Plastic Components of CMOD-Deflection Response (Size B beam, Specimen B11)

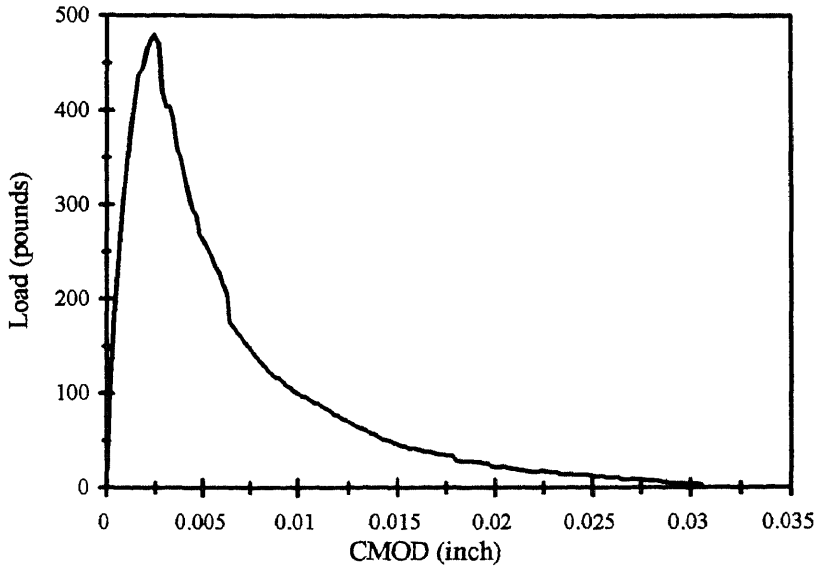

Figure E.2a Load - CMOD Response (Size B beam, Specimen B12)

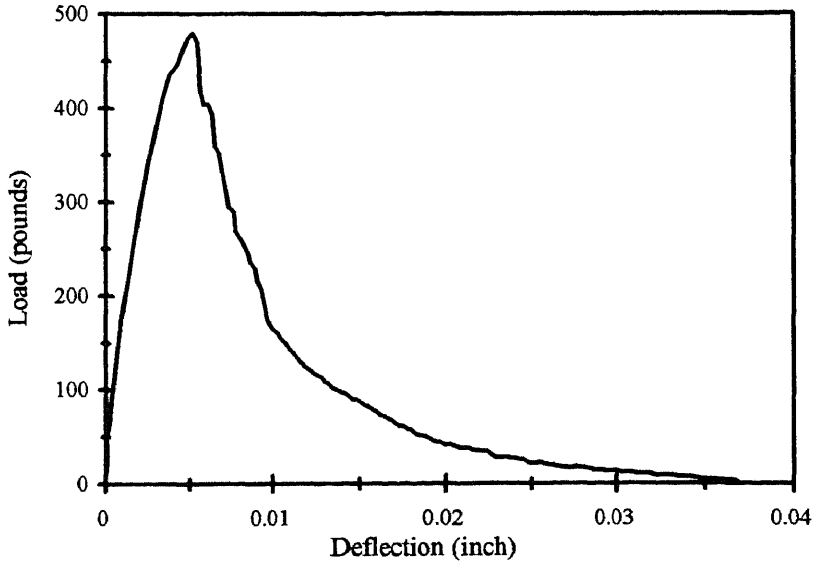

Figure E.2b Load - Deflection Response (Size B beam, Specimen B12)

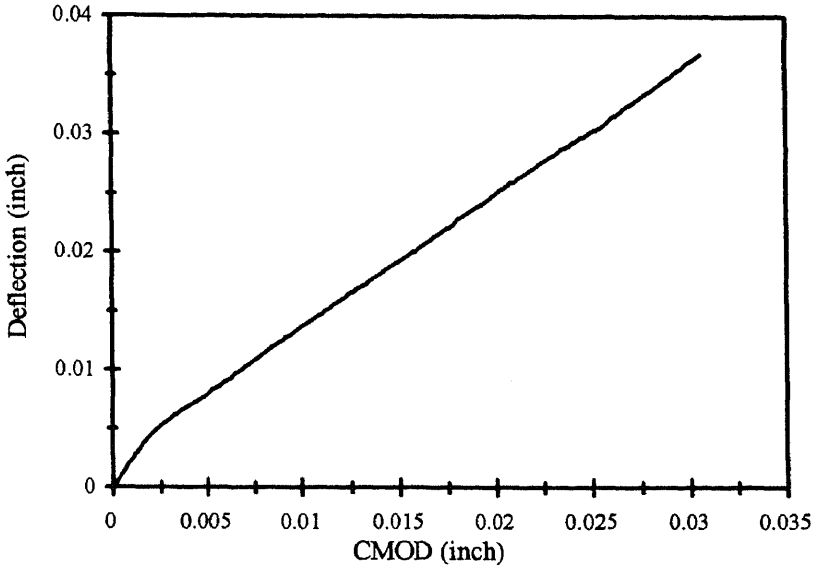

Figure E.2c CMOD-Deflection Response (Size B beam, Specimen B12)

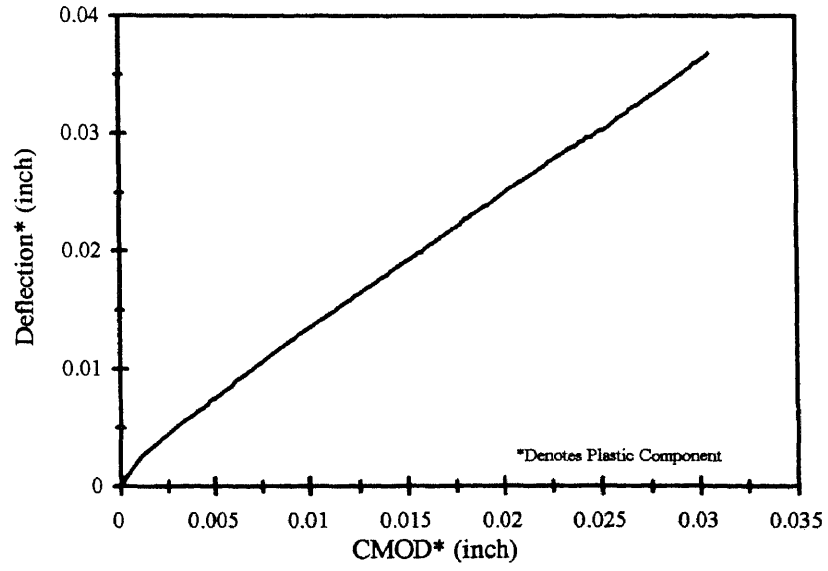

Figure E.2d Plastic Components of CMOD-Deflection Response (Size B beam, Specimen B12)

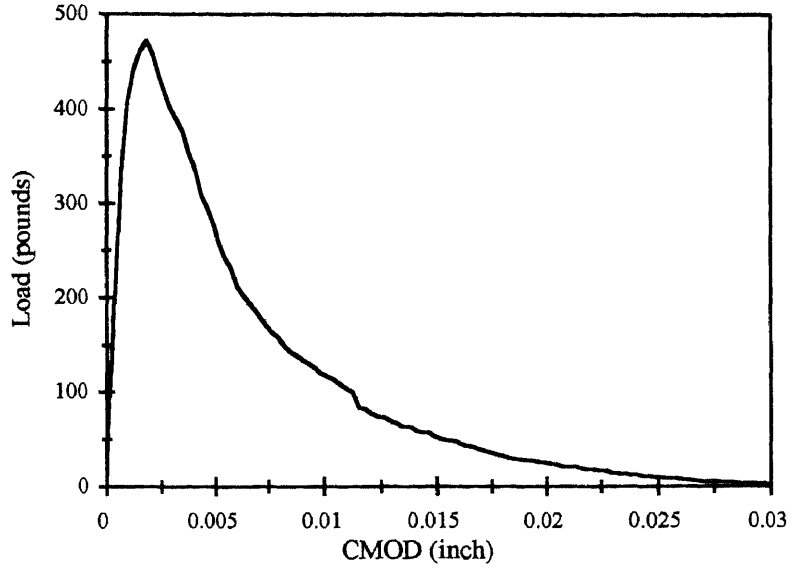

Figure E.3a Load - CMOD Response (Size B beam, Specimen B13)

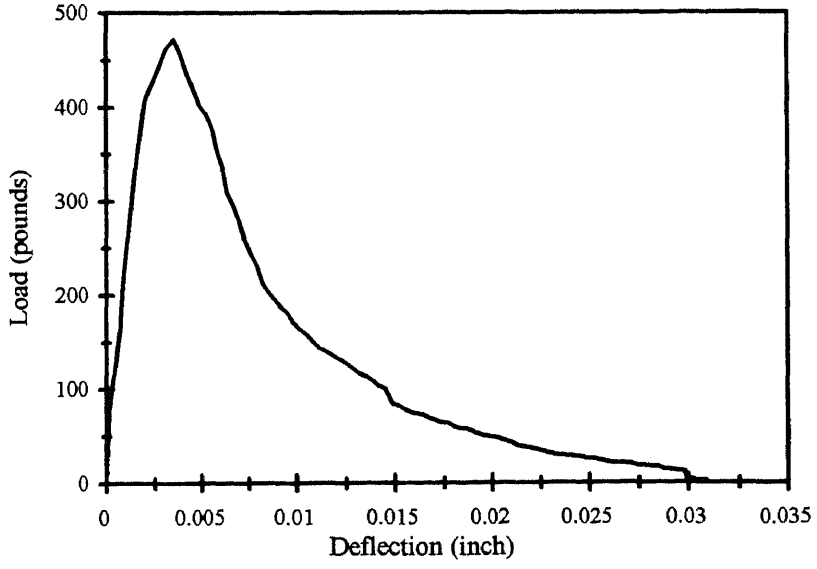

Figure E.3b Load - Deflection Response (Size B beam, Specimen B13)

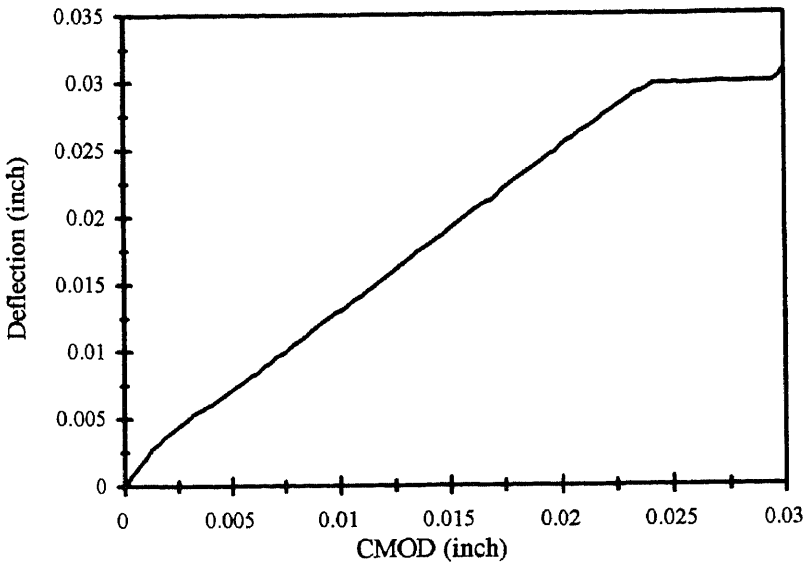

Figure E.3c CMOD-Deflection Response (Size B beam, Specimen B13)

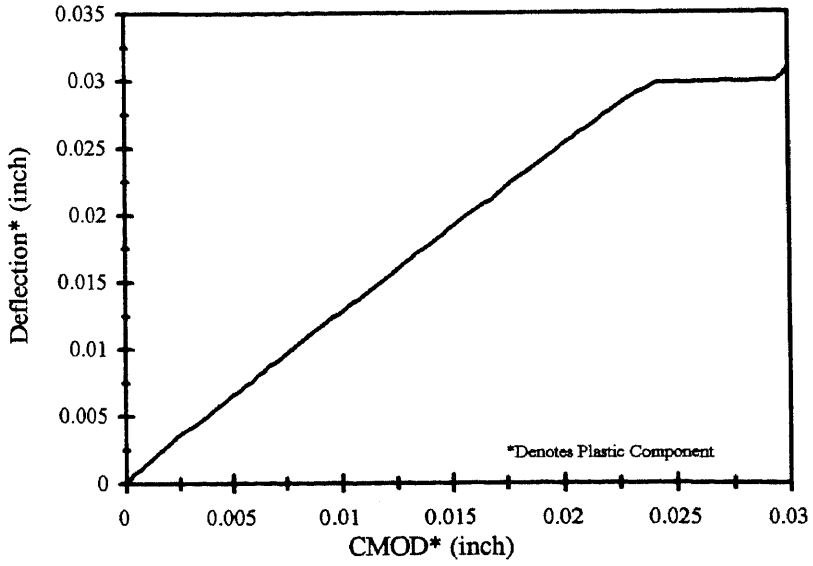

Figure E.3c Plastic Components of CMOD-Deflection Response (Size B beam, Specimen B13)

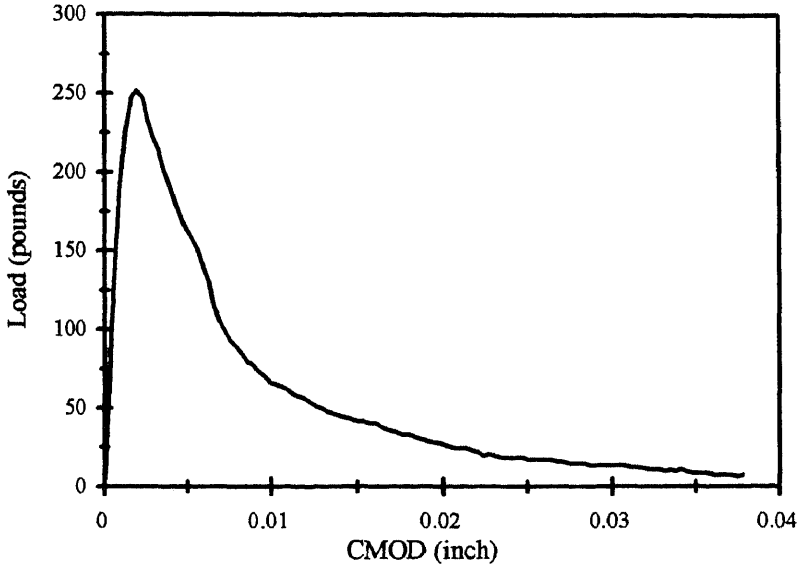

Figure E.4a Load - CMOD Response (Size B beam, Specimen B21)

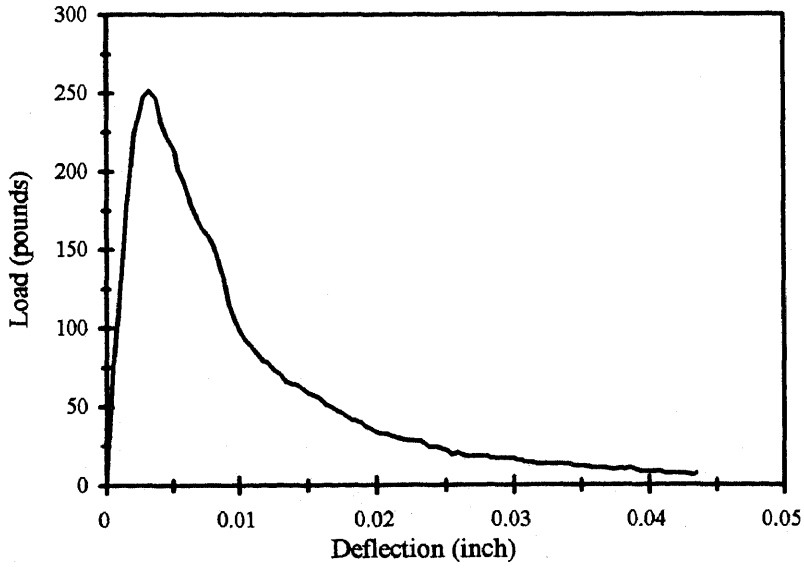

Figure E.4b Load - Deflection Response (Size B beam, Specimen B21)

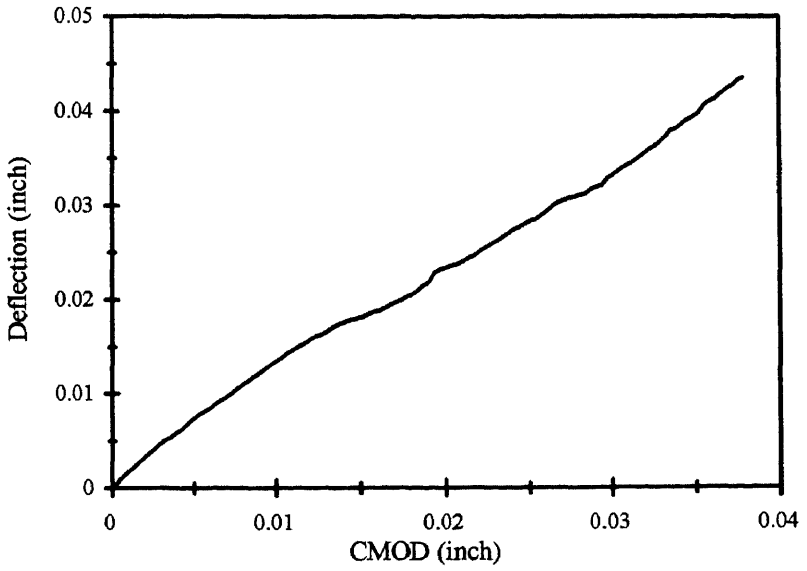

Figure E.4c CMOD-Deflection Response (Size B beam, Specimen B21)

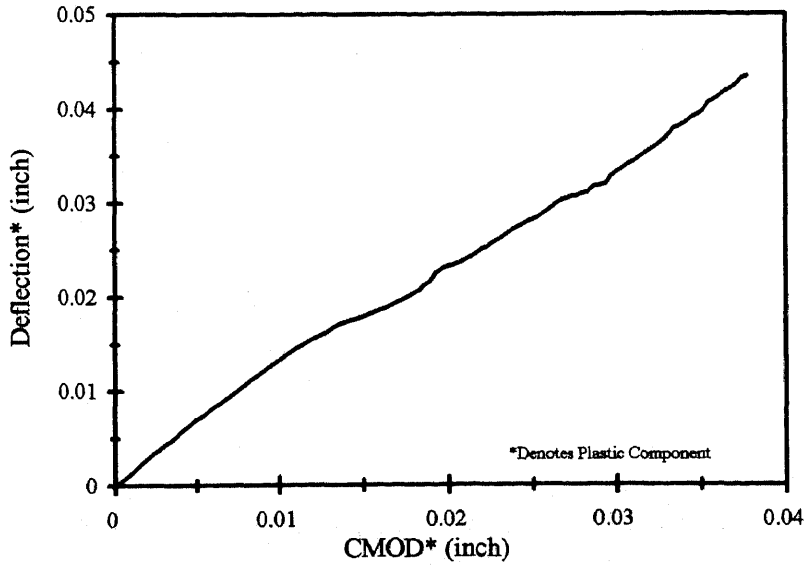

Figure E.4d Plastic Components of CMOD-Deflection Response (Size B beam, Specimen B21)

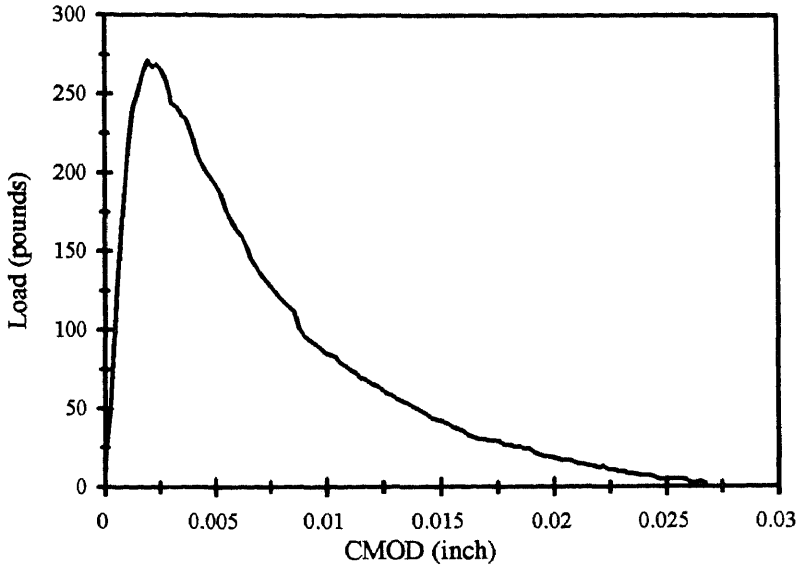

Figure E.5a Load - CMOD Response (Size B beam, Specimen B22)

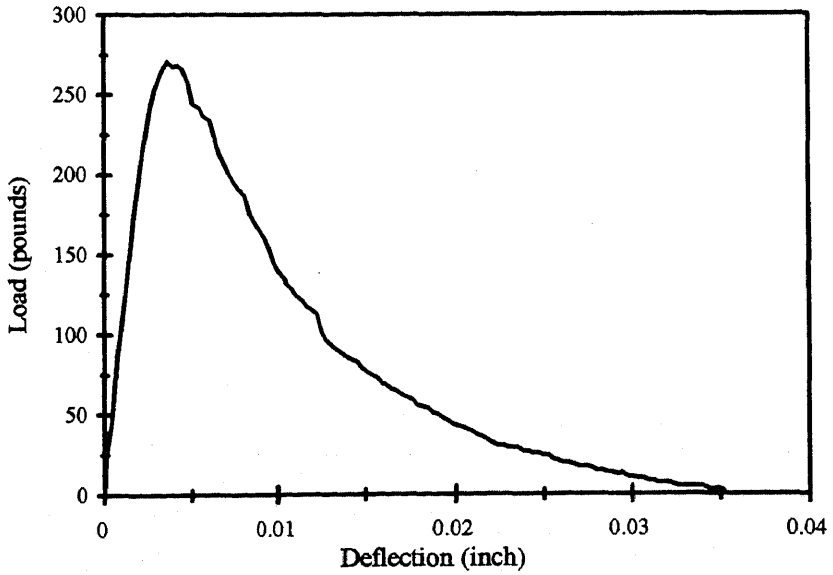

Figure E.5b Load - Deflection Response (Size B beam, Specimen B22)

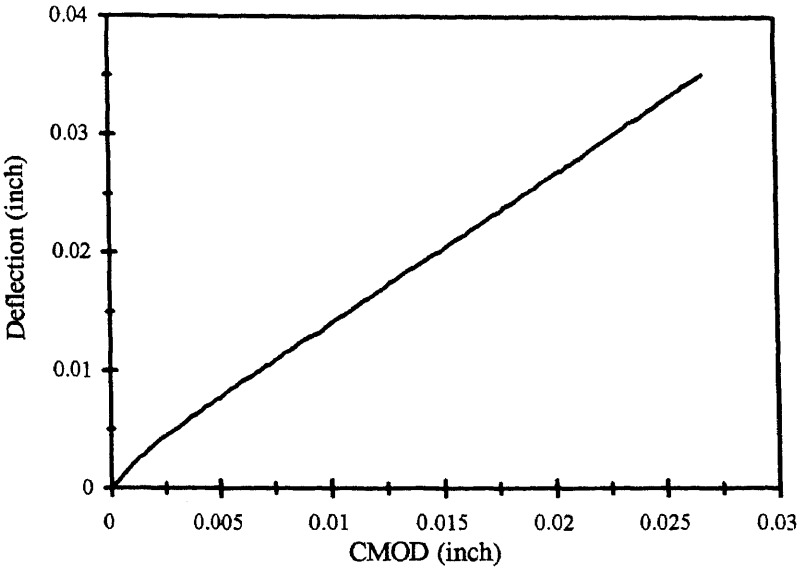

Figure E.5c CMOD-Deflection Response (Size B beam, Specimen B22)

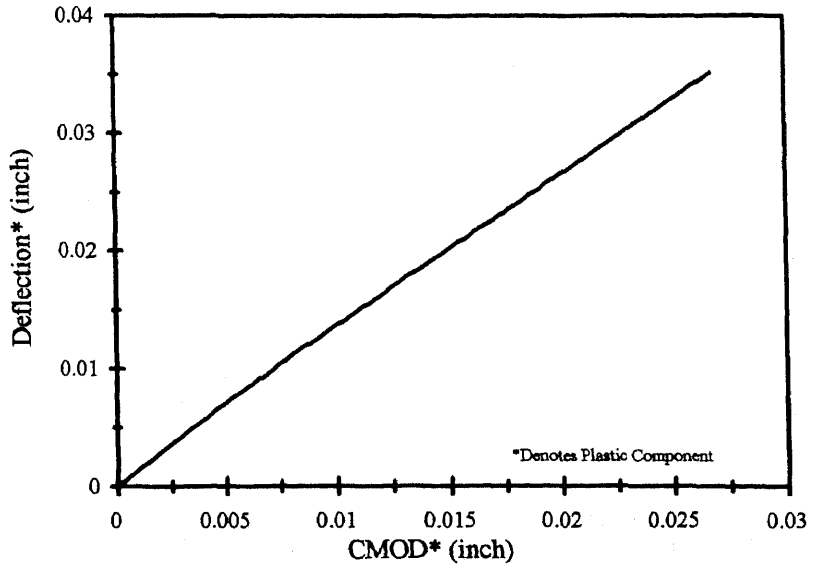

Figure E.5d Plastic Components of CMOD-Deflection Response (Size B beam, Specimen B22)

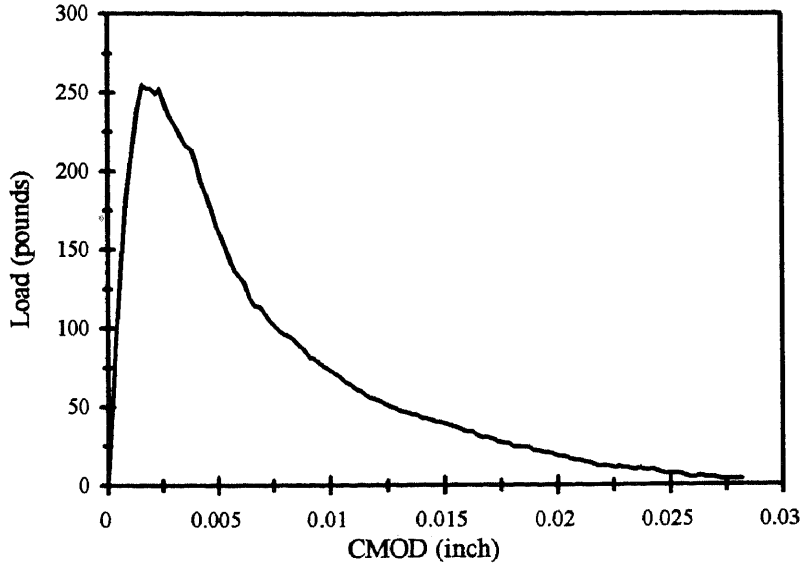

Figure E.6a Load - CMOD Response (Size B beam, Specimen B23)

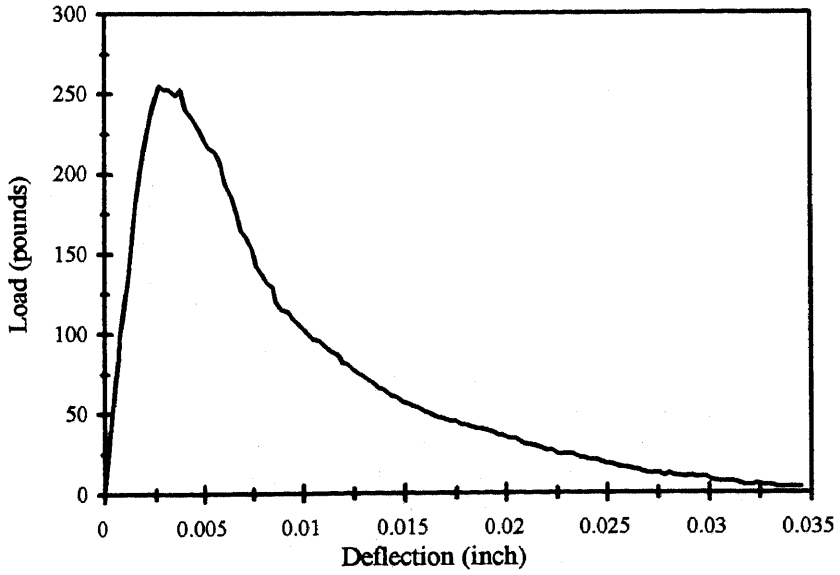

Figure E.6b: Load - Deflection Response (Size B beam, Specimen B23)

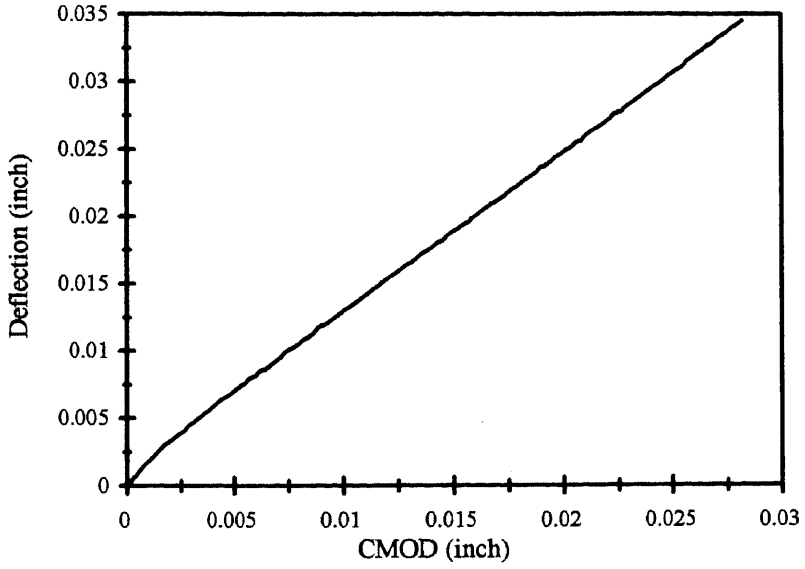

Figure E.6c CMOD-Deflection Response (Size B beam, Specimen B23)

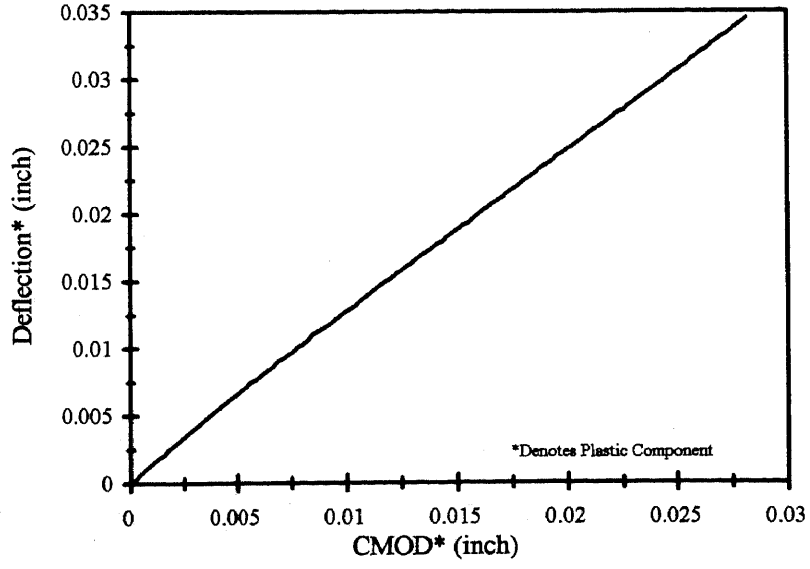

Figure E.6d Plastic Components of CMOD-Deflection Response (Size B beam, Specimen B23)

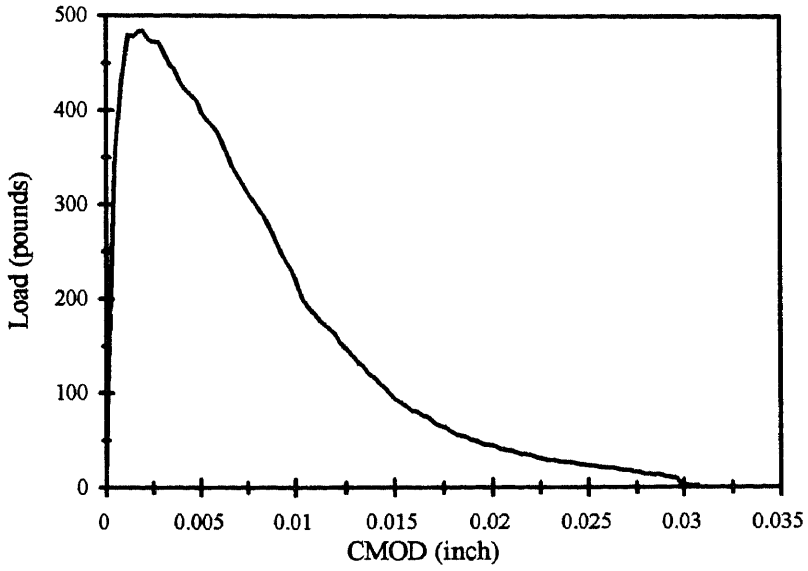

Figure F.1a Load - CMOD Response (Size C beam, Specimen C11)

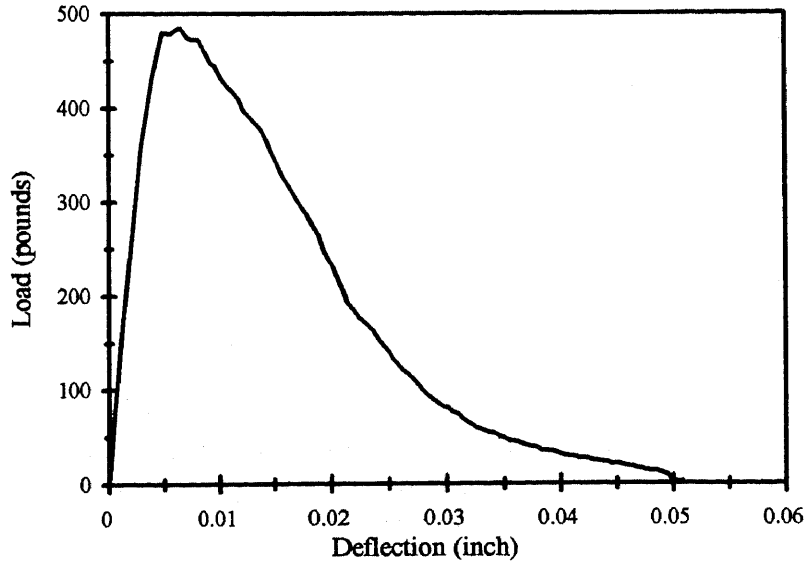

Figure F.1b Load - Deflection Response (Size C beam, Specimen C11)

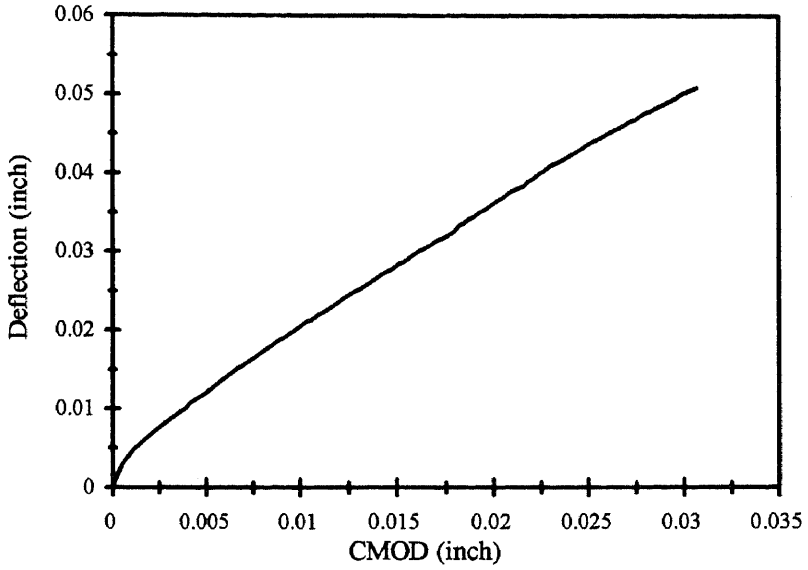

Figure F.1c CMOD-Deflection Response (Size C beam, Specimen C11)

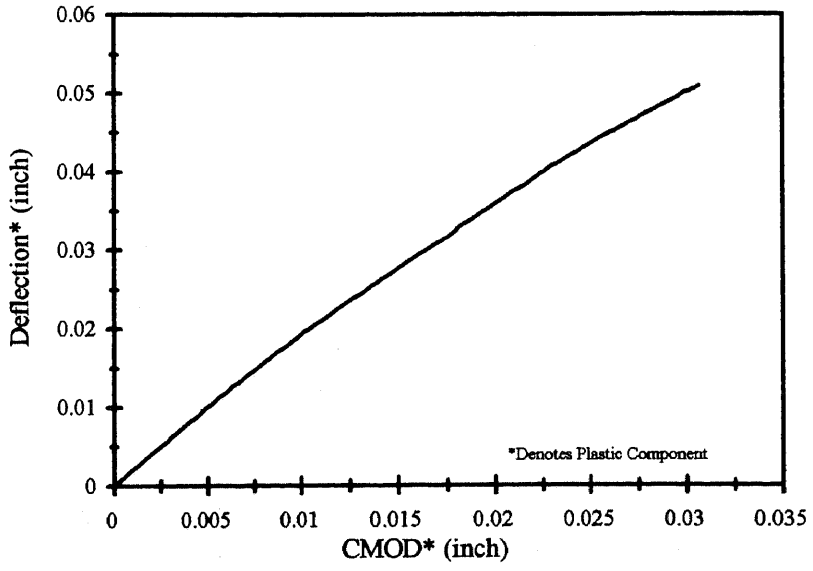

Figure F.1d Plastic Components of CMOD-Deflection Response (Size C beam, Specimen C11)

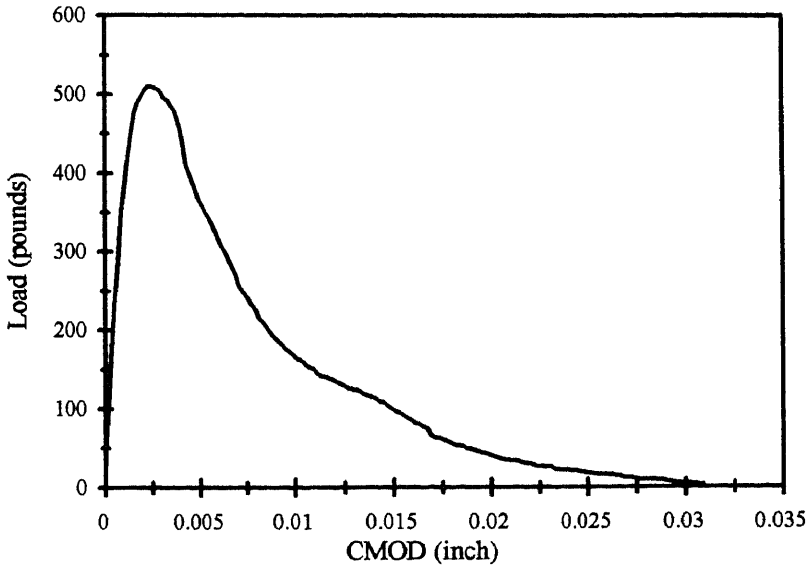

Figure F.2a Load - CMOD Response (Size C beam, Specimen C12)

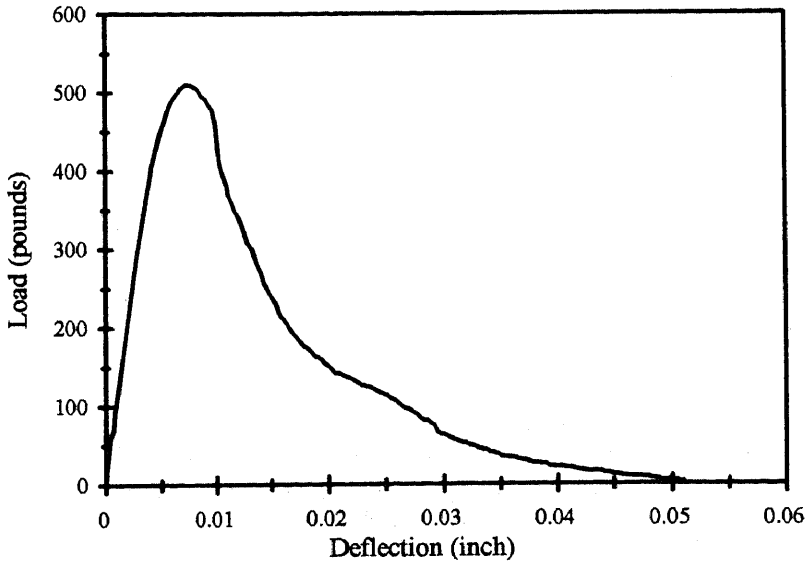

Figure F.2b Load - Deflection Response (Size C beam, Specimen C12)

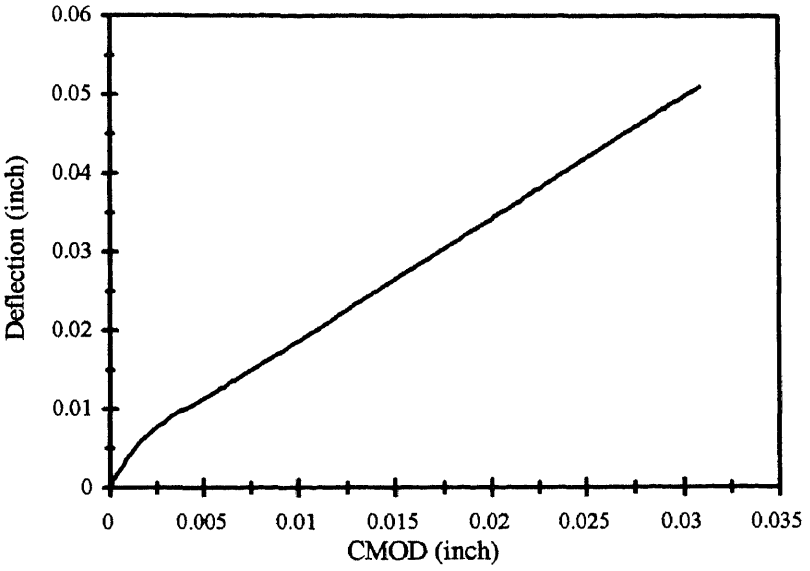

Figure F.2c CMOD-Deflection Response (Size C beam, Specimen C12)

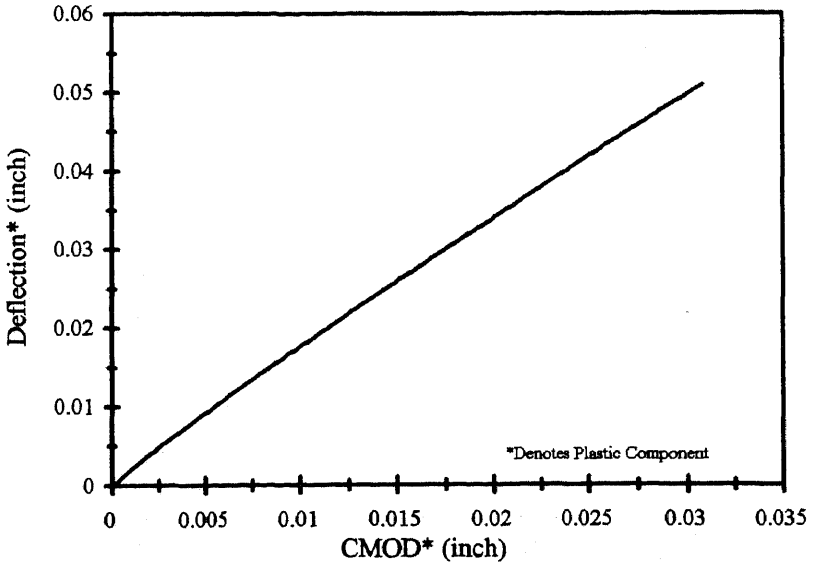

Figure F.2d Plastic Components of CMOD-Deflection Response (Size C beam, Specimen C12)

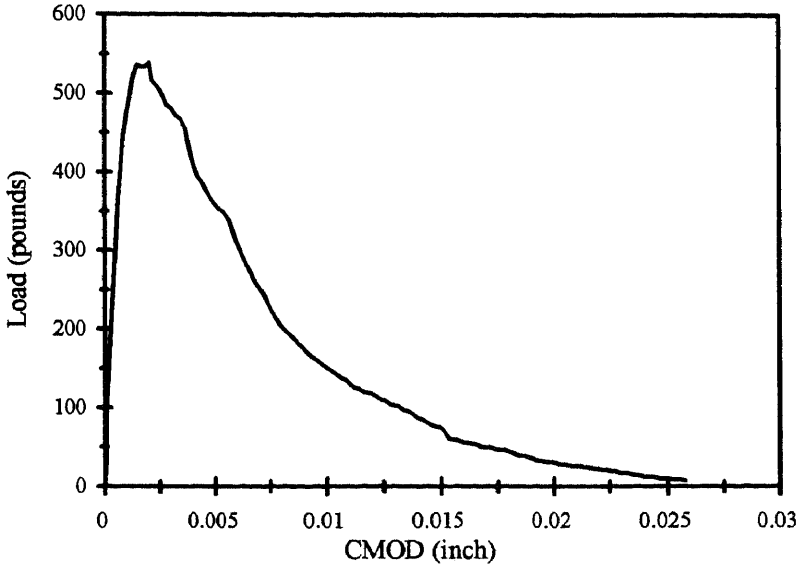

Figure F.3a Load - CMOD Response (Size C beam, Specimen C13)

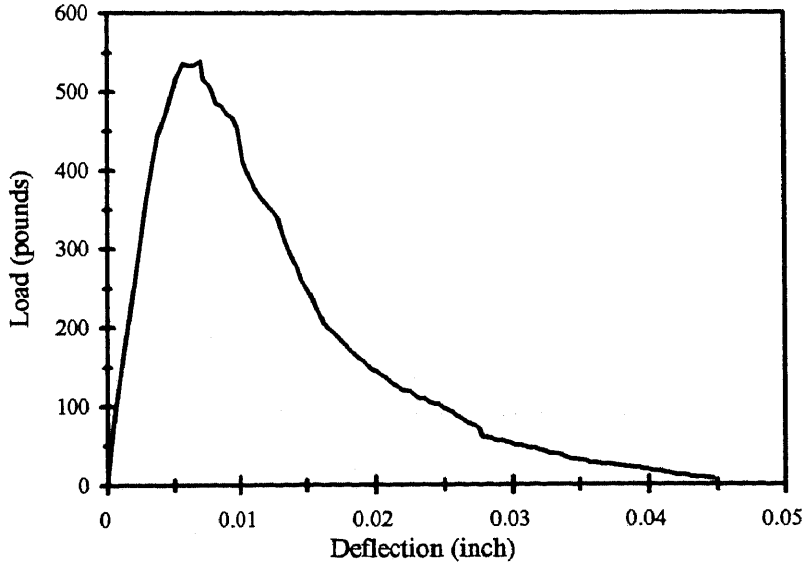

Figure F.3b Load - Deflection Response (Size C beam, Specimen C13)

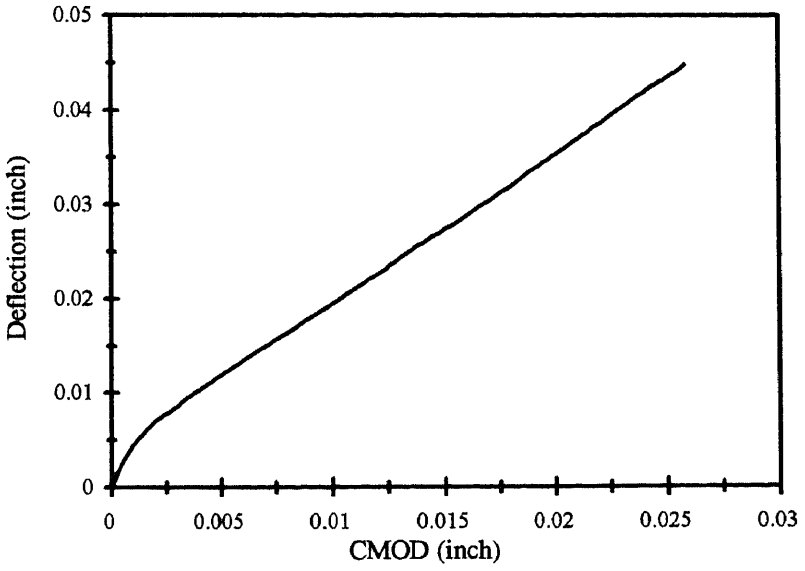

Figure F.3c CMOD-Deflection Response (Size C beam, Specimen C13)

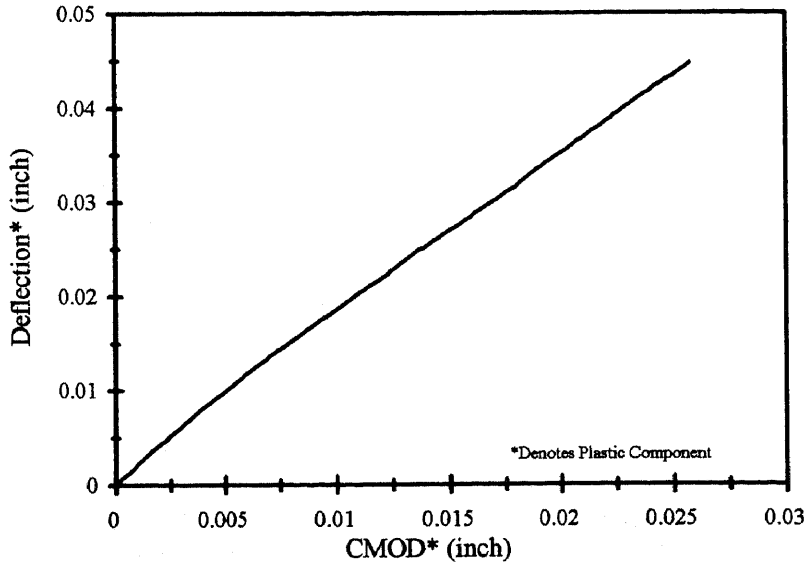

Figure F.3d Plastic Components of CMOD-Deflection Response (Size C beam, Specimen C13)

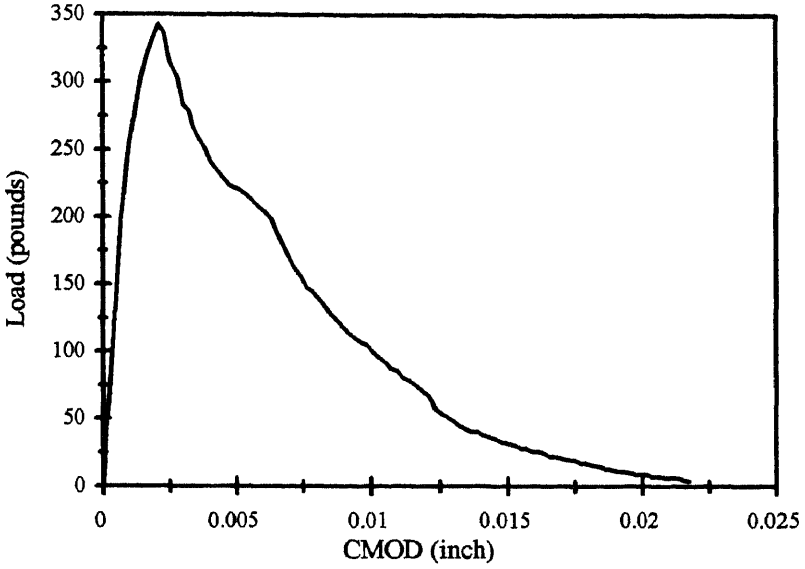

Figure F.4a Load - CMOD Response (Size C beam, Specimen C21)

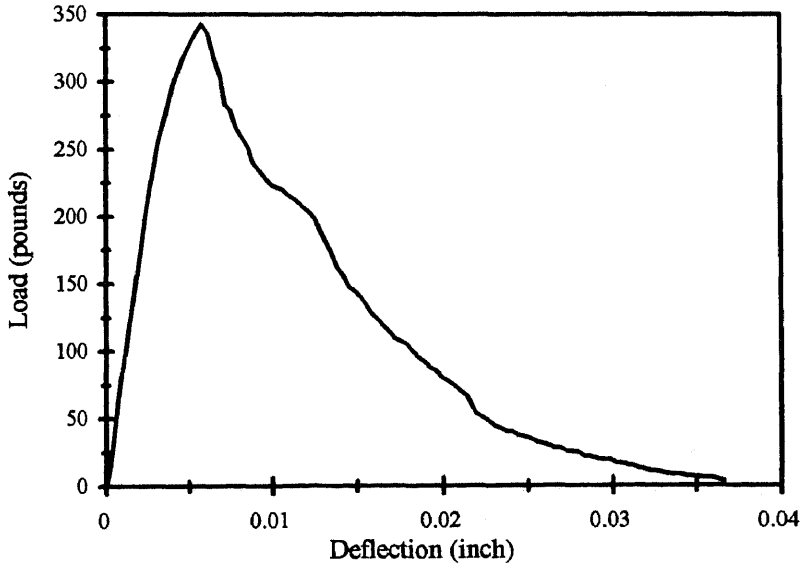

Figure F.4b Load - Deflection Response (Size C beam, Specimen C21)

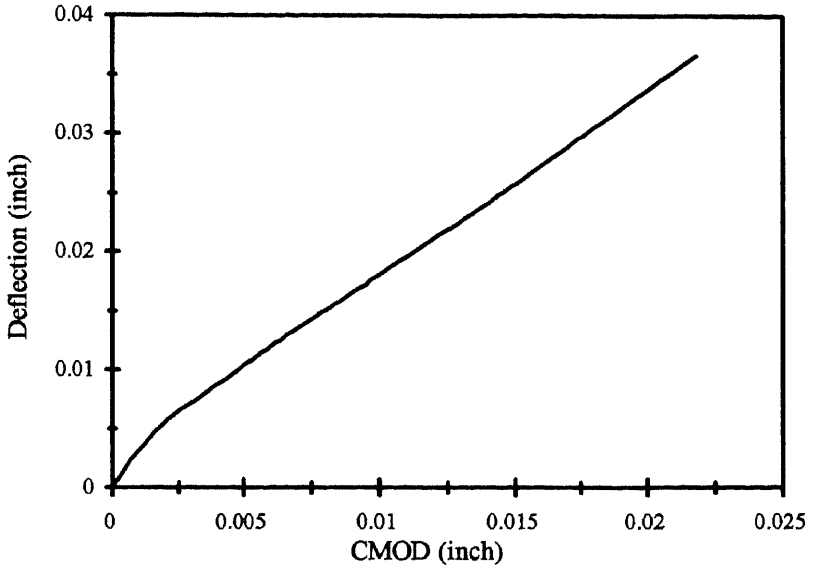

Figure F.4c CMOD-Deflection Response (Size C beam, Specimen C21)

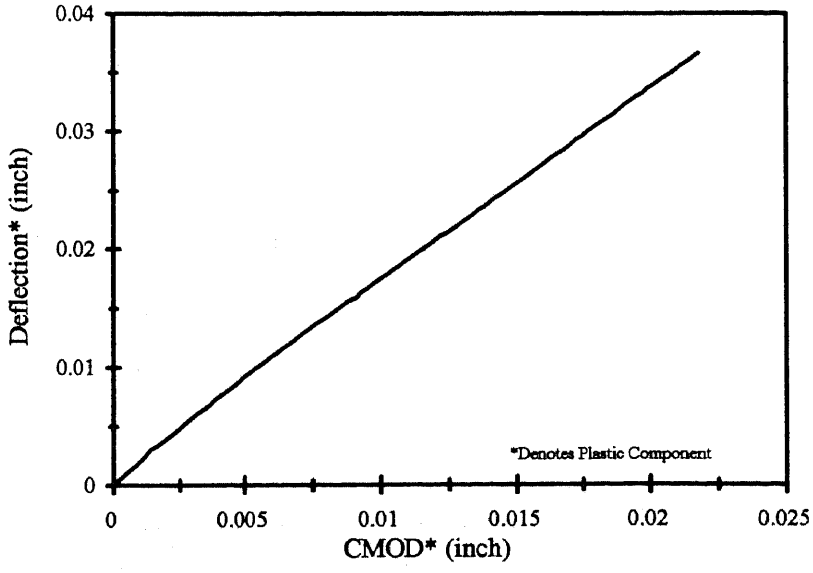

Figure F.4d Plastic Components of CMOD-Deflection Response (Size C beam, Specimen C21)

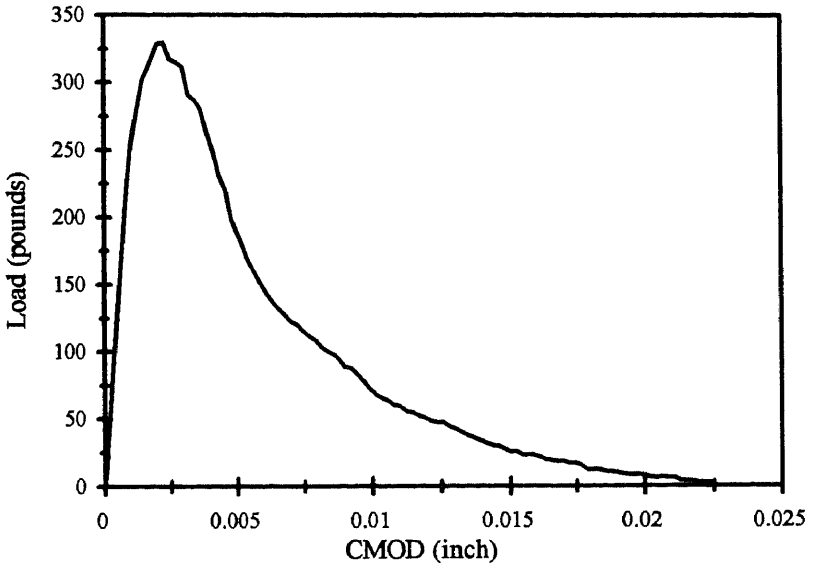

Figure F.5a Load - CMOD Response (Size C beam, Specimen C22)

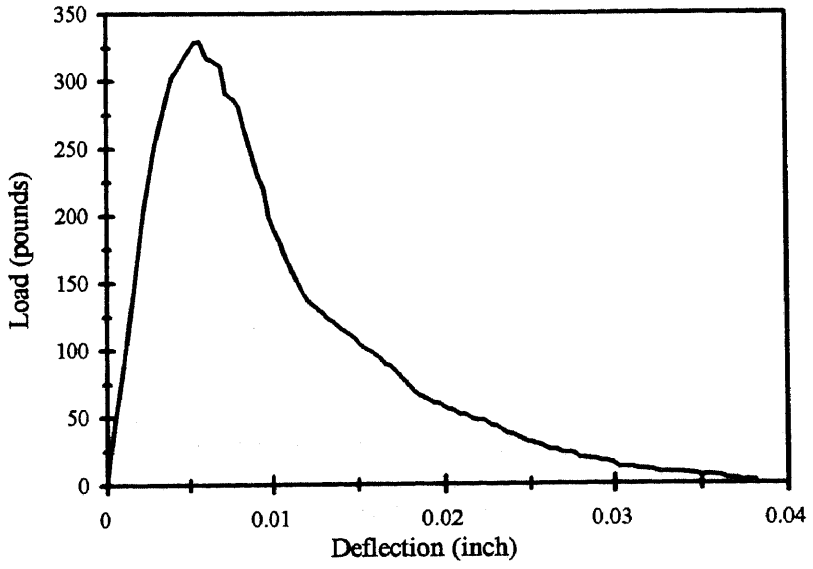

Figure F.5b Load - Deflection Response (Size C beam, Specimen C22)

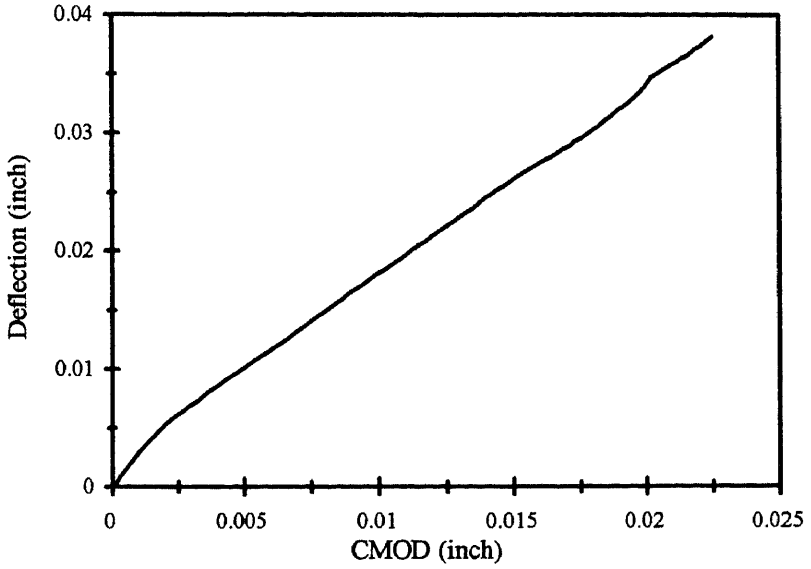

Figure F.5c CMOD-Deflection Response (Size C beam, Specimen C22)

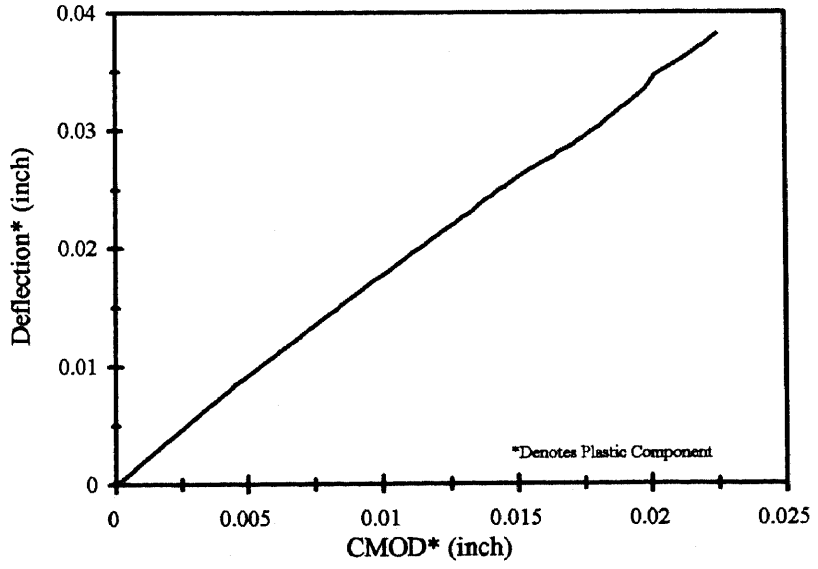

Figure F.5d Plastic Components of CMOD-Deflection Response (Size C beam, Specimen C22)

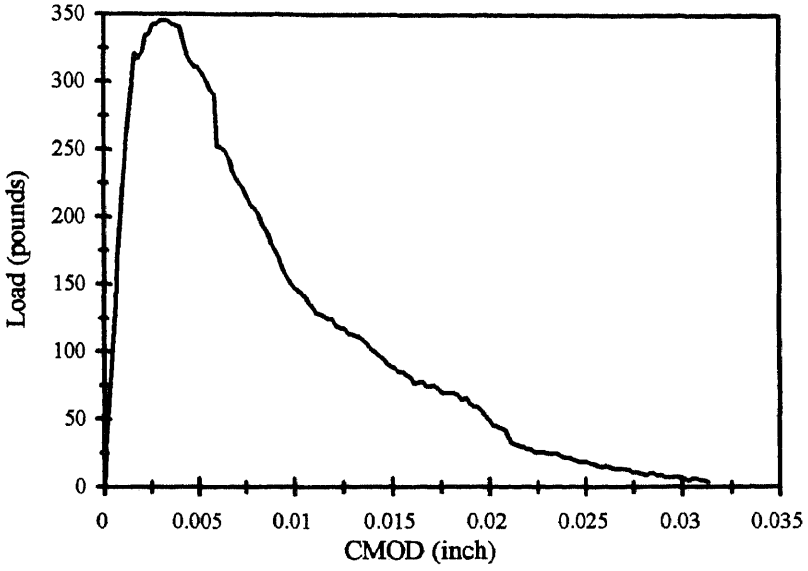

Figure F.6a Load - CMOD Response (Size C beam, Specimen C23)

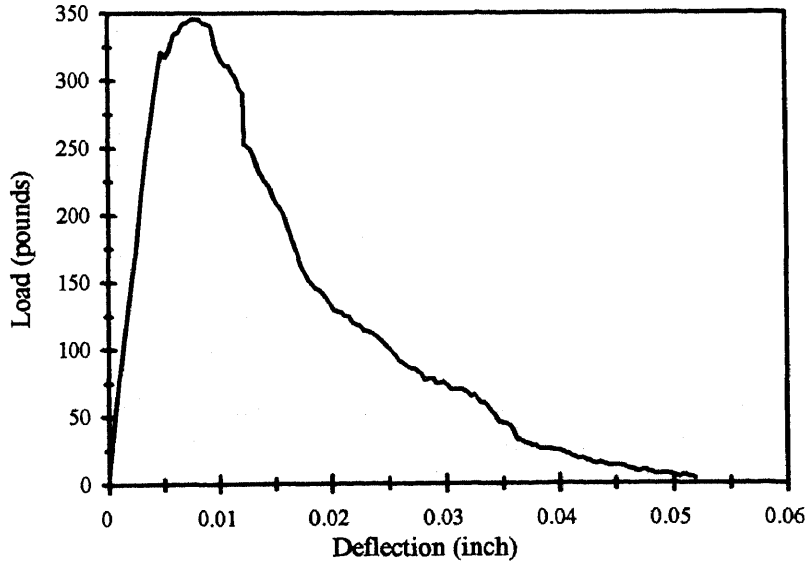

Figure F.6b Load - Deflection Response (Size C beam, Specimen C23)

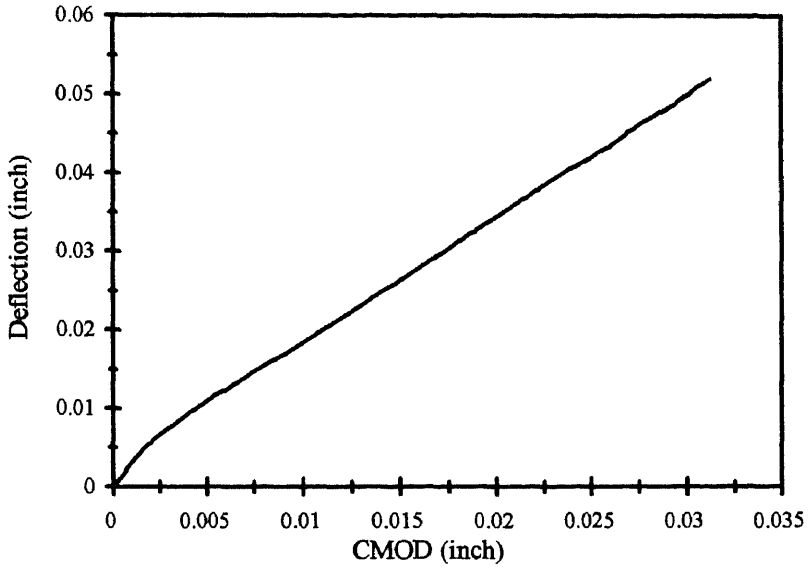

Figure F.6c CMOD-Deflection Response (Size C beam, Specimen C23)

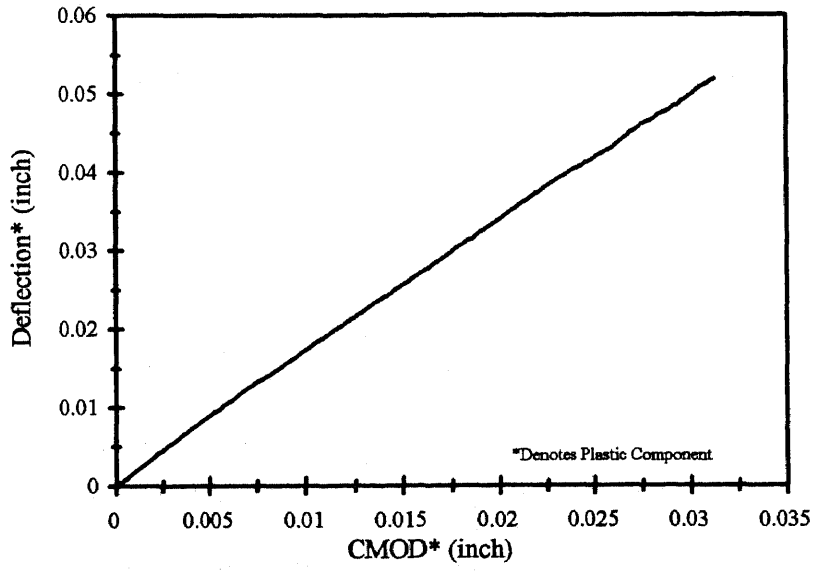

Figure F.6d Plastic Components of CMOD-Deflection Response (Size C beam, Specimen C23)

REFERENCES

ASTM 1983. "Standard Test Method for Plane-Strain Fracture Toughness of Metallic Materials," Standard E399-83. *Annual Book of ASTM Standards. V. 03-01*: 519-554.

Barrenblatt, G. I. 1959. "The Formation of Equilibrium Cracks during Brittle Fracture, General Ideas and Hypothesis, Axially Symmetric Cracks," *Prikl. Mat. Mekh., V. 23, No. 3*: 434-444.

Barrenblatt, G. I.1962. "The Mathematical Theory of Equilibrium Cracks in Brittle Fracture," *Advanced Appl. Mech., V. 7*: 55-129.

Bazant, Z. P. 1976 "Instability, Ductility and Size Effect in Strain- Softening Concrete," *J. of the Engng. Mech. Div., ASCE, V. 102, No. EM2*: 331-344.

Bazant, Z. P. 1982. "Crack Band Model for Fracture of Geomaterials," *Proc., 4th Int. Conf. of Numer. Meth. in Geomech.*, Ed. Eisenstein, Z., Edmonton, Alberta, V. 3: 1137-1152.

Bazant, Z. P. 1984. "Size Effect in Blunt Fracture: Concrete, Rock, Metal," *J. Engng. Mech., ASCE, V. 110, No. 4*: 518-535.

Bazant, Z. P. 1985. "Fracture Mechanics and Strain-Softening in Concrete," *Preprints, U.S.-Japan Seminar on Finite Element Analysis of Reinforced Concrete Structures, Tokyo, V. 1*: 47-69.

Bazant, Z. P., and L. Cedolin. 1979. "Blunt Crack Band Propagation in Finite Element Analysis," *J. Engng. Mech. Div., ASCE, V. 105, No. EM2, Proc. Paper 14529*: 297-315.

Bazant, Z. P., and L. Cedolin. 1983. "Finite Element Modeling of Crack Band Propagation," *J. Struct. Engng., ASCE, V. 109, No. ST2*: 69-92.

Bazant, Z. P., and L. F. Esteussoro. 1979. "Surface Singularity and Crack Propagation," *Int. J. of Solids and Struct., V. 15*: 405-426

Bazant, Z. P. and M. T. Kazemi. 1988. "Determination of Fracture Energy, Process Zone Length and Brittleness Number from Size Effect, with Application to Rock and Concrete," *Report 88-7/498d* Center for Concrete and Geomaterials, Northwestern Univ., Evanston; Illinois.

Bazant, Z. P. and M. T. Kazemi. 1989a. "Size Effect on Diagonal Shear Failure of Beams without Stirrups," *Report No. 89-8/498S*, Center for Advanced Cement-Based Materials, Northwestern Univ., Evanston, Illinois.

Bazant, Z. P. and M. T. Kazemi. 1989b. "Size Dependence of Concrete Fracture Energy Determined by RILEM Work-of-Fracture Method," *Report No. 89- 12/B623s, Center for Advanced Cement-Based Materials, Northwestern Univ.*, Evanston, Illinois.

Bazant, Z. P., J. K. Kim and P. A. Pfeiffer. 1986. "Determination of Fracture Properties from Size Effect Tests," *J. of Struct. Engng., ASCE, V. 112, No. 2*: 289-307.

Bazant, Z. P. and B. H. Oh. 1983a. "Crack Band Theory for Fracture of Concrete," *Mater. and Struct., V. 16, No. 93*: 155-177.

Bazant, Z. P. and B. H. Oh. 1983b. "Spacing of Cracks in Reinforced Concrete," *J. of Struct. Engng., V. 109, No. 9*: 2066-2085

Bazant, Z. P., and P. C. Prat. 1988a. "Measurement of Mode III Fracture Energy of Concrete," *Nuclear Engng. and Des., V. 106*: 1-8.

Bresler, B., and E. Wollack. 1952. "Shear Strength of Concrete," *Report, Dept. of Civil Engng., University of California, Berkeley; presented at Annual Convention, Structural Engineers Association of California, held in Riverside, CA.*

Broek, D. 1982. *Elementary Engineering Fracture Mech*anics, 3rd ed., Martinus Nijhoff, Leyden, Netherlands, (also 4th ed., Martinus Nijhoff, Dordrecht, 1986.)

Crisfield, M. A. 1981., "A Fast Incremental/Iteration Solution Procedure that handles 'Snap Through'," *Computers and Structures, Vol. 13*: 55 - 62

De Borst, R. 1984. "Application of Advanced Solution Techniques to Concrete Cracking and Non-Associated Plasticity," *Numerical Methods for Non-linear Problems, V. 2*: 314-325.

Dugdale, D. S. 1960. "Yielding of Steel Sheets Containing Slits," *J. of Mech. and Phys. of Solids, V. 8*: 100-108.

Evans, R. H., and M. S. Marathe. 1968. "Microcracking and Stress-Strain Curves for Concrete in Tension," *Mater. and Struct., V. 1*: 61-64.

Gettu, R., Z. P. Bazant and M. E. Karr. 1990. "Fracture Properties and Brittleness of High Strength Concrete," *J. of ACI, V. 90*. 608-618.

Gopalaratnam, V. S., and S. P. Shah. 1985 "Softening Response of Plain Concrete in Direct Tension,." *J. of ACI, V. 82*. 310-324.

Griffith, A. 1921. "The Phenomenon of Rupture and Flow in Solids," *Phil. Trans. Royal Soc. of London, Series A, V. 221*: 163-198.

Griffith, A. 1924. "Theory of Rupture," *Proc., Ist Int. Congress on Appl. Mech.*, Delft: 55-63.

Gustaffson, P. J., and A. Hillerborg. 1988. "Sensitivity in Shear Strength of Longitudinally Reinforced Concrete Beams to Fracture Energy of Concrete," *ACI Struct. J., V. 85*: 286-294.

Hassanzadeh, M., A. Hillerborg and Z. Ping. 1987. "Tests of Material Properties in Mixed Mode I and II," *Proc., SEM-RILEM Int. Conf on Fracture of Concrete and Rock*: 353- 358.

Hillerborg, A. 1980. "Analysis of Fracture by Means of the Fictitious Crack Model, Particularly for Fiber Reinforced Concrete," *Int. J. of Cem. Composites, V. 2, No. 4*: 177-185.

Hillerborg, A. 1983 "Examples of Practical Results Achieved by Means of the Fictitious Crack Model," *Preprints, Prager Symp. on Mechanics of Geomaterials: Rocks, Concretes, Soils*: 611-614.

Hillerborg, A. 1985a. "Numerical Methods to Simulate Softening and Fracture of Concrete." *Fract. Mech. of Concrete: Structural Application and Numerical Calculation*: 141-170.

Hillerborg, A. 1985b. "The Theoretical Basis of Method to Determine the Fracture Energy G_F of Concrete," *Mater. and Struct. V. 18, No. 106*: 291-296

Hillerborg, A. 1985c "Results of Three Comparative Test Series for Determining the Fracture Energy G_F of Concrete," *Mater. and Struct., V. 18*, No: 106: 407-413.

Hillerborg, A., M. Modeer and P. E. Petersson. 1976. "Analysis of Crack Formation and Crack Growth in Concrete by Means of Fract. Mech. and Finite Elements," *Cem. and Concr. Res., V. 6*: 773-782.

Hsu, L. S. M. and C. T. T. Hsu, 1994. "Complete Stress-Strain Behavior of High Strength Concrete under Compression," *Magazine of Concrete Research, V. 46,* No. 169. 301-312.

Hughes, B. P. and B. P. Chapman, 1966. "The Complete Stress-Strain Curve for Concrete in Direct Tension," *RILEM (Paris) Bull. No. 30*, 95-97.

Ingraffea, A. R., and M. J. Panthaki,. 1985. "Shear Fracture Tests of Concrete Beams," *Finite Element Analysis of Reinforced Concrete Structures, Tokyo*: 151-173.

Ingraffea, A. R., and W. Gerstle. 1985 "Nonlinear Fracture Models for Discrete Crack Propagation," *Application of Fract. Mech. to Cementitious*: 171-209.

Ingraffea, A. R. and V. Saouma. 1985. "Numerical Modeling of Discrete Crack Propagation in Reinforced and Plain Concrete," *Fract. Mech. of Concrete: Structural Application and Numerical Calculation.*: 171-225.

Irwin, G.R. 1958. "Fracture" *Handbuch der Physik, Vol. VI*, Ed. Flugge, Springer: Berlin, Germany.: 551-590.

Jenq, Y. S., and S. P. Shah. 1985a. "A Fracture Toughness Criterion for Concrete," *Engng. Fract. Mech., V. 21, No. 5*: 1055-1069.

Jenq, Y. S., and S. P. Shah. 1985b. "Two Paramaeter Fracture Model for Concrete," *J. of Engng. Mech., ASCE, V. 111, No. 10*: 1227-1241.

Jenq, Y. S., and S. P. Shah. 1986 "Crack Propagation in Fiber Reinforced Concrete," *J. of Struc. Engng., ASCE*, V. 112, No. 1: 19-34.

Jenq, Y. S., and S. P. Shah. 1987a. "Fract. Mech. and Constitutive Modeling of Concrete," *Constitutive Laws for Engineering Materials: Theory and Applications*, ed. Desai, C. S. et al., Vol. II, Elsevier, New York, NY.

Jenq, Y. S., and S. P. Shah. 1987b "Mixed Mode Fracture Parameters of Concrete,". *Proc., SEM-RILEM Int. Conf on Fracture of Concrete and Rock*, eds. Shah, S. P. and Swartz, S. E., Houston, TX: 359-369.

Jenq, Y. S., and S. P. Shah. 1988b. "On the Concrete Fracture Testing Methods," *Preprints of the Proc., Int. Workshop on Fracture Toughness and Fracture Energy - Test Methods for Concrete and Rock*, Sendai, Japan.

John, R. and S. P. Shah. 1985. "Strain Rate Effects on Mode I Crack Propagation in Concrete," *Proc., Int. Conf on Fract. Mech. of Concrete*, Lausanne.

John, R. and S. P. Shah. 1987 "Effect of High Strength and Rate of Loading on Fracture Parameters of Concrete," *Proc., SEM-RILEM Int. Conf. on Fracture of Concrete and Rock*, eds. Shah, S. P. and Swartz, S. E., Houston, TX.: 35-52.

John, R. and S. P. Shah. 1989b. "Fract. Mech. Analysis of High Strength Concrete," *J. of Mater. in Civil Engng., ASCE*, V. 1, No. 4: 185-198.

Kaplan, M. F. 1961. "Crack Propagation and the Fracture of Concrete," *ACI J.*, V. 58, No. ll.: 591-610.

Kesler, C. E.; D. J. Naus and J. L. Lott. 1971. "Fract. Mech.- Its Applicability to Concrete," *Proc., Int. Conf. on the Mechanical Behavior of Materials, Kyoto, The Soc. of Mater. Sci.*, Vol. IV, 1972: 113-124.

Kim, S. K. 1991. "The Constant Fracture Angle Model for Cementitious Materials." *Dissertation Draft,* Submitted in May 1991 to the Dept. of Civil and Environmental Engng., NJIT. (Ph.D. Dissertation submitted in May 1996).

Navalurkar, R. K. and F. Ansari. 1994. "Tensile Properties of High Performance Concrtete," , *Proc. Int. Workshop on High Performance Concrete*, ACI, Bangkok, Thailand, Nov. 21-22 : 283-293.

Petersson, P. E. 1980a. "Fracture Energy of Concrete: Method of Determination," *Cem. Concr. Res., V. 10,* : 78-79.

Petersson, P. E. 1980b. "Fracture Mechanical Calculations and Tests for Fiber-Reinforced Concrete," *Proc., Advances in Cement Matrix Composites, Mater. Res. Soc. Annual Meeting*, Boston, MA,: 95-106.

Petersson, P. E. 1981, "Crack Growth and Development of Fracture Zones in Plain Concrete and Similar Materials," *Report TVBM - 1006, Div. of Building Materials, Lund Inst. of Tech.*, Lund, Sweden.

Planas, J. and M. Elices. 1988b. "Conceptual and Experimental Problems in the Determination of the Fracture Energy of Concrete," *Proc., Int. Workshop on "Fracture Toughness and Fracture Energy, Test Methods for Concrete and Rock*, Tohoku Univ., Sendai, Japan.: 203-212.

Powell, G. and J. Simons. 1981. "Improved Iterative Strategy for Nonlinear Structures," *Int. J. for Numer. Methods in Engng. Vol. 17.*: 1455-1467

Ramm, E. 1981 "Strategies for Tracing the Nonlinear Response Near Limit Points," *Nonlinear Finite Element Analysis in Structural Mechanics*, Eds. By Wunderlich, E., K. J. Bathe and E. Stein, Springer-Verlag, Berlin.

Rashid, Y. R. , 1968, "Analysis of Prestressed Concrete Pressure Vessels," *Nuclear Engng. and Des., Vol. 7,* No. 4.: 334-355.

Ratanalert, S. , and M. Wecharatana. 1989. "Evaluation of Existing Fracture Models in Concrete,", *Fracture Mechanics: Application to Concrete*, Eds. By Li V. C. and and Z. P. Bazant, SP-118, American Concrete Institute, Detriot.

Reinhardt, H. W., and H. A. W. Cornelissen. 1984. "Post-Peak Cyclic Behavior of Concrete in Uniaxial Tensile and Alternating Tensile and Compressive Loading,." *Cem. Concr. Res., V. 14.* No. 2: 263-270.

RILEM, 1985-TC 50-FMC, Fract. Mech. of Concrete, "Determination of the Fracture Energy of Mortar and Concrete by Means of Three-Point Bend Tests on Notched Beams," *RILEM Recommendation, Mater. and Struct., V. 18*, No. 106: 285-296.

Rots, J. G. 1988. "Stress Rotation and Stress Locking in Smeared Analysis of Separation," *Proc., Int. Workshop on Fracture Toughness and Fracture Energy, Test Methods for Concrete and Rock*, Tohoku Univ., Sendai, Japan.

Rots, J. G., and R. de Borst. 1987 "Analysis of Mixed-Mode Fracture in Concrete," *J. of Engng. Mech., ASCE*, V. 113, No. 11: 1739-1758.

Shah, S. P. 1990. "Determination of fracture parameters (KIC and CTODc) of plain concrete using three-point bend tests," *Mater. and Struct., V. 23* : 457-460.

Swartz, S. E. and S. T. Yap. 1988. "The Influence of Dead Load on Fracture Energy Measurements Using the RILEM Method." *Mater. and Struct., V. 21*: 410-415.

Tada, H., P. C. Paris and Irwin. 1985. *The Stress Analysis of Cracks Handbook*, 2nd ed., Paris Productions, St. Louis.

Wang, W. and C. T. T. Hsu. 1994. " Fatigue Crack Growth Rate of Metal by Plastic Energy Damage Accumulation Theory," *Engng. Mech., ASCE V. 120, No. 4:* 776-795.

Wang, W., C. T. T. Hsu and D. Blackmore. 1994. "Mathematical Treatments in Generalized Process Zone Theory in Fracture Mechanics," *Tech. Report Struct. Series, No. 94-1*. Dept. of Civil and Environmental Engng., NJIT.

Wecharatana, M. and S. P. Shah. 1983a. "Predictions of Nonlinear Fracture Process Zone in Concrete," *J. Engng. Mech., ASCE V. 109, No. 5*: 1231-1246.

Wecharatana, M. and S. P. Shah. 1983b. "A Model for Predicting Fracture Resistance of Fiber Reinforced Concrete," *Cem. and Conc. Res., V. 13*, No. 6: 819-829.

Xie, J, A. E. Alaa and J. G. MacGregor. 1994. "Numerical Investigation of Eccentrically loaded Tied High Strength Concrete Columns," Structural Engng Report No. 204. Department of Civil Engineering, University of Alberta, Canada.